



저작자표시-비영리-변경금지 2.0 대한민국

이용자는 아래의 조건을 따르는 경우에 한하여 자유롭게

- 이 저작물을 복제, 배포, 전송, 전시, 공연 및 방송할 수 있습니다.

다음과 같은 조건을 따라야 합니다:



저작자표시. 귀하는 원저작자를 표시하여야 합니다.



비영리. 귀하는 이 저작물을 영리 목적으로 이용할 수 없습니다.



변경금지. 귀하는 이 저작물을 개작, 변형 또는 가공할 수 없습니다.

- 귀하는, 이 저작물의 재이용이나 배포의 경우, 이 저작물에 적용된 이용허락조건을 명확하게 나타내어야 합니다.
- 저작권자로부터 별도의 허가를 받으면 이러한 조건들은 적용되지 않습니다.

저작권법에 따른 이용자의 권리는 위의 내용에 의하여 영향을 받지 않습니다.

이것은 [이용허락규약\(Legal Code\)](#)을 이해하기 쉽게 요약한 것입니다.

[Disclaimer](#)

August, 2022
Doctoral
Dissertation

Study on Performance on Volumetric Absorption Solar Collector based on Photo Thermal Conversion Characteristics of Nanofluid

Graduate School of Chosun University

Department of Mechanical Engineering

Jeonggyun Ham

나노유체의 광열변환특성 기반 체적흡수 태양열 집열기의 성능 연구

Study on Performance on Volumetric Absorption
Solar Collector based on Photo Thermal Conversion Characteristics
of Nanofluid

08. 26. 2022

Graduate School of Chosun University

Department of Mechanical Engineering

Jeonggyun Ham

Study on Performance on Volumetric Absorption Solar Collector based on Photo Thermal Conversion Characteristics of Nanofluid

Advisor Cho Hong-Hyeon

This study has been submitted as a doctoral dissertation
in engineering.


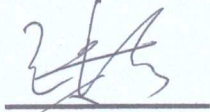
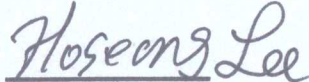
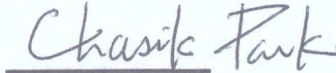
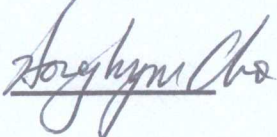
April, 2022

Graduate School of Chosun University

Department of Mechanical Engineering

Jeonggyun Ham

The doctoral dissertation of Jeonggyun Ham has been approved.

Chairman	Chosun University	Dong-Wook Oh, PhD	
Committee member	Chosun University	Jungsoo Park, PhD	
Committee member	Korea University	Hoseong Lee, PhD	
Committee member	Hoseo University	Chasik Park, PhD	
Committee member	Chosun University	Honghyun Cho, PhD	

June, 2022

Graduate School of Chosun University

Contents

CONTENTS	i
LIST OF FIGURES	v
LIST OF TABLES	ix
ABSTRACT(ENGLISH)	x
1. INTRODUCTION	1
1.1. BACKGROUND	1
1.2. NANOFLUID	5
1.3. SOLAR COLLECTING SYSTEM.....	10
1.3.1. Surface absorption solar collector method	13
1.3.2. Volumetric absorption solar collecting method	17
1.4. PURPOSE OF THIS STUDY	22
2. MANUFACTURE AND STABILITY OF NANOFLUID	24
2.1. PREPARATION OF NANOFLUID AND SYNTHESIS OF NANOPARTICLE.....	24
2.2. MANUFACTURE OF NANOFLUIDS	28
2.3. NANOFLUID STABILITY EVALUATION.....	31
2.3.1. TEM image analysis	33
2.3.2. Zeta potential analysis result	36
2.4. THERMAL PROPERTIES OF NANOFLUID	38

2.4.1. Thermal conductivity of nanofluid	38
2.4.2. Viscosity of nanofluid.....	42

3. OPTICAL PROPERTIES AND PHOTO THERMAL

CONVERSION PERFORMANCE OF NANOFLUID 46

3.1. OPTICAL PROPERTIES MEASUREMENT METHOD OF NANOFLUID.....	46
3.2. EXPERIMENT METHOD TO MEASURE PHOTO THERMAL CONVERSION PERFORMANCE OF NANOFLUID.....	53
3.2.1. Experimental setup for photo thermal conversion.....	53
3.2.2. Analysis method for photo thermal conversion performance.....	56
3.2.3. Economic analysis of photo thermal conversion performance.....	59
3.2.4. Uncertainty analysis of photo thermal conversion experiment	60
3.3. RESULT AND DISCUSSION ON OPTICAL PROPERTIES AND PHOTO THERMAL CONVERSION PERFORMANCE OF NANOFLUID.....	61
3.3.1. Optical characteristics of single nanofluid	61
3.3.2. Optical characteristics of Fe ₃ O ₄ /ATO hybrid nanofluid	72
3.3.3. Receiving efficiency and thermal characteristics of MWCNT, Fe ₃ O ₄ , and ATO nanofluid during the solar receiving process	76
3.3.4. Receiving efficiency and thermal characteristics of Fe ₃ O ₄ /ATO hybrid nanofluid during the solar receiving process	84
3.3.5. Photo thermal conversion efficiency of MWCNT, Fe ₃ O ₄ , ATO, Fe ₃ O ₄ /ATO hybrid NF.....	88
3.3.6. Economy analysis on photo thermal conversion of MWCNT, Fe ₃ O ₄ , ATO,	

Fe ₃ O ₄ /ATO hybrid NF	90
---	----

**4. NUMERICAL MODELING METHOD ON THE
PERFORMANCE OF FLAT PLATE VOLUMETRIC
ABSORPTION SOLAR COLLECTOR 94**

4.1. A NUMERICAL MODEL FOR FLAT PLATE VOLUMETRIC ABSORPTION SOLAR COLLECTOR	94
4.1.1. Boundary condition	98
4.1.2. Optical properties of nanofluid based on Rayleigh scattering.....	100
4.2. THERMAL PERFORMANCE ANALYSIS METHOD OF SOLAR COLLECTOR	103
4.3. EXERGY ANALYSIS METHOD	105
4.4. SIMULATION RESULT AND DISCUSSION	107
4.4.1. Numerical analysis of optical characteristics of Fe ₃ O ₄ nanofluid.....	107
4.4.2. Thermal performance of FPVASC.....	109

**5. EXPERIMENTAL STUDY ON THE PERFORMANCE OF
VASC SOLAR COLLECTOR 119**

5.1. EXPERIMENTAL SETUP OF VASC SOLAR COLLECTOR.....	119
5.2. EXPERIMENTAL METHOD AND CONDITION OF VASC SOLAR COLLECTOR 127	
5.3. UNCERTAINTY ANALYSIS OF THE PERFORMANCE OF THE SOLAR COLLECTOR	129

5.4. EXPERIMENTAL RESULT AND DISCUSSION ON SOLAR COLLECTOR PERFORMANCE.....	130
5.4.1. Result and discussion on comparison SASC with VASC.....	130
5.4.2. VASTC with using Fe ₃ O ₄ , ATO, and Fe ₃ O ₄ /ATO hybrid NF	144
6. CONCLUSION	170
7. FUTURE WORK.....	173
REFERENCE	175
ABSTRACT(KOREAN).....	183

LIST OF FIGURES

Fig. 1.1 Earth's solar energy budget [8]	4
Fig. 1.2 World solar energy potential map	4
Fig. 1.3 Thermal conductivity of NFs [29]	7
Fig. 1.4 Overview of type of low-temperature solar collector	11
Fig. 1.5 Structure of Solar collector; (a) Flat plate, (b) Heat pipe evacuated tube, (c) Double evacuated solar collector [55]	12
Fig. 1.6 Surface absorption solar collecting method	15
Fig. 1.7 Volumetric absorption solar collecting method	20
Fig. 2.1 Preparation process of Fe ₃ O ₄ NF with PAA surfactant grafting	26
Fig. 2.2 Preparation process of NF	29
Fig. 2.3 Ultrasonic disperser for preparation of NF	29
Fig. 2.4 Prepared NF; (a) MWCNT, (b) Fe ₃ O ₄ , (c) ATO and (d) Fe ₃ O ₄ /ATO hybrid NF	30
Fig. 2.5 Schematic of the distribution of charges around NP	32
Fig. 2.6 TEM image of NF (a) MWCNT NF, (b) Fe ₃ O ₄ , (c) ATO NF, (d) Fe ₃ O ₄ /ATO hybrid NF	34
Fig. 2.7 NP diameter distribution (a) MWCNT NF, (b) Fe ₃ O ₄ NF, (c) ATO NF, (e) Fe ₃ O ₄ /ATO hybrid NF	35
Fig. 2.8 Zeta potential analyzer	37
Fig. 2.9 Zeta potential of MWCNT, Fe ₃ O ₄ , ATO, Fe ₃ O ₄ /ATO hybrid NF	37
Fig. 2.10 Thermal conductivity measurement device	40
Fig. 2.11 Vibro viscometer SV-10	44
Fig. 3.1 Schematic of optical transmittance measurement experiment setup	51
Fig. 3.2 Calculation process about absorbance and reflectance by TDTTM	52
Fig. 3.3 Experimental setup for photo thermal conversion experiment	54
Fig. 3.4 Temperature variation during the cooling process	58
Fig. 3.5 Spectral transmittance of NF; (a) MWCNT NF, (b) Fe ₃ O ₄ NF, (c) ATO NF	66
Fig. 3.6 Extinction coefficient of NF at optical depth = 0.005 m and 0.01 m; (a) MWNCT, (b) Fe ₃ O ₄ , (c) ATO NF	68

Fig. 3.7 Spectral absorbance of NF; (a) MWCNT NF (b) Fe₃O₄ NF (c) ATO NF69

Fig. 3.8 Spectral reflectance of NF; (a) MWCNT NF (b) Fe₃O₄ NF, (c) ATO NF..... 70

Fig. 3.9 Solar weight absorption coefficient of NF; (a) MWCNT NF (b) Fe₃O₄ NF, (c) ATO NF71

Fig. 3.10 Spectral absorbance of Fe₃O₄/ATO hybrid NF according to $m_{Fe3O4}/m_{Total,NP}$ 74

Fig. 3.11 Spectral reflectance of Fe₃O₄/ATO hybrid NF according to $m_{Fe3O4}/m_{Total,NP}$ 74

Fig. 3.12 Solar weight absorption coefficient of Fe₃O₄/ATO hybrid NF according to $m_{Fe3O4}/m_{Total,NP}$ 75

Fig. 3.13 Average increased temperature of NF according to exposed time under irradiance80

Fig. 3.14 Receiving efficiency of NF according to exposed time under irradiance81

Fig. 3.15 Temperature difference between top and bottom temperature sensor according to time exposed time under irradiance82

Fig. 3.16 Increased temperature of NFs with the various location at 9000s, (a) MWCNT NF, (b) Fe₃O₄ NF, (c) ATO NF83

Fig. 3.17 Average increased temperature of Fe₃O₄/ATO hybrid NF according to mixing ratio at total concertation = 0.1wt%86

Fig. 3.18 Receiving efficiency of Fe₃O₄/ATO hybrid NF86

Fig. 3.19 Increased temperature of Fe₃O₄/ATO hybrid NF87

Fig. 3.20 Photo thermal conversion efficiency MWCNT, Fe₃O₄ and ATO NFs89

Fig. 3.21 Photo thermal conversion efficiency of Fe₃O₄/ATO hybrid NF89

Fig. 3.22 Specific absorption rate of MWCNT, Fe₃O₄, and ATO NF92

Fig. 3.23 Specific absorption rate of Fe₃O₄/ATO hybrid NF according to $m_{Fe3O4}/m_{Total,NP}$ 92

Fig. 3.24 Manufacturing cost of NF for generated thermal energy93

Fig. 4.1 Geometry and mesh design of FPVASC using Fe₃O₄ NF for numerical analysis; (a) geometry of FPVASC, (b) Mesh image of FPVASC96

Fig. 4.2 Boundary condition schematic of FPVASC99

Fig. 4.3 Comparison of Am 1.5 spectral irradiation intensity, Plank’s blackbody distribution, and designed spectral solar irradiance for FPVASC99

Fig. 4.4 Real and imaginary parts of complex refractive index102

Fig. 4.5 Absorbance of Fe₃O₄ NF according to wavelength108

Fig. 4.6 Solar weight absorption coefficient according to centration of Fe₃O₄ NF108

Fig. 4.7 Optical efficiency of FPVASC according to the concentration of Fe₃O₄ NF 114

Fig. 4.8 Heat loss coefficient of FPVASC according to the concentration of Fe₃O₄ NF 114

Fig. 4.9 Temperature contour in FPVASC; (a) Water, (b) 0.05wt% Fe₃O₄ NF, (c) 0.1wt% Fe₃O₄ NF
..... 115

Fig. 4.10 Temperature difference between inlet and outlet of FPVASC 116

Fig. 4.11 Thermal and exergy efficiency of FPVASC; (a) according to normalized temperature
difference, (b) according to the concentration 117

Fig. 4.12 Thermal and exergy efficiency of FPVASC; (a) according to concentration, (b) according
to the mass flow rate at T_i=45°C 118

Fig. 5.1 Schematic of the experimental setup to evaluate solar collector performance indoor; (a)
Schematics of the experimental setup to evaluate the performance of solar collector, (b) Photo
about the experimental setup for comparison with solar collecting method, (c) Photo about the
experimental setup for comparison with the comparison with VASC performance according to
NF 122

Fig. 5.2 Irradiance contour at the solar collector by an artificial light source; (a) solar collector for
comparison with solar collecting method, (b) Solar collector for performance evaluation
according to NF 123

Fig. 5.3 Structure of VASC solar collector used in the experiment; (a) Solar collector for
comparison with solar collecting method, (b) Solar collector for performance evaluation
according to NF 124

Fig. 5.4 Useful heat of the SASC according to the inlet temperature; (a) $\dot{m} = 0.0025$ kg/s, $\dot{m} = 0.005$
kg/s..... 135

Fig. 5.5 Useful heat of the VASC according to the inlet temperature; (a) $\dot{m} = 0.0025$ kg/s, $\dot{m} = 0.005$
kg/s..... 136

Fig. 5.6 Portion of non-absorbed energy, useful heat, and heat loss in the SASC and VASC; (a) $\dot{m} =$
0.0025 kg/s, $\dot{m} = 0.005$ kg/s 137

Fig. 5.7 Heat removal factor according to the Fe₃O₄ NF concentration 138

Fig. 5.8 Overall heat loss coefficient according to the Fe₃O₄ NF concentration 138

Fig. 5.9 Exergy destruction of the SASC and VASC; (a) Effect of inlet temperature, (b) Effect of Fe_3O_4 NF concentration142

Fig. 5.10 Thermal and exergy efficiencies of the SASC and VASC; (a) Effect of inlet temperature, (b) Effect of Fe_3O_4 NF concentration143

Fig. 5.11 Temperature difference of ATO NF between inlet and outlet; (a) $Q = 0.4$ lpm, (b) $Q = 0.6$ lpm, (c) $Q = 0.8$ lpm152

Fig. 5.12 Temperature difference of Fe_3O_4 NF between inlet and outlet; (a) $Q = 0.4$ lpm, (b) $Q = 0.6$ lpm, (c) $Q = 0.8$ lpm153

Fig. 5.13 Temperature difference of Fe_3O_4 /ATO hybrid NF between inlet and outlet; (a) $Q = 0.4$ lpm, (b) $Q = 0.6$ lpm, (c) $Q = 0.8$ lpm154

Fig. 5.14 Comparison with transmission absorbance coefficient and solar weight absorption coefficient according to the concentration of NF155

Fig. 5.15 Comparison with heat removal factor and overall loss coefficient according to the concentration of NF156

Fig. 5.16 Comparison with improvement ratio of solar absorb and heat loss and LNTD according to concentration of NF157

Fig. 5.17 Exergy efficiency of VASC using ATO NF; (a) Concentration effect, (b) Volumetric flow rate effect162

Fig. 5.18 Exergy efficiency of VASC using Fe_3O_4 NF; (a) Concentration effect, (b) Volumetric flow rate effect163

Fig. 5.19 Exergy efficiency of VASC using Fe_3O_4 /ATO Hybrid NF; (a) Concentration effect, (b) Volumetric flow rate effect164

LIST OF TABLES

Table 1.1 Thermal conductivity improvement of NF	8
Table 1.2 Summary of NF heat transfer study.....	9
Table 1.3 Summary of surface absorption solar collecting method	16
Table 1.4 Summary of volumetric absorption solar collecting method.....	21
Table 2.1 Properties of NPs.....	27
Table 2.2 Specification of ultrasonic disperser for preparation of NF	30
Table 2.3 Stability behavior of a colloid depending on zeta potential [79].....	32
Table 2.4 The thermal conductivity of the NFs.....	41
Table 2.5 The viscosity of the NFs.....	45
Table 3.1 Performance specifications of the solar simulator.....	55
Table 4.1 FPVASC design specification.....	97
Table 4.2 Simulation conditions.....	97
Table 5.1 Specification of solar collector for comparison with solar collecting method	125
Table 5.2 Specification of solar collector for performance evaluation according to NF.....	126
Table 5.3 Experimental conditions for comparison with SASC and VASC.....	128
Table 5.4 Experimental conditions for comparison with the performance of VASC according to NF	128
Table 5.5 Performance parameter comparison with existing study.....	169

Nomenclature

A	Area (m ²)
A(λ)	Optical absorption
B	Heat dissipation rate (1/s)
c _p	Specific heat (J/kg· °C)
c ₀	Speed of light
D _{np}	Nanoparticle diameter
ETSC	Evacuated tube solar collector
f _v	Volume fraction of nanofluid
F _R	Heat removal factor
F _R U _L	Heat loss coefficient (W/m ² · °C)
F _R ($\tau\alpha$)	Optical efficiency
FPSC	Flat plate solar collector
G	Mass flux (kg/m ² ·s)
h	Heat transfer coefficient (W/m ² · °C)
HP-ETSC	Heat pipe type evacuated tube solar collector
I	Incident intensity or Intensity of irradiance
I ₀	transmitted intensity
k	Thermal conductivity (W/m· °C)
k _b	Boltzmann constant
k _{ex}	Extinction coefficient (1/m)
L _{op}	Optical length (m)
LNTD	Limited normalized temperature difference (m ² · °C/W)
m	Mass (kg), normalized refractive index
\dot{m}	Mass flow rate (kg/s)
MWCNT	Multi wall carbon nano tube

n	Average refractive index
NF	Nanofluid
NP	Nanoparticle
NTD	Normalized temperature difference ($m^2 \cdot ^\circ C/W$)
Q	Volumetric flow rate (lpm) or Energy (W)
Q_u	Useful heat of solar collector (W)
Q_o	Heat loss to the surrounding air (W)
Q_{sol}	Solar energy entering the solar collector (W)
Re	Reynolds number
$R(\lambda)$	Optical reflectivity
$RPIP_{hg-hl}$	Relative parameter improvement ratio
S	Concentration ratio of solar collector
\dot{S}_{gen}	Entropy generation (W/K)
SAR	Specific absorption rate (kW/g)
SASC	Surface absorption solar collecting
t	Time (s)
T	Temperature (K or $^\circ C$)
$T(\lambda)$	Optical transmittance
TDTTM	Traditional double thickness transmittance method
U_L	Overall heat loss coefficient ($W/m^2 \cdot ^\circ C$)
VASC	Volumetric absorption solar collecting
VASTC	Volumetric absorption solar thermal collector

Greek symbols

α	Particle size parameter
η	Efficiency
κ	Imaginary part of complex refractive index

λ	Wavelength (nm)
μ	Viscosity (mPa·s)
$\tau\alpha$	Optical transmittance and absorbance
ρ	Reflectance of interface between air and the cuvette
ψ_d	Exergy loss (W)
ψ_s	Exergy inflow due to solar radiation

Subscript

AM1.5	ASTM G173-3 AM 1.5
a	Absorption, surrounding air
as	Assumption
bf	Base fluid
bot	Bottom
dis	Discharge
eq	Equilibrium
i	Inlet
mid	Middle
nf	Nanofluid
np	Nanoparticle
o	outlet
s	Scatter
sol	Solar
top	Top
w	Water

Abstract

Study on Performance on Volumetric Absorption Solar Collector based on Characteristics on Photo Thermal Conversion of Nanofluid

Jeonggyun Ham

Advisor: Prof. Honghyun Cho, Ph.D.

Department of Mechanical Engineering,

Graduate School of Chosun University

In this study, the characteristics of volume absorption solar collectors (VASC) using nanofluids (NFs) were investigated to improve the performance of solar collectors. To understand the characteristics of the VASC using NFs, the mechanism of the photothermal conversion process of MWCNT, Fe₃O₄, and ATO NFs was investigated. Through the numerical analysis, the heat transfer characteristics of a flat plate volumetric absorption solar collector (FPVASC) using Fe₃O₄ NF were investigated. In addition, experimentally, evaluation of the effect of NFs on the solar collecting method and the effect of optical absorption properties on the thermal characteristics of solar collectors were investigated using Fe₃O₄, ATO NFs, and Fe₃O₄/ATO hybrid NF with different optical absorption properties.

The improvement of the optical absorption of the NF was shown in the order of MWCNT > Fe₃O₄ > ATO, and the photothermal conversion coefficient of 0.002wt% MWCNT NF was 0.933, which was the best for a single NF. However, it is possible to improve optical absorption by mixing Fe₃O₄ and ATO NFs with different optical absorption characteristics for each wavelength. In the case of $m_{\text{Fe}_3\text{O}_4}/m_{\text{Total,NP}} = 0.2$ in 0.1wt% Fe₃O₄/ATO hybrid NF, the photothermal

conversion efficiency is 0.932, which is the MWCNT NF. It was confirmed that the optical absorption equivalent to that could be secured. In terms of manufacturing cost considering the optical absorption performance of the NF, the manufacturing cost considering the heat production of 0.002wt% MWCNT NF is lower than others because it has high optical absorption performance at low concentration compared to other NFs. The cost of the NF for thermal energy production was high, and it is in the order of 0.0075wt% Fe₃O₄ NF > 0.1wt% Fe₃O₄ /ATO NF ($m_{Fe_3O_4}/m_{Total,NP} = 0.2$) > 0.1wt% ATO NF > 0.002 wt% MWCNT NF. Because using 0.1 wt% Fe₃O₄ /ATO NF ($m_{Fe_3O_4}/m_{Total,NP} = 0.2$) has higher optical absorption than 0.075wt% Fe₃O₄ NF and 0.1wt% ATO NF, reducing manufacturing costs than 0.075wt% Fe₃O₄ NF. It is judged that that can be used as an alternative to 0.002wt% MWCNT NF.

As a result of investigating the thermal characteristics of the FPVASC using Fe₃O₄ NF through numerical analysis, it was confirmed that the improvement of optical absorption by the concentration change of the NF is a major variable that determines the performance of the VASC. As the concentration of Fe₃O₄ NF increased from 0 to 0.1wt%, the optical efficiency of the FPVASC was improved up to 43.5%, and the maximum exergy efficiency up to 0.0844.

It was confirmed through the use of Fe₃O₄ NF that the effects of NF were different depending on the heat collection method of the solar collector and that the approach to improving the properties of NFs to improve the performance of the solar collector according to the heat collection method was also different. In the case of the SASC method, as the Fe₃O₄ NF concentration increased to 0.1wt%, F_R , the heat transfer performance index in the solar collector, and U_L , the heat loss index of the solar collector, increased by 4.27% and 5.19%, respectively, up to 4.27% and 5.19%, respectively, compared to using water. However, in the VASC method, F_R continuously increased as the concentration of the Fe₃O₄ NF increased up to 0.1wt%, increasing to 11.75%, whereas U_L decreased by up to 6.37% compared to water when the concentration of Fe₃O₄ NF increased up to 0.05wt%. After that, it increased. This is determined by the optical absorbance of the NF used in the optimal absorption solar heat collector, and it

was confirmed that the excessively increased optical absorption occurred near the surface of the collector, thereby reducing the thermal efficiency of the VASC.

The optical absorption characteristics of NFs are the main variables that determine the performance of VASC, and it was confirmed that the performance of VASC could be improved by mixing NFs with different optical absorption for each wavelength band. When $m_{\text{Fe}_3\text{O}_4}/m_{\text{Total,NP}}$ was 0.25 in 0.1wt% $\text{Fe}_3\text{O}_4/\text{ATO}$ hybrid NF, thermal and exergy efficiency were improved compared to 0.1wt% Fe_3O_4 NF and 0.1wt% ATO NF. For 0.1wt% $\text{Fe}_3\text{O}_4/\text{ATO}$ hybrid NF, when the volumetric flow rate was 0.6 lpm, the exergy efficiency was 0.277, and the maximum exergy efficiency was 0.277 and 0.094 at an inlet temperature of 55°C, 0.1wt% Fe_3O_4 NF and 0.1wt% ATO NF under the same conditions. It was confirmed that the exergy efficiencies of the ATO NF was 0.189, 0.086 and the thermal and exergy efficiencies of 0.1wt% the ATO NF were 0.27 and 0.93. It is judged to be the effect of improving the optical absorption in the visible light band of the ATO NF through the mixing of the Fe_3O_4 NF. Judging from this, the VASC method using NF can improve the performance of the solar collector by improving the optical absorption performance of the NF, and it is judged to be a method that can replace the SASC method.

In comparison with existing studies of the flat plate solar collector and the evacuated tube solar collector, it was confirmed that the volumetric absorption solar thermal collector (VASTC) used in this study has equivalent solar energy absorption capacity, low heat loss and has a wide operating range. However, problems such as securing long-term dispersion stability of the NF and reducing the manufacturing cost of the NF should be solved by using the VASC method. It is judged that it is necessary to review the applicability of the VASC method because the solar collector with a high concentration ratio has problems with high heat loss and damage to the absorber plate.

1. INTRODUCTION

1.1. Background

For humankind to keep advancing in the 21st century, it is necessary to solve the energy problem. Following the rapid industrialization in the 20th century, centered on developing countries in Asia, Central and South America, and Africa, the populations of developing countries rapidly increased, as did energy consumption with the development of electricity, electronics, and IT industries. The use of fossil fuels has grown significantly to meet the ever-increasing energy demand. While energy obtained through the combustion process of fossil fuels has the advantages of high energy density and ease of use, by-products of combustion such as NO_x and SO_x accelerate global warming and are pointed out as the cause of acid rain. As a by-product of combustion, particulate matter leads to problems such as air pollution and respiratory diseases [1,2]. In addition, as the importance of energy becomes more prominent as industrialization progresses rapidly, energy independence is the most critical issue in each country. However, because fossil fuels, the primary energy sources, are intensively buried in the Middle East and Central and South America, the weaponization of fossil fuels causes political problems in each country. Furthermore, with the development of mining technology, the reserves of fossil fuels are increasing compared to the previous forecast, but after all, fossil fuels are limited resources, requiring alternative energy sources to replace them [3].

For all humankind to live a universally prosperous life, it is necessary to ensure easy energy production regardless of the region. Various new and renewable energies such as solar power, heat, wind power, and geothermal heat are being touted as eco-friendly energy sources to replace fossil fuels [4–6]. Among them, solar energy has the potential to replace fossil fuels or support energy supply and demand. Solar energy consists of radiation energy such as electromagnetic waves, infrared rays, ultraviolet rays, and visible rays that are radiated from the sun and reach the earth's surface. A significant amount of 1.8 PW solar energy enters Earth [7,8]. Among them, 50% of solar energy reaches the earth's surface but is not utilized.

Furthermore, solar energy is cheaper than renewable energy sources such as wind and geothermal energy. Fig. 1.1 shows the map of the world's solar energy potential. As shown in Fig. 1.2, solar energy is uniformly distributed except in high latitudes, and in particular, the annual average insolation in low latitudes is higher than in temperate regions. Low latitudes include developing countries in Asia and Africa, and the countries in the region do not fully meet their energy demands, requiring active solar energy utilization [9].

Solar energy is divided into photovoltaic energy, which produces solar energy as electrical energy through solar panels, and solar thermal energy, which makes solar energy as thermal energy through solar thermal collecting facilities. Among them, solar thermal energy is used for large-scale power generation through high-concentration solar power generation facilities [10–12]; steam and hot water facilities through thermal energy production [13–16]; and heating and cooling of medium-to-large building complexes in combination with absorption systems [17–19]. Furthermore, with recent advances in latent heat [20–22], chemical heat storage [23], and long-term heat storage [24–26] technologies to solve the energy supply and demand mismatch, which is a disadvantage of using solar energy, the utilization of solar energy has improved. Therefore, to more actively and efficiently use solar thermal energy, it is necessary to improve solar thermal collection technology.

A solar collector that converts solar energy into thermal energy is required to utilize solar thermal energy. According to the conversion of solar energy into thermal energy, the type of solar collector using solar heat is divided into a surface absorption solar collector (SASC) and a volumetric absorption solar collector (VASC). SASC involves ① solar energy absorption, ② conversion to heat energy, and ③ heat transfer between the absorber and the working fluid, and such a heat collecting process is used in most of the currently commercialized flat plate and heat pipe solar collectors. The SASC has a disadvantage because it has a higher heat loss than the VASC. After all, the absorber that absorbs solar energy is locally heated.

On the other hand, in VASC, the working fluid plays the role of an absorber, and the process in which the working fluid acquires solar energy is reduced compared to the SASC method.

Because the working fluid uniformly absorbs solar energy, local heat does not occur, so the heat loss is slight compared to SASC. However, water, antifreeze, and oil used as the working fluid of the solar collector are characterized by low optical absorption, making it challenging to utilize VASC. As the development of nanotechnology has enabled optical absorption through the dispersion of a small number of nanoparticles (NPs) in a working fluid with high light transmittance, VASC is attracting attention.

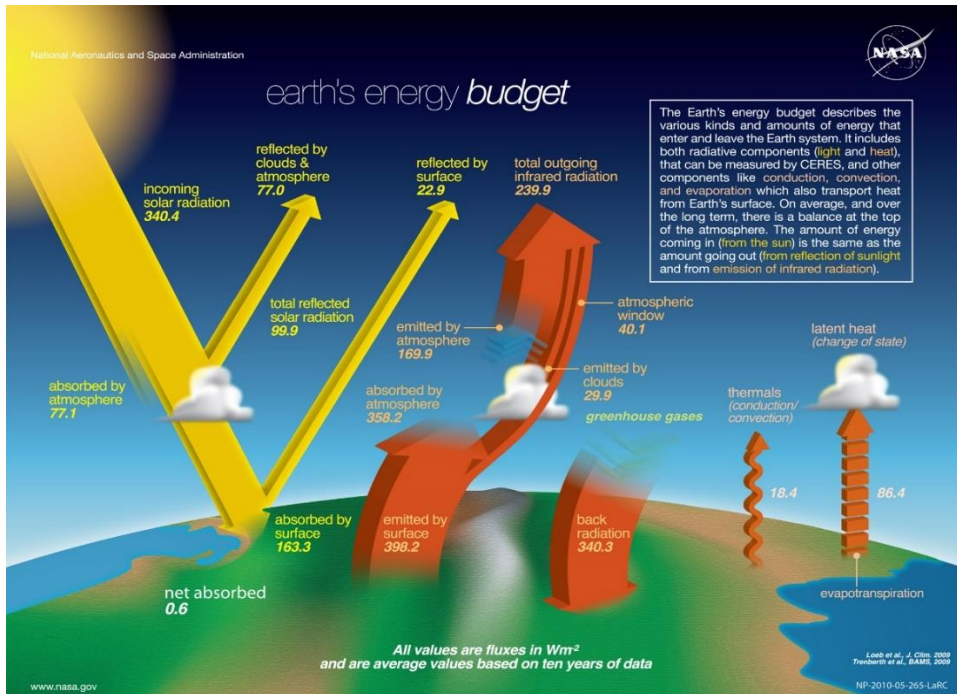


Fig. 1.1 Earth's solar energy budget [8]

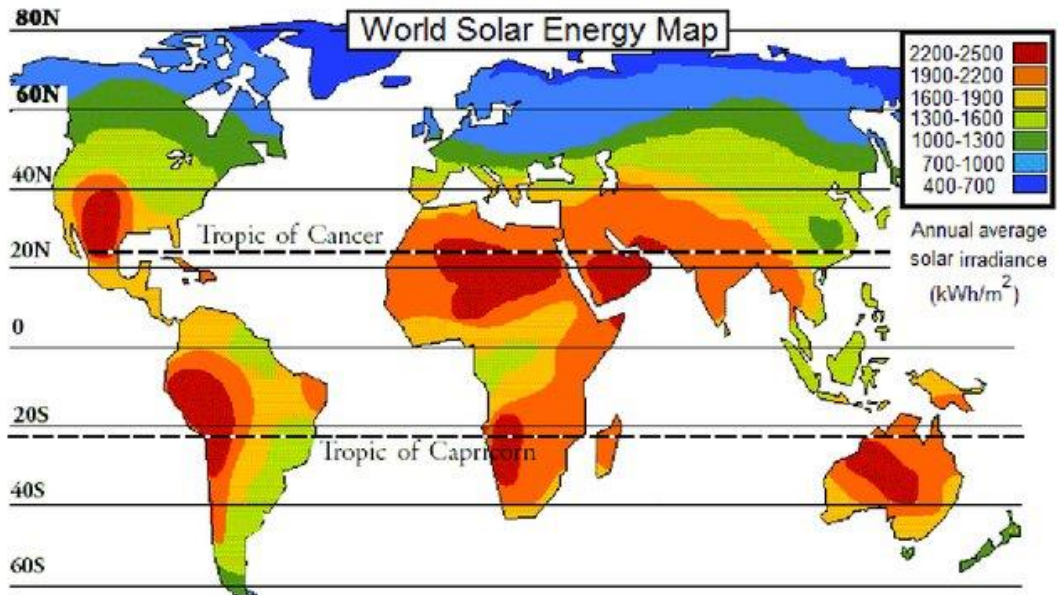


Fig. 1.2 World solar energy potential map

1.2. Nanofluid

The term “nanofluid” was proposed by Choi and Estman [27]. A nanofluid (NF) is a fluid in which solid particles with an excellent thermal conductivity of 100 nm or less are dispersed in a fluid, and the thermal conductivity is improved as volume concentration of the the NF increases. Before the concept of NFs was proposed, Maxwell [28] theoretically established that thermal properties could be enhanced by mixing solid particles with excellent thermal conductivity into the fluid. Until the advent of NFs, an attempt was made to improve the thermal properties of fluids by making solid particles in the sizes of millimeters (mm) or micrometers (μm) due to technical limitations. Although mixtures containing milli- and micro-sized particles have been shown to improve the thermal properties of the fluid, there is a problem with usability due to clogging and corrosion of pipes caused by particle agglomeration and precipitation.

However, unlike conventional micro fluids, NFs are considered next-generation heat transfer fluids with their improved thermal properties and dispersion stability by dispersing metallic and non-metallic particles of less than 100 nm, thus having superior thermal conductivity to the base fluid. Fig. 1.3 shows the thermal conductivity of NFs [29]. NPs dispersed in the NF have been confirmed to have a larger relative surface area than microparticles, and thermal conductivity and heat transfer can be improved through active Brownian motion. Table 1.1 and Table 1.2 show various effects of improving heat conduction [30–39] and heat transfer (convective heat transfer [40–43], boiling heat transfer [44,45], and phase change [46]) of NFs. While the thermal conductivity of NFs has different improvement effects depending on the combination of NFs and base fluid, it has been confirmed to increase as the concentration and temperature of the NFs increase.

Furthermore, heat transfer performance indicators such as convective heat transfer coefficient and Nusselt number are found to improve with an increase in the concentration of NF when NFs perform convective heat transfer. However, the viscosity and pressure drop also increases with an increase in the concentration of NF. Considering the effects of improvement in heat transfer performance and pressure drop from using NFs, research on the applicability of NFs

in various heating devices such as heat exchangers, heat sinks, and solar collectors is being conducted to improve the performance of heating devices. As for using NFs in heating devices, heat exchange performance can be enhanced simply by exchanging the working fluids with NFs. Dayou et al. [47] investigated the heat transfer performance of a concentric pipe heat exchanger according to the change in volumetric flow rate (1.5–2.5 lpm) and concentration of GnP and MWCNT NFs (0.01–0.35 vol%). GnP NF showed a 16.8%–26.1% higher heat transfer performance improvement than the mother fluid, which was confirmed to be higher than MWCNT (8.8%–14.4%). Zhang et al. [48] investigated the thermal performance of using various NFs (Al_2O_3 , SiC, CuO, and Fe_3O_4) in a plate heat exchanger, reporting the highest improvement in the thermal performance with Fe_3O_4 followed by Al_2O_3 , SiC, and CuO. They also confirmed that the convective heat transfer coefficient improved by 21.9% compared to water when using 1.0wt% Fe_3O_4 NF, but the pressure drop also increased by 10.1%. As NFs not only improve heat transfer but also impart new properties to existing working fluids, such as improved magnetism [49,50], lubrication [51], and optical absorption [52–54], the contribution of NFs to the industrial field is expected to keep increasing in the future.

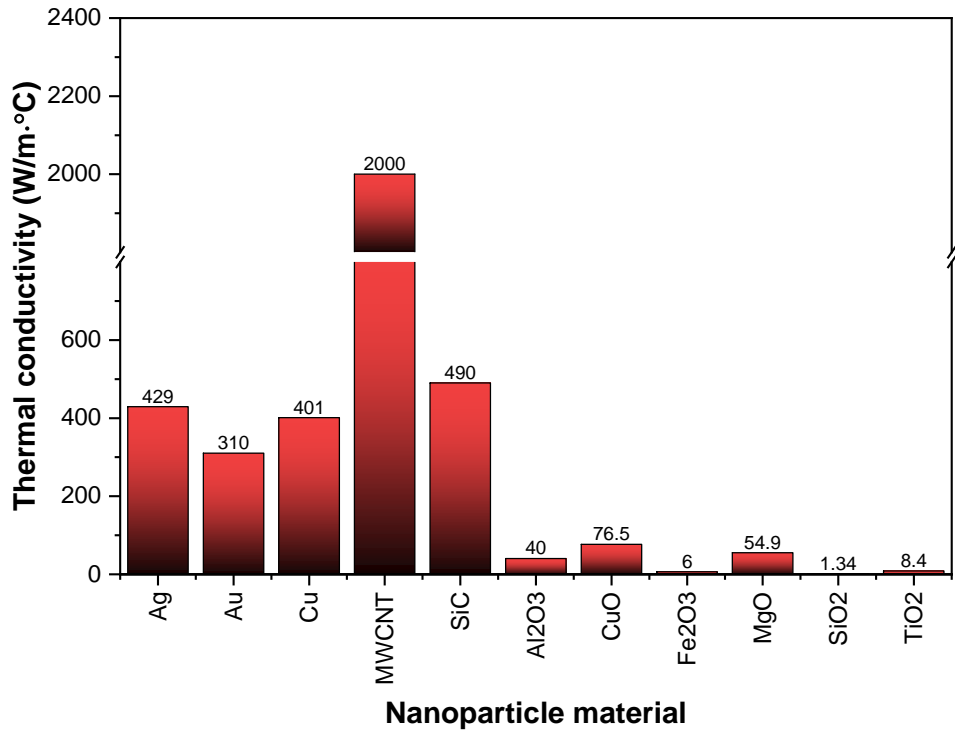


Fig. 1.3 Thermal conductivity of NFs [29]

Table 1.1 Thermal conductivity improvement of NF

Nanomaterial	Base fluid	Temperature	Concentration	Maximum thermal conductivity improvement
MWCNT [30]	Water	25–55°C	0.01–3%	45%
Graphene [31]	Water	10–50°C	0.05–0.15wt%	4.5%
	Water/Ethylene glycol (50/50)	-20–40°C		18%
	Ethylene glycol	-10–50°C		6.8%
SiC [32]	Water	20–50°C	0.5–1.0wt%	17.62%
Al ₂ O ₃ [33]	Bioglycol/water (40/60%)	30–80°C	0.5–2.0vol.%	24%
	Bioglycol/water (60/40%)			13%
MgO [34]	Water/Ethylene glycol	20–50°C	0.1–2vol%	34.5%
Fe ₃ O ₄ [36]	Water	10–40°C	0.25–3vol%	11.5%
CuO [37]	Water, Ethylene glycol, Engine oil	10–70°C	0.25–1vol%	24%
				21%
				14%
Fe ₃ O ₄ /CNT [38]	Water	25–55°C	Fe ₃ O ₄ NF: 0.1–0.9% CNT NF: 0.05–1.35% The volume ratio of CNT and Fe ₃ O ₄ Np: 1/2, 1/1, 2/1	44.6%
Al ₂ O ₃ /Cu [39]	Water	20–60°C	0.1–2%	12.11%

Table 1.2 Summary of NF heat transfer study

NF	Concentration	Heat transfer mode	Contents
SiO ₂ Water NF [40]	0.001–0.007vol%	Forced convective heat transfer	<ul style="list-style-type: none"> - Re=8000–20000 - SiO₂ NF with 0.007vol% shows almost 27% enhanced in heat transfer
SWCNT water NF [41]	0.1–1vol%	Forced convective heat transfer	<ul style="list-style-type: none"> - Re=800–2600 - The improvement of Nu is from 90 to 270% - When using NF, exergy destruction was decreased from 23–43%
Al ₂ O ₃ EG/Water NF [42]	1.43vol%	Forced convective heat transfer	<ul style="list-style-type: none"> - The convective heat transfer coefficients of NFs increased from 12.4 to 22.7% depending on the NBT values at the fixed Re
TiO ₂ Water NF [43]	0.05–0.8vol%	Natural convection heat transfer	<ul style="list-style-type: none"> - Square cavity with opposite walls heated and cooled - Ra = 4.9×10⁸ to 1.47×10⁹ - The maximum heat transfer enhancement of 8.2% was found at a volume concentration of 0.05%
Cerium oxide water NF [45]	0.001–0.04vol%	Pool boiling	<ul style="list-style-type: none"> - Pool boiling heat transfer coefficient of NF was improved - The enhancement ratio of pool boiling heat transfer coefficient was about 1.7 at 0.007vol% NF
Cu paraffin NF [46]	0.5, 1.0, 1.5, 2wt%	Melting and freezing	<ul style="list-style-type: none"> - For composites with 1wt % Cu NF, the heating and cooling times can be reduced by 30.3 and 28.2%, respectively.

1.3. Solar collecting system

A solar collecting system is a system that converts solar energy into thermal energy and stores it. In the solar collecting system, the solar collector is a device that converts solar energy into thermal energy, which is a key device that determines the performance of the solar collecting system. Because the energy density of solar energy reaching the earth's surface is low, the structure of the solar collector is determined by the purpose of use, temperature, and heat capacity at the places in demand. For industrial processes and electric power generation requiring high-temperature and large-capacity energy, parabolic trough and dish-type solar collectors with high-concentration reflectors such as parabolic troughs, dish Stirling, and Fresnel reflectors are used. On the other hand, when a relatively low temperature is required, such as hot water production, hot water supply, and building air conditioning, flat plate, heat pipe, and evacuated tube solar collectors are used. Fig. 1.4 shows the classification of solar collectors by operating temperature.

Fig. 1.5 shows the structures of (a) flat plate, (b) heat pipe evacuated tube, and (c) double evacuated tube solar collectors. The flat plate solar collector has a form in which a riser tube through which the working fluid flows is attached to an absorption plate with high solar energy absorption. To suppress heat loss, the riser tube is wrapped around with an insulating material or manufactured in an evacuated tube structure. In the absorption plate and heat pipe solar collector, the evaporator of the heat pipe is coupled to the absorption plate, and the condenser is located in the manifold. To minimize heat loss from the absorption plate, the absorption plate and the evaporator of the heat pipe are located in the evacuated tube. The double evacuated tube solar collector has a U-type tube attached to the absorption tube, and the absorption tube is installed in the evacuated tube to prevent heat loss.

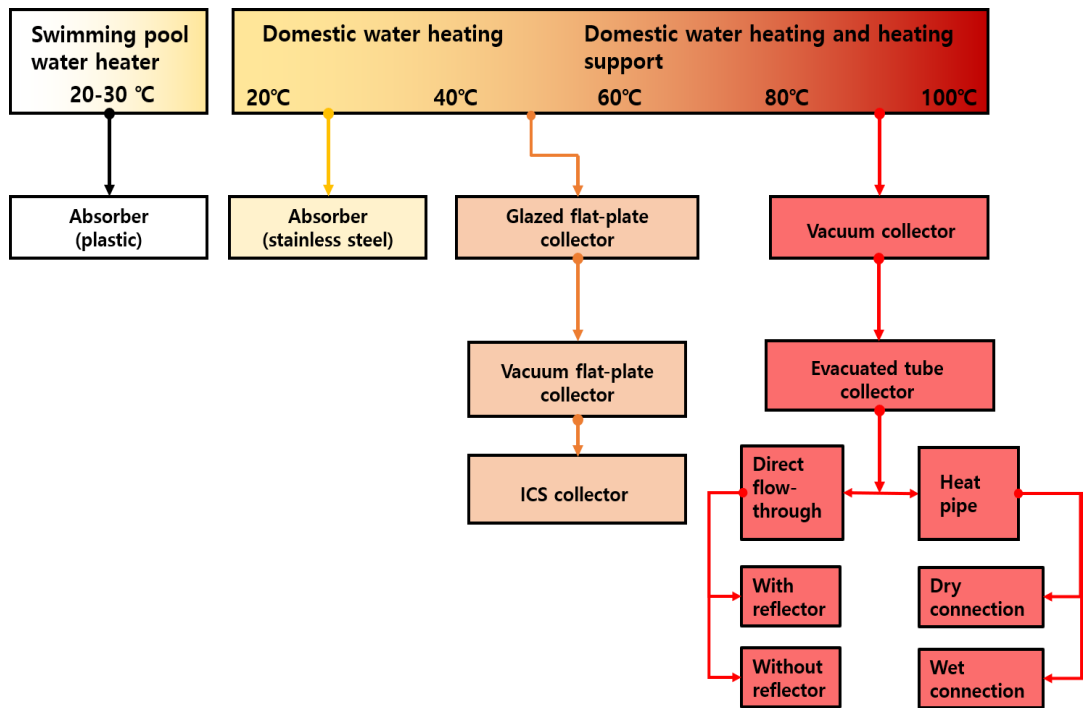


Fig. 1.4 Overview of type of low-temperature solar collector

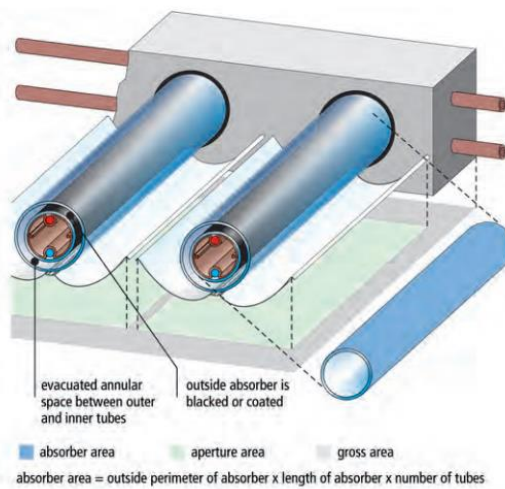
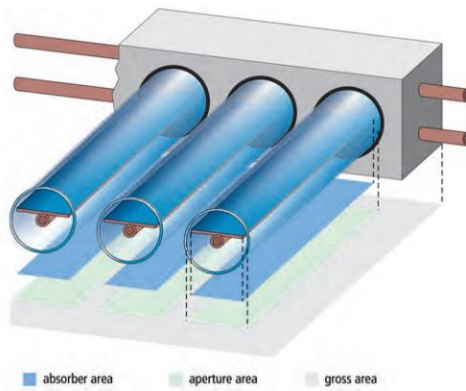
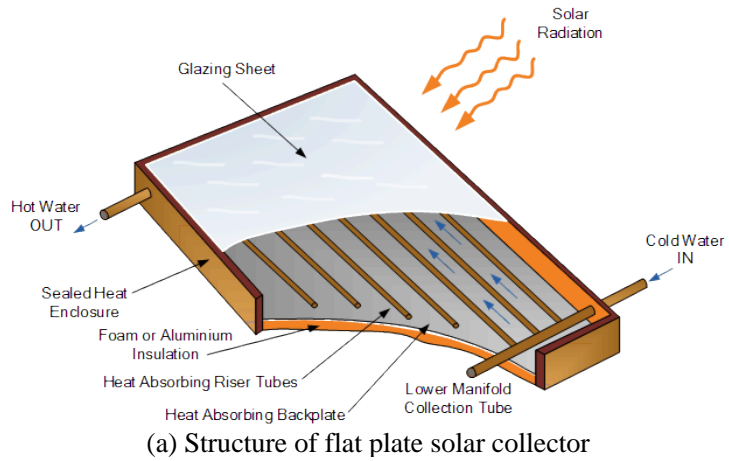


Fig. 1.5 Structure of Solar collector; (a) Flat plate, (b) Heat pipe evacuated tube, (c) Double evacuated solar collector [55]

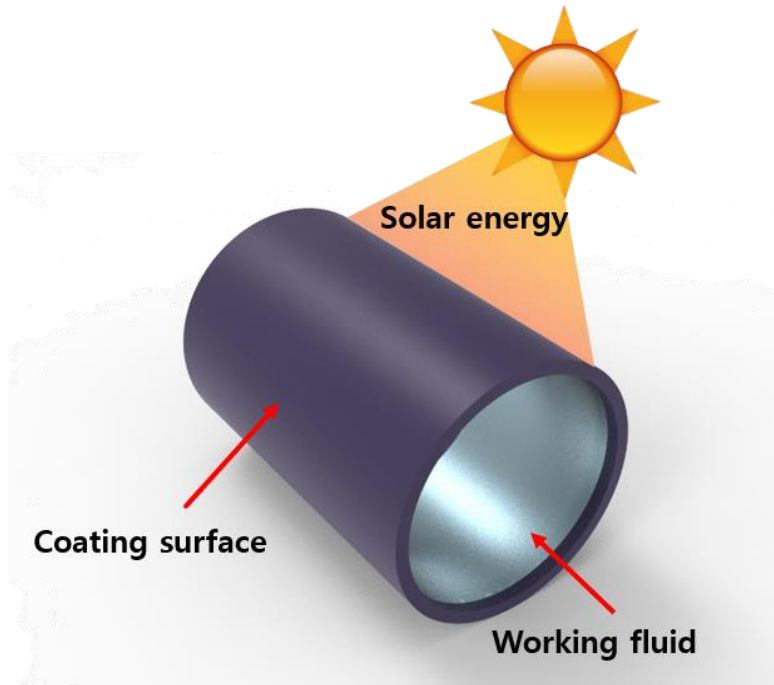
1.3.1. Surface absorption solar collector method

The Surface absorption solar collecting method (SASC) is used as a heat collection method for currently commercialized heat pipe and flat plate solar collectors. Fig. 1.6 shows the concept and schematic diagram of the SASC method. The SASC method is the primary heat collection method used for currently commercialized solar collectors. An absorber coated with an absorbent material with excellent optical absorption absorbs solar energy and is heated; the heated absorber and the working fluid flowing through the solar collector exchange heat to generate thermal energy. SASC aims to minimize the heat loss of the absorber and maximize the heat energy gain from the absorber.

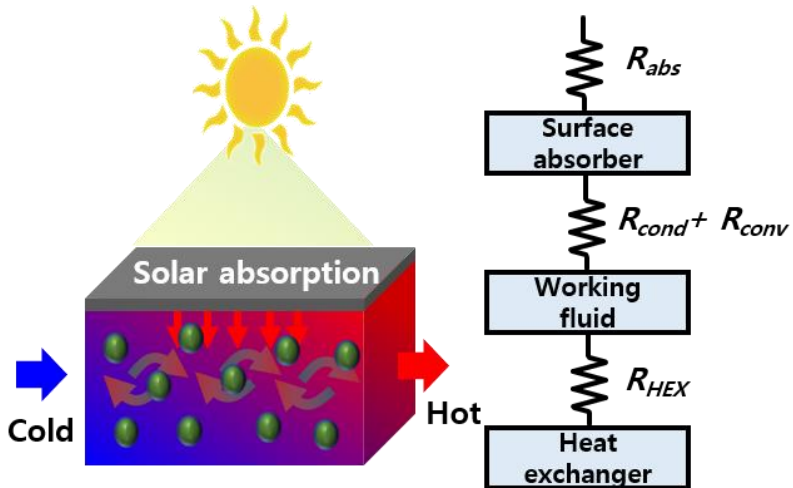
Due to the structural characteristics of SASC, the absorber is locally overheated compared to the rest of the solar collector. For this reason, the SASC method has a disadvantage in heat loss due to convection and radiation, requiring superior insulation technology like vacuum insulation to suppress heat loss in conduction and convection. Because the absorber has a higher temperature than its surroundings, the absorbed light energy radiates heat loss. A selective absorption coating method that reduces radiation energy after absorbing solar energy is used to solve this problem. For selective absorption coating, techniques such as light trapping, particle coating, and multi-layer film are used [56–59].

In the SASC method, the working fluid generates heat energy through heat exchange with the absorber. Therefore, the heat exchange performance between the absorber and the working fluid is essential in the SASC method. To improve the heat exchange performance between the absorber and the working fluid, studies on the introduction of heat transfer promoting structures such as fins and baffles [60–62] and the use of NFs were conducted to improve heat transfer performance by increasing the heat exchange area and inducing turbulence. Table 1.3 summarizes the performance study of a solar collector using the SASC method. Kansara et al. [60] attempted to improve the performance by installing a fin and porous media in a flat plate solar collector, reporting performance improvements of 8.19% and 16.17% with the installation of a fin and porous media, respectively, compared to the existing solar collector. Kumer et al.

[61] examined the performance of an evacuated tube solar collector with a baffle, reporting that an increase in the medium length had a positive effect on the improvement of the outlet temperature and thermal efficiency but increased the pump power consumption. Choudhary et al. [63] reviewed the applicability of MgO NFs in a flat plate solar collector. They recommended the use of MgO NF as the working fluid for solar collectors, reporting that 0.2 vol% MgO NF flowing through the solar collector at 1.5 lpm reduced the absorbed energy factor by 16.74% and the heat loss parameter by 52.2%, compared to using ethyl glycol/water as the working fluid. In addition, the performance of the solar collector was found to be improved when NF was used as the working fluid in the evacuated tube solar collector. Sharafeldin and GyulaGrófa [64] investigated the performance improvement of 0.015–0.035% CeO₂/Water NF in the evacuated tube solar collectors, reporting that 0.035% CeO₂ NF flowing at a mass flow rate of 0.017 kg/m² s improved the maximum efficiency by 34% compared to that of water. Edian et al. [65] investigated the performance of a heat pipe-type solar collector filled with Al₂O₃ and CuO/Acetone NFs at 0.025 and 0.05 vol%. They reported that the evaporation heat transfer coefficient (EHTC) of Al₂O₃/Acetone and CuO/Acetone NFs with 0.025 and 0.05 vol% concentrations increased by 37%, 34%, 32%, and 73%, respectively. However, NF precipitation problems occurred at 0.05 vol% of NF, and CuO NF with a high NF density showed more substantial precipitation than Al₂O₃ NF. Sharafeldin et al. [66] investigated the effect of Cu/Water NFs in evacuated tube solar collectors. They observed that the maximum inlet and outlet temperature difference increased from 17% to 51.5% as the Cu/Water NF concentration increased from 0.01wt% to 0.03wt%. However, the heat removal factor also increased as the NF concentration increased.



(a) Concept of surface absorption solar collecting method



(b) Schematic on surface absorption solar collecting method

Fig. 1.6 Surface absorption solar collecting method

Table 1.3 Summary of surface absorption solar collecting method

Author	Solar collector type	Performance improvement method	summary
Kansara et al. [60]	FPSC	Using fin and porous media	- Thermal efficiency of ESC with fin and porous media was improved up to 8.19 and 16.17%
Kumer et al. [61]	ETSC	Add baffle	- Thermal efficiency of ESC with fin and porous media was improved up to 8.19 and 16.17%
Saravanan and Jaisankar [62]	FPSC with V trough reflector	Add V trough reflector Modified absorber tube: helix with square-cut twisted tape (HSCTT), helix with V-cut twisted tape (HVCTT)	- Thermal efficiency improvement using V trough reflector: 8.66% - Thermal efficiency improved by modified absorber tube: HSCTT > HVCTT > Plain tube
Choudhary et al. [63]	FPSC	Using MgO NF (0.08-0.4%)	- MgO NF with 0.2 vol% was stable for 15 days, while sediment occurred at 0.4vol%.
Sharafeldin and GyulaGrófa [64]	ETSC	Using CeO ₂ /Water (0.015, 0.025, 0.035vol%)	- Maximum thermal efficiency was increased up to 34%
Edian et al. [65]	HP-ETSC	Using Al ₂ O ₃ and CuO/Acceton NF (0.025 and 0.05vol%)	- EHTC enhancement of Al ₂ O ₃ and CuO NF with 0.025 and 0.05vol% was increased by 34, 74, 32, and 73%, respectively - Sediment occurred in CuO and Al ₂ O ₃ NF
Sharafeldin et al.[66]	ETSC	Using Cu NF (0.01, 0.02, 0.03wt%)	- Temperature difference improvement: 17–51.5% - F _R was increased by the increase of concentration of NF

1.3.2. Volumetric absorption solar collecting method

In the volumetric absorption solar collecting (VASC) method, the working fluid absorbs solar energy, converts it into thermal energy, and transports the energy. The VASC method can reduce the thermal resistance in the heat transfer mechanism in the solar collector as the working fluid plays the role of an absorber. Fig. 1.7 shows the concept and schematic diagram of the VASC method. Because the working fluid is an absorber, localized heat does not occur in the solar collector, with a more uniform temperature distribution than in the SASC method, thereby reducing heat loss. However, water, oil, and antifreeze used as the heating medium of the solar collector have high light transmittance, making it difficult to use them as an absorber [67]. Therefore, the VASC method requires improving the optical absorption performance to use the working fluid as an absorber.

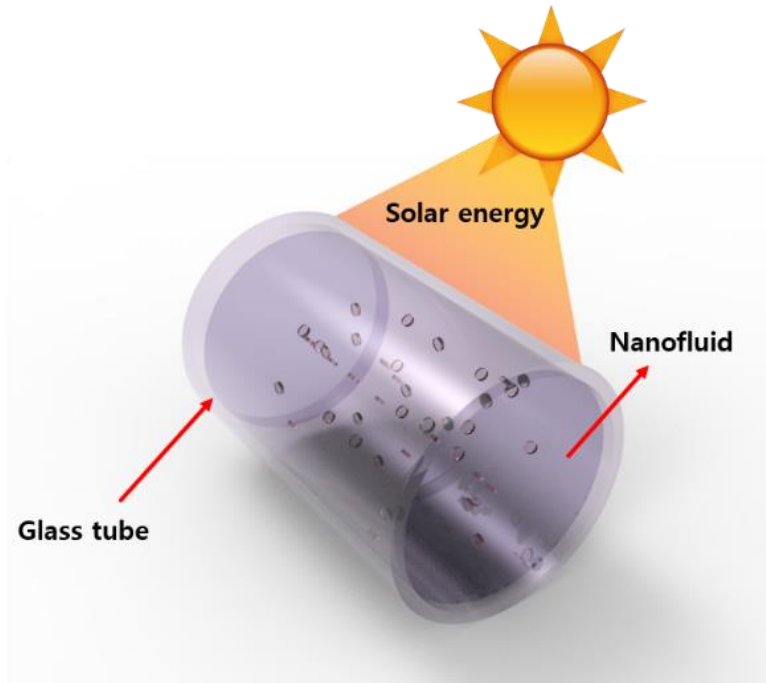
In the early days when the VASC method was proposed, India ink and organic and inorganic dyes were considered working fluids [68,69]. However, when these working fluids were used for an extended period or exposed to high temperatures, their optical absorption performance was reduced, or precipitation occurred due to light and thermal decomposition, posing usability problems [70]. The emergence of NFs has suggested the possibility of improving the dispersion stability of the working fluid and improving the optical absorption. Table 1.4 shows a summary of previous studies on the VASC method.

As for metal NFs, it is possible to improve optical absorption by localized surface plasmon resonance due to the resonance of light energy and NFs. Localized surface plasmon resonance occurs by interaction with light and the surface of metal NFs with a size smaller than the wavelength of light. When metal NFs are exposed to sunlight, surface plasmon resonance occurs at the boundary between the metal surface and the dielectric, enabling an improvement in optical absorption. Amjad et al. [71] investigated the optical absorption performance of Cu, Ag, Zn, Si, Fe, and β -Al₂O₃ NFs by exposing them to a solar environment of 12 suns, and the highest optical absorption was observed with Ag, followed by Fe, Zn, Cu, Si, and β -Al₂O₃. Furthermore, Jin et al. [72] compared the optical absorption performance of plasmonic NFs (Au, Cu) and non-

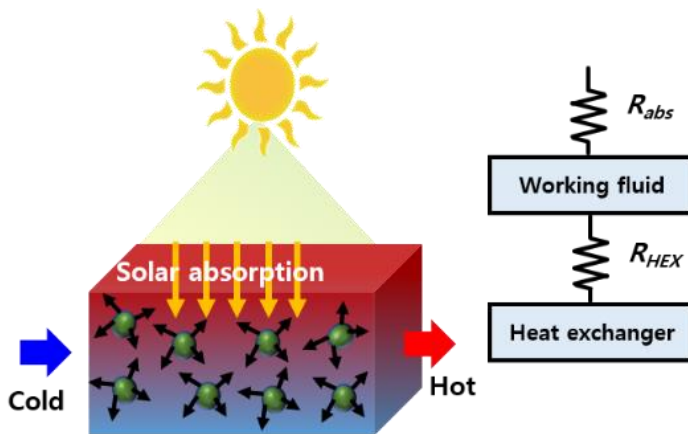
plasmonic NFs (Fe_3O_4), reporting that plasmonic NFs had superior optical absorption performance compared to non-plasmonic NFs due to the localized surface plasmon resonance effect. They mentioned that the photothermal conversion efficiency could be further improved by mixing two NFs having different absorption peaks. Because metal NFs have problems with oxidation and deterioration, the applicability of carbon-based NFs and metal oxide NFs using CNTs, graphene, graphite, etc., which have excellent optical absorption ability, was considered. Guo et al. [73] investigated the photothermal conversion properties of MWCNT NFs and confirmed that the maximum photothermal conversion efficiency was 65.4% at 0.01wt% of MWCNT NFs. Milanese et al. [52] investigated the optical properties of water-based NFs using metal oxide NFs such as Al_2O_3 , CuO , TiO_2 , ZnO , CeO_2 , and Fe_2O_3 , reporting that metal oxide NFs had an increased transmittance from visible light to infrared light, and 0.05vol% TiO_2 NF, with excellent optical absorption performance even at low concentrations, could completely absorb solar energy even within 1 cm of penetration depth. Hazra et al.[74] investigated the optical absorption efficiency of Carban black (CB) NFs. They confirmed that the 15 ppm CB NF had a 15% higher optical absorption efficiency than that of EG, the base fluid, and that the photothermal conversion efficiency increased as the depth of the liquid as well as the NF concentration increased.

Studies have been conducted on the performance experiment with VASC to evaluate the applicability of the VASC method. Gorji and Ranjbar [75] experimentally and numerically investigated the efficiency of small DASCs using graphite, magnetite, and silver, reporting a thermal efficiency of up to 57.4% with 40 ppm magnetite NF, which was higher than that of other NFs. Gupta et al. [76] investigated the performance of DASC using Al_2O_3 NFs. They mentioned that the thermal efficiency improved as the concentration and flow rate of Al_2O_3 NF increased. In addition, the study by Menbari et al. [77], which investigated the heat collection performance of a direct absorption parabolic trough collector (DAPTC) using CuO NF, also confirmed that increasing the concentration and flow rate of the NF increased the thermal efficiency. They reported that as the volume concentration of CuO NF increased from 0.002 vol% to 0.008 vol%, the thermal efficiency increased from 18% to 52%. Delfani et al. [78] investigated the influence

of the concentration of MWCNT NFs and the optical absorption properties in the bottom part of DASC. They confirmed that the collector efficiency of DASC using MWCNT NF was improved by 10–29% compared to that of the base fluid, mentioning that the collector efficiency decreased when the lower plate of DASC was highly reflective.



(a) Concept of volumetric absorption solar collecting method



(b) Schematic on volumetric absorption solar collecting method

Fig. 1.7 Volumetric absorption solar collecting method

Table 1.4 Summary of volumetric absorption solar collecting method

Author	NF	summary
Amjad et al. [71]	Cu, Ag, Zn, Si, Fe and β -Al ₂ O ₃ NF	- Optical absorption: Ag > Fe > Zn > Cu > Si > β -Al ₂ O ₃
Milanese et al. [52]	Al ₂ O ₃ , CuO, TiO ₂ , ZnO, CeO ₂ and Fe ₂ O ₃ NF	- Optical absorption of metal oxides NFs was decreased from visible to infrared light - Optical absorption:
Jin et al. [72]	Au, Cu, and Fe ₃ O ₄ NF	- Optical absorption of plasmonic NF (Au and Cu NF) was higher than non-plasmonic NF (Fe ₃ O ₄ NF) - Optical absorption can be improved by mixing of NFs with the different absorption peak
Guo et al. [73]	MWCNT NF	- The maximum photothermal conversion efficiency of MWCNT NF was 65.4%
Hazra et al. [74]	Carbon black NF	- Overall photo thermal conversion efficiency of CB NF with 15 ppm was 15% higher than EG - Local photo thermal conversion efficiency was increased by liquid layer thickness as well as concentration
Gorji and Ranjbar [75]	Graphite, magnetite, and silver NF	- Thermal efficiency is magnetite > graphite > silver - The thermal efficiency of magnetite NF with 40 ppm is Max. 54.7% - Thermal efficiency is mainly affected by the optical absorption of NF than <i>k</i> of NF
Gupta et al. [76]	Al ₂ O ₃ NF	- The thermal performance of the DASC using Al ₂ O ₃ NF and the thermal performance of the DASC were improved by increasing the concentration and flow rate of NF.
Menbari et al. [77]	CuO/Water NF	- Thermal efficiency was increased from 18 to 57.4% by increasing from 0.002 to 0.008vol%
Delfani et al. [78]	MWCNT NF	- The efficiency was decreased when both MWCNT NF and an aluminum absorption plate were used - The increase in the concentration and velocity of the NF improved the efficiency of the VASC by 10%–29% when the MWCNT NF was used compared with the base fluid

1.4. Purpose of this study

To actively and efficiently use solar thermal energy, it is necessary to improve the efficiency and miniaturization of the solar collector by performance improvement. In a solar collector, thermal energy is produced by absorbed solar energy and minimizing heat loss. Therefore, to improve the performance of solar collector, it is necessary to improve the solar energy absorption, heat transfer performance, and reducing heat loss. SASC method is widely used as a solar thermal collecting method due to its simple structure and low manufacturing cost. The thermal energy production mechanism of SASC has the process; (a) absorption of solar energy at receiver surface, (b) conversion from solar energy to thermal energy at receiver surface, (c) heat exchange between a receiver and working fluid like water, antifreeze, and oil, (d) transportation of thermal energy by working fluid. To improve the performance of solar collector with SASC, turbulence-inducing structures such as fin, baffle, and porous materials and NF with improved thermal properties have been used because thermal energy is produced by heat transfer between the receiver and working fluid. However, in the SASC method, there are problems with high convection and radiant heat loss due to local heating at the receiver. Different solar thermal collecting methods are required to improve solar collector performance.

In the VASC method, the solar energy is absorbed into the working fluid and converted to thermal energy. It has the advantages of reducing thermal resistance by simplified thermal energy production mechanism and heat loss to prevent local overheating. However, generally used working fluid such as water, oil, and antifreeze has low optical absorbance. It is challenging to use the VASC method because the performance of the solar collector depends on optical absorbance significantly. However, the VASC method can be used in the solar collector because it can improve the optical absorbance and the thermal properties of the working fluid through the development of the NF manufacturing method. Therefore, it is necessary to consider improving the performance of solar collector through the VASC method. In addition, application of the VASC method should be investigated. To utilize the VASC method, it is necessary to understand the optical absorption characteristics of NFs and a systematic design methodology for the VASC.

For these, it is needed to investigate the optical absorption performance of various NFs as well as the performance of the VASC for each operating condition.

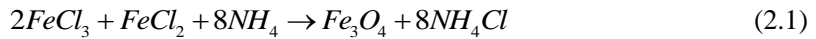
Investigations into the light absorption performance of NFs have been conducted. By focusing only on the light absorption performance of NFs, it is suggested that the VASC using NFs can be applied to the solar collector. There is no review of the applicability of the VASC method by comparing the performance of the general solar heat collection method (SASC) and the VASC method. To utilize the VASC, it is necessary not only to improve the light absorption performance by the NF but also to consider the heat transfer characteristics of the VASC and to review the utility through comparison with the existing solar collectors.

In this study, the optical absorbance and photo thermal conversion performance of NFs were investigated to consider the application in the VASC. To investigate the relation between optical characteristics of NFs and the performance of the flat plate solar collector (FPVASC), optical absorption performance on the FPVASC was numerically investigated. Besides, the effects of solar collecting methods such as VASC and SASC on applying NFs were experimentally investigated. Finally, the performance of the VASTC was investigated using Fe_3O_4 and ATO NFs with different optical absorption characteristics, and the performance improvement of the VASTC was experimentally investigated when the optical absorption performance was supplemented by mixing Fe_3O_4 and ATO NFs. Based on the results of this study, the performance of the existing solar collector and the VASTC was compared, and the application possibility of VASTC was evaluated.

2. Manufacture and stability of nanofluid

2.1. Preparation of nanofluid and synthesis of nanoparticle

This study attempted to produce water-based multi-walled carbon nanotube (MWCNT), iron oxide (Fe_3O_4), antimony doped tin oxide (ATO), and Fe_3O_4 /ATO hybrid NFs were prepared to select NFs suitable for VASC. MWCNT used in the preparation of NFs was prepared using 50wt% aqueous solution of ATO NFs prepared by KnPNano for the ATO NPs. Fe_3O_4 NPs were prepared using the co-precipitation method. Fig. 2.1 shows the synthesis of Fe_3O_4 NPs and the adsorption process of surfactants. Extra pure grade reagents ($\text{FeCl}_2 \cdot 4\text{H}_2\text{O}$, $\text{FeCl}_3 \cdot 4\text{H}_2\text{O}$, NaOH, and HCl) were used to prepare Fe_3O_4 NPs. The chemical formula for manufacturing Fe_3O_4 is as shown in Eq. (2.1).



In order to obtain the Fe^{2+} and Fe^{3+} salts necessary to prepare Fe_3O_4 NPs, a FeCl_3 solution (2.0 M FeCl_2 in 2 M HCl) and a FeCl_2 solution (1.0 M FeCl_3 in 2 M HCl) were prepared. As in Eq. (2.1), the FeCl_3 and FeCl_2 solutions were mixed at 150 rpm according to the chemical reaction ratio and stirred, while the mixture of FeCl_3 and FeCl_2 was heated to 70°C . Then, 1 mol of ammonia was added to the FeCl_3 and FeCl_2 mixture. The mixture to which ammonia is added produces a black precipitate (Fe_3O_4). After ammonia was completely added to the mixture, the reaction was allowed for 10 minutes, and the Fe_3O_4 NPs produced were collected using a magnet. The collected NPs were washed three times using ethanol and distilled water.

After that, to stably disperse Fe_3O_4 NPs in water, which is the base fluid, Fe_3O_4 was adsorbed with polyacrylic acid. After adding 0.01 mol of Fe_3O_4 NPs and 7.2 mL of 25wt% polyacrylic acid aqueous solution to 200 mL of distilled water, the Fe_3O_4 -polyacrylic acid aqueous solution was adjusted to pH7 using an aqueous NaOH solution. Then, to obtain the surface grafting of Fe_3O_4 NPs to PAA, the Fe_3O_4 NP mixture was reacted for 2 hours while

maintaining 70°C. Fe₃O₄ NPs were collected using a magnet, washed three or more times, and dried. Table 2.1 shows the physical properties of MWCNT, Fe₃O₄, and ATO NPs.

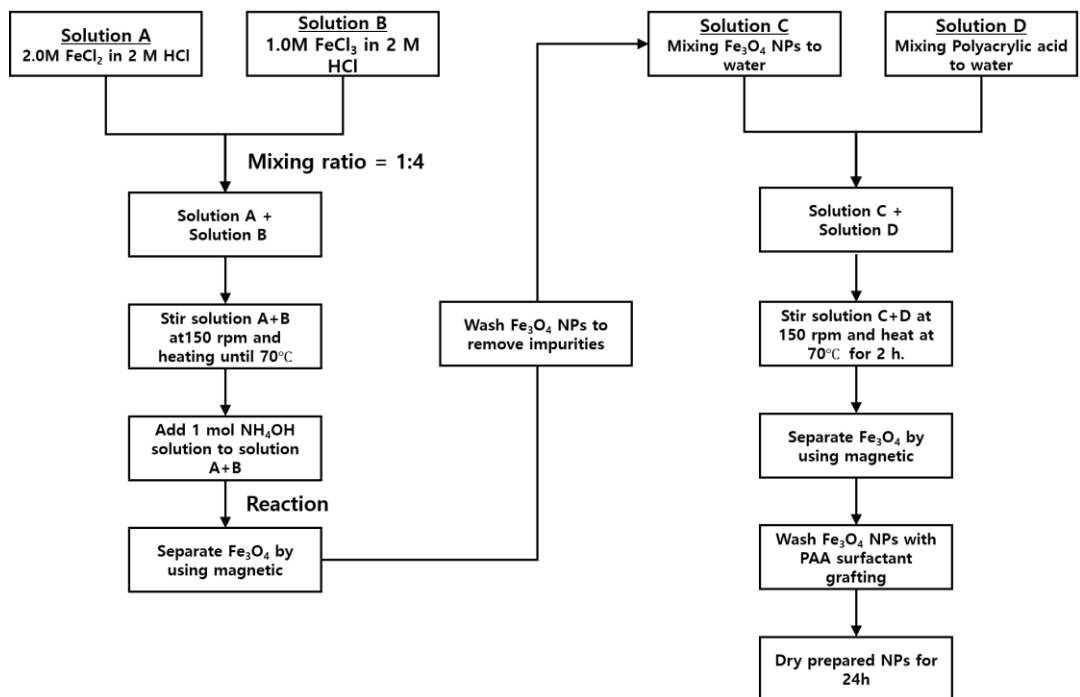


Fig. 2.1 Preparation process of Fe₃O₄ NF with PAA surfactant grafting

Table 2.1 Properties of NPs

NP	MWCNT	Fe ₃ O ₄	ATO
Purity	> 95%		99%
Color	Black	Dark brown	Blue
Outer diameter	20–30 nm	5–20 nm	10 ± 5 nm
Inner diameter	5–10 nm		
Length	10–30 μm		
Thermal conductivity	1500 W/m·K	80 W/m·K	4.4 W/m·K
True density	2.1 g/cm ³	5.1 g/cm ³	6.8 g/cm ³
Manufacturing method	Chemical vapor deposition	Co-precipitation	50% aqua solution

2.2. Manufacture of nanofluids

In this study, a two-step method was used to mechanically disperse the NPs prepared in the base fluid after generating NPs to prepare NFs. Fig. 2.2 shows the manufacturing process of NFs. To prepare NFs, NPs, surfactants, and base fluids corresponding to the quantity and concentration of NFs were weighed using a precision balance (FX-200i, AND Co., Japan). After that, the weighed NPs, surfactants, and base fluids were filled in a beaker and stirred at 500 rpm for 2 hours. Finally, the dispersion was performed by irradiating ultrasonic waves of 200,000 Hz into the mixed fluid. The ultrasonic dispersion process was different according to the experiment due to the consumed amount of NFs. In the performance experiment of the solar collector, a large amount of the NF was required compared to the measurement of the optical properties of NFs and the photothermal conversion experiment. Therefore, NFs were prepared for 2 hours by using small ultrasonic dispersion (SHT 750, Sonictopia Co., Korea) in the experiment for measuring optical properties and the photo thermal conversion performance.

In contrast, a large amount of NFs with 10 L or more was required in the performance experiment of the solar collector. Therefore, a high concentration NF with NFs required for the experiment was prepared using low capacity ultrasonic dispersion. And then, the high concentration of the NF was diluted by adding base fluid. Finally, diluted NFs were dispersed for 12 hours by the continuous circulation ultrasonic disperser (HUH-2000, HANTECH CO., Korea). Fig. 2.3 and Table 2.2 show actual photos and specifications of the small ultrasonic dispersion and the continuous circulation ultrasonic disperser used in the experiment. Fig. 2.4 shows images of prepared NFs

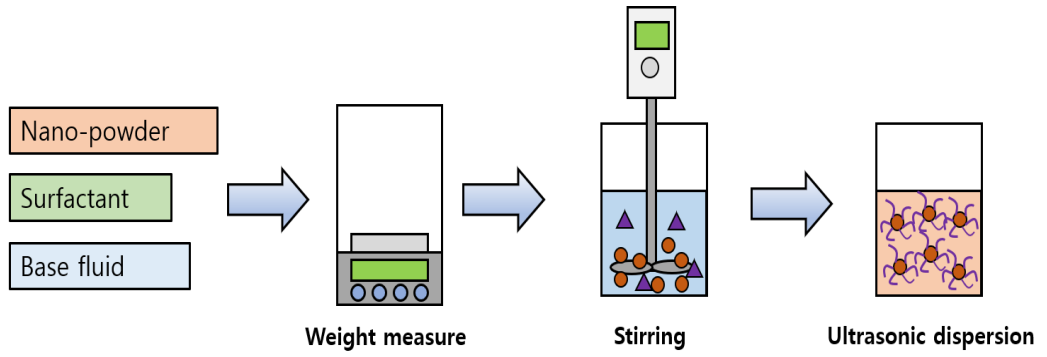


Fig. 2.2 Preparation process of NF



(a) Small ultrasonic dispersion



(b) Continuous circulation ultrasonic disperser

Fig. 2.3 Ultrasonic disperser for preparation of NF

Table 2.2 Specification of ultrasonic disperser for preparation of NF

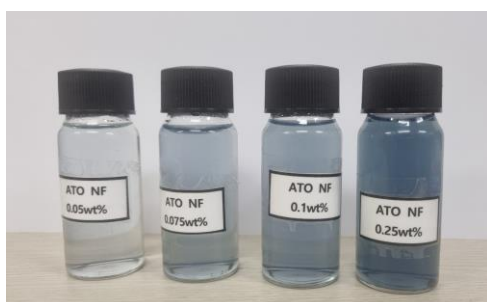
Type	Small ultrasonic dispersion	Continuous circulation ultrasonic disperser
Model	SHT 750	HUH 2000
Output power	750 W	2000 W
Frequency	19.97 kHz	20 kHz \pm 100 Hz
Converter	PZT (40mm PZT-81) Length = 160 mm	PZT, BLT type
Booster	Φ 48 \times 140 mm	
Horn	Φ 30 \times 123 mm	Ti type



(a) MWCNT NF



(b) Fe₃O₄ NF



(c) ATO NF



(d) Fe₃O₄/ATO hybrid NF

Fig. 2.4 Prepared NF; (a) MWCNT, (b) Fe₃O₄, (c) ATO and (d) Fe₃O₄/ATO hybrid NF

2.3. Nanofluid stability evaluation

To evaluate the dispersion stability of NFs, transmission electron microscopy (TEM) image analysis and zeta potential measurement were performed. TEM image analysis is a method of observing NP clusters in dispersed NF, having the advantage of confirming the size, shape, and degree of particle aggregation of NPs through the two-dimensional image of the NP cluster dispersed in the base fluid. The size of NPs was analyzed using Image J.

Zeta potential is a unit for the size of repulsion or attraction between particles, which is widely used as a quantitative indicator to evaluate the stability of NFs. Fig. 2.5 shows a schematic diagram of the charge distribution around the NPs. When NPs are suspended in the base fluid, NPs are electrically charged negatively or positively by dissociation of surface polar groups and adsorption of ions. Therefore, when NPs are dispersed in the base fluid, they are surrounded by a stern layer and a diffuse layer. In the stern layer, ions and NPs are strongly attached, whereas in the diffuse layer, ions have the opposite charge to the stern layer, and a small amount of the same ions are diffusely distributed to form an electric double layer. NPs with an electric charge in the NF move at a constant speed in response to an externally applied electric field. A slip plane is created in the electric double layer, and the zeta potential means an electrical potential in the slip plane. The more significant the zeta potential, the higher the repulsion between particles, with a low occurrence of agglomeration. Table 2.3 shows the stability criteria of colloids according to the zeta potential [79].

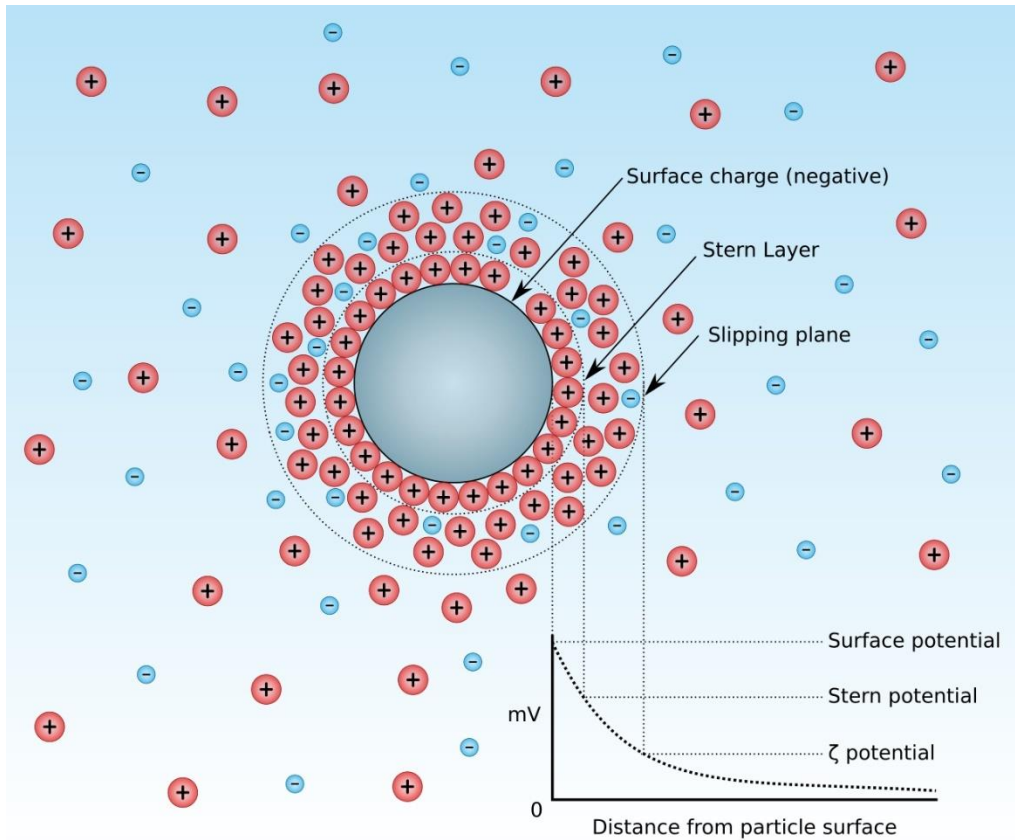


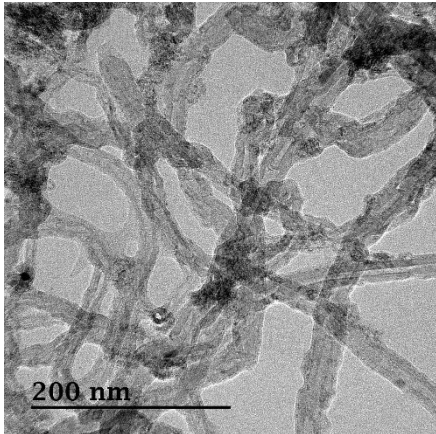
Fig. 2.5 Schematic of the distribution of charges around NP

Table 2.3 Stability behavior of a colloid depending on zeta potential [79]

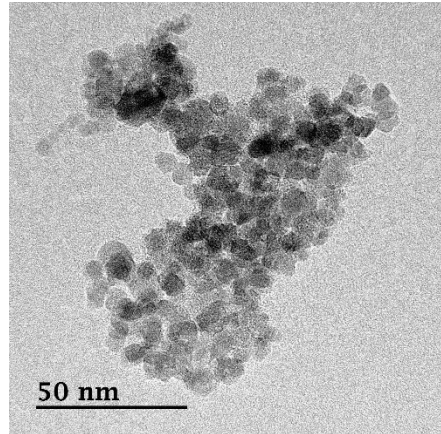
The magnitude of zeta potential (mV)	Stability behavior
0 to 5	Rapid coagulation or flocculation
10 to 30	Incipient instability
30 to 40	Moderate stability
40 to 60	Good stability
> 61	Excellent stability

2.3.1. TEM image analysis

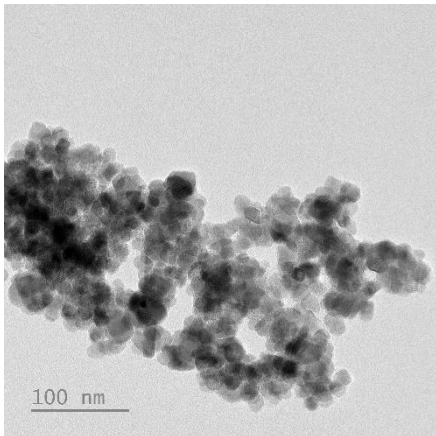
TEM image analysis was performed to analyze the shape and size of the prepared NPs. Fig. 2.6 shows TEM images of MWCNT NF, Fe₃O₄ NF, ATO NF, and Fe₃O₄/ATO hybrid NFs. NPs present in NF were forming clusters. The MWCNT NPs were observed to have a wire shape with a large aspect ratio, and the MWCNT NPs were tangled to form clusters. The outer diameter of the dispersed MWCNT NPs was measured to be $26.3\text{nm} \pm 4.2\text{ nm}$. It coincided with the outer diameter of 20–30 nm provided by the manufacturer. Fig. 2.7 shows the analysis results of Fe₃O₄ NF, ATO NF, and Fe₃O₄/ATO hybrid NF based on TEM images. As shown in Fig. 2.6, Fe₃O₄ and ATO NFs showed that individual NPs were dispersed to form clusters. The sizes of the Fe₃O₄ and ATO NPs forming the cluster are $10.9 \pm 4.2\text{ nm}$ and $11.72 \pm 4.2\text{ nm}$, respectively. The outer shape of each Fe₃O₄ NP was distorted. Several NPs were entangled to form a cluster. The Fe₃O₄ NF showed a distorted shape of the NPs according to the characteristics of the co-precipitation method. The shape of the ATO NF was also somewhat distorted. It was observed that the size of NPs in the Fe₃O₄/ATO hybrid NF was $12.4 \pm 1.9\text{ nm}$, reporting that Fe₃O₄ and ATO NPs coexisted and dispersed well.



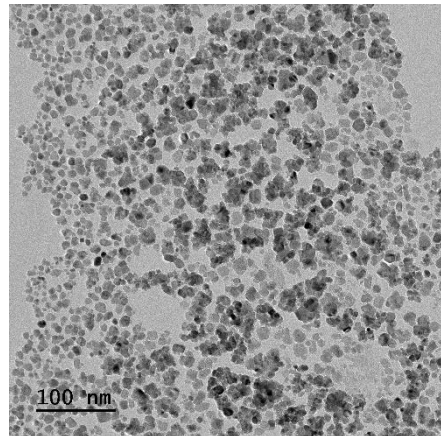
(a) MWCNT NF



(b) Fe₃O₄ NF

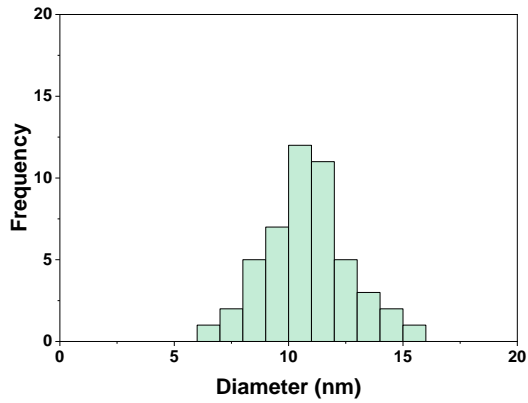


(c) ATO NF

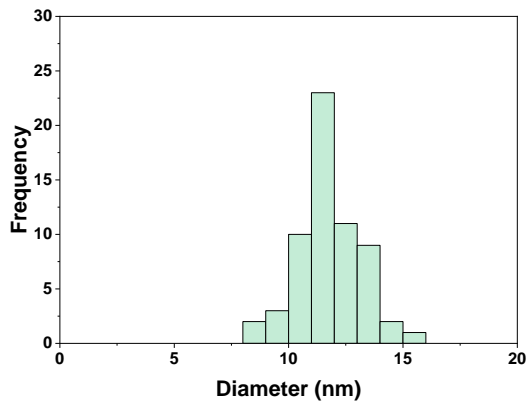


(d) Fe₃O₄/ATO hybrid NF

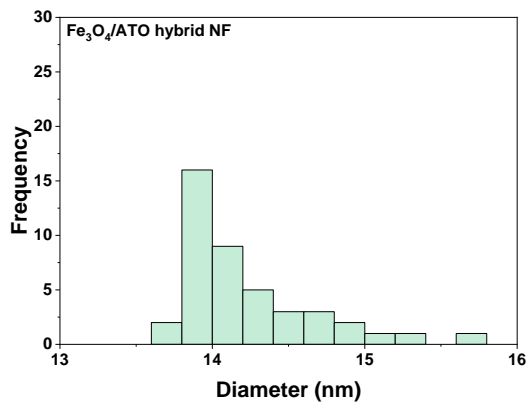
Fig. 2.6 TEM image of NF (a) MWCNT NF, (b) Fe₃O₄, (c) ATO NF, (d) Fe₃O₄/ATO hybrid NF



(a) Fe₃O₄ NF



(b) ATO NF



(c) Fe₃O₄/ATO hybrid NF

Fig. 2.7 NP diameter distribution (a) MWCNT NF, (b) Fe₃O₄ NF, (c) ATO NF, (e) Fe₃O₄/ATO hybrid NF

2.3.2. Zeta potential analysis result

To evaluate the dispersion stability of the prepared NF, the zeta potential of the prepared NF was measured using a zeta potential analyzer (ELSZ-2000ZS, Otsuka Electronics, Japan). Fig. 2.8 shows the actual photo of the zeta potential analyzer used for the zeta potential analysis of NFs. The zeta potential of the MWCNT, Fe₃O₄, ATO NF, and Fe₃O₄/ATO hybrid NF NFs was measured three days after preparation, and three measurements were performed for each NF sample. Fig. 2.9 shows the zeta potential of MWCNT, Fe₃O₄, ATO NF, and Fe₃O₄/ATO hybrid NFs. The measured zeta potentials of MWCNT, Fe₃O₄, ATO NF, and Fe₃O₄/ATO hybrid NFs were -40.4 ± 0.87 mV, -40.4 ± 2.0 mV, -49.9 ± 0.41 mV, and -40.2 ± 1.8 mV, respectively. The zeta potential indicates the surface electrical properties of NPs in a liquid, and the repulsive force between NPs increases with the size of the zeta potential. As the repulsive force between particles is greater than the van der Waals force, the agglomeration of NPs is prevented. Table 2.3 shows the standard of dispersion stability of colloids according to the magnitude of the zeta potential. When the dispersion stability of the NF is measured, a zeta potential of 30 mV or more is considered to indicate that the dispersion is stable. The prepared NF was evaluated to have stable dispersion when the zeta potential was 30 mV or more. The prepared MWCNT, Fe₃O₄, ATO, and Fe₃O₄/ATO hybrid NF satisfied the dispersion stability of the NF by meeting the minimum zeta potential of 30 mV for dispersion stability.



Fig. 2.8 Zeta potential analyzer

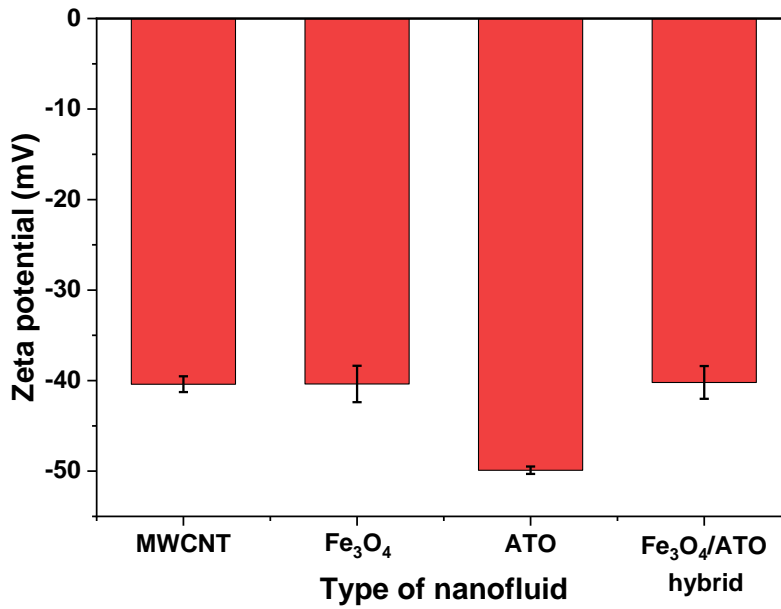


Fig. 2.9 Zeta potential of MWCNT, Fe₃O₄, ATO, Fe₃O₄/ATO hybrid NF

2.4. Thermal properties of nanofluid

2.4.1. Thermal conductivity of nanofluid

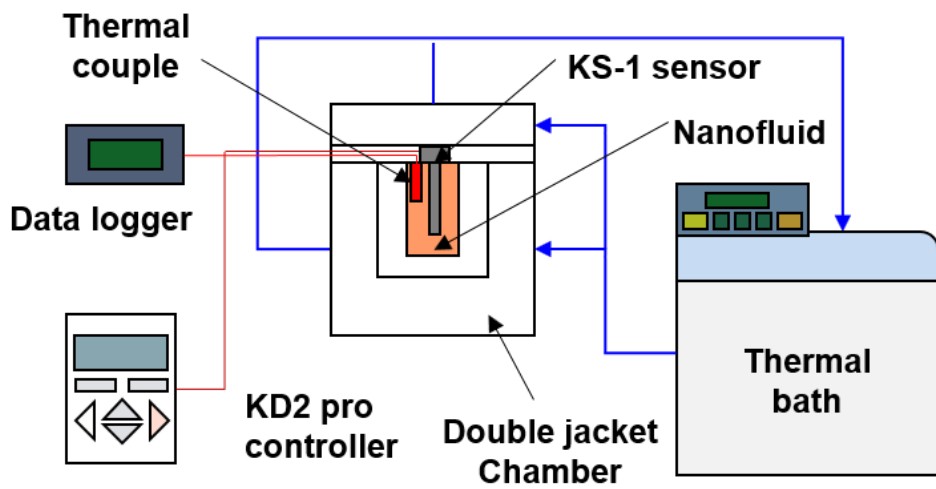
To evaluate the thermal conductivity of NFs according to the NF concentration and the NF type, the thermal conductivity of the NF was measured by using KD2-PRO, KS-1 sensor (DECAGON, USA). The thermal conductivity measurement method of the KD2-PRO is the transient hot-wire method. Its measurement error is 5%, and the measurement temperature range is from -50°C to 150°C . The KS-1 sensor among the KD2 pro sensors is suitable for measuring the liquid thermal conductivity with low viscosity. The thermal conductivity measurement range of the KS-1 sensor is from $0.02 \text{ W/m}\cdot^{\circ}\text{C}$ to $2 \text{ W/m}\cdot^{\circ}\text{C}$. The micro convection should be prevented in the transient hot-wire method because the measurement error can be increased. To prevent the micro convection, agar was added to NFs to make it into a gel state and measured. The state of NF is fixed by adding the agar, and the accuracy of measured thermal conductivity was improved due to the suppression of the micro convection [80]. Also, this method is recommended by the manufacturer of KD2-pro when the thermal conductivity of the liquid is measured [81]. The NF was contained in a glass bottle with a diameter of 30 mm and a length of 70 mm, and the container with the nanofluid was installed in the center of a double-jacket beaker. The sensor of KS-1 was mounted vertically in the center of the glass bottle. The temperature of the NF was maintained by constantly supplying the fluid with constant temperature from the thermal bath (LX-C200-H12, Labexchange, Germany) to the double-jacket beaker. The thermal conductivity of the NF was measured three times at the same temperature.

Table 2.4 shows the thermal conductivity of MWCNT, Fe_3O_4 , ATO, and $\text{Fe}_3\text{O}_4/\text{ATO}$ hybrid NF. In general, the thermal conductivity was increased with the increase in concentration and temperature. The thermal conductivity of the MWCNT, Fe_3O_4 , ATO, and $\text{Fe}_3\text{O}_4/\text{ATO}$ hybrid NF also increased with the increase in concentration and temperature. In the case of MWCNT NF, the thermal conductivity slightly increased from $0.603 \text{ W/m}\cdot^{\circ}\text{C}$ to $0.604 \text{ W/m}\cdot^{\circ}\text{C}$ as the concentration of the MWCNT NF was increased from 0wt% to 0.004wt% when the nanofluid

temperature was 20°C. As the temperature of the NF increased from 20°C to 50°C, the thermal conductivity of 0.1wt% MWCNT NF increased from 0.605 W/m·°C to 0.644 W/m·°C. However, it was confirmed that there was few improvements in thermal conductivity with an effect of less than 1wt%. Fe₃O₄ NF, ATO NF, and Fe₃O₄/ATO hybrid NF also improved thermal conductivity with increasing nanofluid concentration and temperature. To improve the thermal conductivity of NFs, high thermal conductivity and high concentration of NPs are required. However, the thermal conductivity is judged to be slightly improved in the concentration range in which the optical absorption is improved due to the low concentration.



(a) KD2 pro thermal conductivity device



(b) Schematic of thermal conductivity measurement

Fig. 2.10 Thermal conductivity measurement device

Table 2.4 The thermal conductivity of the NFs

Unit: W/m· °C

Thermal conductivity of MWCNT NF					
Temp.	Concentration of MWCNT NF				
	0wt%	0.0005wt%	0.001wt%	0.002wt%	0.004wt%
20°C	0.603	0.603	0.603	0.603	0.604
30°C	0.616	0.616	0.616	0.616	0.617
40°C	0.63	0.63	0.63	0.631	0.632
50°C	0.64	0.64	0.64	0.642	0.643

Thermal conductivity of Fe₃O₄ NF					
Temp.	The concentration of Fe₃O₄ NF				
	0wt%	0.025wt%	0.05wt%	0.075wt%	0.1wt%
20°C	0.603	0.603	0.604	0.604	0.605
30°C	0.616	0.616	0.617	0.618	0.619
40°C	0.63	0.631	0.631	0.632	0.634
50°C	0.64	0.641	0.642	0.642	0.644

Thermal conductivity of ATO NF					
Temp.	The concentration of Fe₃O₄ NF				
	0wt%	0.05wt%	0.075wt%	0.1wt%	0.25wt%
20°C	0.603	0.603	0.603	0.603	0.604
30°C	0.616	0.616	0.617	0.617	0.618
40°C	0.63	0.63	0.631	0.632	0.634
50°C	0.64	0.64	0.642	0.642	0.645

Thermal conductivity of Fe₃O₄/ATO hybrid NF						
Temp.	Mixing ratio of m_{Fe3O4}/m_{Total,NP}					
	0	0.2	0.4	0.6	0.8	1
20°C	0.603	0.604	0.604	0.604	0.604	0.604
30°C	0.616	0.618	0.618	0.618	0.618	0.618
40°C	0.632	0.632	0.632	0.632	0.632	0.632
50°C	0.642	0.642	0.642	0.642	0.642	0.642

2.4.2. Viscosity of nanofluid

To investigate the viscosity according to the type and concentration of the NFs, the viscosity was measured using a Vibro viscometer (SW-10, AND Co, Japan). Fig. 2.11 shows the image of the Vibro viscometer used in this study. Vibro viscometer measures the viscosity by resonantly vibrating a roller in a fluid with a certain amplitude, amplifying the viscous resistance of the viscosity measuring sensor, and measuring the current value. The measuring range of the viscometer is 0.3–10000 mPa·s, the accuracy of the viscometer is 1%, and the measurable fluid temperature is less than 160°C.

Table 2.5 shows the measured viscosity of the MWCNT, Fe₃O₄, ATO NFs, and Fe₃O₄/ATO hybrid NF. The viscosity of each NF was slightly increased by the increase of the concentration. In the case of the MWCNT NF, the viscosity increased from 1 mPa·s to 1.02 mPa·s according to the increase of the concentration from 0wt% to 0.004wt% and maximum μ_{nf}/μ_{bf} was 1.02 when the temperature of MWCNT NF was 20°C. As the temperature of the MWCNT NF was increased from 20°C to 50°C, the viscosity was decreased, while the μ_{nf}/μ_{bf} was almost not increased in measurement range. It is considered that the viscosity did not increase significantly due to the low concentrations. In the case of Fe₃O₄ NF and ATO NF, the viscosity improvement was significant compared to MWCNT NF.

The Fe₃O₄ NF and ATO NF viscosity improvement were higher than MWCNT NF. In the case of the Fe₃O₄ NF, the viscosity was increased from 1 mPa·s to 1.06 mPa·s according to the concentration from 0wt% to 0.1wt% when the temperature of working fluid was 20°C. The maximum μ_{nf}/μ_{bf} was 1.06 at the 0.1wt%. Fe₃O₄ NF. As the temperature of Fe₃O₄ NF was increased from 20°C to 50°C, the μ_{nf}/μ_{bf} was measured less than 1.06. In the case of the ATO NF, the viscosity increase due to the increase in concentration was lower than that of Fe₃O₄ NF. As the temperature of ATO NF was 20°C, the viscosity was increased from 1 mPa·s to 1.06 mPa·s by increasing the concentration from 0wt% to 0.25wt%. the μ_{nf}/μ_{bf} of 0.25wt% ATO NF was maximum and it was equal to the 0.1wt% Fe₃O₄ NF. As the temperature was increased from 20°C

to 50°C, the viscosity of the 0.25wt% ATO NF was decreased from 1.06 to 0.59 mPa·s and the μ_{nf}/μ_{bf} was between 1.06 and 1.11. The viscosity of the 0.1wt% Fe₃O₄/ATO hybrid NF was between 0.1wt% ATO NF and 0.1wt% Fe₃O₄ NF. Although there is a difference in viscosity increase according to the types of MWCNT, Fe₃O₄, ATO, and Fe₃O₄/ATO hybrid NF, it is determined that the viscosity increase is insignificant according to the increase in the concentration of the NF within the optical absorption improvement range.



Fig. 2.11 Vibro viscometer SV-10

Table 2.5 The viscosity of the NFs

Unit: mPa·s

The viscosity of MWCNT NF						
Temp.	Concentration of MWCNT NF					
	0wt%	0.0005wt%	0.001wt%	0.002wt%	0.004wt%	
20°C	1	1	1	1.01	1.02	
30°C	0.8	0.8	0.8	0.8	0.81	
40°C	0.65	0.65	0.65	0.654	0.66	
50°C	0.55	0.55	0.55	0.55	0.55	

The viscosity of Fe₃O₄ NF						
Temp.	The concentration of Fe₃O₄ NF					
	0wt%	0.025wt%	0.05wt%	0.075wt%	0.1wt%	
20°C	1	1.02	1.03	1.04	1.05	
30°C	0.8	0.81	0.82	0.83	0.84	
40°C	0.65	0.66	0.67	0.68	0.69	
50°C	0.55	0.55	0.56	0.57	0.58	

The viscosity of ATO NF						
Temp.	The concentration of Fe₃O₄ NF					
	0wt%	0.05wt%	0.075wt%	0.1wt%	0.25wt%	
20°C	1	1.01	1.02	1.02	1.06	
30°C	0.8	0.81	0.81	0.81	0.87	
40°C	0.65	0.66	0.67	0.68	0.72	
50°C	0.55	0.56	0.57	0.58	0.59	

The viscosity of Fe₃O₄/ATO hybrid NF						
Temp.	Mixing ratio of m_{Fe3O4}/m_{Total,NP}					
	0	0.2	0.4	0.6	0.8	1
20°C	1.02	1.03	1.03	1.04	1.04	1.05
30°C	0.81	0.82	0.82	0.83	0.83	0.84
40°C	0.68	0.68	0.68	0.69	0.69	0.69
50°C	0.58	0.58	0.58	0.58	0.58	0.58

3. Optical properties and photo thermal conversion performance of nanofluid

3.1. Optical properties measurement method of nanofluid

The optical absorption properties of the NFs were measured using an ultraviolet-visible spectrometer (AVANTES-2048, Inc. AVANTES, Netherlands). Fig. 3.1 shows a schematic diagram and an actual photo of the light transmittance measuring device. The light source of the spectrometer passes through the optical cable, and the light source is exposed to the cuvette filled with NF. The intensity of light energy transmitted through the NF was measured through the detector of the spectrometer, and the light transmittance was measured using AvaSoft 8, an analysis tool provided by AVANTES.

The light transmittance of the NF is defined as Eq. (3.1), which is a function of the incident intensity and the projected light intensity on the NF.

$$T(\lambda) = \frac{I}{I_0} = \exp(-k_{ex} L_{op}) \quad (3.1)$$

Where I_0 and I denote the incident and transmitted intensities to the reference line, respectively, and k_{ex} and L_{op} denote the extinction coefficients and the optical depth, respectively.

The incident intensity was measured while the cuvette filled with NF was removed from the beam's path. The intensity of transmission in the light path was measured while the cuvette was filled with NF. To accurately measure the optical properties of the NF, the data were obtained by averaging 200 data during one measurement, and each NF was measured three times to evaluate its reproducibility.

The traditional double thickness transmittance method (TDTTM) measured optical properties such as optical absorption, reflection, and transmission of NFs. TDTTM is a method for evaluating optical properties using two optical transmittances of the same fluid with different

light penetration depths [82,83]. To use TDTM, this study measured light transmittance at 5 mm and 10 mm optical transmission depths. To calculate the reflectance in the visible light band, the reflectance was calculated using TDTM under the following assumptions.

- (a) The fluid and glass are homogeneous, causing no scattering.
- (b) The influence of quartz cuvettes is negligible.
- (c) The optical characteristics of the fluid-filled quartz cuvette are uniform.
- (d) The spectral transmittance, reflectance, and absorptivity of the fluid-filled quartz cuvette are independent at the same thickness.

The low concentration of NF is unlikely to be affected by scattering, and NPs are uniformly distributed in the NF. In addition, the quartz cuvette used in this experiment has uniform optical properties within 250 nm to 2500 nm. Because the stone cuvette has similar light transmittance to water, it is an environment in which the optical influence can be neglected, meeting the assumption.

The optical absorption, reflectivity, and absorption of the NF contained in the cuvette under the condition that light is vertically incident on the cuvette can be expressed in Eqs. (3.2)–(3.4).

$$A(\lambda) = 1 - R(\lambda) - T(\lambda) \quad (3.2)$$

$$R(\lambda) = \rho + \frac{(1 - \rho)^2 \exp\left(\frac{-8\pi k_{ex} L_{op}}{\lambda}\right)}{1 - \rho^2 \exp\left(\frac{-8\pi k_{ex} L_{op}}{\lambda}\right)} \quad (3.3)$$

$$T(\lambda) = \frac{(1 - \rho)^2 \exp\left(\frac{-4\pi k_{ex} L_{op}}{\lambda}\right)}{1 - \rho^2 \exp\left(\frac{-8\pi k_{ex} L_{op}}{\lambda}\right)} \quad (3.4)$$

Where ρ denotes the reflectance of the interface between air and the cuvette, k_{ex} denotes the average extinction coefficient of the NF filled in the cuvette, L_{op} denotes the optical depth of the NF filled in the cuvette, and λ denotes the wavelength of light.

ρ can be calculated by Eq. (3.5).

$$\rho = \frac{(n-1)^2 + \kappa^2}{(n+1)^2 + \kappa^2} \quad (3.5)$$

Where n denotes the average refractive index of the NF in the cuvette.

While ρ is needed to estimate the absorption and reflectance of the NF in the cuvette, ρ and R cannot be calculated without knowing n and k of the NF. This problem can be solved by TDTTM, which investigates optical properties through two transmittances with different light penetration depths. TDTTM calculates the absorption, reflection, and transmission properties of a fluid by combining two transmittances with different light penetration depths in the same fluid and Fresnel's relation, which calculates optical properties using the formulas described below.

$T_1(\lambda)$ and $T_2(\lambda)$, which have different light transmission depths, can be expressed as Eq. (3.6) and Eq. (3.7), respectively.

$$T_1(\lambda) = (1 - \lambda)^2 \exp\left(\frac{-4kL_{op,1}}{\lambda}\right) \quad (3.6)$$

$$T_2(\lambda) = (1 - \lambda)^2 \exp\left(\frac{-4kL_{op,2}}{\lambda}\right) \quad (3.7)$$

$k(\lambda)$ calculated by Eq. (3.6) and Eq. (3.7) is assumed by using Eq. (3.8).

$$k(\lambda) = -\frac{\lambda \ln\left(\frac{T_1(\lambda)}{T_2(\lambda)}\right)}{4\pi(L_{op,1} - L_{op,2})} \quad (3.8)$$

ρ and k can be expressed as Eq.(3.9) and Eq.(3.10) by combining Eqs. (3.5)–(3.7).

$$\rho = \frac{1 - \sqrt{T_1^2 + T_1 \left[\exp\left(\frac{4\pi k L_1}{\lambda}\right) - \exp\left(\frac{-4\pi k L_2}{\lambda}\right) \right]}}{1 + T_1 \left(\frac{-4\pi k L_1}{\lambda}\right)} \quad (3.9)$$

$$k = \frac{\lambda}{4\pi L_2} \ln \left[\frac{\left(1 + \sqrt{1 + 4c^2 \rho^2}\right)}{2c} \right] \quad (3.10)$$

In Eq. (3.10), c can be expressed by Eq. (3.11).

$$c = \frac{T_2}{(1 - \rho)^2} \quad (3.11)$$

To track the optical properties accurately, iterative calculations are performed sequentially from Eq. (3.9) to (3.12).

Because solar energy has a different energy intensity for each wavelength, it is necessary to evaluate the light transmission distance of the NF and the solar energy distribution for each wavelength to evaluate the solar energy absorption capacity of the NF quantitatively. The solar weight absorption coefficient considering the solar energy distribution according to wavelength can be calculated as Eq. (3.12).

$$A_{sw}(L_{op}) = \frac{\int I_{AM1.5}(\lambda)(1 - \exp(-k_{b,\lambda}L_{op}))d\lambda}{\int I_{AM1.5}(\lambda)d\lambda} \quad (3.12)$$

Where, $I_{Am1.5}(\lambda)$ denotes the spectral solar irradiance based on ASTM G173-3 AM 1.5 Global [84].

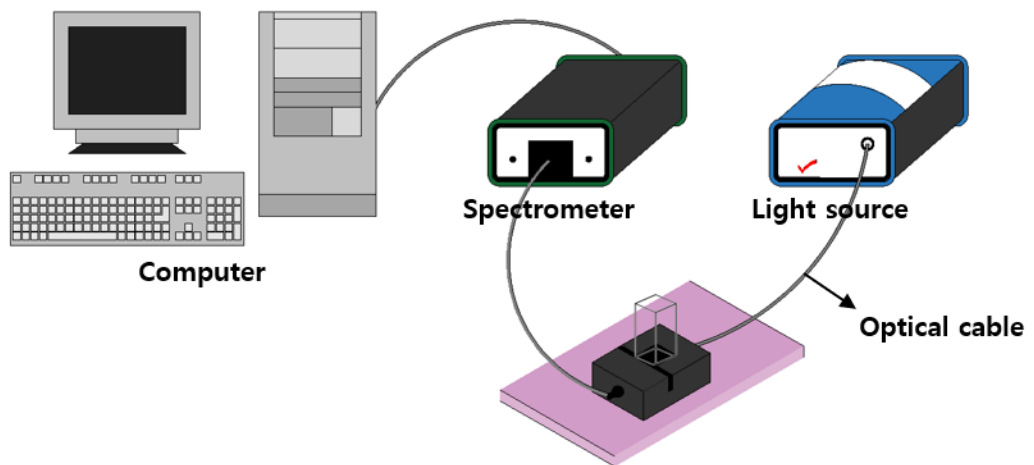


Fig. 3.1 Schematic of optical transmittance measurement experiment setup

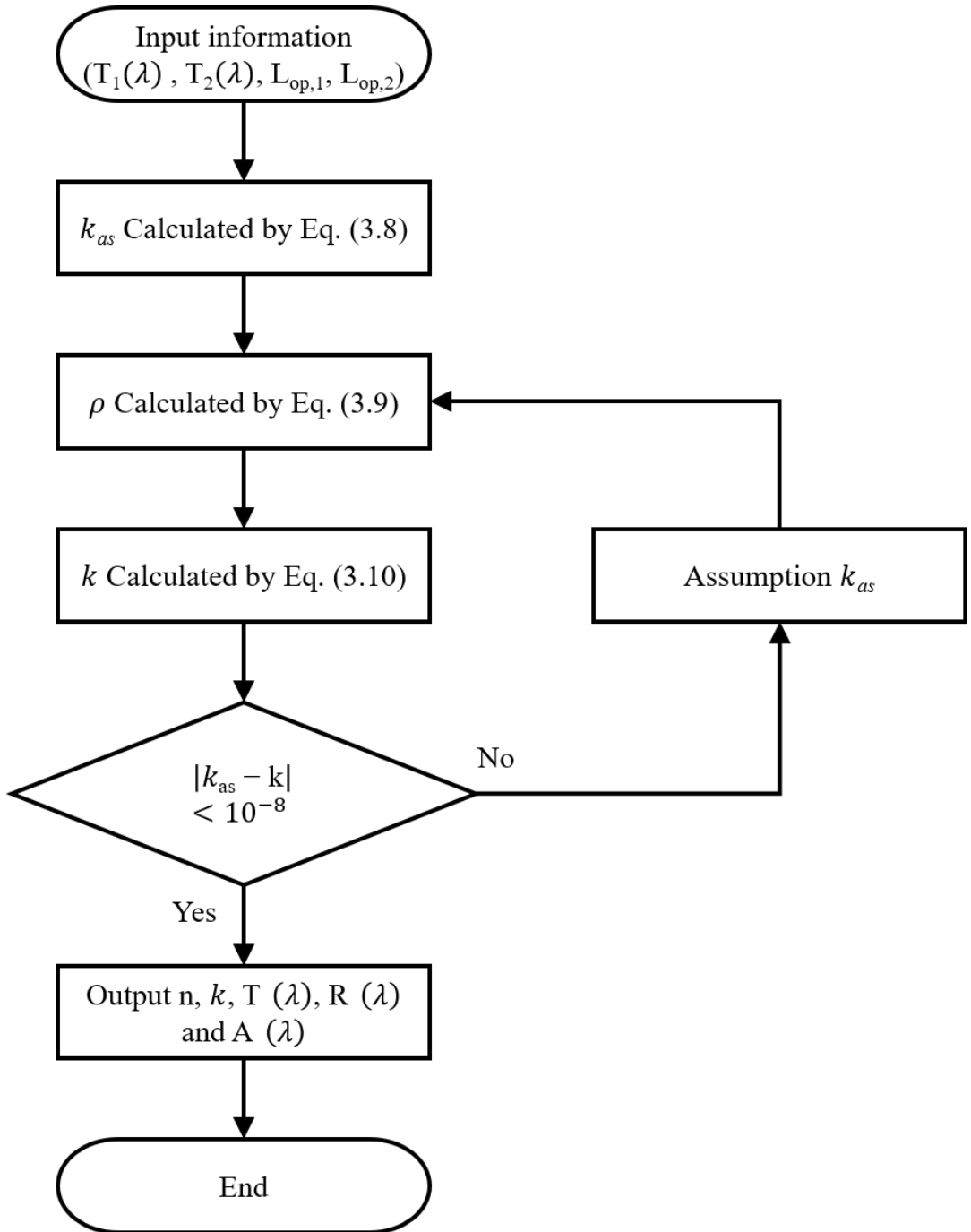


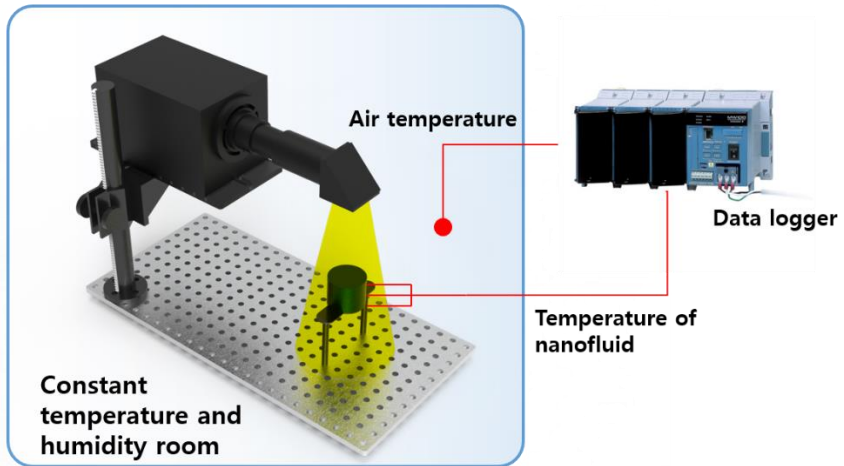
Fig. 3.2 Calculation process about absorbance and reflectance by TDDTM

3.2. Experiment method to measure photo thermal conversion performance of nanofluid

3.2.1. Experimental setup for photo thermal conversion

In the photothermal conversion experiment, it is important to uniformly supply light energy according to ambient temperature and time changes. Therefore, to evaluate the photothermal conversion characteristics of the NF, it was measured using a solar simulator in a constant temperature and humidity room. Fig. 3.3 shows an experimental apparatus for photothermal conversion properties of NFs. A solar simulator (Oriel Xenon Arc lamp, Newport Co, LCS-100, America) was used to irradiate the NF with solar-like light energy for a certain period. The solar simulator satisfies the spectral agreement of class A, spatial non-uniformity of the illuminance of class B, and temporal instability of class B according to the ASTM standard (ASTE E927-05). Table 3.1 shows the main performance indicators of the solar simulator. To uniformly irradiate the NF with solar energy, the container containing the NF is placed in the center of the illumination, at a point 178 mm from the light-irradiated surface.

1 Sun is secured in the solar simulator's solar intensity at this point. The container containing the NF is made of 3 mm glass, and the sides are made of acrylic. The inside container containing the NF is $\phi 40 \text{ mm} \times 42 \text{ mm}$ in size. Three T-type thermocouples ($\pm 0.1^\circ\text{C}$) with $\pm 0.1^\circ\text{C}$ precision were installed at equal intervals in the height direction in the NF container to determine the temperature change by the location of the NF exposed to light. The temperature and ambient temperature for each position of the NF were collected through a data accumulator (MX-100, Yokogawa Inc., Japan) at 1-second intervals. The temperature in the temperature and humidity chamber was kept constant at 25°C . To evaluate the effects of NFs on optical absorption and heat loss, light exposure was performed on NFs for 2.5 hours using a solar simulator, and the temperature distribution of NFs was measured by cooling for 0.5 hours after the end of light exposure.



(a) Illustration of the experimental setup for photo thermal conversion



(b) Photo of the experimental setup

Fig. 3.3 Experimental setup for photo thermal conversion experiment

Table 3.1 Performance specifications of the solar simulator

Item	Value
Illumination Area (inches) [mm]	1.5×1.5 [40×40]
Maximum Angle of Incidence (°)	< ± 6
Variable Output Control (Irradiance Adjustment)	Height: ~0.18 Sun/inch
Nominal Working Distance (inches) [mm]	7.0 [178]
Light Ripple:	< 0.5% RMS
Lamp Type:	100 W, Ozone Free Xenon
Average Lamp Lifetime	750 Hours

3.2.2. Analysis method for photo thermal conversion performance

The receiving efficiency (η_{rec}) indicates the energy conversion efficiency for each light exposure time as the ratio of the light exposure time and the amount of thermal energy change of the NF. Because the concentration of the NF is not high enough to affect the change in specific heat, the receiving efficiency can be calculated by Eq. (3.13).

$$\eta_{rec} = \frac{(c_{p,w}m_w + c_{p,np}m_{np})(T(t) - T(0))}{IA\Delta t} \approx \frac{c_{p,w}m_w(T(t) - T(0))}{IA\Delta t} \quad (3.13)$$

The photo thermal conversion efficiency of NFs can be calculated through heating and cooling processes depending on whether or not light exposed [85]. Because NFs generate heat loss during continuous light exposure, the thermal environment around the NF container can be expressed by the energy equation of Eq. (3.14).

$$\dot{Q}_{ab} = \sum_i m_{nf} c_{p,i} \frac{dT}{dt} = \dot{Q}_{in} - \dot{Q}_{dis} \quad (3.14)$$

Where, m_i and $c_{p,i}$ denote the mass and specific heat of the thermal system (NF, container parts, etc.) affected by light exposure, respectively. \dot{Q}_{in} denotes the solar energy irradiated to the NF, and can be expressed as Eq. (3.15) considering the photo thermal conversion efficiency.

$$\dot{Q}_{in} = IA\eta \quad (3.15)$$

Because the difference between the temperature of the NF and the surrounding temperature is not large, \dot{Q}_{dis} can be expressed as Eq. (3.16) under the assumption that radiative heat transfer is neglected.

$$\dot{Q}_{dis} = h_{c,l} A_{dis} (T(t) - T_{air}) \quad (3.16)$$

Through Eq. (3.15) and Eq. (3.16), Eq. (3.14) can be expressed as Eq. (3.17).

$$\frac{dT}{dt} = \frac{IA\eta}{\sum_i m_i c_{p,i}} - \frac{h_{cl} A_{dis} (T(t) - T_{air})}{\sum_i m_i c_{p,i}} \quad (3.17)$$

Because it is a cooling process $Q_{in} = 0$ in which light is not irradiated to the NF, Eq. (3.17) can be expressed as Eq. (3.18).

$$\frac{dT}{dt} = - \frac{h_{cl} A_{dis} (T(t) - T_{air})}{\sum_i m_i c_{p,i}} \quad (3.18)$$

Therefore, Eq. (3.18) can be expressed as Eq. (3.19).

$$\ln \frac{T(t) - T_{air}}{T_{eq} - T_{air}} = - \frac{h_{cl} A_{dis}}{\sum_i m_i c_{p,i}} t = -Bt \quad (3.19)$$

In Eq. (3.19), constant B denotes the heat dissipation rate to the surroundings, and the temperature change at the end of light exposure under normal conditions can be statistically calculated. Fig. 3.4 shows the temperature change after exposing water to light during the cooling process. Constant B denotes the slope of the temperature function in Fig. 3.4. In this study, the B of each NF was measured from 4.1×10^{-4} to 4.5×10^{-4} .

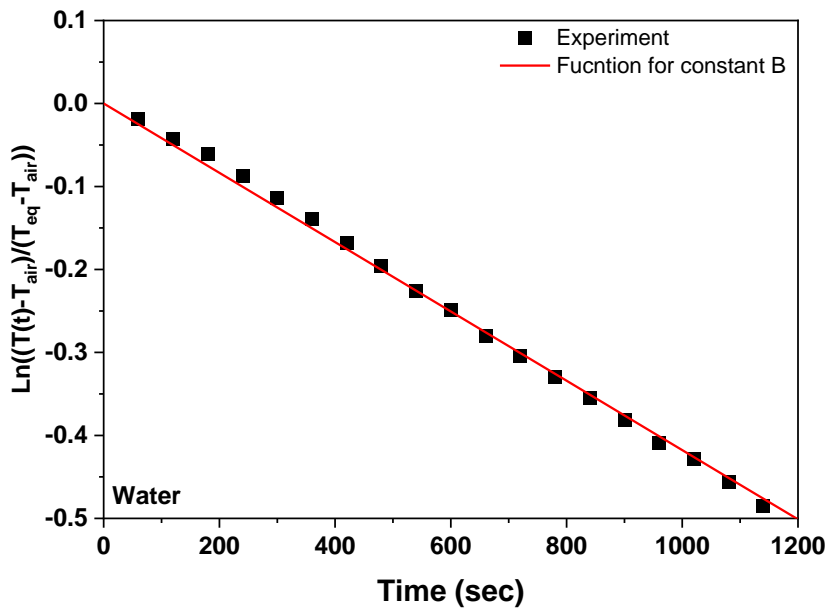


Fig. 3.4 Temperature variation during the cooling process

3.2.3. Economic analysis of photo thermal conversion performance

To perform economic analysis on the optical absorption performance of NFs, it is necessary to evaluate the solar energy absorbed by NPs dispersed in NFs. Specific absorption rate (SAR) is widely used as a method to evaluate the solar energy absorbed per unit mass of NPs. SAR is Eq. It can be expressed as Eq. (3.20).

$$SAR = \frac{(c_w m_w + c_n m_n) \Delta T_n - c_w m_w \Delta T_w}{m_n \Delta t} \approx \frac{c_w m_w (\Delta T_n - \Delta T_w)}{m_n \Delta t} \quad (3.20)$$

The cost of improving the optical absorption performance of NFs can be calculated by using the cost of NP required for NF manufacturing and the SAR, it can be calculated by Eq. (3.21).

$$\text{Cost/kW} = \text{cost}_{np} / SAR \quad (3.21)$$

The cost of MWCNT, Fe₃O₄, and ATO NPs is the purchase price of the manufacturer used in this study. The price of MWCNT, Fe₃O₄, ATO per 1g is 5370 won, 2360 won, 400 won [86,87].

3.2.4. Uncertainty analysis of photo thermal conversion experiment

The uncertainty of the receiver efficiency of photo thermal conversion experiment is calculated by Eq. (3.22)

$$\frac{\delta\eta_{receiv}}{\eta_{receiv}} = \sqrt{\left(\frac{\delta m}{m}\right)^2 + \sum_{i=1}^3 \left(\frac{\delta T}{T_i}\right)^2 + \left(\frac{\delta A}{A}\right)^2 + \left(\frac{\delta I}{I}\right)^2 + \left(\frac{\delta t}{t}\right)^2} \quad (3.22)$$

Where the uncertainty of the mass of NF, the rising temperature, area, the intensity of irradiance, and the time were 2.36%, 2.47%, 0.5%, 0.5%, and 0.01%, respectively, thus the maximum uncertainty of the receiving efficiency is 3.5%.

The uncertainty of the photo thermal conversion efficiency is calculated by Eq. (3.23)

$$\frac{\delta\eta_{receiv}}{\eta_{receiv}} = \sqrt{\left(\frac{\delta m}{m}\right)^2 + \sum_{i=1}^3 \left(\frac{\delta T}{T_i}\right)^2 + \left(\frac{\delta A}{A}\right)^2 + \left(\frac{\delta I}{I}\right)^2 + \left(\frac{\delta B}{B}\right)^2} \quad (3.23)$$

Where the uncertainty of the mass of NF, the rising temperature, area, the intensity of irradiance, and the rate of heat dissipation to the surroundings were 2.36%, 2.47%, 0.5%, 0.5%, and 2.35%, respectively, therefore the maximum uncertainty of the photo thermal conversion efficiency is 4.21%.

The uncertainty of the receiving efficiency and photo thermal conversion efficiency is acceptable compared to previous studies.

3.3. Result and discussion on optical properties and photo thermal conversion performance of nanofluid

3.3.1. Optical characteristics of single nanofluid

Fig. 3.5 shows the light transmittance of MWCNT, Fe₃O₄, and ATO NFs at optical depths of 0.005 m and 0.01 m. The light transmittance of each NF decreased as the concentration of the NF increased. Each NF was affected by a change in light transmittance concerning a change in concentration, and the sensitivity of the change in light transmittance to a change in concentration differed depending on the type of dispersed NPs. As for water as the base fluid for the NF in this study, at the optical depth of 0.005 m and 0.01 m, with a wavelength of 800 nm, the light transmittance was the highest at 0.951 and 0.913, respectively. This point is the wavelength that separates infrared light from visible light. As a result of comparing the light transmittance of NFs with a wavelength of 800 nm, when the concentration of MWCNT, Fe₃O₄, and ATO NF increased to 0.004wt%, 0.1wt%, and 0.25wt% at an optical depth of 0.005 m, the light transmittance decreased to 0.038, 0.274, and 0.462, respectively. In addition, when the concentrations of MWCNT, Fe₃O₄, and ATO NFs increased to 0.004wt%, 0.1wt%, and 0.25wt% at an optical depth of 0.01 m, the light transmittance decreased to 0.002, 0.034, 0.078, and 0.2421, respectively. This indicated that the change in light transmittance according to the change in NF concentration was the most sensitive with MWCNT, followed by Fe₃O₄ and ATO NFs.

As for water, excellent optical absorption was observed in the near-infrared band, while optical absorption was insufficient in the visible and ultraviolet bands. The increased concentration of the NF was found to increase the light transmittance in the near-infrared and visible light bands. However, the characteristics of improving optical absorption by wavelength differed according to the NF. As for the CNT NFs, the light transmittance at 400–1200 nm decreased almost uniformly as the NF concentration increased from 0.005wt% to 0.004wt%. As the conductivity of the Fe₃O₄ NF increased to 0.1wt%, the light transmittance in the visible and

ultraviolet bands of 800 nm or less showed a significant decrease in the light transmittance in the near-infrared band of 800 nm or more. On the other hand, unlike the Fe_3O_4 NF, the ATO NF had a more significant decrease in light transmittance in the near-infrared band above 800 nm than in the visible and ultraviolet bands below 800 nm. This meant that the light transmittance of the NF was affected by the optical properties of the dispersed NPs, and thus the optical absorption properties for each wavelength band were different.

Optical absorption characteristics for each wavelength band can be identified through extinction coefficients measured under conditions of different optical distances. Fig. 3.6 shows the extinction coefficient of NFs at optical depths of 0.005 m and 0.01 m. The extinction coefficient of the NF is the sum of the optical absorption coefficient and the scattering coefficient, indicating the optical absorption capacity of the NF. The extinction coefficient of MWCNT, FeFe_3O_4 , and ATO NFs at an optical depth of 0.01 m was decreased compared to the extinction coefficient of the optical depth of 0.005 m. As the NF concentration increased, the difference in extinction coefficient at the optical depths of 0.005 m and 0.01 m increased. In particular, the difference in the extinction coefficients at the optical depths of 0.005 m and 0.01 m was significant at a short wavelength of 500 nm, compared to the extinction coefficients at 800 nm and 1100 nm. At wavelengths of 500 nm, 800 nm, and 1100 nm, the difference in extinction coefficients at the optical depth of 0.005 m and 0.01 m of the MWCNT NF increased to 4.2–174, 1–20.4, and 0.4–12.8 1/m, as the concentration of the NF increased from 0wt% to 0.004wt%. In the Fe_3O_4 NF, the difference in the extinction coefficients at the optical depths of 0.005 m and 0.01 m was the largest compared to MWCNT and ATO NFs. As the Fe_3O_4 NF concentration increased from 0wt% to 0.1wt%, it increased to 4.2–265.6, 1–12.3, and 0.4–16.2 1/m. Compared to MWCNT and Fe_3O_4 NFs, ATO NF showed the lowest decrease in the extinction coefficients at the optical depths of 0.005 m and 0.01 m. As the ATO NF concentration increased from 0wt% to 0.4wt%, it increased to 4.2–9.9, 1–11.9, and 0.4–12.4 1/m. The decrease in the extinction coefficient with the increase in the optical depth meant that the light entering the NF could not pass through the medium due to the interference by the NPs floating in the NF, thereby reducing the optical absorption ability.

Fig. 3.7 shows the contour image of optical absorption for the wavelength band of MWCNT, Fe₃O₄, and ATO NFs. The light absorbance of NFs increased with the increase in NF concentration, but the light absorbance for each wavelength was different. An increase in NF concentration was not necessarily directly related to an increase in optical absorption. Uniform optical absorption within 400–1200 nm was observed in MWCNT NF, compared to other NFs. However, the optical absorption was reduced when the NF concentration exceeded 0.002wt%. Fe₃O₄ NF showed excellent optical absorption improvement by increasing the NF concentration from 600 nm to 1100 nm, whereas the improvement in optical absorption by increasing the concentration of Fe₃O₄ NF in the light wavelength band below 600 nm was low. As the Fe₃O₄ NF concentration increased to 0.075wt%, the optical absorption increased, but when it exceeded 0.075wt%, the optical absorption gradually decreased. In particular, as the NF concentration increased, the optical absorption decreased from 400 nm to a shorter wavelength. Unlike the Fe₃O₄ NF, ATO NF showed excellent optical absorption in the near-infrared band at near 1100 nm but showed low optical absorption in the ultraviolet and visible light bands with short wavelengths. In addition, unlike NFs such as MWCNT and Fe₃O₄ NF, ATO NFs showed insufficient improvement in optical absorption according to NF concentration change.

As for the optical absorption of the NF, the optical absorption area increases due to the number of NPs as the concentration of the NF increases. MWCNT NF not only has the excellent optical absorption ability of MWCNT NPs but also has a large aspect ratio of the NPs and a large surface area for optical absorption due to the entanglement of many NPs in the NF. On the other hand, ATO NF has not only the low optical absorption ability of ATO NPs but also a higher density of ATO NPs than MWCNT and Fe₃O₄ NPs, making it difficult to secure a large surface area for optical absorption.

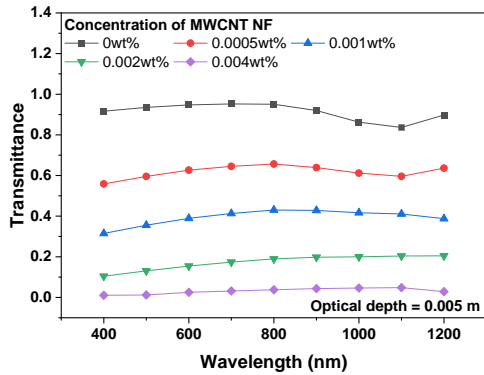
Fig. 3.8 shows the contour image of the light reflectance for the wavelength bands of MWCNT, Fe₃O₄, and ATO NFs. MWCNT and Fe₃O₄ NFs exhibited light reflection near 400 nm and 1200 nm, whereas ATO NF exhibited light reflection near 1200 nm. In MWCNT NF, when the NF concentration exceeded 0.002wt%, the reflectance rapidly increased near 400 nm, with a maximum reflection of 0.47 observed at 0.004wt%. Fe₃O₄ NF showed more substantial light

reflection near 400 nm than MWCNT and ATO NFs, and the intensity of reflection increased as the NF concentration increased. In ATO NF, a small intensity of light reflection of 0.1 was observed near 1200 nm as the NF concentration increased to 0.25wt%. This may have been because the light was reflected rather than diffracted when it collided with NPs in some visible and ultraviolet bands with short wavelengths. As the concentration of the NF increased, the light was less likely to be transmitted but reflected due to the dense spacing between NPs.

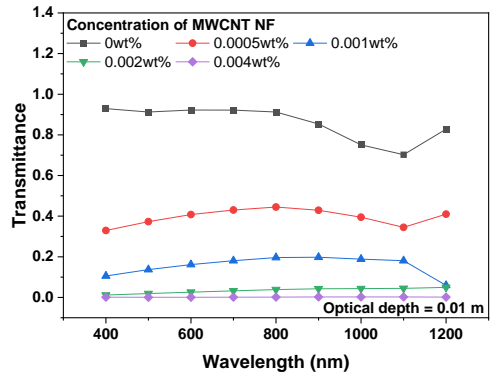
Considering that the solar energy reaching the earth's surface was composed of 49% infrared light, 44% visible light, and 7% ultraviolet light, the solar energy absorption coefficient was compared with A.M 1.5, a model of solar energy reaching the earth's surface to evaluate the optical absorption capacity of NFs. Fig. 3.9 shows the solar weight absorption coefficients of MWCNT, Fe₃O₄, and ATO NFs. The solar weight absorption coefficient was the highest in MWCNT NF, followed by Fe₃O₄ and ATO NFs. With an optical length of 0.02 m or longer or the NF concentration of 0.002wt% or higher, MWCNT NF could absorb more than 90% of solar energy regardless of the optical depth. When the optical depth was more significant than 0.03 m, the solar weight absorption coefficient decreased with the concentration of MWCNT NF exceeding 0.001–0.002wt%.

The maximum solar weight absorption coefficient of MWCNT NF was 0.935 when the MWCNT NF concentration was 0.001wt%, and the optical depth was 0.06 m. The solar weight absorption coefficient of Fe₃O₄ NF was also similar to that of MWCNT NF. Fe₃O₄ NF showed a lower solar weight absorption coefficient than MWCNT NF. The solar weight absorption coefficient of Fe₃O₄ NF was almost constant from the optical depth of 0.03 m at the same concentration. When the Fe₃O₄ NF concentration exceeded 0.075wt%, the solar weight absorption coefficient decreased after reaching a maximum value. The maximum solar weight absorption coefficient for Fe₃O₄ NF was 0.891. ATO NF showed a noticeable optical depth improvement in the solar weight absorption coefficient. The maximum solar weight absorption coefficient of ATO NF was 0.904 when the ATO NF concentration was 0.25wt%, and the optical depth was 0.06 m.

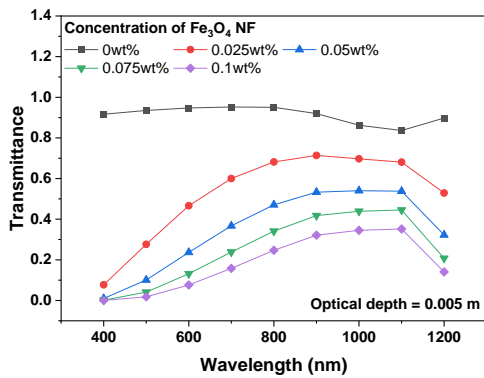
As shown in Fig. 3.7 and Fig. 3.8, MWCNT NF showed consistent improvement in optical absorption in the visible and infrared bands according to the change in NF concentration. When the NF concentration exceeded 0.002wt%, there was an excellent improvement in the optical absorption ability as the reflectance in the ultraviolet and visible light bands with short light wavelengths increased. On the other hand, Fe_3O_4 NF had excellent optical absorption improvement in the visible light band, but the maximum solar weight absorption coefficient was lower than that of MWCNT NF as the reflectance in the short-wavelength ultraviolet, and visible light bands sharply increased with an increase in the NF concentration. While ATO NF exhibited a low optical absorption capacity, the effect of reflection with an increase in the NF concentration was shallow compared to MWCNT and Fe_3O_4 NFs. Therefore, the solar weight absorption coefficient improved as the light transmission depth increased. Because Fe_3O_4 NF and ATO NF have opposite light transmission properties, mixing Fe_3O_4 and ATO NFs was expected to complement each other.



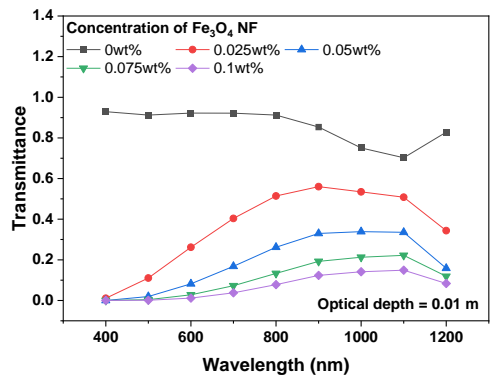
(a1) MWCNT NF, Optical depth = 0.005 m



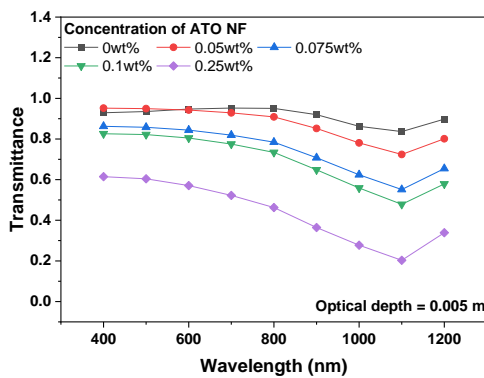
(a2) MWCNT NF, Optical depth = 0.01 m



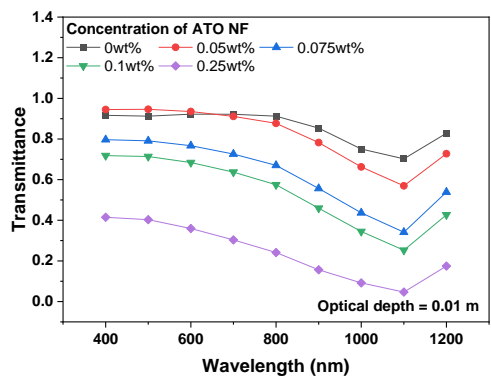
(b1) Fe₃O₄ NF, Optical depth = 0.005 m



(b2) Fe₃O₄ NF, Optical depth = 0.01 m

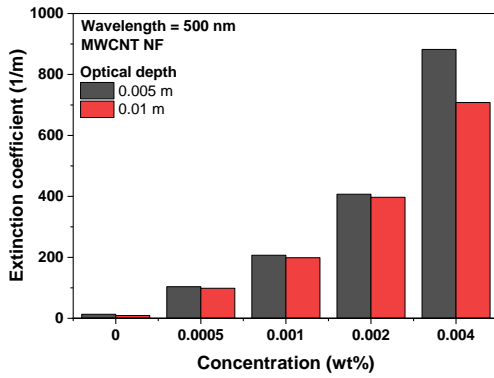


(c1) ATO NF, Optical depth = 0.005 m

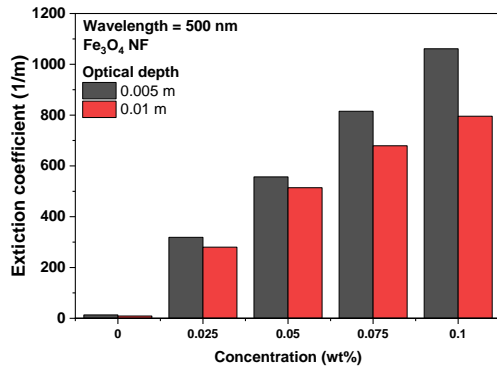


(c2) ATO NF, Optical depth = 0.01 m

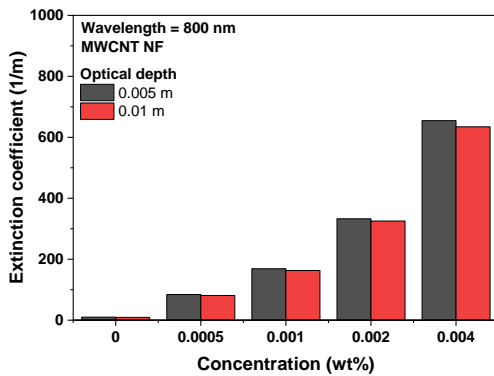
Fig. 3.5 Spectral transmittance of NF; (a) MWCNT NF, (b) Fe₃O₄ NF, (c) ATO NF



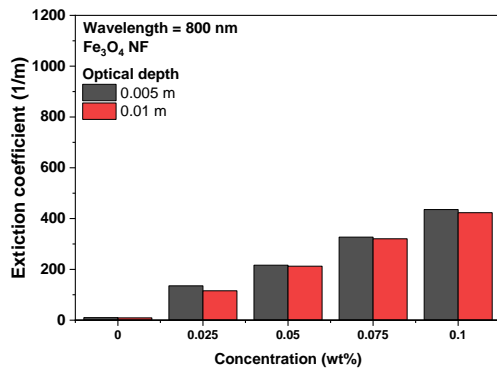
(a1) MWCNT NF, Wavelength = 500 nm



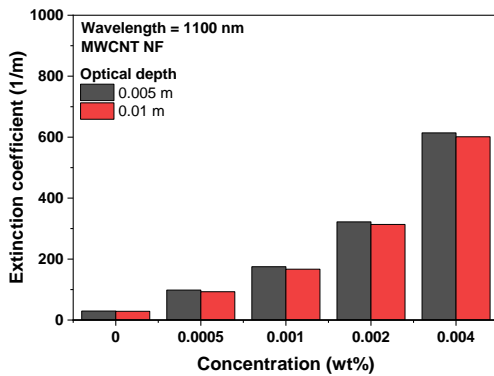
(b1) Fe₃O₄ NF, Wavelength = 500 nm



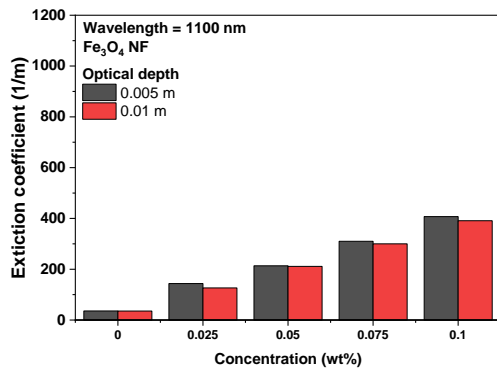
(a2) MWCNT NF, Wavelength = 800 nm



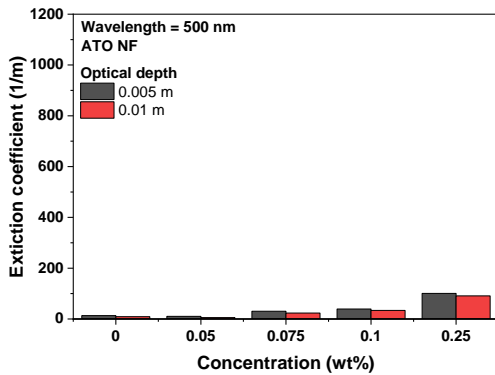
(b2) Fe₃O₄ NF, Wavelength = 800 nm



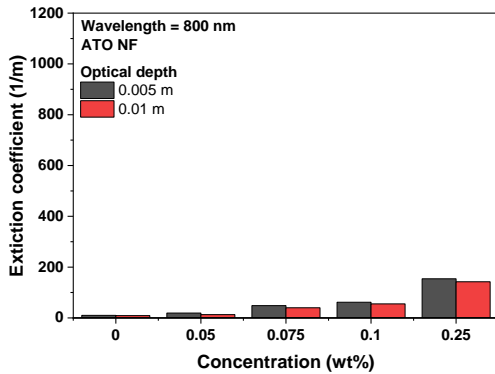
(a3) MWCNT NF, Wavelength = 1100 nm



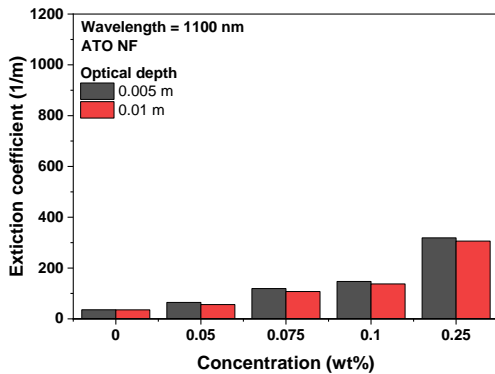
(b3) Fe₃O₄ NF, Wavelength = 1100 nm



(c1) ATO NF, Wavelength = 500 nm

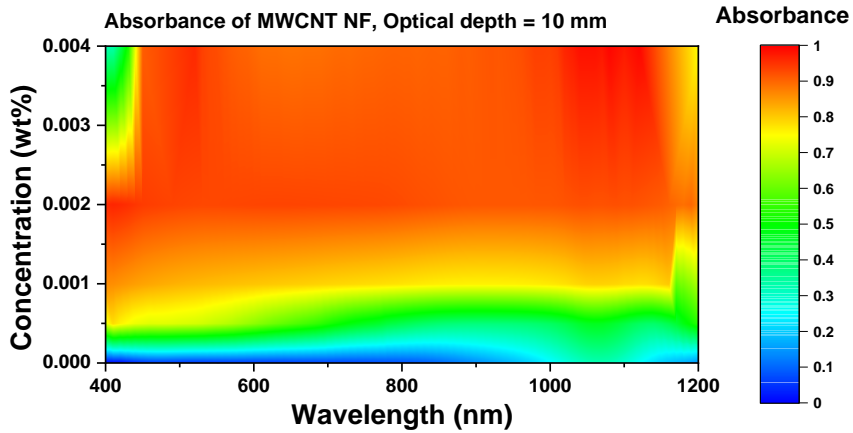


(c2) ATO NF, Wavelength = 800 nm

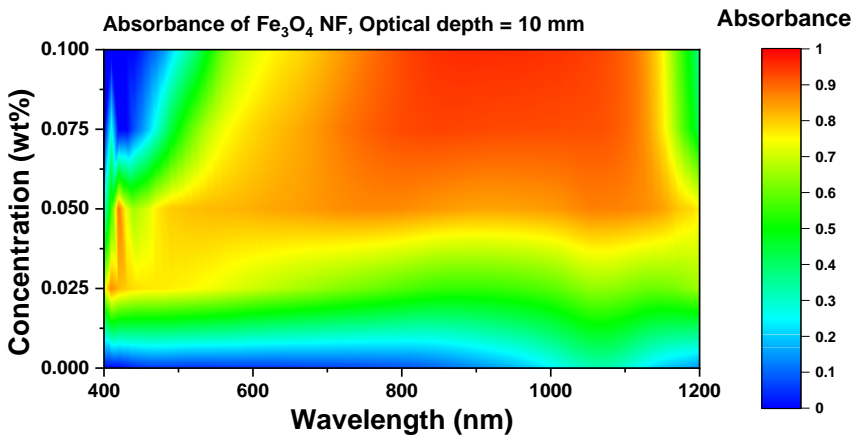


(c3) ATO NF, Wavelength = 1100 nm

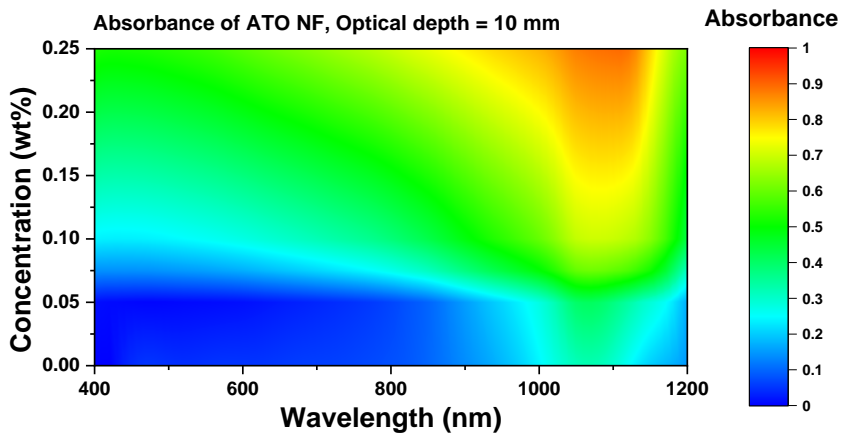
Fig. 3.6 Extinction coefficient of NF at optical depth = 0.005 m and 0.01 m; (a) MWNT, (b) Fe_3O_4 , (c) ATO NF



(a) MWCNT NF

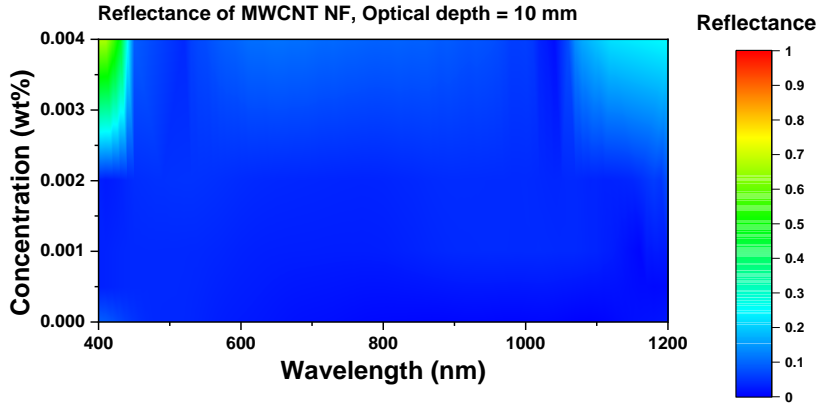


(b) Fe₃O₄ NF

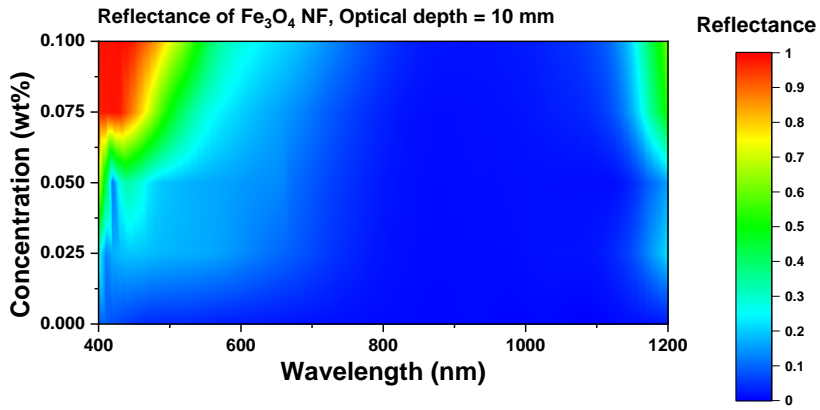


(c) ATO NF

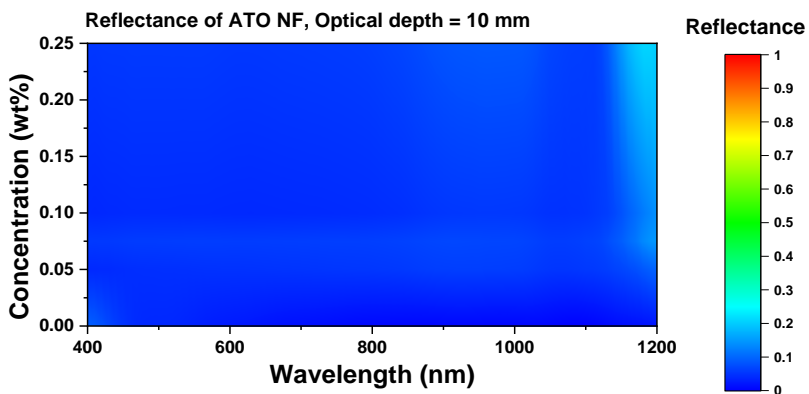
Fig. 3.7 Spectral absorbance of NF; (a) MWCNT NF (b) Fe₃O₄ NF (c) ATO NF



(a) MWCNT NF

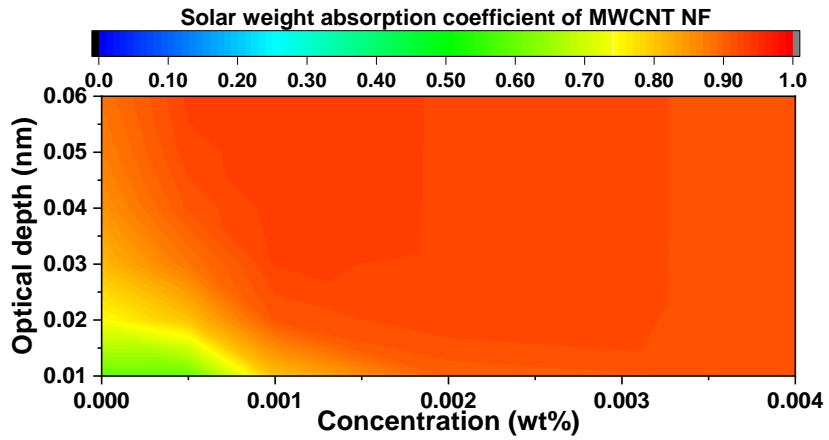


(b) Fe_3O_4 NF

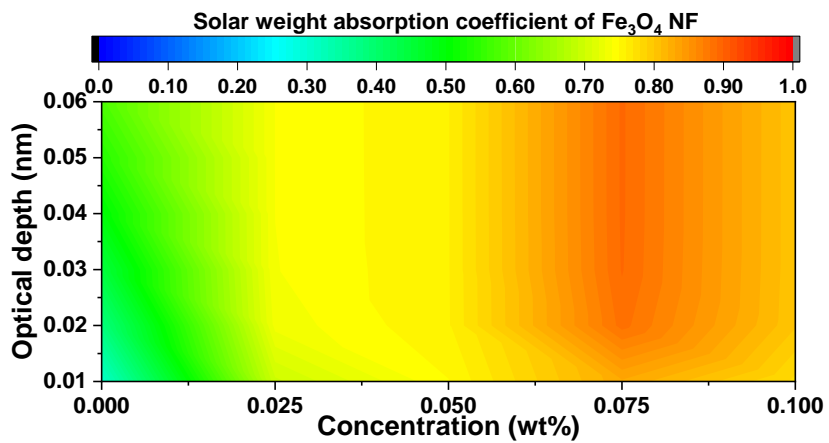


(c) ATO NF

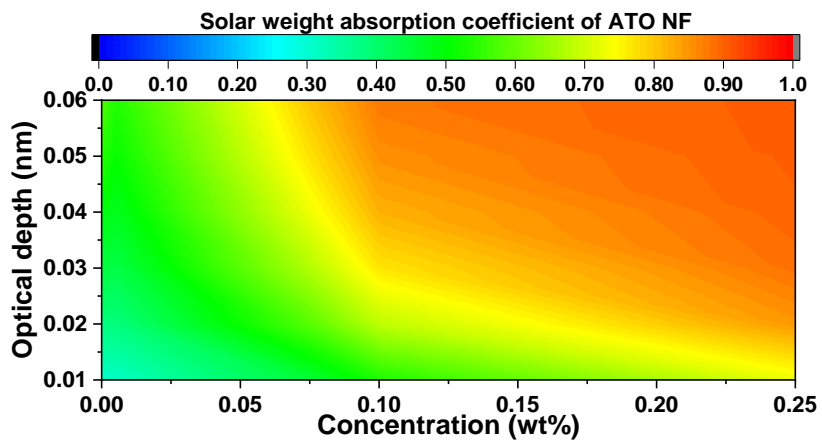
Fig. 3.8 Spectral reflectance of NF; (a) MWCNT NF (b) Fe_3O_4 NF, (c) ATO NF



(a) MWCNT NF



(b) Fe₃O₄ NF



(c) ATO NF

Fig. 3.9 Solar weight absorption coefficient of NF; (a) MWCNT NF (b) Fe₃O₄ NF, (c) ATO NF

3.3.2. Optical characteristics of Fe₃O₄/ATO hybrid nanofluid

Fe₃O₄ and ATO NFs exhibited opposite optical absorption properties to each other. Therefore, the optical absorption performance can be improved by adequately mixing Fe₃O₄ and ATO NFs. Fig. 3.10 shows the optical absorption of the Fe₃O₄/ATO hybrid NF according to the Fe₃O₄ and ATO mixing ratio for a total concentration of 0.1wt%. The Fe₃O₄/ATO hybrid NF exhibited different degrees of improvement in optical absorption for each wavelength band according to the mixing ratio of Fe₃O₄ and ATO. Because the 0.1wt% ATO NF has lower optical absorption in the light wavelength band of 800 nm or less than the 0.025wt% Fe₃O₄ NF, the optical absorption was dramatically improved even with a small amount of Fe₃O₄ in the Fe₃O₄/ATO hybrid NF. Although the light absorbance at 800–1000 nm decreased as $m_{\text{Fe}_3\text{O}_4}/m_{\text{Total,NP}}$ increased to 0.2–0.6 in Fe₃O₄/ATO hybrid NF, the optical absorption in other bands was improved, and the optical absorption in the 600–1000 nm light wavelength had linearity.

Fig. 3.11 shows the reflectivity of the Fe₃O₄/ATO hybrid NF according to the Fe₃O₄ and ATO mixing ratio when the total concentration is 0.1wt%. Fe₃O₄ NF showed a disadvantage of high reflectance in the ultraviolet and visible light bands with short optical wavelengths. However, the reflectivity of Fe₃O₄/ATO hybrid NF decreased with the reduction of the portion of Fe₃O₄ NPs. The reflectivity decreased from 0.98 to 0.09 as the $m_{\text{Fe}_3\text{O}_4}/m_{\text{Total,NP}}$ decreased from 1 to 0 at the light wavelength of 400 nm. When the wavelength of light was 1200 nm, the reflectivity decreased from 0.522 to 0.181 as $m_{\text{Fe}_3\text{O}_4}/m_{\text{Total,NP}}$ decreased from 1 to 0. When the Fe₃O₄/ATO hybrid NF has a low content of Fe₃O₄, optical absorption is generally reduced, but high optical absorption can be expected when the optical length is extended due to a decrease in reflectance.

Fig. 3.12 shows the solar weight absorption coefficient of the Fe₃O₄/ATO hybrid NF according to the mixing ratio for different optical depths. In Fe₃O₄/ATO hybrid NF, the solar weight absorption coefficient was improved compared to the Fe₃O₄ and ATO NFs, and the improvement effect of the solar weight absorption coefficient was different depending on the

optical depth. The solar weight absorption coefficient of the Fe₃O₄/ATO hybrid NF showed a considerable improvement with a short optical depth and a high Fe₃O₄ content, whereas a remarkable improvement in the solar weight absorption coefficient by an increase in the optical depth was observed with a high ATO content. When the optical depth was 0.01 m, the solar weight absorption coefficient was 0.861 when $m_{\text{Fe}_3\text{O}_4}/m_{\text{Total,NP}}=0.8$, slightly improved compared to 0.854 of 0.1wt% Fe₃O₄ NF and 0.529 of 0.1wt% ATO NF. However, the maximum solar weight absorption coefficient of Fe₃O₄ NF was lower than 0.891. On the other hand, when $m_{\text{Fe}_3\text{O}_4}/m_{\text{Total,NP}}=0.2$, the optical depth increased from 0.748 to 0.938 as the optical depth increased from 0.01 m to 0.06 m, and the solar weight absorption coefficient was almost equal to 0.395 of 0.001wt% MWCNT NF, having the best optical absorption performance among single component NFs. Unlike MWCNT NFs, Fe₃O₄ATO hybrid NFs had lower optical absorption performance than MWCNT NFs, as optical absorption continued depending on the optical depth. MWCNT and Fe₃O₄ NFs were suitable for volume absorption collectors with an extended optical depth, and single NFs were suitable for volume absorption collectors with a short optical absorption length.

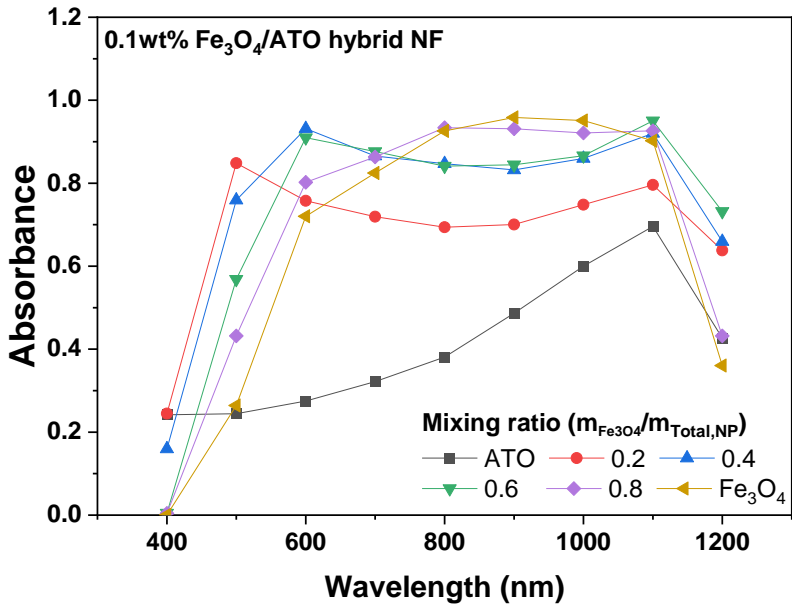


Fig. 3.10 Spectral absorbance of Fe₃O₄/ATO hybrid NF according to $m_{\text{Fe}_3\text{O}_4}/m_{\text{Total,NP}}$

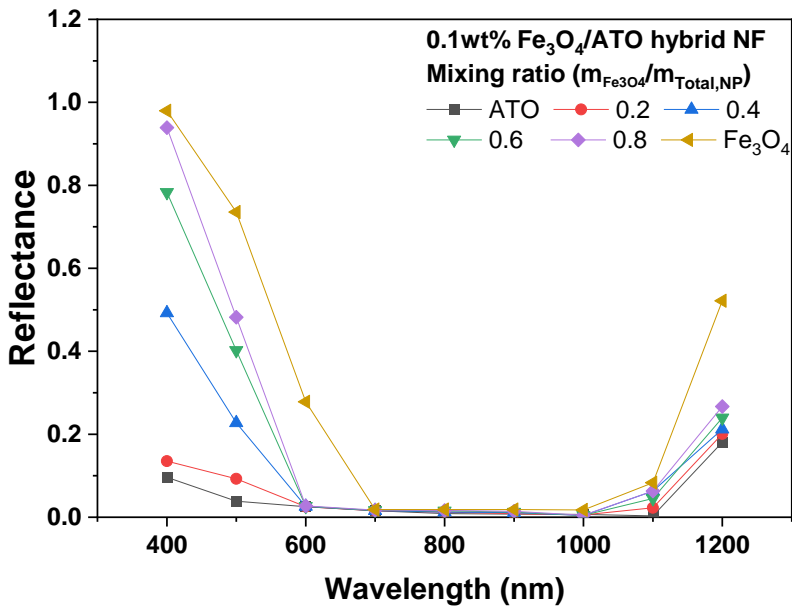


Fig. 3.11 Spectral reflectance of Fe₃O₄/ATO hybrid NF according to $m_{\text{Fe}_3\text{O}_4}/m_{\text{Total,NP}}$

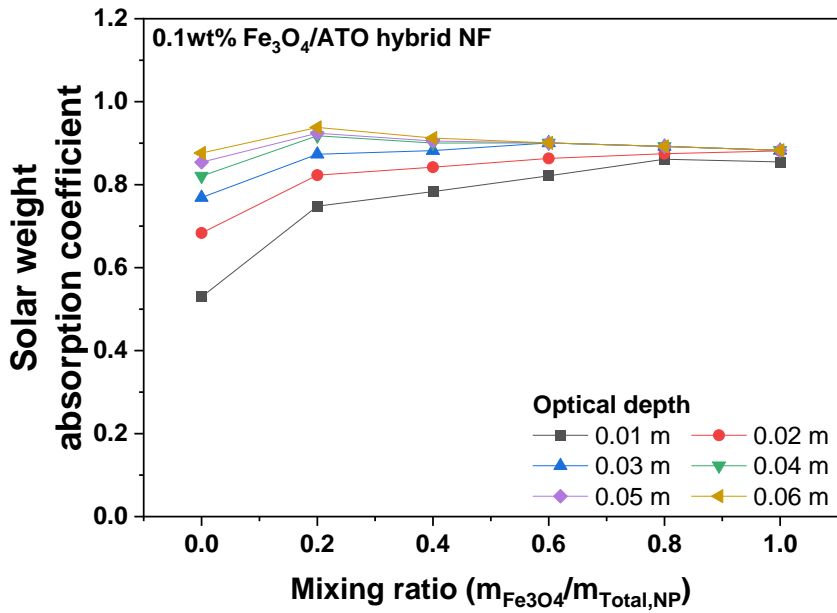


Fig. 3.12 Solar weight absorption coefficient of Fe₃O₄/ATO hybrid NF according to $m_{\text{Fe3O4}}/m_{\text{Total,NP}}$

3.3.3. Receiving efficiency and thermal characteristics of MWCNT, Fe₃O₄, and ATO nanofluid during the solar receiving process

Fig. 3.13 shows the average increased temperature according to the light exposure time of MWCNT, Fe₃O₄, and ATO NFs. As the light exposure time increased up to 9000 s, the difference between the amount of energy absorbed by the NF and the heat loss became almost the same, leading to a gradual average increased temperature. Each NF had a higher average temperature increase than water; the average temperature increase was improved with an increase in the NF concentration. The average increased temperature of the water was the highest at 8.2°C, at 9000 s. The average increased temperature of the NF was improved the most in MWCNT, followed by Fe₃O₄ and ATO. The average increased temperature of the MWCNT NF (0.0005-0.004wt%) showed the most remarkable improvement in average increased temperature, which was measured to be 11.4–12.5°C, 1.39–1.52 times higher than water. The average increased temperature decreased when the NF concentration exceeded 0.002wt%. As the Fe₃O₄ NF concentration increased from 0.025wt% to 0.075wt%, the average temperature at 9000 s increased to 11.4–11.9°C. As the NF concentration increased from 0.075wt% to 0.1wt%, the average temperature slightly decreased to 11.9–11.8°C. As the optical absorption of ATO NF was lower than that of MWCNT and Fe₃O₄ NFs, the average increasing temperature of ATO NF was lower than that of MWCNT and Fe₃O₄ NFs. The ATO NF increased from 8.7°C to 11.5°C at 9000 s as the NF concentration increased from 0.05wt% to 0.25wt%.

Fig. 3.14 shows the time-dependent collection efficiency of MWCNT, Fe₃O₄, and ATO NFs. The collection efficiency of each NF reached its maximum collection efficiency at 300–600 s, after which the collection efficiency decreased. The maximum collection efficiency of MWCNT NF is 0.878 at 0.001 wt% at 300 s. As the MWCNT NF concentration increased to 0.004 wt%, the time to reach the maximum collection efficiency of the corresponding concentration increased while the maximum collection efficiency decreased. The time at which the MWCNT NF concentration reached the maximum collection efficiency of 0.733 at 0.004wt% was 600 s.

Fe_3O_4 and ATO NFs also showed an increased time to reach the maximum collection efficiency as the NF concentration increased. The concentrations that reach the maximum collection efficiency of Fe_3O_4 and ATO NFs were 0.075wt% and 0.1wt%, respectively, and the maximum collection efficiencies of Fe_3O_4 and ATO were 0.782 and 0.75, respectively. The maximum collection efficiency of the NF was the highest in MWCNT NF (0.002wt%, 0.821), followed by Fe_3O_4 NF (0.075wt%, 0.782) and ATO NF (0.25wt%, 0.75). As described above, the increase in the time to reach the maximum collection efficiency as the NF concentration increased was related to the optical absorption according to the increase in the NF concentration.

Fig. 3.15 shows the temperature difference between the top and bottom temperature sensors according to the light exposure time. When the NF was exposed to light, the NF started to be heated from the top, and the light passing through the NF heated the bottom. However, with excellent optical absorption of the NF, the light was absorbed only at the top part, making it difficult for the NF in the container to induce internal convection due to the temperature difference. When NFs were continuously exposed to light, a stratified flow was formed. The time it took for MWCNT, Fe_3O_4 , and ATO NFs to form a stratified flow was about 3300 s. After 3300 s, thermal energy is diffused from top to bottom by internal convection and conduction, and the temperature difference between the top and bottom is reduced. At 9000 s, as the NF concentration increased from 0.0005wt% to 0.002wt%, the temperature difference between the top and bottom sensors of MWCNT NFs increased from 5°C to 7.4°C. The temperature difference between the top and bottom of the 0.002wt% MWCNT and 0.004wt% MWCNT NFs was the same. As shown in Fig. 3.7, when the concentration of the MWCNT NF was 0.002wt% or more significant, the optical absorption was hardly improved. Improving optical absorption by increasing the concentration of the NF increases the temperature difference between the top and the bottom. This can be confirmed through the temperature difference between the top and bottom of the Fe_3O_4 NF.

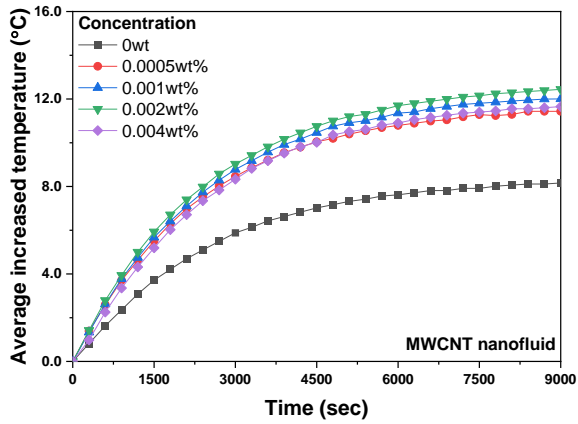
As shown in Fig. 3.5, as the Fe_3O_4 NF increased from 0.025wt% to 0.1wt%, the light transmittance gradually decreased, and the temperature difference between the top and bottom parts increased from 5.5°C to 6.7°C. The reduced light transmittance and increased optical

absorption by increasing the concentration of the NF absorb most of the light energy in the top part of the NF, causing stratification. Compared to the MWCNT and Fe₃O₄ NFs, the ATO NF was formed with a lower temperature difference between the top and bottom. As the concentration of ATO NF increased from 0.025wt% to 0.2wt%, the top and bottom temperature difference increased from 4°C to 6.6°C. As shown in Fig. 3.14, the collection efficiencies of 0.1wt% ATO NF and 0.25wt% ATO NF were not significantly different. However, their collection efficiencies were almost equal to each other. While the optical absorption of ATO NF was lower than that of MWCNT and Fe₃O₄ NFs, the improvement in optical absorption according to the optical depth was excellent.

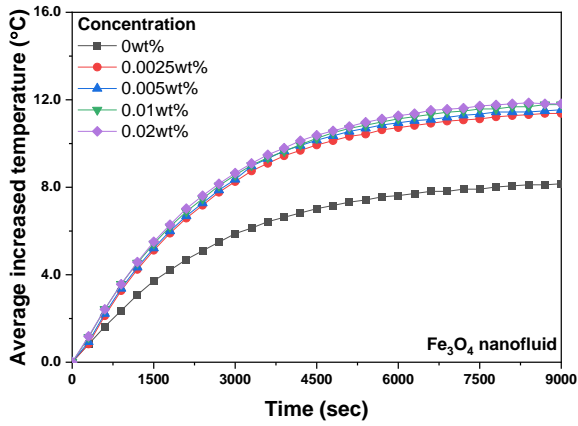
Fig. 3.16 shows the increasing temperature for each position of the NF at 9000 s. As the MWCNT NF concentration increased from 0wt% to 0.002wt%, the temperature at the top increased from 10.3°C to 16.8°C. After that, as the MWCNT NF increased from 0.002wt% to 0.004wt%, the temperature decreased slightly from 16.8°C to 16°C. On the other hand, the increased temperatures in the lower and middle parts decreased after reaching the maximum values ($T_{\text{btm}}=9.6^\circ\text{C}$ and $T_{\text{mid}}=12.5^\circ\text{C}$) at 0.001wt%. A decrease in the increased temperature at the top of MWCNT NF was associated with reflectance. As shown in Fig. 3.8, the reflectance of MWCNT NF rapidly increased when the concentration exceeded 0.002wt%, reducing the amount of energy MWCNT could acquire.

The temperature in the bottom and middle parts was related to optical absorption. As shown in Fig. 3.7, for the optical absorption of the MWCNT NF, the concentration of the MWCNT NF increased, and the light energy was absorbed in the top. Because it was not transmitted to the lower and middle parts, it depended on heat diffusion from top to bottom. In the Fe₃O₄ NF, the temperatures at the top and middle parts were almost constant despite the increase in the Fe₃O₄ NF concentration compared to the MWCNT NF. As shown in Fig. 3.7 and Fig. 3.8, Fe₃O₄ NF had excellent optical absorption of long-wavelength visible light and near-infrared light, whereas the optical absorption in the visible light band with short wavelengths and ultraviolet light was poor, even causing light reflection. Therefore, ultraviolet light and short-wavelength visible light

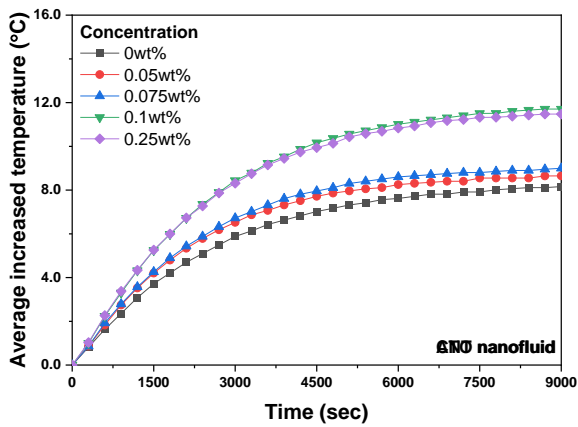
bands were not absorbed, and long-wavelength visible light and near-infrared light were absorbed in the top part. Unlike MWCNT NF, Fe_3O_4 and ATO NFs had low optical absorption, leading to an overall temperature increase as the NF concentration increased. On the other hand, the increased temperatures in the lower and middle parts of ATO NF decreased after reaching the maximum values ($T_{\text{btm}}=9.5^\circ\text{C}$ and $T_{\text{mid}}=11.4^\circ\text{C}$) at 0.1wt%, while the temperature at the top position increased steadily up to 15.4°C as the ATO NF concentration increased up to 0.2wt%. Improving the optical absorption in the visible light band based on the ATO NF would be possible to improve the collection efficiency while minimizing stratification.



(a) MWCNT NF

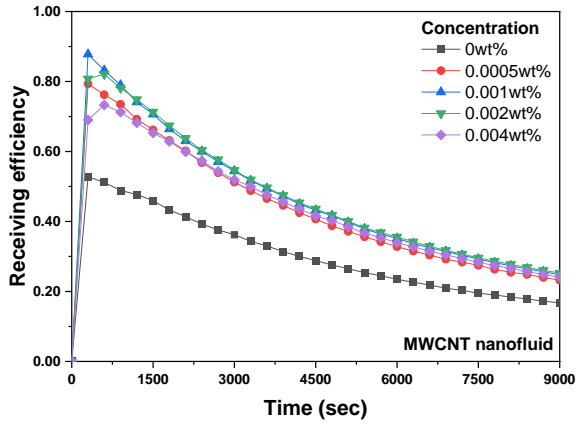


(b) Fe₃O₄ NF

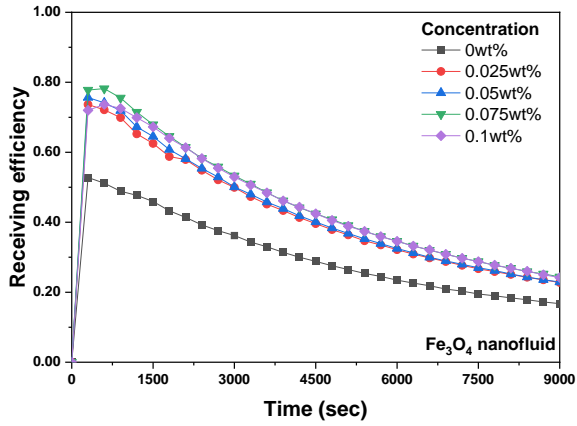


(c) ATO NF

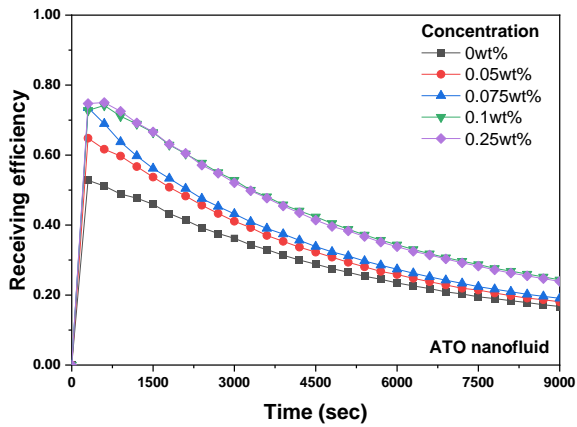
Fig. 3.13 Average increased temperature of NF according to exposed time under irradiance



(a) MWCNT NF

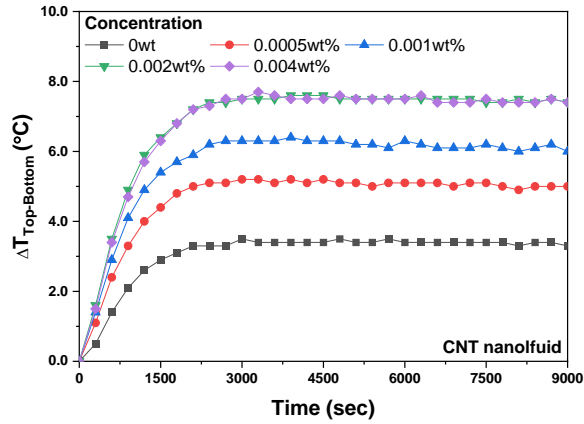


(b) Fe₃O₄ NF

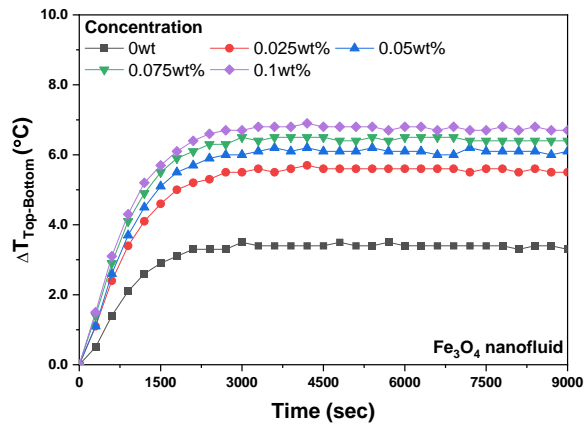


(c) ATO NF

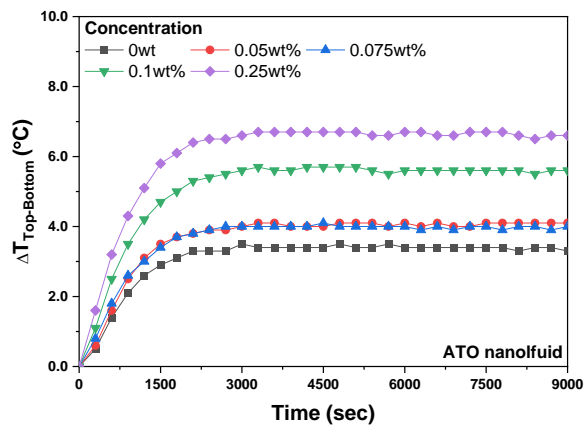
Fig. 3.14 Receiving efficiency of NF according to exposed time under irradiance



(a) MWCNT NF

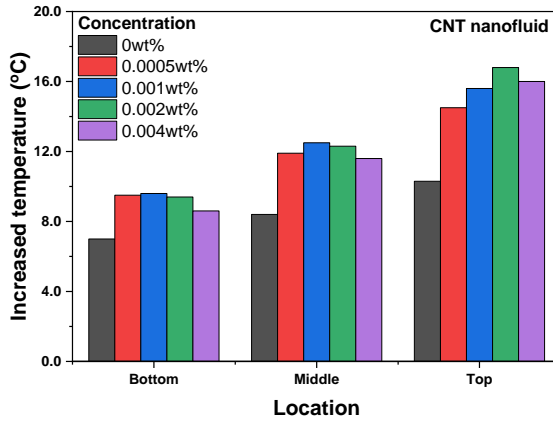


(b) Fe₃O₄ NF

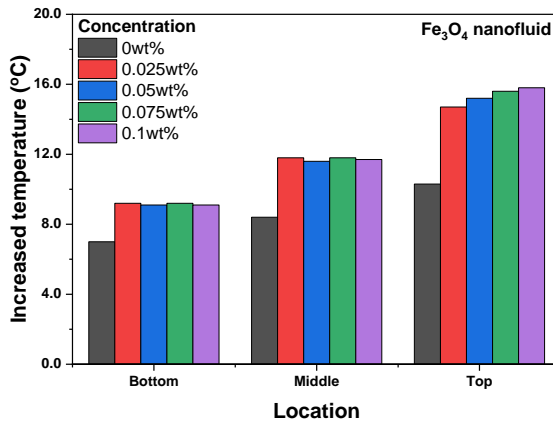


(c) ATO NF

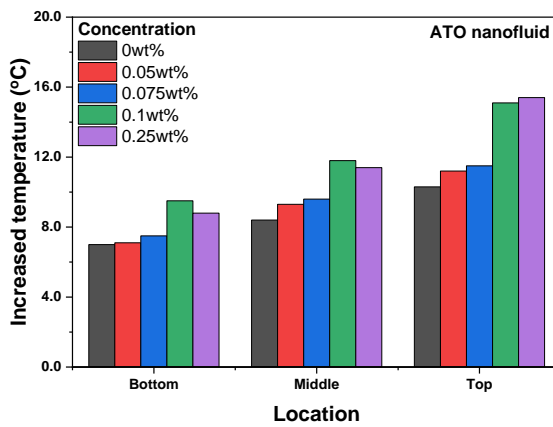
Fig. 3.15 Temperature difference between top and bottom temperature sensor according to time exposed time under irradiance



(a) MWCNT NF



(b) Fe₃O₄ NF



(c) ATO NF

Fig. 3.16 Increased temperature of NFs with the various location at 9000s, (a) MWCNT NF, (b) Fe₃O₄ NF, (c) ATO NF

3.3.4. Receiving efficiency and thermal characteristics of Fe₃O₄/ATO hybrid nanofluid during the solar receiving process

To investigate the light energy collection performance of Fe₃O₄/ATO hybrid NF and the thermal characteristics of the collection process, the temperature, collection efficiency, and temperature of each location increased with the time of the Fe₃O₄/ATO hybrid NF were compared according to $m_{\text{Fe}_3\text{O}_4}/m_{\text{Total,NP}}$ when the total concentration was 0.1wt%. Fig. 3.17 shows the increased temperature according to the light exposure time of the Fe₃O₄/ATO hybrid NF. As for the increased temperature of the Fe₃O₄/ATO hybrid NF, the highest temperature increase was observed at $m_{\text{Fe}_3\text{O}_4}/m_{\text{Total,NP}}=0.2$. At 9000 s, the increased temperature of the Fe₃O₄/ATO hybrid NF at $m_{\text{Fe}_3\text{O}_4}/m_{\text{Total,NP}}=0.2$ was 12.2°C. On the other hand, the increased temperature was lower than that of 0.1wt% Fe₃O₄ NF at $m_{\text{Fe}_3\text{O}_4}/m_{\text{Total,NP}}=0.6$ and 0.8. At 9000 s, the increased temperature of the 0.1wt% Fe₃O₄ NF was 11.8°C, and at $m_{\text{Fe}_3\text{O}_4}/m_{\text{Total,NP}}=0.6$ and 0.8 of the Fe₃O₄/ATO hybrid NF, the increased temperature was 11.75 °C and 11.84 °C, respectively.

Fig. 3.18 shows the collection efficiency according to the light exposure time of the Fe₃O₄/ATO hybrid NF. Similar to the time to reach the maximum collection efficiency of the MWCNT, Fe₃O₄, and ATO NFs in Fig. 3.15, the Fe₃O₄/ATO hybrid NF showed that the collection efficiency reached its maximum at 600 s of light exposure time and decreased after that. The Fe₃O₄/ATO hybrid NF showed the best collection efficiency at $m_{\text{Fe}_3\text{O}_4}/m_{\text{Total,NP}}=0.2$. The maximum efficiency of receiving efficiency of the Fe₃O₄/ATO hybrid NF was 0.768, 0.763, 0.767, and 0.763 at $m_{\text{Fe}_3\text{O}_4}/m_{\text{Total,NP}}=0.2, 0.4, 0.6,$ and 0.8, respectively, which was higher than 0.737 and 0.742 of 0.1wt% Fe₃O₄ and ATO. At the light exposure time of 9000 s, the collection efficiency was 0.253, 0.248, 0.244, and 0.244 when $m_{\text{Fe}_3\text{O}_4}/m_{\text{Total,NP}}=0.2, 0.4, 0.6,$ and 0.8, respectively. Compared to the Fe₃O₄ NF, ATO NF had a weak effect on improving optical absorption according to the concentration change. However, compared to Fe₃O₄ NF, ATO NF has lower light reflectance in the region with shorter ultraviolet and visible light wavelengths. Adding

a small amount of Fe₃O₄ NF, which has excellent optical absorption in the visible light band, enabled the absorption of energy in the band where 0.1 wt% of Fe₃O₄ NF and 0.1 wt% of ATO NF could not be absorbed, thereby improving the collection efficiency. The temperature distribution of the NF can explain this.

Fig. 3.19 shows the increased temperature by location of Fe₃O₄/ATO hybrid NF according to $m_{\text{Fe}_3\text{O}_4}/m_{\text{Total,NP}}$. The temperatures in the top and middle parts of Fe₃O₄/ATO hybrid NF increased compared to those of Fe₃O₄ and ATO NFs. The increased temperature in the top part of Fe₃O₄/ATO hybrid NF was 16.5°C, 16.4°C, 16.1°C, and 16.3°C when $m_{\text{Fe}_3\text{O}_4}/m_{\text{Total,NP}}=0.2, 0.4, 0.6,$ and $0.8,$ respectively, and the increased temperature in the top part of 0.1 wt% Fe₃O₄ was higher than 15.8°C. However, it was lower than the increased temperature of 16.8°C at the top of 0.002 wt% MWCNT NF. The temperature in the middle part of the Fe₃O₄/ATO hybrid NF was also higher than that of the Fe₃O₄ NF, and the highest temperature was observed in the middle part at $m_{\text{Fe}_3\text{O}_4}/m_{\text{Total,NP}}=0.2$. The middle temperature of the Fe₃O₄/ATO hybrid NF with $m_{\text{Fe}_3\text{O}_4}/m_{\text{Total,NP}}=0.2$ was 13.4°C, which was higher than 11.7°C and 12.3°C, the temperature in the middle part of 0.1 wt% Fe₃O₄ NF and 0.002 wt% MWCNT NF, respectively. On the other hand, the temperature in the bottom part of the Fe₃O₄/ATO hybrid NF was lower than that of 0.1 wt% Fe₃O₄ NF and 0.1 wt% ATO. The bottom part of Fe₃O₄/ATO hybrid NF temperature was 9.1, 8.9, 8.6, and 8.6 when $m_{\text{Fe}_3\text{O}_4}/m_{\text{Total,NP}} = 0.2, 0.4, 0.6,$ and $0.8,$ respectively. At $m_{\text{Fe}_3\text{O}_4}/m_{\text{Total,NP}}=0.2,$ it was the same as the temperature in the bottom part of 0.1 wt% Fe₃O₄ NF at 9.4, but it was slightly lower than that of 0.1 wt% ATO.

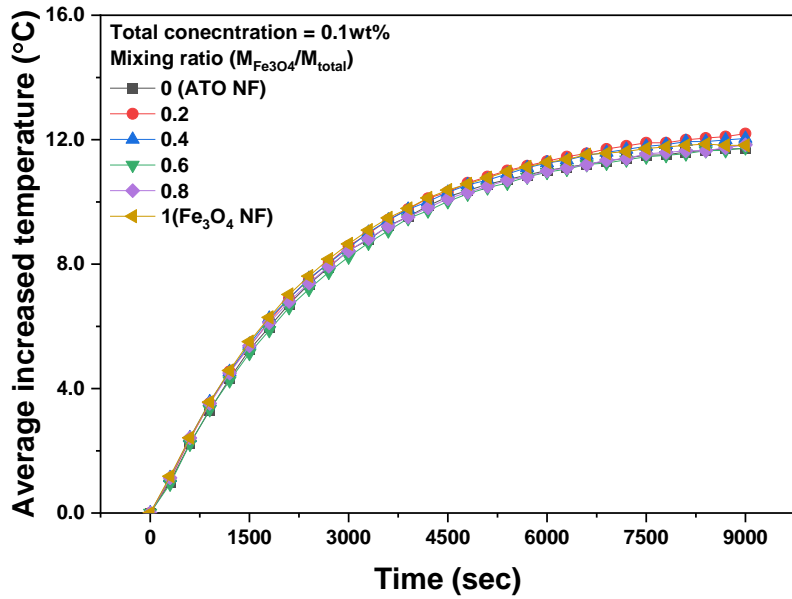


Fig. 3.17 Average increased temperature of Fe_3O_4 /ATO hybrid NF according to mixing ratio at total concentration = 0.1wt%

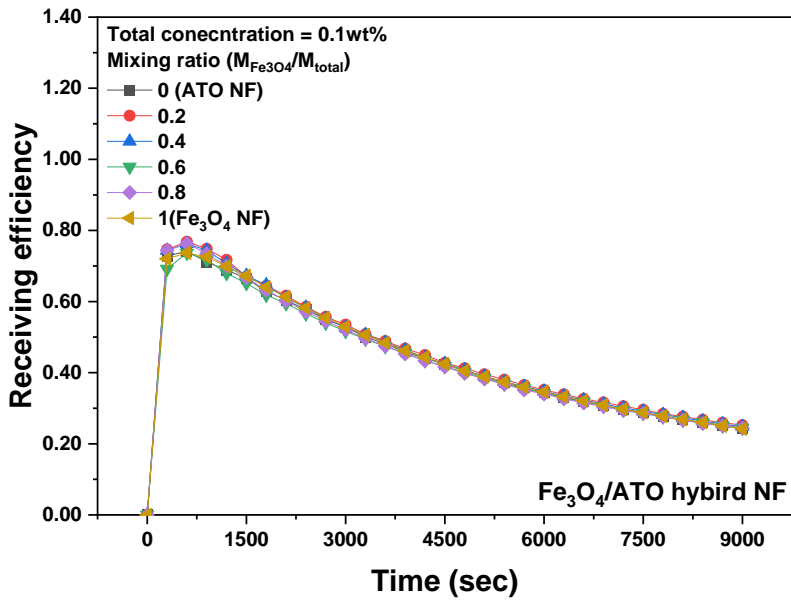


Fig. 3.18 Receiving efficiency of Fe_3O_4 /ATO hybrid NF

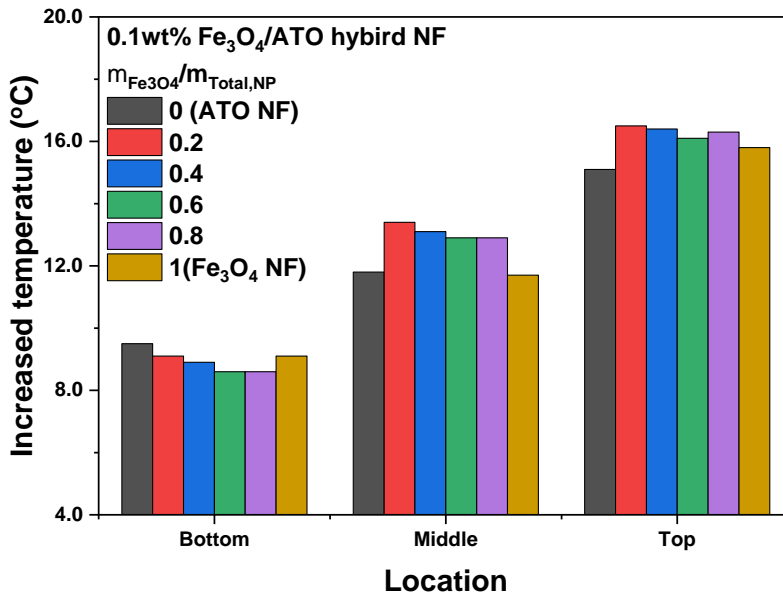


Fig. 3.19 Increased temperature of Fe₃O₄/ATO hybrid NF

3.3.5. Photo thermal conversion efficiency of MWCNT, Fe₃O₄, ATO, Fe₃O₄/ATO hybrid NF

Photo thermal conversion efficiency is a quantitative indicator of how much light energy is converted into thermal energy by the NF contained in the collector. Fig. 3.20 shows the photo thermal conversion efficiency of MWCNT, Fe₃O₄, and ATO NFs. The MWCNT NF exhibited improved optical absorption at low concentrations compared to Fe₃O₄ and ATO NFs due to its excellent optical absorption ability. The critical photo thermal conversion efficiency of MWCNT NF was 0.933 at 0.002wt%, and the photo thermal conversion efficiency decreased when the concentration of MWCNT NF was 0.004wt%. As shown in Fig. 3.8, when the concentration of the MWCNT NF exceeded 0.002wt%, the reflectance increased in the ultraviolet and near-infrared bands, thereby reducing the amount of light energy absorbed by the MWCNT NF. The critical photo thermal conversion efficiency of Fe₃O₄ NF is 0.9 at a Fe₃O₄ NF concentration of 0.075wt%. The photo thermal conversion efficiency of 0.1wt% Fe₃O₄ NF was 0.892, slightly decreased compared to that of 0.075wt% Fe₃O₄ NF. Although ATO NF had lower optical absorption than MWCNT and Fe₃O₄ NF, the photo thermal conversion efficiency was 0.898 at 0.1wt%, almost equal to that of 0.075wt% Fe₃O₄. Although the optical absorption capacity of ATO NF was lower than that of Fe₃O₄ NF, as shown in Fig. 3.7, high photo thermal conversion efficiency could be obtained when there was sufficient optical depth.

Fig. 3.21 shows the photo thermal conversion efficiency of 0.1wt% Fe₃O₄/ATO hybrid NF according to $m_{\text{Fe}_3\text{O}_4}/m_{\text{Total,NP}}$. Fe₃O₄/ATO hybrid NF of 0.1wt% had the maximum photo thermal conversion efficiency at $m_{\text{Fe}_3\text{O}_4}/m_{\text{Total,NP}} = 0.2$. When exceeding $m_{\text{Fe}_3\text{O}_4}/m_{\text{Total,NP}} = 0.2$, the photo thermal conversion efficiency decreased. At $m_{\text{Fe}_3\text{O}_4}/m_{\text{Total,NP}} = 0.2$, the photo thermal conversion efficiency was 0.932. With a photo thermal conversion efficiency equivalent to that of 0.002wt% MWCNT NF, it was demonstrated that optical absorption performance similar to that of MWCNT NF with excellent optical absorption could be secured by mixing NFs with different optical absorption properties.

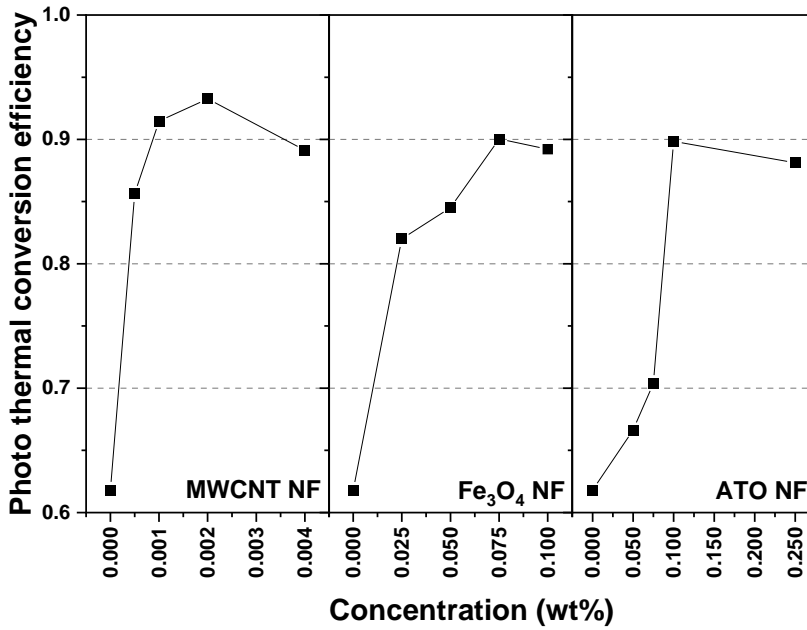


Fig. 3.20 Photo thermal conversion efficiency MWCNT, Fe₃O₄ and ATO NFs

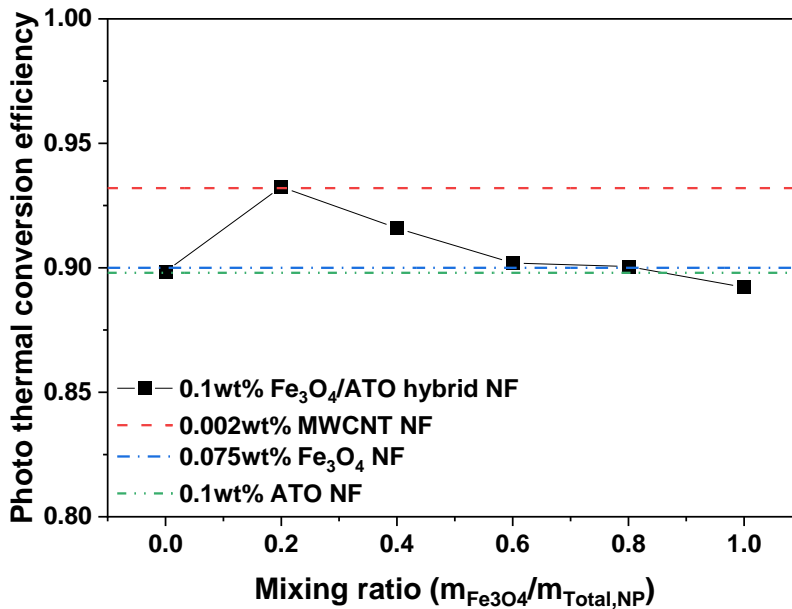


Fig. 3.21 Photo thermal conversion efficiency of Fe₃O₄/ATO hybrid NF

3.3.6. Economy analysis on photo thermal conversion of MWCNT, Fe₃O₄, ATO, Fe₃O₄/ATO hybrid NF

A specific absorption rate (SAR) is an indicator of the optical absorption capacity of NPs. Because the amount of optical absorption in the NF is different according to the time exposed to solar energy, the NF with the constant concentration has different SAR. When the receiving efficiency is high, the SAR is the maximum, and the SAR is decreased as the time exposing the solar energy increases. Therefore, the SAR is the minimum when the photo thermal conversion experiment is finished.

Fig. 3.22 shows the range of SAR of the MWCNF NF, Fe₃O₄ NF, and ATO NF according to the concentration of the NF. The SAR in the MWCNF NF, Fe₃O₄ NF, and ATO NF was decreased according to the increase of the NF. The SAR was higher in the order of the MWCNT > Fe₃O₄ NF > ATO NF. In the MWCNT NF, the maximum SAR was decreased from 1.268 kW/g to 0.129 kW/g, and the minimum SAR was decreased from 0.308 kW/g to 0.059 kW/g when the concentration of MWCNT was increased from 0.0005wt% to 0.004wt%. The SAR of the Fe₃O₄ NF and the ATO NF was about 10–100 times lower than that of the MWCNT NF. It is because a higher concentration was required in the Fe₃O₄ and ATO NF compared to MWCNT NF. When the concentration of the Fe₃O₄ was increased from 0.025wt% to 0.1wt%, the maximum SAR was decreased from 0.0025 kW/g to 0.0046 kW/g, and the minimum SAR was decreased from 0.0058 kW/g to 0.0018 kW/g. The ATO NF has the lowest range of the SAR. However, the SAR did not increase simply as the concentration of the ATO NF was increased. When the concentration of the ATO was increased from 0.005wt% to 0.0075wt%, the maximum SAR was increased from 0.0057 kW/g to 0.0066 kW/g as the concentration of the ATO was increased from 0.05wt% to 0.075wt%. The maximum SAR of the SAT NF was decreased when the concentration was above 0.075wt%. The minimum SAR was increased from 0.0006 kW/g to 0.0018 kW/g as the concentration of the ATO was increased from 0.05wt% to 0.1wt% and then decreased when the

concentration was above 0.1wt%. It is because the photo thermal conversion efficiency was rapidly increased in the concentration range of the ATO NF from 0.05wt% to 0.1wt%.

Fig. 3.23 shows the SAR of 0.1wt% Fe₃O₄/ATO hybrid NF according to the $m_{\text{Fe}_3\text{O}_4}/m_{\text{Total,NP}}$. When the $m_{\text{Fe}_3\text{O}_4}/m_{\text{Total,NP}}$ was 0.2 in 0.1wt% Fe₃O₄/ATO hybrid NF, the SAR was higher than others of $m_{\text{Fe}_3\text{O}_4}/m_{\text{Total,NP}}$. Maximum and minimum SAR was 0.0062 and 0.002, respectively, when the $m_{\text{Fe}_3\text{O}_4}/m_{\text{Total,NP}}$ was 0.2 in 0.1wt% Fe₃O₄/ATO hybrid NF. It was due to adding the Fe₃O₄ NF with good optical absorption in the visible band of solar energy.

Fig. 3.24 shows the manufacturing cost of the NF for the production of thermal energy. The cost of the NF for thermal energy production was calculated based on 0.002wt% MWCNT NF, 0.0075wt% Fe₃O₄ NF, 0.1wt% ATO NF, and 0.1wt% Fe₃O₄/ATO hybrid NF with high receiving efficiency and photo thermal conversion efficiency. The cost of the NF for thermal energy production was high and it was in the order of 0.0075wt% Fe₃O₄ NF > 0.1wt% Fe₃O₄ /ATO NF ($m_{\text{Fe}_3\text{O}_4}/m_{\text{Total,NP}} = 0.2$) > 0.1wt% ATO NF > 0.002wt% MWCNT NF. It takes 274,060 won to produce 1 kW when using 0.0075wt% Fe₃O₄ NF. However, in the case of the MWCNT NF, it takes 52,758 Won to produce 1 kW thermal energy. Using 0.002wt% MWCNT NF is about 5.2 times lower than 0.0075wt% Fe₃O₄ NF. To produce 1 kW, using 0.1wt% Fe₃O₄ /ATO hybrid NF ($m_{\text{Fe}_3\text{O}_4}/m_{\text{Total,NP}} = 0.2$) can reduce 2.15 times low cost rather than 0.075wt% Fe₃O₄ NF, but this cost is higher than using 0.1wt% ATO NF. The manufacturing cost for 1 kW when using 0.1wt% Fe₃O₄ /ATO hybrid NF ($m_{\text{Fe}_3\text{O}_4}/m_{\text{Total,NP}} = 0.2$) was 1.78 times higher than using 0.1wt% ATO NF. From this, it can be inferred that it is economical to use MWCNT NF. However, using the Fe₃O₄ /ATO hybrid NF ($m_{\text{Fe}_3\text{O}_4}/m_{\text{Total,NP}} = 0.2$) can be an alternative because this cost is lower than 0.0075wt% Fe₃O₄ NF, and the photo thermal conversion efficiency of the Fe₃O₄ /ATO hybrid NF ($m_{\text{Fe}_3\text{O}_4}/m_{\text{Total,NP}} = 0.2$) is higher than 0.0075wt% Fe₃O₄ NF.

/

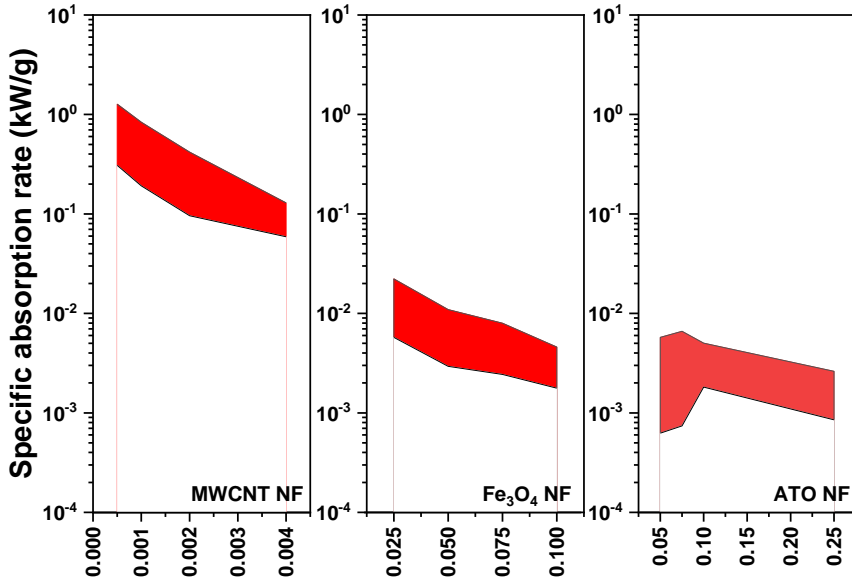


Fig. 3.22 Specific absorption rate of MWCNT, Fe₃O₄, and ATO NF

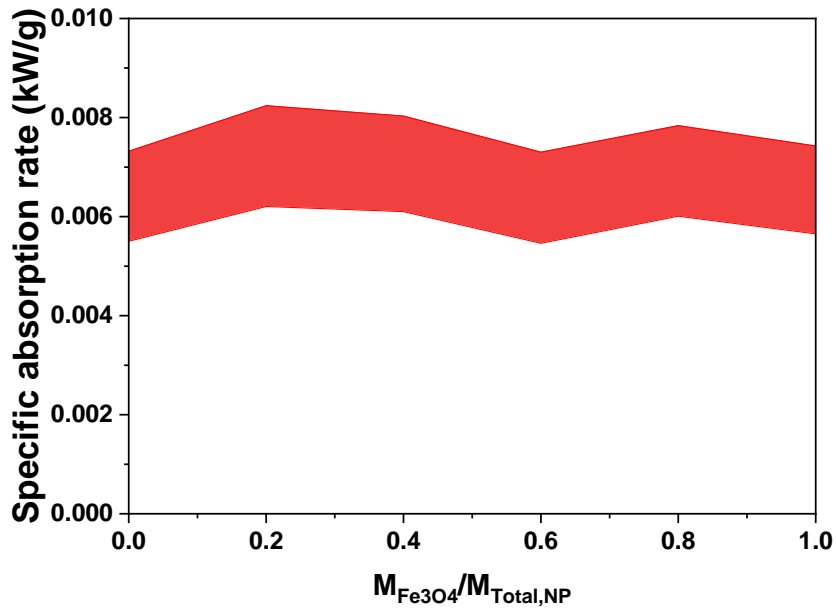


Fig. 3.23 Specific absorption rate of Fe₃O₄/ATO hybrid NF according to $m_{Fe_3O_4}/m_{Total,NP}$

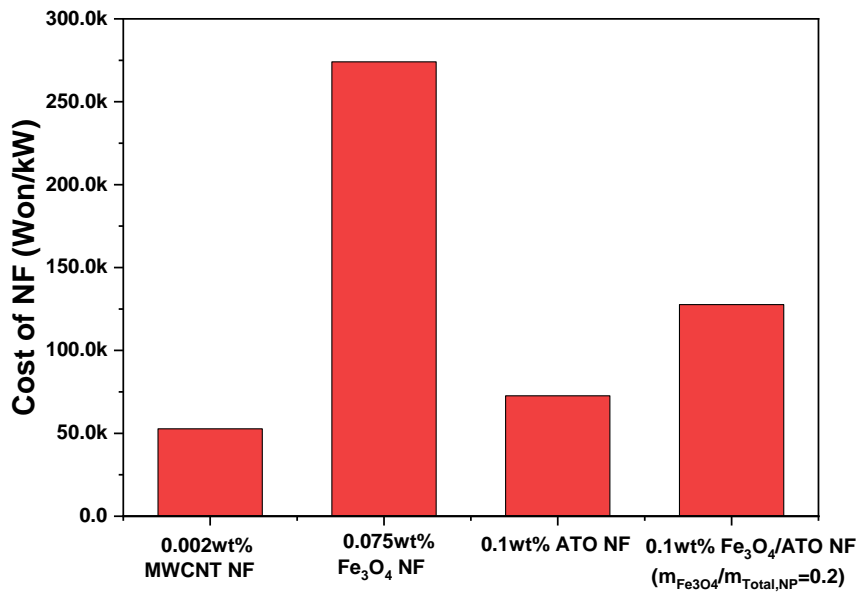


Fig. 3.24 Manufacturing cost of NF for generated thermal energy

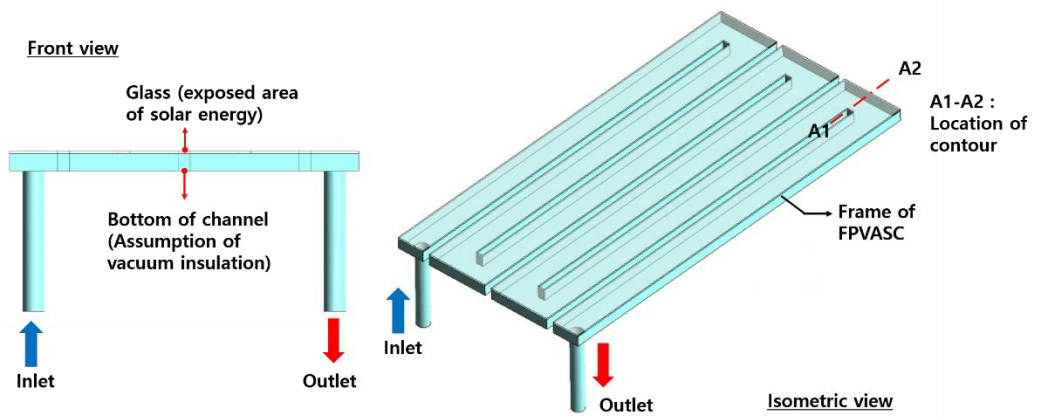
4. Numerical modeling method on the performance of flat plate volumetric absorption solar collector

4.1. A numerical model for flat plate volumetric absorption solar collector

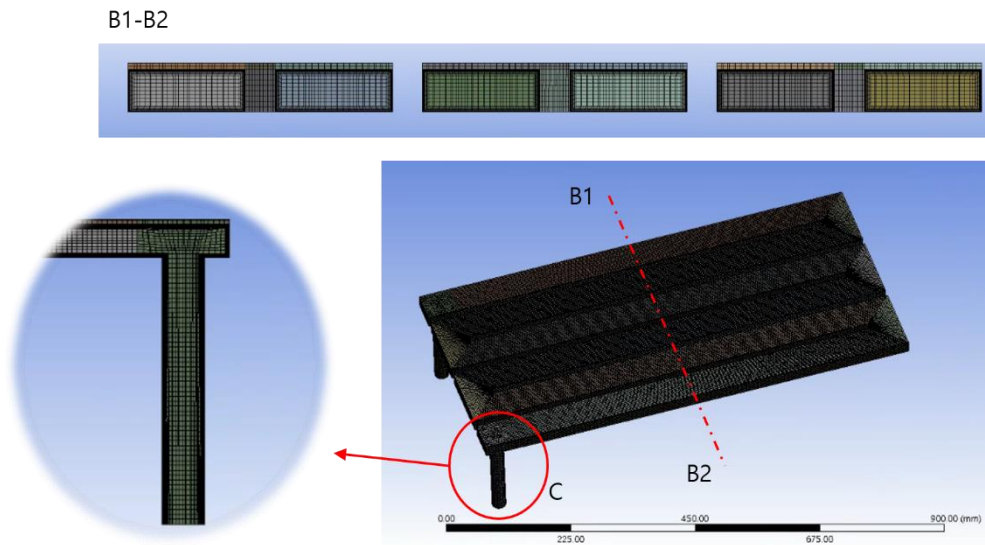
To evaluate the performance of a flat plate solar collector using the VASC method, numerical analysis modeling was performed to confirm the performance improvement of the solar collector by increasing the concentration of the NF. Fig. 4.1 shows the geometry and mesh design of a flat plate volumetric absorption solar collector (FPVASC). The frame of FPVASC is made of aluminum. Table 4.1 shows the specifications of FPVASC. The frame of FPVASC consists of a series of channels through which Fe_3O_4 NF, the working fluid, flows. The width, length, and height of the channels are 55 mm, 800 mm, and 10 mm. On the top of the FPVASC, a glass of 3 mm in thickness is installed. In addition, there is a vacuum insulation space under the channel to suppress the heat loss of the FPVASC. Because the temperature difference between the inlet and outlet of the FPVASC is slight, it is difficult to recognize the effect of the temperature distribution in the height direction according to the concentration change of the NF. Therefore, the temperature distribution of the FPVASC according to the concentration change of the NF was investigated through the temperature control image at A1-A2.

The analysis of the FPVASC is performed using only glass and channel shapes. The mesh design of the FPVASC is designed by the Ansys meshing tool. Meshes at the inlet and outlet region are designed by the multizone meshing method, and the fluid domain of the channel and the solid domain of the glass are designed by the sweep meshing method. Because the width and length of the FPVASC are long, but the height is short, a large number of unnecessary mesh numbers are required by designing lots of mesh numbers in the height direction. In addition, meshes near the channel wall were densely designed by using the inflection method to investigate the flow characteristics of the wall. For analysis, 1312271 nodes and 1228695 elements are used.

An analysis of FPVASC was performed using Fluent 2021 R2, a commercial computational fluid analysis program. The spectral intensity of solar radiation on the top of FPVASC, the source term of radiation energy, was modeled based on the Plank's blackbody distribution. To analyze the thermal and flow characteristics in the FPVASC, the numerical model was designed by combining the continuity equation, and Navier-Stokes equation, the energy equation, and the radiative transfer equation (RTE). For modeling spectral intensity of solar radiation inputted to FPVASC, the solar irradiance model is designed based on Plank black body distribution. To simulate FPVASC numerical model, it is assumed that the working fluid is an incompressible Newtonian fluid and the flow is a steady-state laminar. To simulate the numerical model, the semi-implicit method for pressure-linked equation-consistent (SIMPLE-C) as a pressure-based coupled algorithm was used, and the continuity and energy equation is discretized in 2nd order. To calculate the RTE equation, the Monte Carlo model is used. The Monte Carlo model is a method of statistically calculating effective radiative heat transfer in analysis domains. It has the disadvantages of considerable calculation time and memory requirements but has the advantage of increasing the accuracy of calculation results as the number of samples increases. The residuals of continuity, momentum, and energy equations were 10^{-6} . Table 4.2 shows the analysis conditions for the performance evaluation of FPVASC. The performance of the FPVASC was analyzed in an environment with a radiation intensity of 1000 W/m^2 and an ambient temperature of 30°C . The performance of FPVASC according to changes in Fe_3O_4 NF concentration, inlet temperature, and the mass flow rate was reviewed analytically.



(a) Geometry of FPVASC



(b) Mesh image of FPVASC

Fig. 4.1 Geometry and mesh design of FPVASC using Fe_3O_4 NF for numerical analysis; (a) geometry of FPVASC, (b) Mesh image of FPVASC

Table 4.1 FPVASC design specification

Specification	Value
NF	Fe ₃ O ₄ NF
Glass height	3 mm
Solar collector material	Aluminum
Solar collector width	400 nm
Solar collector length	800 nm
Channel width	55 mm
Channel height	10 mm

Table 4.2 Simulation conditions

Simulation condition	Value
Irradiance intensity	1000 W/m ²
Mass flow rate	0.005, 0.01, 0.015, 0.02 kg/s
Weight concentration	0, 0.025, 0.05, 0.075, 0.1wt%
Inlet temperature	35–60°C
Air temperature	30°C

4.1.1. Boundary condition

Fig. 4.3 shows the Am 1.5 spectral radiation intensity, the Plank's blackbody radiation distribution, and the modeled radiation distribution. The modeled spectral radiation distribution is used as the source term of the RTE equation. As radiative heat loss and convective heat loss occur around the top of the FPVASC due to the radiation of the heat absorbed through the glass, heat loss due to convection and radiation was considered. On the other hand, only convective heat loss was considered heat loss due to slight heat radiation because light does not pass through the frame of FPVASC. Furthermore, the heat loss coefficient due to convection was defined as 10 W/m²·K. At the bottom of the FPVASC, vacuum insulation with a vacuum degree of 0.1 was assumed. The heat loss coefficient of the lower part of FPVASC was assumed to be 0.5 W/m²·K referring to the study by Mao et al. [88].

To simulate the spectral intensity of solar radiation on the top of FPVASC, the source term of radiation energy was modeled based on the Plank's blackbody distribution. Eq. (4.1) shows the Plank's blackbody distribution.

$$I(T_{sol}, \lambda) = \frac{2hc_0^2}{\lambda^5 \left[\exp\left(\frac{hc_0^2}{\lambda k_b T}\right) - 1 \right]} \quad (4.1)$$

Where, T_{sol} denotes the color temperature of solar radiation, which is 5500 K. Also, h denotes the Plank constant, c_0 denotes the speed of light, and k_b denotes the Boltzmann constant.

A non-gray model was used to consider the radiation intensity for each radiation band. To model a radiation distribution similar to Plank's blackbody distribution, from 300 nm to 1000 nm, at 100 nm intervals, the spectral radiation intensity of FPVASC was modeled by dividing it into wavelength bands at 200 nm intervals from 1000 nm to 2400 nm.

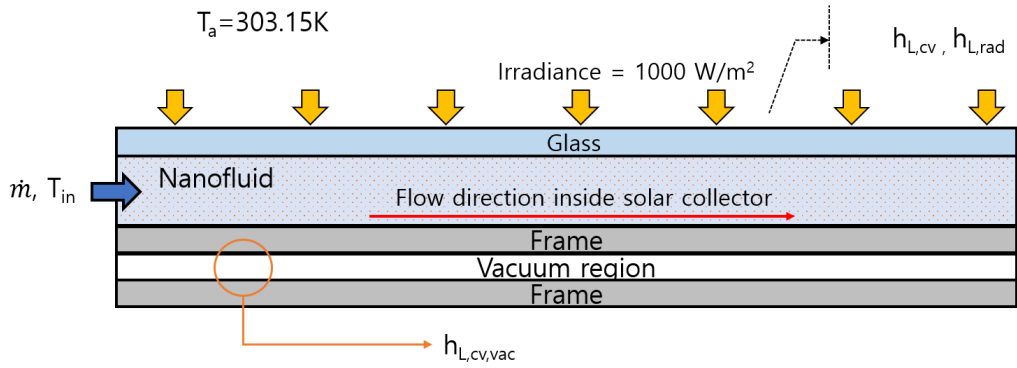


Fig. 4.2 Boundary condition schematic of FPVASC

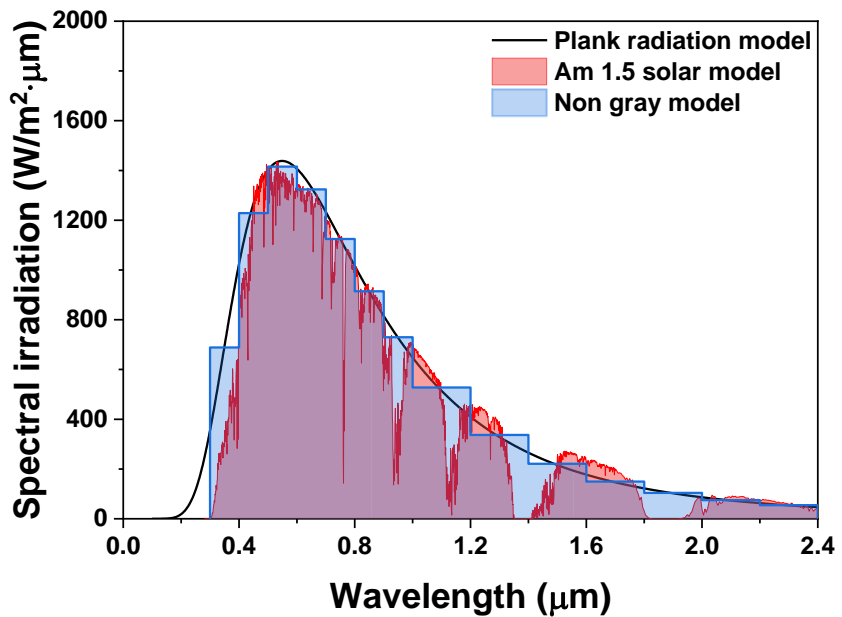


Fig. 4.3 Comparison of Am 1.5 spectral irradiation intensity, Plank's blackbody distribution, and designed spectral solar irradiance for FPVASC

4.1.2. Optical properties of nanofluid based on Rayleigh scattering

Information about the NF's mineral properties is required to calculate the RTE equation. The absorption and scattering coefficients of NFs were modeled based on the Rayleigh scattering estimation method. By the Rayleigh scattering estimation method, the extinction coefficient of the NF is defined as Eq. (4.2). For the Rayleigh scattering estimation method to be suitable, the particle size parameter (α) must satisfy the relationship of Eq. (4.3). The shortest wavelength in this study was 300 nm, and the NP size satisfying the Rayleigh scattering estimation method should be 95 nm or less at the maximum. The size of the NPs selected for this analysis study was assumed to be 50 nm, consistent with the Rayleigh scattering estimation method.

$$k_{e,nf}(\lambda) = k_{e,bf}(\lambda) + k_{e,np}(\lambda) \quad (4.2)$$

$$\alpha = \frac{\pi D_{np}}{\lambda} \ll 1 \quad (4.3)$$

Because the scattering coefficient of water, which was the base fluid of Fe₃O₄ NF, was very small, the scattering coefficient of water could be neglected, with the extinction coefficient of water being defined as Eq. (4.4).

$$k_{e,bf}(\lambda) = k_{a,bf}(\lambda) = \frac{4\pi\kappa_{bf}(\lambda)}{\lambda} \quad (4.4)$$

The extinction coefficient of NPs suspended in Fe₃O₄ NF was defined as Eq. (4.5).

$$k_{e,np}(\lambda) = \frac{3f_v Q_{e,np}(\lambda)}{2D_{np}} = \frac{3f_v (Q_{a,np}(\lambda) + Q_{s,np}(\lambda))}{2D_{np}} \quad (4.5)$$

In Eq. (4.5), $Q_{a,np}(\lambda)$ and $Q_{s,np}(\lambda)$ were expressed as Eq. (4.6) and Eq. (4.7), respectively.

$$Q_{a,np}(\lambda) = 4\alpha \operatorname{Im} \left[\left(\frac{m^2(\lambda) - 1}{m^2(\lambda) + 2} \right) \left[1 + \left(\frac{\alpha^2(\lambda)}{15} \right) \left(\frac{m^2(\lambda) - 1}{m^2(\lambda) + 2} \right) \left(\frac{m^4(\lambda) + 27m^2 + 38}{2m^2(\lambda) + 3} \right) \right] \right] \quad (4.6)$$

$$Q_{s,np}(\lambda) = \frac{8\alpha^4(\lambda)}{3} \left| \frac{m^2(\lambda) - 1}{m^2(\lambda) + 2} \right| \quad (4.7)$$

In Eq. (4.6) and Eq. (4.7), m is defined as a normalized refractive index as in Eq. (5.8).

$$m = \frac{(n + i\kappa)_p}{n_{bf}} \quad (4.8)$$

n and κ are integers and imaginary parts of the complex refractive index.

As expressed in Eq. (4.6) and Eq. (4.7), $Q_{s,np}$ was proportional to D^4 , and $Q_{a,np}$ was proportional to D , leading to the overestimation of the scattering coefficient for NPs in the Rayleigh scattering estimation method. Therefore, the effect of the scattering of NPs in the NF was neglected [89]. Fig. 4.4 shows the integer and imaginary parts of the composite refractive index of water and Fe_3O_4 NPs used to model the mineral properties of Fe_3O_4 NF.

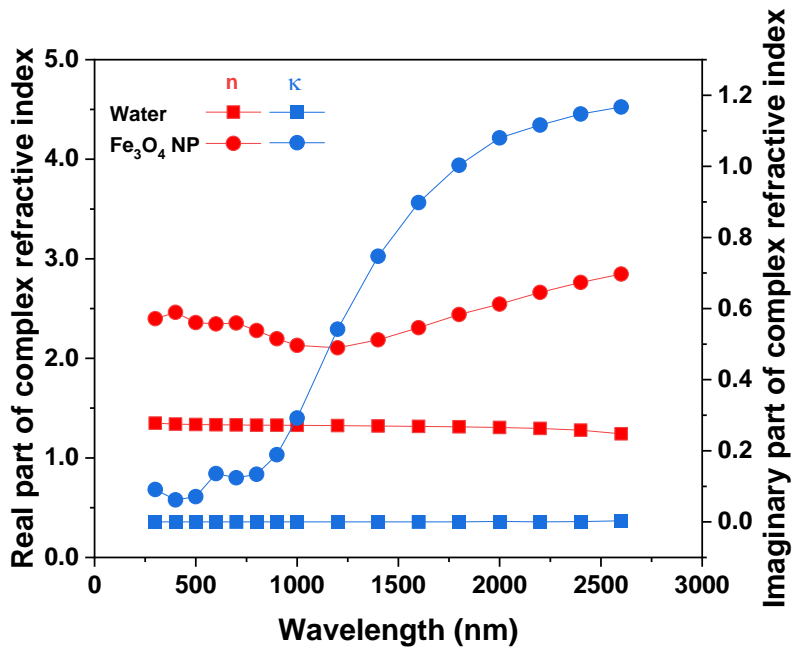


Fig. 4.4 Real and imaginary parts of complex refractive index

4.2. Thermal performance analysis method of solar collector

The performance analysis of the solar collector was used equally in the analytical and experimental studies. The efficiency of a solar collector is defined as the ratio of the solar energy introduced into the solar collector and the effective energy obtained by the solar collector. The first law of thermodynamics defines the effective energy obtained by the solar collector as Eq. (4.9).

$$Q_u = \dot{m} \cdot c_p \cdot (T_o - T_i) \quad (4.9)$$

Also, Eq. (4.9) can be expressed as Eq. (4.10) based on the difference between absorbed energy and lost energy.

$$Q_u = A_c F_R \left[I(\tau\alpha) - \frac{U_L}{S}(T_i - T_a) \right] \quad (4.10)$$

The thermal efficiency of a solar collector can be expressed by the Hottel–Whillier equation, which defines the thermal efficiency as the ratio of the effective heat gain from the solar collector, which can be expressed as Eq. (4.11).

$$\eta_{th} = \frac{\dot{m} \cdot c_p \cdot (T_o - T_i)}{IA_c} = \frac{A_c F_R \left[I(\tau\alpha) - \frac{U_L}{S}(T_i - T_a) \right]}{IA_c} = F_R (\tau\alpha) - F_R \frac{U_L}{S} \left(\frac{T_i - T_a}{I} \right) \quad (4.11)$$

Normalized temperature difference (NTD) is defined as Eq.(4.12) as a parameter that considers the inlet temperature of the solar collector, the outside air temperature, and the amount of insolation. When the efficiency of a solar collector is zero, the normalized temperature is defined as the operating limit normalized temperature difference (LNTD).

$$NTD = \frac{T_i - T_a}{I} \quad (4.12)$$

The thermal performance analysis method of this section was used in analysis of the simulation and experiment result.

4.3. Exergy analysis method

In this study, Reynolds (Re) range was about $100 < \text{Re} < 700$, demonstrating a laminar flow. Also, the concentration range of the NFs in this study has little effect on the viscosity increase. Because the differential pressure in the solar collector was insignificant, the influence of pressure drop on entropy generation and exergy analysis was excluded. The exergy input to the solar collector by solar radiation can be calculated by Eq. (4.13).

$$\psi_s = \left(1 - \frac{T_a}{T_{sun}}\right) \dot{Q}_{sol} \quad (4.13)$$

Q_{sol} denotes the solar energy flowing into the solar collector, and T_{sun} denotes the solar radiation temperature, defined as the color temperature of the light, 4300 K.

As for the exergy loss, the effective exergy output was expressed as Eq. (4.14).

$$\psi_d = T_a \dot{S}_{gen} \quad (4.14)$$

Where \dot{S}_{gen} denotes the entropy produced by the solar collector, which can be calculated by Eq. (4.15).

$$\dot{S}_{gen} = \dot{m} c_p \ln \frac{T_o}{T_i} - \frac{Q_{sol}}{T_{sun}} + \frac{Q_o}{T_a} \quad (4.15)$$

Where, \dot{Q}_o denotes the heat loss to the surrounding air, which can be expressed as Eq. (4.16).

$$Q_o = Q_{sol} - \dot{m} c_p (T_o - T_i) \quad (4.16)$$

Using these equations, the exergy in the solar collector was analyzed.

The exergy efficiency analysis method was used in analysis of the simulation and experiment result.

4.4. Simulation result and discussion

4.4.1. Numerical analysis of optical characteristics of Fe₃O₄ nanofluid

The optical properties of the Fe₃O₄ NF, the working fluid in FPVASC, are an essential factor in determining the performance of FPVASC. Fig. 4.5 shows the optical absorption for each light wavelength of Fe₃O₄ NF. The water exhibited an excellent optical absorption rate at wavelengths above 1400 nm, whereas the optical absorption rate in the visible and near-infrared bands decreased as the light wavelength became shorter. The utilization of Fe₃O₄ NF improved the insufficient optical absorption of water in the visible and near-infrared bands. Solar energy has a wide range of light wavelengths, and light is divided mainly into ultraviolet rays (380 nm) or less, visible rays (visible rays: 380–780 nm), and infrared rays (780 nm or more). For wavelengths of light at 400 nm, 600 nm, and 800 nm, the optical absorption increased from 0.004 to 0.615, 0.004 to 0.708, and 0.043 to 0.707, respectively, as the concentration of Fe₃O₄ NF increased from 0wt% to 0.1wt%. As the content of Fe₃O₄ NPs in the base fluid (water) increased, the optical absorption increased linearly. Fig. 4.6 compares the solar weight absorption coefficients of Fe₃O₄ NF calculated through experiments and analyses. The solar weight absorption coefficient calculated based on the measurement results of optical absorption of Fe₃O₄ NFs in Chapter 3 increased from 0.301 to 0.854 as the concentration of Fe₃O₄ NF increased from 0wt% to 0.1wt%. The solar weight absorption coefficient of Fe₃O₄ NF calculated through the Rayleigh scattering estimation method increased from 0.258 to 0.783 as the concentration of Fe₃O₄ NF increased from 0wt% to 0.1wt%. Fe₃O₄ calculated through the experiment was higher by 0.12 on average than the solar weight absorption coefficient of Fe₃O₄ NF calculated through the Rayleigh scattering estimation method. This may have been because it was calculated on the assumption that light energy was wholly absorbed in the unmeasurable ultraviolet and infrared bands when measuring the optical absorption of Fe₃O₄ NF, considering the error of the measuring equipment and the limit of the measuring range.

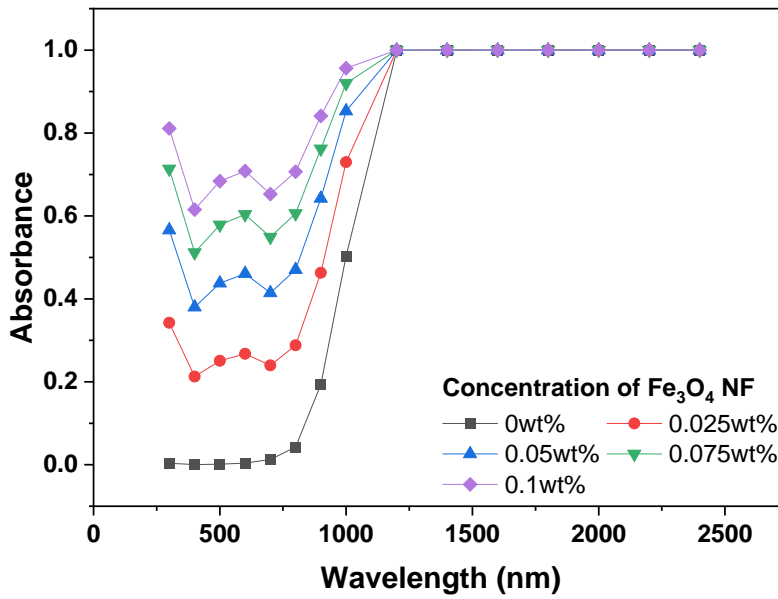


Fig. 4.5 Absorbance of Fe₃O₄ NF according to wavelength

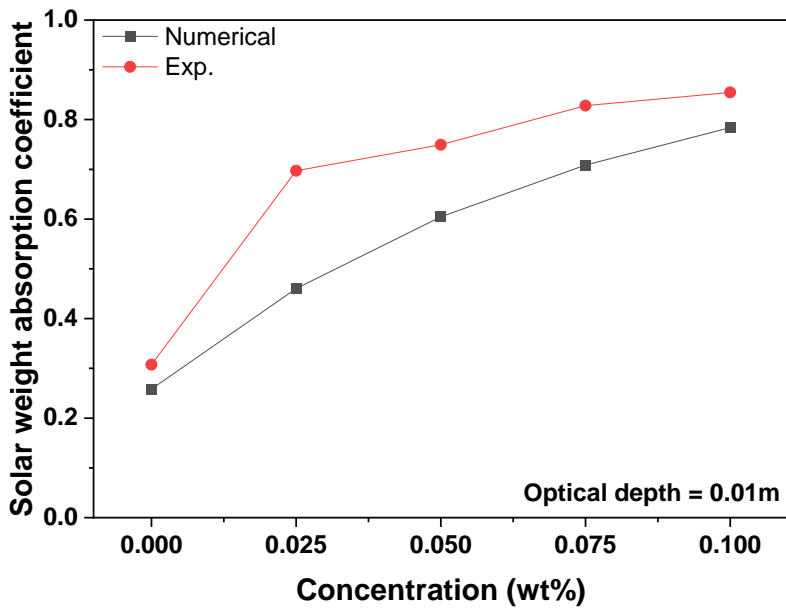


Fig. 4.6 Solar weight absorption coefficient according to centration of Fe₃O₄ NF

4.4.2. Thermal performance of FPVASC

The efficiency of solar collectors is determined by optical efficiency and heat loss coefficient. Optical efficiency refers to the heat collection efficiency of the solar collector when there is no heat loss from the solar collector. Fig. 4.7 shows the optical efficiency of FPVASC with increasing Fe₃O₄ NF concentration. As the concentration of Fe₃O₄ NF increased to 0.6wt%, the optical efficiency of FPVASC was improved. As Fe₃O₄ NF increased from 0wt% to 0.1wt%, it increased from 0.504 to 0.723, and when Fe₃O₄ NF was used, optical efficiency was improved up to 1.6 times compared to water. The increased optical efficiency was due to the improved optical absorption by increased Fe₃O₄ NF concentration.

As the concentration of Fe₃O₄ NF increases, the optical absorption of Fe₃O₄ NF is improved, as shown in Fig. 4.5. Increasing the mass flow also increases the optical efficiency of the VASC. As the water mass flow rate in FPVASC increased from 0.005 kg/s to 0.02 kg/s, the optical efficiency improved from 0.504 to 0.563. As the mass flow rate of 0.1wt% Fe₃O₄ NF in FPVASC increased from 0.005 kg/s to 0.02 kg/s, the optical efficiency increased from 0.723 to 0.801. When the mass flow rate was from 0.005 kg/s to 0.02 kg/s, the improvement in optical absorption using Fe₃O₄ NF was the highest at 0.1wt%. Compared to water, the optical efficiency improved from 42.1% to 43.5%. The increase in optical efficiency of FPVASC was dependent on the improvement of optical absorption by increasing the concentration of Fe₃O₄ NF. However, because the increase in mass flow did not contribute to the optical absorption performance, the increase in optical efficiency was associated with the improvement of the thermal environment of the FPVASC by increasing the mass flow. The fluid in FPVASC exhibited a laminar, with a thick and transparent thermal boundary layer. However, the increase in mass flow reduced the inertial force in the fluid, which reduced the thickness of the thermal boundary layer and enhanced heat transfer in the FPVASC, contributing to an improvement in optical efficiency.

Fig. 4.8 shows the heat loss coefficient of FPVASC according to the concentration change of Fe₃O₄ NF. The heat loss coefficient of FPVASC using Fe₃O₄ NF was lower than when water was used. The heat loss coefficient of FPVASC using water at a mass flow rate of 0.005 kg/s was

16.02 W/m²·°C. When Fe₃O₄ NF was used as the working fluid of FPVASC, the heat loss coefficient was lower than that of water. As the concentration of Fe₃O₄ NF increased, the heat loss coefficient increased.

When the mass flow rate was 0.005 kg/s, the heat loss coefficient of FPVASC using 0.025 wt% Fe₃O₄ NF was 14.47 W/m²·°C. As the Fe₃O₄ NF increased from 0.025wt% to 0.075wt%, there was little change in the heat loss coefficient. When the concentration of Fe₃O₄ NF was 0.1wt%, the heat loss coefficient of FPVASC was slightly increased to 15.14 W/m²·°C. This may have been due to the increased concentration of Fe₃O₄ NF on the internal temperature distribution of FPVASC. Fig. 4.9 shows water temperature distribution, 0.05wt% Fe₃O₄ NF and 0.1wt% Fe₃O₄ NF in FPVASC. As light energy was hardly absorbed due to the high light transmittance of water in FPVASC, optical absorption occurred intensively on the inner channel wall of FPVASC, causing heat loss to the surroundings, thereby contributing to a high heat loss coefficient. However, as the concentration of Fe₃O₄ NF increased, the optical absorption increased, and the light penetration depth decreased. As Fe₃O₄ NPs absorb a certain amount of light energy in Fe₃O₄ NF, the heat loss due to local overheating on the inner wall of the FPVASC was reduced compared to water. However, when optical absorption occurred near the glass wall with a continuous increase in the concentration of Fe₃O₄ NF, the proportion of convective and radiative heat transfer through the glass wall increased, and the heat loss coefficient increased.

The mass flow rate was associated with an increased heat loss coefficient. When water and Fe₃O₄ NF were used, the heat loss coefficient of FPVASC increased as the mass flow rate increased from 0.005 kg/s to 0.02 kg/s. When using water, the heat loss coefficient increased from 16.02 W/m²·°C to 17.88 W/m²·°C as the mass flow rate increased from 0.005 kg/s to 0.01 kg/s. The heat loss coefficient of 0.1wt% Fe₃O₄ NF increased from 15.14 W/m²·°C to 17.29 W/m²·°C as the mass flow rate increased from 0.005 kg/s to 0.01 kg/s. An increase in the mass flow increases the heat transfer coefficient inside the FPVASC. Because the FPVASC had a higher temperature than its surroundings, an increase in the internal heat transfer coefficient of the FPVASC due to an increase in the mass flow caused the effect of reducing the thermal resistance

of the FPVASC and the surrounding air, and the heat loss coefficient increased. By improving the optical absorption of Fe_3O_4 NF, FPVASC could produce higher heat and temperature.

Fig. 4.10 shows the temperature difference between the inlet and outlet of the FPVASC. When water was used, the mass flow rate was 0.015 kg/s, and the inlet and outlet temperature differences decreased from 2.34°C to 0.19°C as the inlet temperature increased from 30°C to 55°C. When 0.1wt% Fe_3O_4 NF was used, the temperature difference between the inlet and outlet of FPVASC, as well as the inlet temperature at which FPVASC was operable, was also increased due to the improved optical absorption compared to water. When the 0.1wt% Fe_3O_4 NF was used, and the mass flow rate was 0.015 kg/s, the inlet and outlet temperature difference decreased from 3.66°C to 0.6°C as the inlet temperature increased from 30°C to 65°C. While the increase in the concentration of Fe_3O_4 NF increased the amount of heat obtained by FPVASC by improving optical absorption, FPVASC using Fe_3O_4 NFs can produce heat even at a higher inlet temperature compared to water by improving the thermal properties of Fe_3O_4 NF. The increase in mass flow increased the heat capacity of the FPVASC and thus decreased the inlet and outlet temperature difference.

Fig. 4.11 shows the thermal efficiency of FPVASC using Fe_3O_4 NFs. The thermal efficiency decreased with an increase in the inlet temperature. This may have been due to increased heat loss from the FPVASC to the surroundings by the increase in the inlet temperature. The increased concentration of Fe_3O_4 NF improved the thermal efficiency and the heat production temperature. The improvement in thermal efficiency with Fe_3O_4 NF in FPVASC depended on the improvement in optical absorption by increasing the Fe_3O_4 NF concentration. The improved optical absorption compared to water improved the optical efficiency of the FPVASC, thereby increasing the maximum collectible heat of the FPVASC. When the inlet temperature was 40°C, and the mass flow rate was 0.015 kg/s, the thermal efficiency of FPVASC increased from 0.287 to 0.54 as the concentration of Fe_3O_4 NF increased from 0wt% to 0.1wt%.

The increase in mass flow reinforced the improvement in the thermal efficiency by increasing the Fe_3O_4 NF concentration. With water, when the inlet temperature was 45°C, the

thermal efficiency increased by 0.021 from 0.184 to 0.205 as the mass flow increased from 0.005 kg/s to 0.02 kg/s, respectively. On the other hand, in the case of 0.1wt% Fe₃O₄ NF, the thermal efficiency increased by 0.037 from 0.412 to 0.459 as the mass flow increased from 0.005 kg/s to 0.02 kg/s when the inlet temperature was 45°C. This meant that, although weak, the increase in mass flow improved the heat collection efficiency of FPVASC with an increase in the Fe₃O₄ NF concentration. In this study, 0.1wt%, the maximum concentration of Fe₃O₄ NF, was too low to improve thermal properties. The effect of improving the thermal efficiency by increasing the mass flow rate was considered to be due to the decrease in heat loss induced by the average temperature of FPVASC lowered by an increase in heat capacity.

Fig. 4.12 shows the exergy efficiency of FPVASC using Fe₃O₄ NFs. When the mass flow rate is 0.015 kg/s, the exergy efficiency of FPVASC is minimized at an inlet temperature of 40–45°C, and the exergy efficiency is high. It was shown that exergy efficiency decreased when the inlet temperature was higher than that. With water, as the inlet temperature increased from 30°C to 45°C, the exergy efficiency increased from 0.0636 to 0.0686. At higher temperatures, the exergy efficiency decreased.

As the Fe₃O₄ NF concentration increased from 0wt% to 0.1wt%, the maximum exergy efficiency increased from 0.0686 to 0.0844. As the concentration of Fe₃O₄ NF increased, the inlet temperature at which the maximum exergy efficiency was formed also increased along with the improvement of the exergy efficiency. As the concentration of Fe₃O₄ NF increased from 0wt% to 0.1wt%, the inlet temperature at which the maximum exergy efficiency was formed also increased from 40°C to 45°C. The improvement of exergy efficiency of FPVASC may have been due to the irreversibility of FPVASC to heat production is reduced by the optical efficiency of FPVASC improved by an increase in Fe₃O₄ NF concentration and a reduction in heat loss coefficient. The increase in mass flow rate has the effect of slightly reducing the heat loss and thus slightly reducing the thermal efficiency. However, in terms of exergy efficiency, increasing the mass flow rate for FPVASC was insignificant. The effect of reducing heat loss due to the mass flow rate was very insignificant, and the increase in the effective heat production capacity

of FPVASC by increasing the concentration of Fe_3O_4 NF was a significant factor determining the performance of FPVASC.

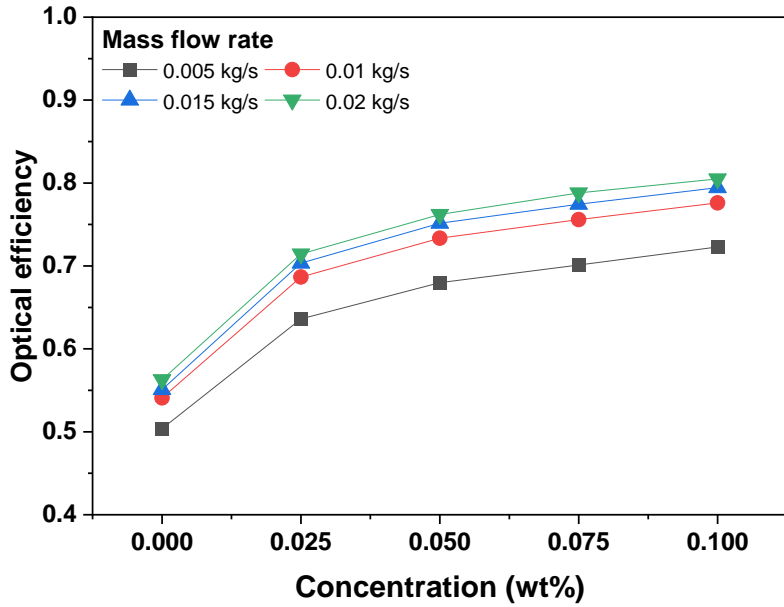


Fig. 4.7 Optical efficiency of FPVASC according to the concentration of Fe₃O₄ NF

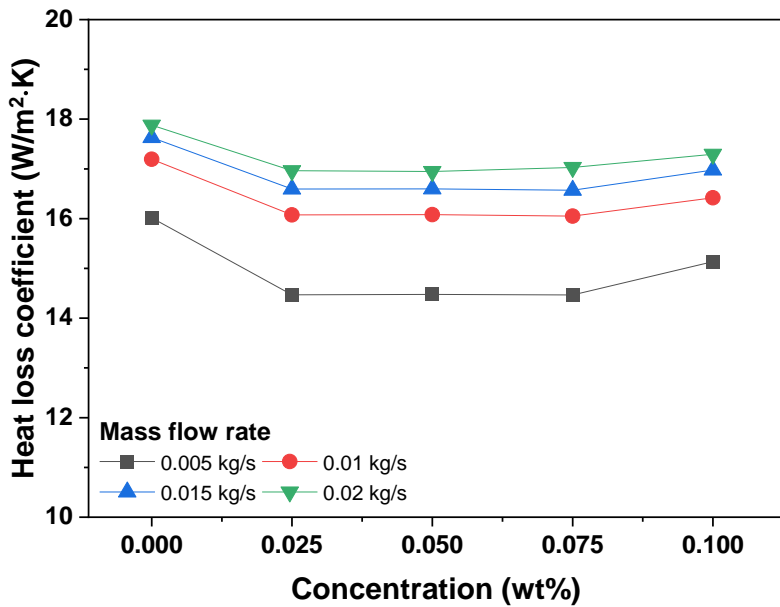
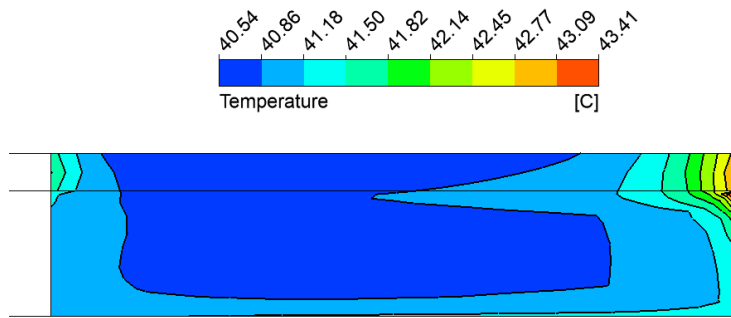
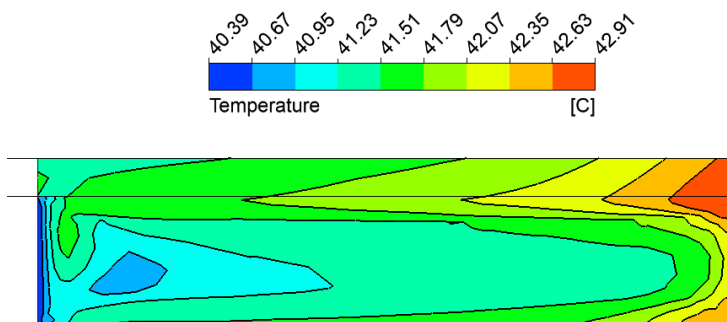


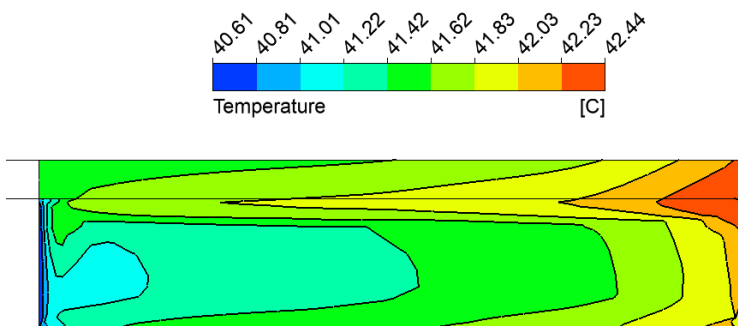
Fig. 4.8 Heat loss coefficient of FPVASC according to the concentration of Fe₃O₄ NF



(a)



(b)



(c)

Fig. 4.9 Temperature contour in FPVASC; (a) Water, (b) 0.05wt% Fe₃O₄ NF, (c) 0.1wt% Fe₃O₄ NF

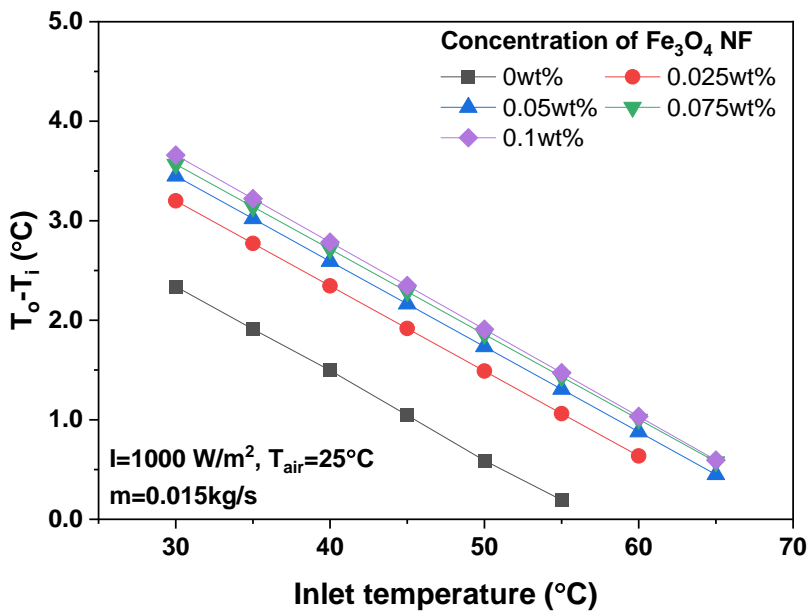
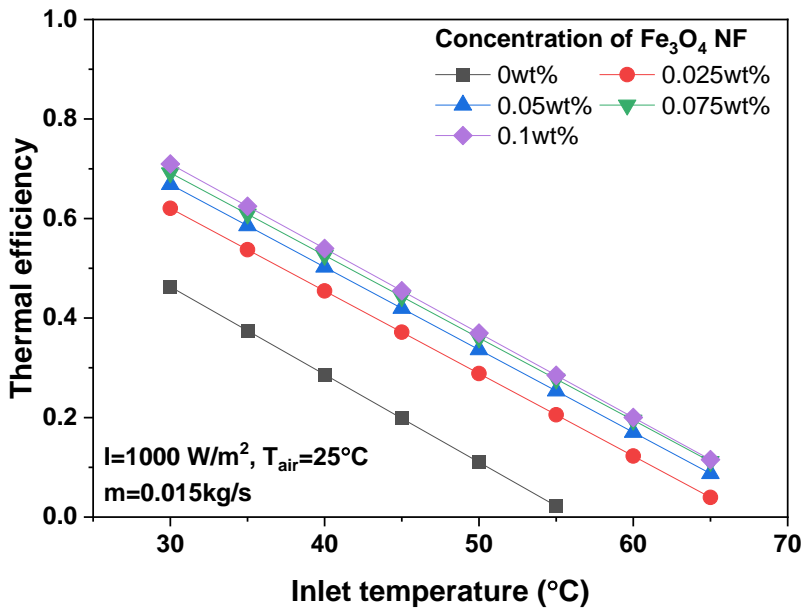
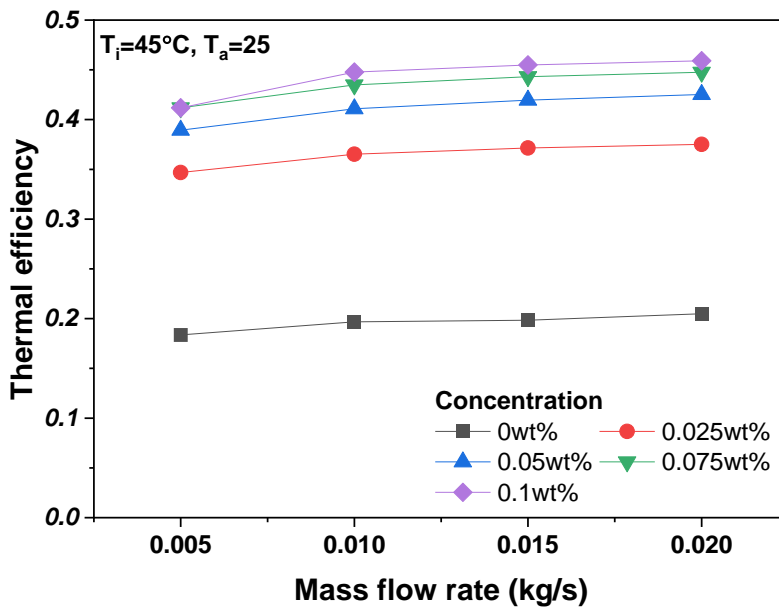


Fig. 4.10 Temperature difference between inlet and outlet of FPVASC

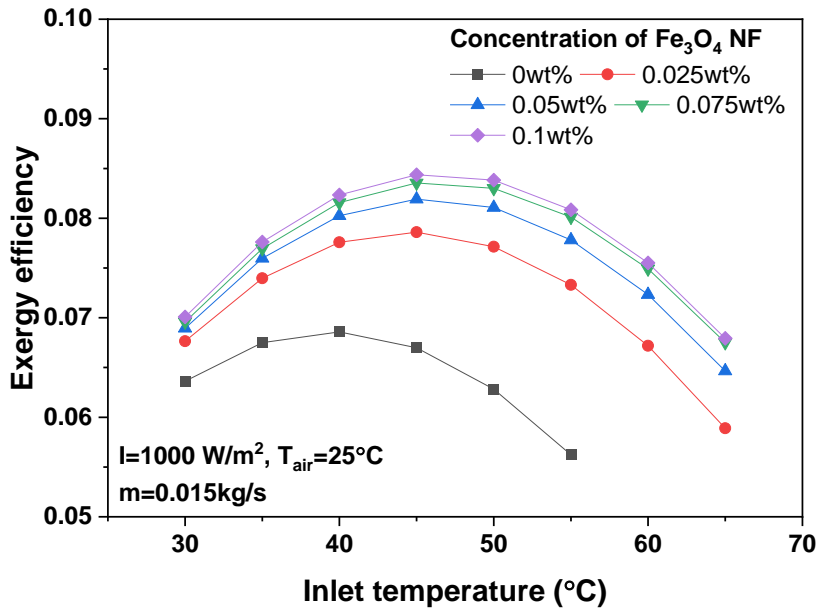


(a)

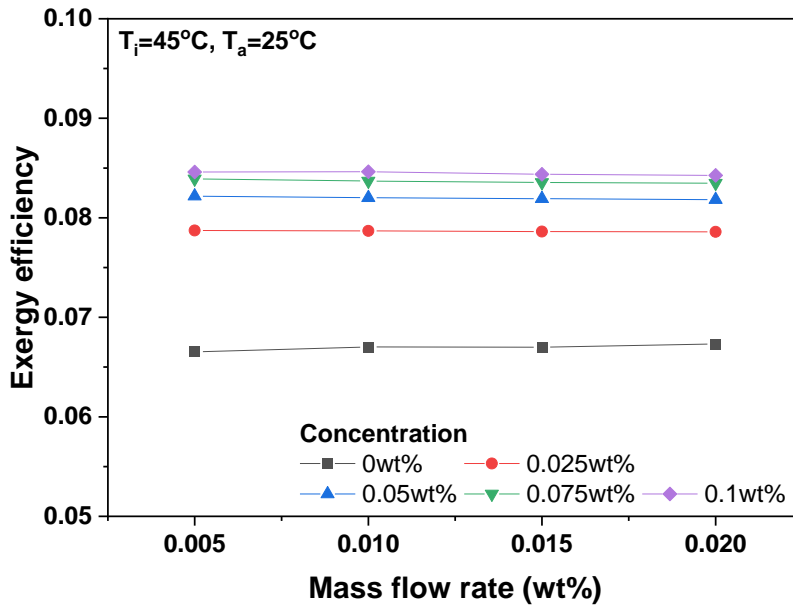


(b)

Fig. 4.11 Thermal and exergy efficiency of FPVASC; (a) according to normalized temperature difference, (b) according to the concentration



(a)



(b)

Fig. 4.12 Thermal and exergy efficiency of FPVASC; (a) according to concentration, (b) according to the mass flow rate at $T_i=45^\circ\text{C}$

5. Experimental study on the performance of VASC solar collector

5.1. Experimental setup of VASC solar collector

To evaluate the performance of VASC, (a) comparison with SASC and VASC and (b) performance evaluation of VASC using Fe_3O_4 NF, ATO NF, and $\text{Fe}_3\text{O}_4/\text{ATO}$ hybrid NF were conducted. Because MWCNT NF has high optical absorption, the high thermal performance can be expected when using the MWCNT NF, but it was challenging that MWCNT NPs were precipitated quickly during the experiment using MWCNT NF although the MWCNT NF has a high zeta potential value. Experiments in (a) and (b) were conducted indoors using an artificial light source; except for the shape and capacity difference of the solar collector, the configuration of the experimental device was the same. Fig. 5.1 shows the schematic diagram and real photo of the volume absorption solar collector performance test apparatus. The experimental solar heat collector consisted of the NF storage tank, a pump, an artificial solar light source, a collector, a plate heat exchanger, and a thermostat.

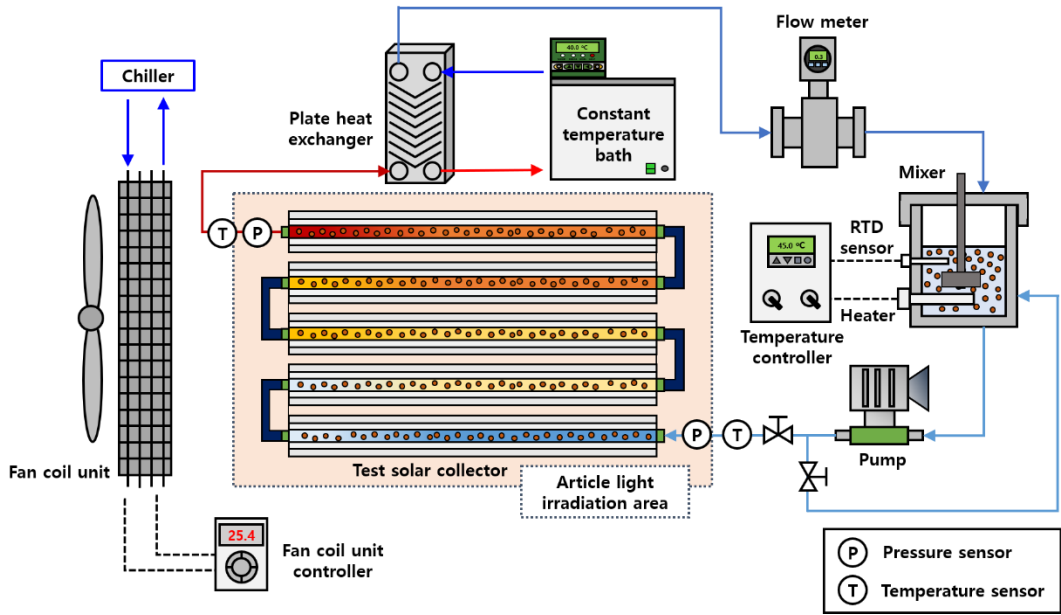
The NF was pumped into a solar collector exposed to an artificial sunlight source and was heated. Because the solar collectors used in experiments (a) and (b) were different in size, the flow rate ranges in the pipe were also different. Therefore, a peristaltic pump (BT100-2J, Baoding Longer Precision Pump Co., China) was used in experiment (a), and a magnetic circulation pump (TL-B10, TOPSFLO Co., China) was used in experiment (b). The heated NF was cooled through a plate heat exchanger and flew back into the NF storage tank. A 1000W heater was installed to form a constant temperature of the working fluid in the NF storage tank that could store 5 L of NF, and the temperature was maintained constant by PID control. PT 100, a type of RTD sensor, was installed at the inlet and outlet of the solar collector to measure the NF temperature. A flow meter was installed at the rear end of the plate heat exchanger for the flow rate of the NF flowing to the solar collector. In experiment (a), a mass flow meter (RHM04, Rheonik messtechnik

GmbH, Germany) was used for flow measurement; in experiment (b), a magnetic flow meter (E-MAG-I, Autoflow Co., Korea) was used.

The artificial light source used in the experiment was a halogen lamp, referring to previous studies [90–92]. The color temperature of sunlight is about 5500K at noon. To simulate natural light as closely as possible, a halogen lamp with a color temperature of 4200 K was used. ASHRAE 93-77 [93] mentioned that to perform performance measurements of solar collectors indoors, the intensity of solar radiation simulated by an artificial light source should be 700 W/m² or more. To ensure the minimum standard solar intensity of ASHRAE 93-77 [93], in experiment (a), seven halogen lamps with 300 W capacity were placed in the flow direction of the solar collector; in experiment (b), six halogen lamps having a capacity of 1000 W were arranged at 2×3. To understand the average insolation amount and distribution in experiments (a) and (b), the insolation was measured by evenly dividing it in the width and length directions. In experiment (a), the average insolation was calculated by measuring insolation using a solar irradiometer in the 11×4 grid divided into 11 equal parts in the axial direction and 4 equal parts in the width direction of the receiver tube at the top of the collector. In experiment (b), the average insolation was calculated by measuring insolation at intervals of 0.04 m in the longitudinal and width directions. Fig. 5.2 shows the contour of insolation entering the solar collector. In experiment (a), it was confirmed that the amount of insolation was distributed as 680 ~ 730 W/m² depending on the position of the upper part of the solar collector, and it was confirmed that it had an average insolation amount of 718 ± 22 W/m². In experiment (b), the amount of insolation was distributed as from 896 to 1130 W/m², and the average amount of insolation is 1017 ± 64 W/m².

Fig. 5.3 shows the structure of the solar collector used in the experiment. The solar collector used in the experiment primarily consisted of a collector and a reflector. Table 5.1 shows the main specifications of the solar collector used in experiment (a). The solar collector used in experiment (a) was intended to compare the SASC and VASC methods by using a SASC tub, a copper tube with graphite coating, and a VASC tube, a transparent polycarbonate tube, as receivers. In experiment (b), five receivers for volume absorption heat collection were connected

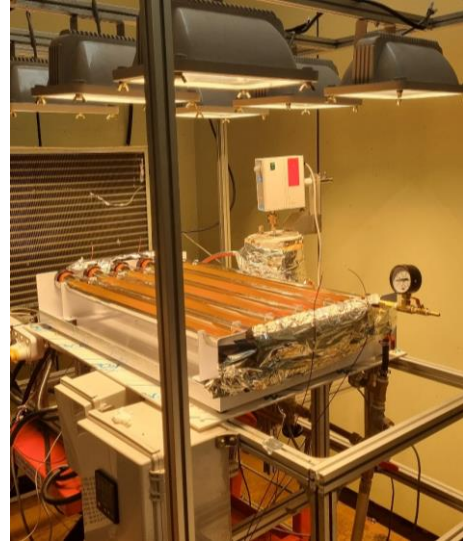
in series to compare the heat collection properties of NFs to form a solar collector. Table 5.2 shows the main specifications of the solar collector used in experiment (b). A vacuum was formed between the receiver tube and the outer tube to minimize heat loss. A vacuum cap was installed at both ends of the receiver to form a vacuum between the receiver and the outer tube.



(a)



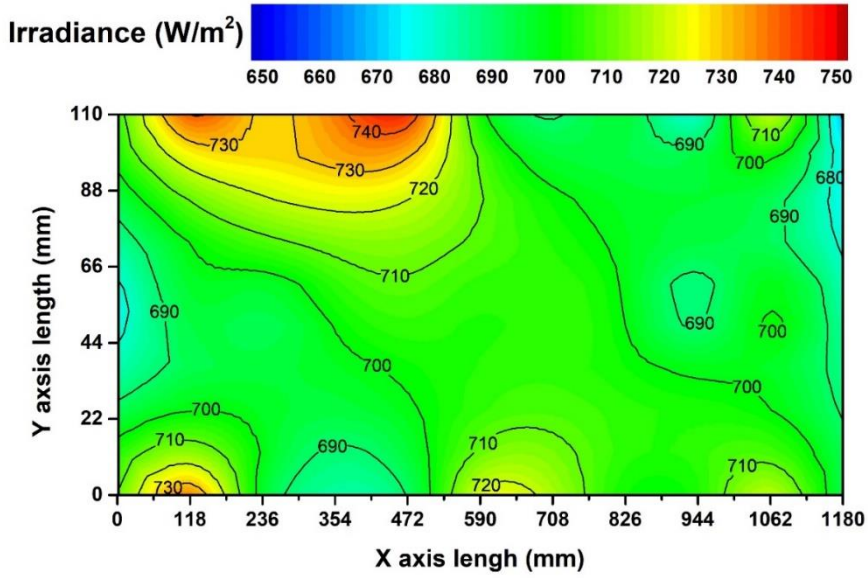
(b)



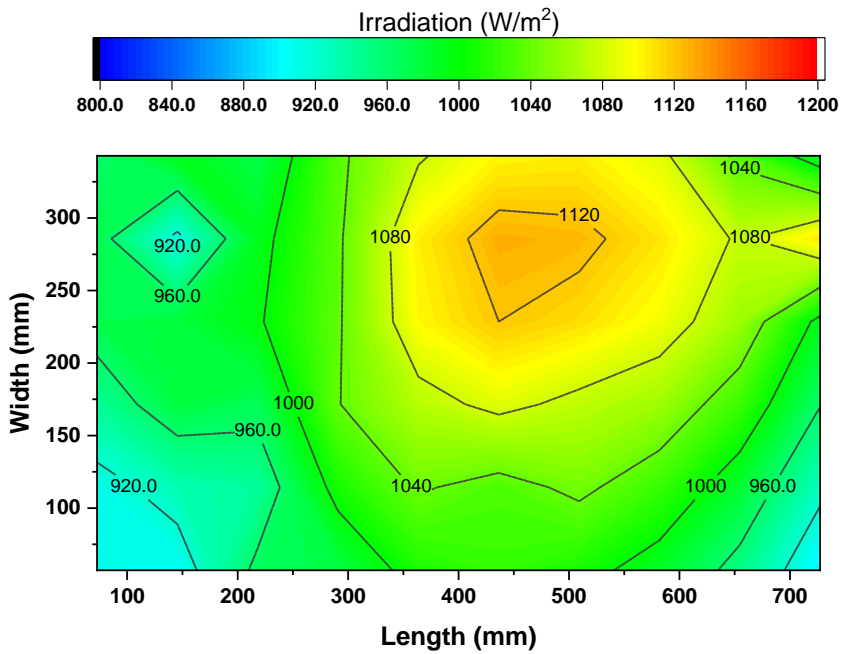
(c)

Fig. 5.1 Schematic of the experimental setup to evaluate solar collector performance indoor; (a)

Schematics of the experimental setup to evaluate the performance of solar collector, (b) Photo about the experimental setup for comparison with solar collecting method, (c) Photo about the experimental setup for comparison with the comparison with VASC performance according to NF

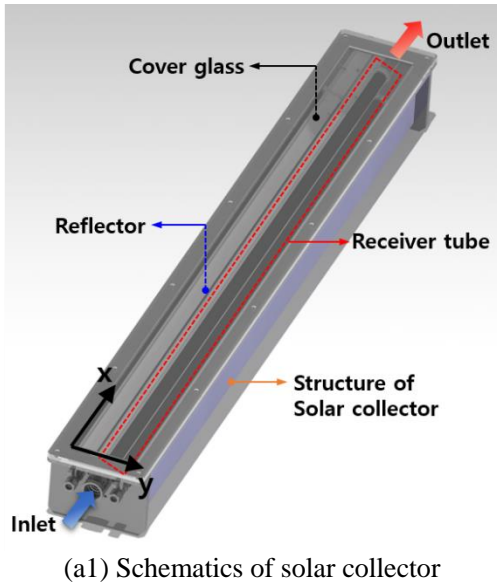


(a)

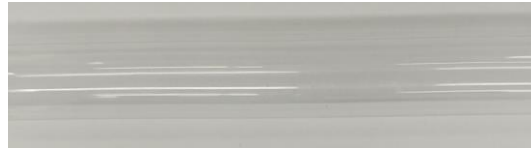


(b)

Fig. 5.2 Irradiance contour at the solar collector by an artificial light source; (a) solar collector for comparison with solar collecting method, (b) Solar collector for performance evaluation according to NF



(a2) Surface absorption receiver tube
(Copper tube coated with graphite)



(a3) Volumetric absorption receiver tube
(Polycarbonate tube)

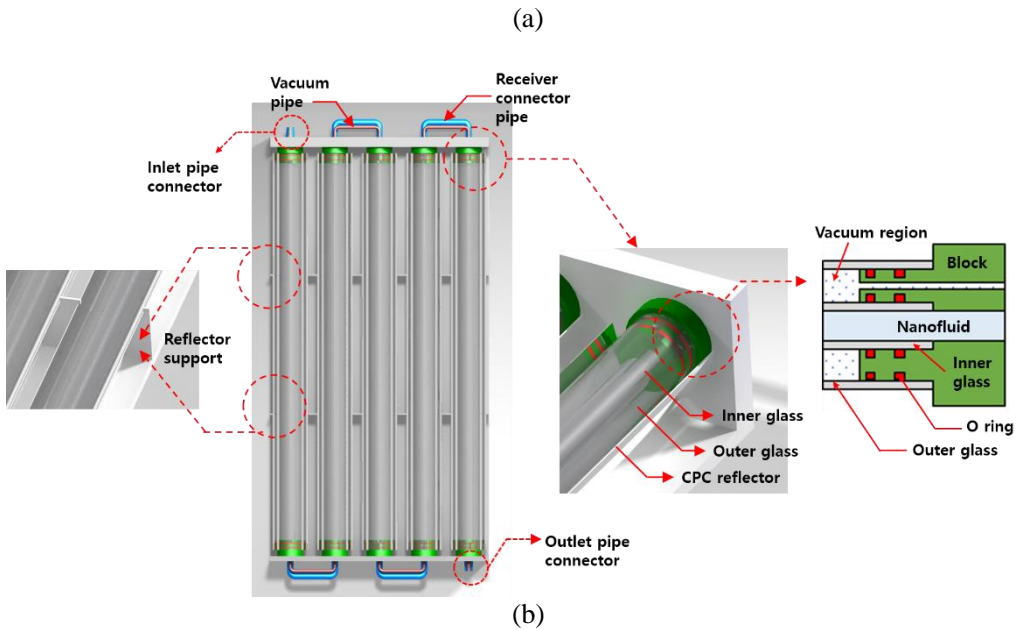


Fig. 5.3 Structure of VASC solar collector used in the experiment; (a) Solar collector for comparison with solar collecting method, (b) Solar collector for performance evaluation according to NF

Table 5.1 Specification of solar collector for comparison with solar collecting method

Item	Specification	Value
Cover of solar collector	Material	Polycarbonate
	Absorptivity	0.93
	Aperture area (m ²)	0.13
	Thickness (m)	0.005
VASC	Receiver tube material	Polycarbonate
	Receiver tube inner diameter (m)	0.018
	Thickness (m)	0.002
	Length (m)	1.18
SASC	Receiver tube material	Copper
	Surface coating material	Graphite
	Receiver tube inner diameter (m)	0.018
	Thickness (m)	0.002
Reflector	Length (m)	1.18
	Reflector's material	Aluminum
	Reflectivity	0.92
	Concentration ratio	1.41

Table 5.2 Specification of solar collector for performance evaluation according to NF

Specification	Value
Receiver tube connecting method	Serial
Receiver tube material	Pyrex glass
Receiver outer diameter	20 mm
Receiver thickness	2.3 mm
Receiver tube number	5 EA
Outer glass tube diameter	46 mm
Outer glass tube thickness	2.3 mm
Vacuum cap material	MC nylon
Reflector material	Aluminum
Reflector reflectivity	0.92
Concentration ratio	1

5.2. Experimental method and condition of VASC solar collector

The performance of solar collectors was evaluated indoors by the steady-state method proposed by ASHRAE 93-2000 [88]. In the steady-state method, the solar collector needed to achieve thermal equilibrium with the surrounding environment during the performance test. Therefore, in this study, the temperature and wind speed around the experimental solar collector during the experiment was set to be constant at 4 m/s. The ambient temperature during the experiment was $28 \pm 1.0^\circ\text{C}$.

The amount of insolation flowing into the solar collector was simulated using an artificial light source. The artificial light source affected the ambient temperature and the initial temperature of the solar collector by radiant heat; the artificial light source was continuously operated throughout the experiment. To maintain a constant initial temperature of the solar collector, the inlet temperature was set while blocking the inflow of light through a dark film with low light transmittance. When the inlet temperature was kept constant for 10 minutes to maintain a steady-state, the blackout was removed to observe the changes in the inlet-outlet temperatures of the solar collector. When the outlet temperature was kept constant for 10 minutes, it was judged that a steady-state was reached. Table 5.3 and show the experimental conditions for comparing the performance of SASC and VASC and the experimental conditions for comparing the performance of VASC using Fe_3O_4 NF, ATO NF, and $\text{Fe}_3\text{O}_4/\text{ATO}$ hybrid NF.

Table 5.3 Experimental conditions for comparison with SASC and VASC

Item	Value
Irradiance (W/m ²)	720
Mass flow rate (kg/s)	0.0025, 0.005
Mass concentration (wt%)	0, 0.001, 0.05, 0.1
Inlet temperature (°C)	40, 45, 50, 55, 60
Air temperature (°C)	28

Table 5.4 Experimental conditions for comparison with the performance of VASC according to NF

Item	Value
Irradiance (W/m ²)	1017
Mass flow rate (kg/s)	0.0067, 0.01, 0.013
Inlet temperature (°C)	40, 45, 50, 55, 60
Air temperature (°C)	28
Mass concentration of Fe ₃ O ₄ NF	0, 0.001, 0.05, 0.075, 0.1
Mass concentration of ATO NF	0, 0.05, 0.075, 0.1, 0.25
Mixing ratio of Fe ₃ O ₄ /ATO hybrid NF	0.2, 0.4, 0.6, 0.8 at total concentration = 0.1 wt%

5.3. Uncertainty analysis of the performance of the solar collector

The thermal efficiency of a solar collector is directly related to its mass flow rate, specific heat, temperature, heat collection area, and solar radiation. The errors of the RTD and irradiance sensors were $\pm 0.1^\circ\text{C}$ and $\pm 5\%$, respectively. The mass flow rate errors were different in the experiment compared to SASC and VASC and the experiment of comparison the performance according to the type of NFs (Fe_3O_4 NF, ATO NF, and $\text{Fe}_3\text{O}_4/\text{ATO}$ hybrid NF). The mass flow rate error in the experiment about the comparison of collection method and the type of NFs was $\pm 1.01\%$ and $\pm 0.5\%$. The uncertainty of the solar collector efficiency can be calculated using Eq. (5.1), and in this study, the uncertainty of thermal efficiency in the comparison SASC and VASC and the comparison with the type of NFs was calculated as 5.38% and 5.21%, respectively.

$$\frac{\delta\eta_{therm}}{\eta_{therm}} = \sqrt{\left(\frac{\delta\dot{m}}{\dot{m}}\right)^2 + \left(\frac{\delta c_p}{c_p}\right)^2 + \left(\frac{\delta(T_o - T_i)}{(T_o - T_i)}\right)^2 + \left(\frac{\delta A_c}{A_c}\right)^2 + \left(\frac{\delta I}{I}\right)^2} \quad (5.1)$$

The exergy efficiency can be calculated using Eq. (5.2)

$$\frac{\delta\eta_{ex}}{\eta_{ex}} = \sqrt{\left(\frac{\delta\dot{m}}{\dot{m}}\right)^2 + \left(\frac{\delta c_p}{c_p}\right)^2 + \left(\frac{\delta T_a}{T_a}\right)^2 + \left(\frac{\delta Q}{Q}\right)^2 + \left(\frac{\delta A}{A_c}\right)^2 + \left(\frac{\delta I}{I}\right)^2} \quad (5.2)$$

In this study, the uncertainty of exergy efficiency in the comparison of SASC and VASC, and the comparison with the type of NFS was calculated by 5.48% and 5.38%, respectively.

5.4. Experimental result and discussion on solar collector performance

5.4.1. Result and discussion on comparison SASC with VASC

5.4.1.1. Thermal efficiency comparison with SASC and VASC

Fig. 5.4 shows the useful heat and LNTD of the SASC. Maximum useful heat at the mass flow rate of 0.0025 and 0.005 kg/s was increased by using Fe₃O₄ NF. When the mass flow rate was 0.0025 and 0.005 kg/s, the useful heat of the water was 71.08 and 72.64 W, respectively. The maximum useful heat at 0.0025 and 0.005 kg/s reached to peak at 0.05wt% Fe₃O₄ NF, and it decreased. The maximum useful heat at 0.0025 and 0.005 kg/s was 73.69 and 74.28 W, respectively, and those were 3.67% and 2.26% improved compared to the water. However, when the concentration of Fe₃O₄ NF was 0.1wt%, the maximum useful heat of 0.0025 and 0.005 kg/s decreased to 70.59 and 71.87 W, 0.7% and 1.1% lower than the water. The thermal harvesting performance of the SASC can be improved by using the NFs, although the concentration is limited. Generally, the laminar convective heat transfer is an effective heat transfer mechanism of the SASC, the increase of the concentration of the NF is advantageous for improving the performance of the SASC because the convective heat transfer can be improved by enhanced thermal properties from active brown motion. However, improving heat transfer by increasing the concentration is not only a key parameter to increasing the thermal harvesting performance of the SASC. In the solar collector, the maximum useful heat is an important performance index; however, the operating range is also an important factor because it is difficult to utilize a solar collecting system with a narrow operating range. When the concentration and mass flow rate of the Fe₃O₄ NF was 0.01wt%, and 0.005 kg/s, the LNTD of the SASC was 0.0186 m²·°C/W higher than the water. However, the LNTD at 0.0025 and 0.005 kg/s was overall decreased from 0.0557 to 0.053 m²·°C/W and 0.0553 to 0.052 m²·°C/W as the concentration of the Fe₃O₄ increased from

0 to 0.1wt%. The SASC confirmed that the maximum useful heat increased, and the LNTD decreased according to the increase of the Fe₃O₄ NF concentration.

Fig. 5.5 shows the useful heat and LNTD of the VASC. The useful heat was increased by increasing the concentration of the Fe₃O₄ NF. The improvement of the useful heat according to increasing the concentration of Fe₃O₄ NF in the VASC was significant compared to the SASC. As the concentration of Fe₃O₄ NF increased from 0 to 0.1wt%, the useful heat at the mass flow rate of 0.0025 and 0.005 kg/s increased from 62.51 to 71.78 W and 67.25 to 76.91 W, respectively. The maximum useful heat was the highest at 0.1wt% Fe₃O₄ NF, and the useful heat at 0.0025 kg/s and 0.005 kg/s was improved by 14.84% and 14.36%, respectively, compared to water. As shown in Fig. 6, the useful heat can be improved due to the improvement of solar absorption. Also, when using Fe₃O₄ NF, the operating range of the VASC was wider than the SASC. The LNTD of the VASC at 0.0025 and 0.005 kg/s increased from 0.0484 to 0.0554 m²·°C/W and 0.0479 to 0.0702 m²·°C/W, respectively, when the concentration of the Fe₃O₄ NF increased from 0 to 0.05wt%. And then, it decreased to 0.0534, and 0.0689 m²·°C/W at 0.0025 and 0.005 kg/s as the concentration of Fe₃O₄ NF increased from 0.05 to 0.1wt%. In the VASC, much solar energy can be obtained by increasing the concentration of the Fe₃O₄ NF due to high solar absorption. However, the heat loss can also be increased by an excessive increase in absorbed solar energy. It can create a similar environment where the solar energy is focused on the surface of the receiver to the SASC.

Fig. 5.6 shows the energy ratio of the SASC and VASC under various operating conditions. In the case of SASC, the unabsorbed energy ratio changed slightly from 0.22 to 0.26 with an increase in the Fe₃O₄ NF concentration. However, in the case of VASC, it was remarkably decreased with an increase in the Fe₃O₄ NF concentration. For the VASC, the unabsorbed energy ratio reached a minimum at 0.05wt% Fe₃O₄ NF, and it was almost similar at the Fe₃O₄ NF concentrations of 0.1wt% and 0.05wt%. The useful heat ratio of the VASC using 0.05wt% Fe₃O₄ NF at 0.0025 and 0.005 kg/s was 0.263 and 0.212, respectively, which were 0.1 and 0.09 lower than the values obtained using water. On the contrary, in the SASC, the heat loss ratio of the absorbed energy at 0.0025 and 0.005 kg/s increased with the Fe₃O₄ NF concentration. At 0.05wt%

Fe_3O_4 NF, the heat loss ratio of the absorbed energy in the SASC at 0.0025 and 0.005 kg/s was 0.412 and 0.405, respectively; these were the maxima values.

Meanwhile, in the VASC, the decrease in the heat loss ratio of absorbed energy differed depending on the mass flow rate of the working fluid. However, the energy loss ratio decreased with an increase in the mass flow rate of the Fe_3O_4 NF. The heat loss ratio of the absorbed energy at 0.0025 kg/s slightly decreased from 0.373 to 0.364 as the Fe_3O_4 NF concentration increased from 0 to 0.01wt% and then slightly increased to 0.388 when the Fe_3O_4 NF concentration was 0.1wt%. At a mass flow rate of 0.005 kg/s, the heat loss ratio increased from 0.322 to 0.317 as the Fe_3O_4 NF concentration increased from 0 to 0.05wt% and remained almost constant when it was further increased to 0.1wt%. This means that the improvement in the heat transfer of Fe_3O_4 NF in the SASC results in a higher heat loss. If the heat transfer medium in the VASC exhibits absorption performance similar to that shown by the SASC absorber under the same environment, the VASC has a smaller heat loss than the SASC. Therefore, the useful heat can be effectively obtained in the VASC compared to the SASC.

The heat removal factor (F_R) and overall heat loss coefficient (U_L) are the critical parameters for determining the solar absorption capacity and heat loss in a solar collector. Fig. 5.7 shows the variation in the F_R values of the VASC and SASC according to the Fe_3O_4 NF concentration. For the VASC, the maximum F_R values obtained at 0.0025 and 0.005 kg/s were 0.8184 and 0.8761, respectively, 7.3% and 11.75% higher than those obtained using water. The F_R of the VASC using 0.1wt% Fe_3O_4 NF was improved over that obtained using water; however, it was lower than that obtained using 0.05wt% Fe_3O_4 NF. The F_R values of the SASC using 0.1wt% Fe_3O_4 at 0.0025 and 0.005 kg/s were 0.7626 and 0.7775, respectively, which were slightly decreased by 2.43% and 1.39% compared to the values obtained using 0.05wt% Fe_3O_4 NF. The F_R value of the VASC using 0.1wt% Fe_3O_4 NF was further dramatically decreased than that of the SASC. For the VASC, the F_R at 0.0025 and 0.005 kg/s decreased after the Fe_3O_4 NF concentration reached an inflection concentration of 0.05wt%. At a Fe_3O_4 NF concentration of 0.05wt%, the F_R values at 0.0025 and 0.005 kg/s were 0.7744 and 0.823, respectively, 7.3% and 11.8% higher than the values obtained using water. In the previous study [94–97], the F_R was increased due to the effective convective

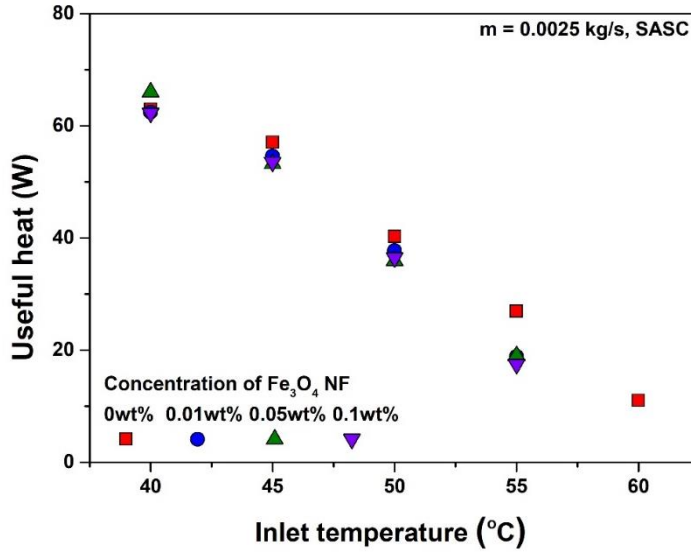
heat transfer by increasing the concentration of Fe_3O_4 NF. However, heat loss can also be increased depending on the operating conditions. Because the SASC has a higher heat loss than the VASC, as shown in Fig. 5.7, the increment rate of F_R for the SASC with an increasing Fe_3O_4 NF concentration was lower than that observed for the VASC.

Fig. 5.8 shows the variation in U_L values for the SASC and VASC according to the Fe_3O_4 NF concentration. With increasing Fe_3O_4 NF concentration, the U_L of the SASC increased, whereas that of the VASC decreased. In SASC, as the Fe_3O_4 NF concentration was increased from 0 to 0.1wt%, the U_L at 0.0025 and 0.005 kg/s was increased from 24.86 to 26.15 $\text{W/m}^2\cdot^\circ\text{C}$ and from 25.05 to 26.71 $\text{W/m}^2\cdot^\circ\text{C}$, respectively. The enhancement of U_L of the SASC using 0.1wt% Fe_3O_4 NF at 0.0025 and 0.005 kg/s was 5.19% and 6.63%, respectively, compared with that obtained using water. However, the U_L of the VASC significantly decreased when the Fe_3O_4 NF was used as the heat transfer medium. The U_L of the VASC at 0.0025 and 0.005 kg/s reached minimum values at 0.05wt% Fe_3O_4 NF, and that at 0.1wt% Fe_3O_4 NF was slightly increased. The U_L values of the VASC using 0.05wt% Fe_3O_4 NF at 0.0025 and 0.005 kg/s were 16.25 and 12.83 $\text{W/m}^2\cdot^\circ\text{C}$, respectively, and decreased by 6.37% and 3% compared with the values obtained using water. However, the U_L of the VASC obtained using 0.1wt% Fe_3O_4 NF at 0.0025, and 0.005 kg/s slightly increased to 17.78 and 13.8 $\text{W/m}^2\cdot^\circ\text{C}$.

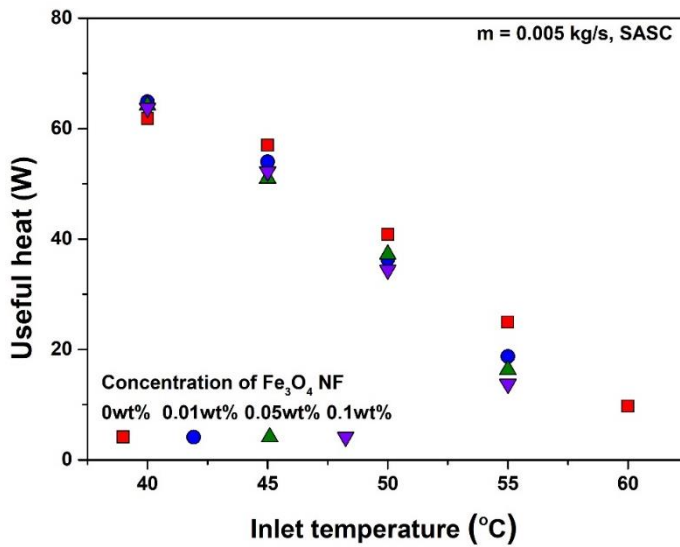
To improve the performance of the solar collector, it is required to increase the F_R and U_L , simultaneously. According to previous studies [94–97], the increase in the NF concentration in the SASC simultaneously increased both F_R and U_L . These effects improved the maximum efficiency of the solar collector while decreasing its operable range under various operating conditions. To enhance the performance of the SASC, it is essential to suppress heat loss and increase the F_R . The SASC has a higher heat loss than the VASC because it has a relatively uniform temperature distribution of solar collectors owing to the intensive heated absorber. In this study, because the absorber of SASC was directly exposed, the effect of improving the solar thermal harvesting performance by increasing the concentration of Fe_3O_4 NF was reduced. Also, the convection heat transfer between the absorber and the working fluid improved by increasing

concentration, promoting heat loss, and reducing the operating range. To improve the solar thermal harvesting performance of the SASC by using the NF, it is required to minimize the heat loss of the SASC.

In the VASC, gained solar energy can be increased by increasing the concentration of Fe_3O_4 NF. However, according to Gupta et al.[98], the efficiency of the VASC decreased over the critical concentration of the NF in the solar collector, where solar energy is intensively absorbed into the NF near the receiver wall. This brings to the decrease in temperature uniformity on the NF. The solar thermal harvesting environment is similar to the SASC due to reduced optical length and increased concentration. Besides, absorbed solar energy can be decreased by increasing the NF concentration due to enhanced light scattering. Therefore, in designing the VASC, a suitable NF concentration corresponding to the VASC's capacity must be considered considering the receiver tube specifications, NF permeability, and NF thermal properties.

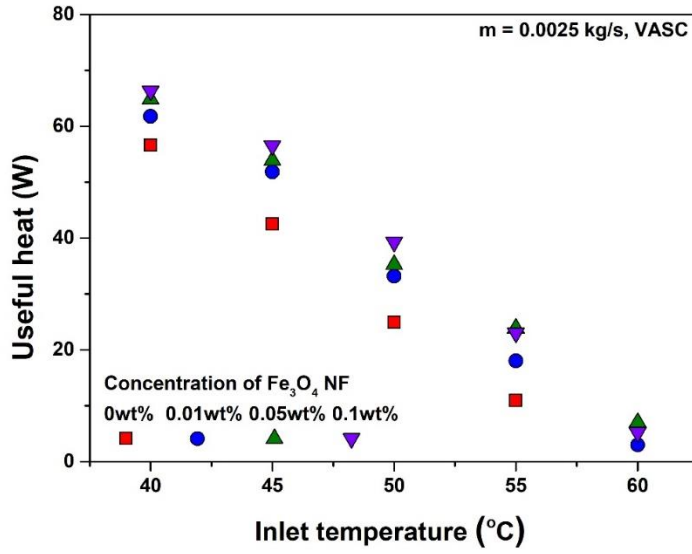


(a)

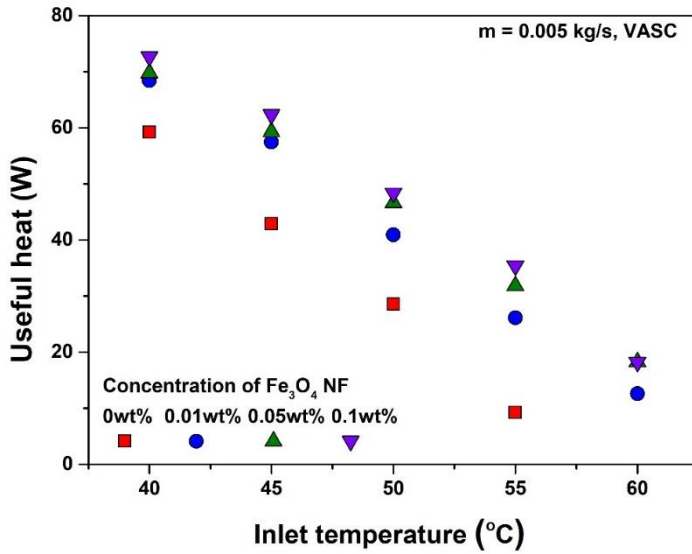


(b)

Fig. 5.4 Useful heat of the SASC according to the inlet temperature; (a) $\dot{m} = 0.0025$ kg/s, $\dot{m} = 0.005$ kg/s

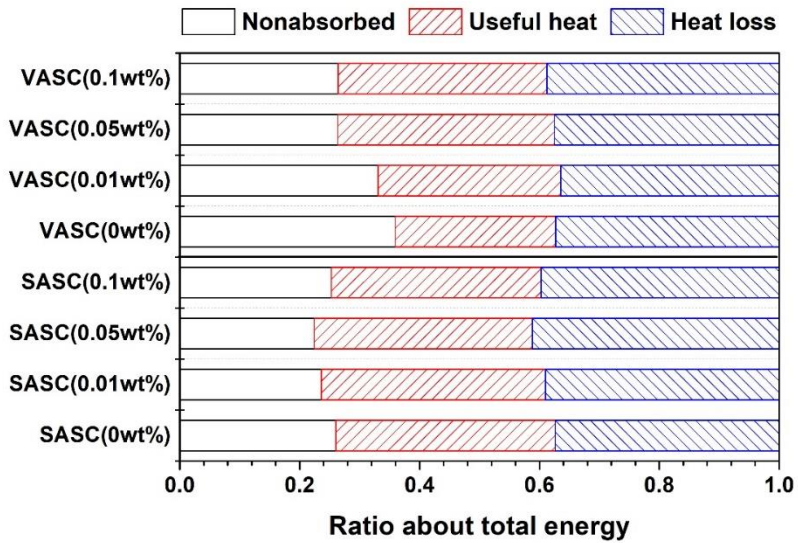


(a)

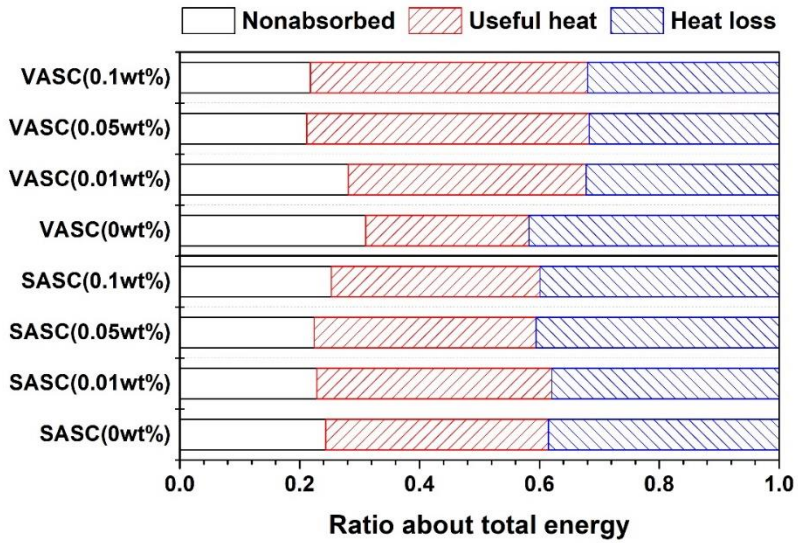


(b)

Fig. 5.5 Useful heat of the VASC according to the inlet temperature; (a) $\dot{m} = 0.0025 \text{ kg/s}$, $\dot{m} = 0.005 \text{ kg/s}$



(a)



(b)

Fig. 5.6 Portion of non-absorbed energy, useful heat, and heat loss in the SASC and VASC; (a)

$\dot{m} = 0.0025 \text{ kg/s}$, $\dot{m} = 0.005 \text{ kg/s}$

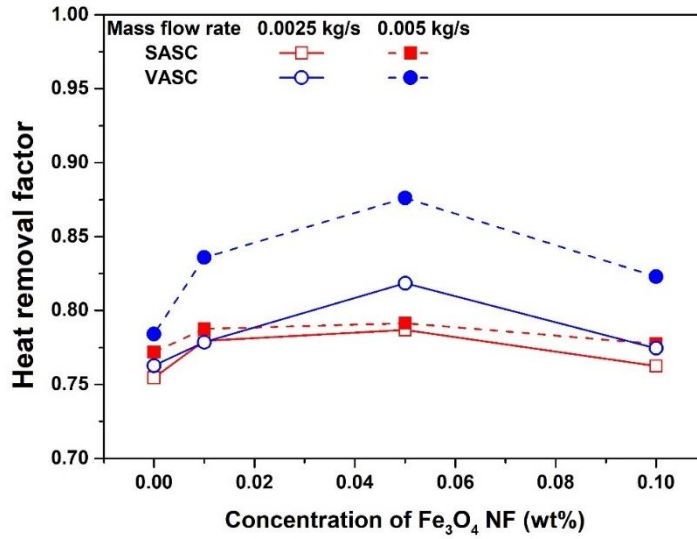


Fig. 5.7 Heat removal factor according to the Fe₃O₄ NF concentration

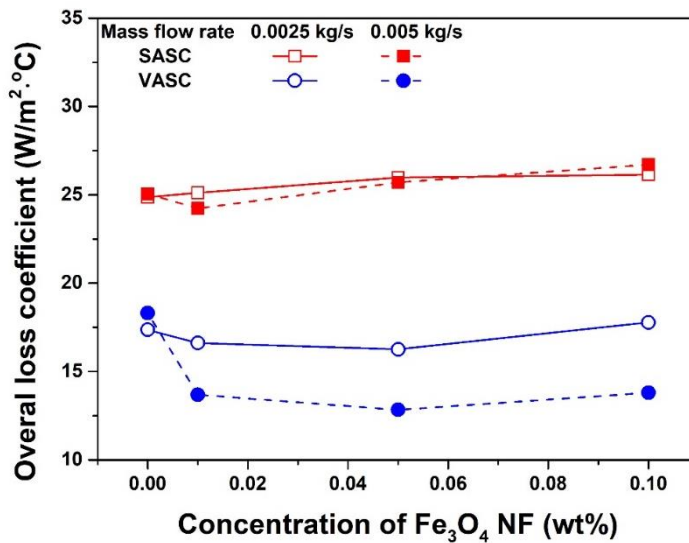


Fig. 5.8 Overall heat loss coefficient according to the Fe₃O₄ NF concentration

5.4.1.2. Comparison of exergy destruction, thermal efficiency, and exergy efficiency between SASC and VASC

Because all heat transfer processes are irreversible, the efficiency of the thermal system can be improved by reducing the irreversibility and minimizing the entropy generated during the process. Fig. 5.9 shows the exergy destruction of the SASC and VASC at a Fe_3O_4 NF concentration of 0.05wt%. In the case of the SASC, the exergy destruction at 0.005 kg/s was higher than that at 0.0025 kg/s. In the SASC, the exergy destruction at 0.0025 and 0.005 kg/s was decreased from 83.47 to 83.25 W and 83.7 to 83.45 W, respectively, when the inlet temperature varied from 40°C to 45°C. And then, the exergy destruction at 0.0025 and 0.005 kg/s was increased to 83.61 and 83.77 W, respectively, when the inlet temperature increased to 55°C. However, the effect of inlet temperature on exergy destruction in the VASC was more seriously affected than in the SASC. Besides, the increase in the mass flow rate in the VASC decreased the exergy destruction, unlike in the case of SASC. At a mass flow rate of 0.0025 kg/s, the exergy destruction in the VASC was similar to that in the SASC. However, at 0.005 kg/s, the exergy destruction decreased from 83.43 to 82.7 W by increasing the inlet temperature from 40°C to 55°C. As the temperature of the working fluid in the solar collector increased, the difference in its temperatures at the inlet and outlet of the solar collector decreased due to the reduction in useful heat gain; thus, the exergy destruction decreased.

The exergy destruction in the SASC and VASC was affected differently by the increase in the Fe_3O_4 NF concentration. In the case of the SASC using Fe_3O_4 NF as the working fluid, the exergy destruction was slightly increased regardless of the mass flow rate. The exergy destruction in the SASC at 0.0025 and 0.005 kg/s increased by 0.1 and 0.14 W, respectively, as the Fe_3O_4 NF concentration was increased from 0 to 0.1wt%. On the other hand, the exergy destruction in the VASC decreased as the Fe_3O_4 NF concentration was increased from 0 to 0.05wt% and then slightly increased at 0.1wt%. The exergy destruction in the VASC at 0.0025 and 0.005 kg/s decreased from 83.91 to 83.32 W and 83.93 to 82.72 W, respectively, as the Fe_3O_4 NF concentration was increased from 0 to 0.05wt%. However, it increased from 83.32 to 83.41 W

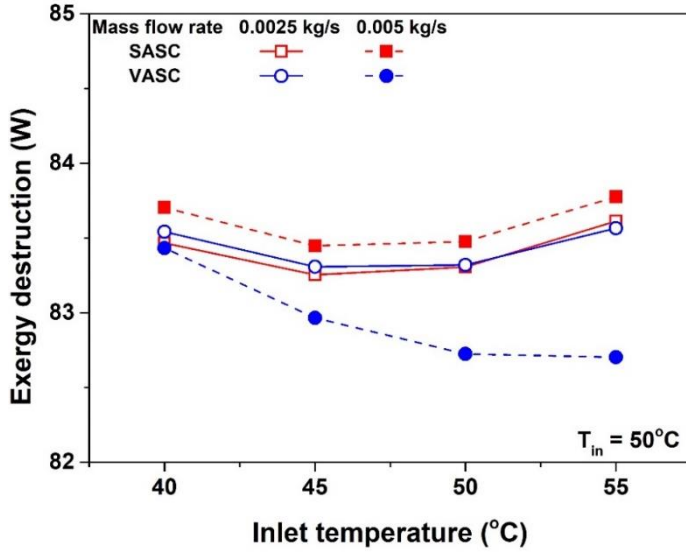
and 82.72 to 82.79 W at 0.0025 and 0.005 kg/s as the Fe_3O_4 NF concentration increased from 0.05wt% to 0.1wt%. In the case of SASC, with an increase in the Fe_3O_4 NF concentration, the exergy destruction increased because the heat lost to the surroundings increased, and the temperature difference between the inlet and outlet of the solar collector decreased. Although the temperature difference between the inlet and outlet increased in the VASC, the heat loss was reduced due to increased absorption of solar energy and reduced heat loss. However, in this study, the heat loss in the VASC increased when the Fe_3O_4 NF concentration exceeded 0.05wt%. Therefore, the exergy destruction in the VASC increased when using 0.05wt% Fe_3O_4 NF.

Fig. 5.9 shows the thermal and exergy efficiency variations in the SASC and VASC. In the SASC, when the Fe_3O_4 NF concentration was 0.1wt%, the thermal efficiencies at 0.0025 and 0.005 kg/s were 0.382 and 0.36, respectively, which were 0.035 and 0.06 lower obtained using water. The exergy efficiency at 0.0025 and 0.005 kg/s reached maximum values of 0.0264 and 0.0267 when the Fe_3O_4 NF concentration was 0.01wt%. However, the exergy efficiency over the concentration of 0.01wt% was decreased to 0.0246 and 0.0236, respectively, which was lower than the water. In the SASC, the increase in Fe_3O_4 NF concentration negatively affected the improvement in the thermal and exergy efficiencies. However, the thermal and exergy efficiencies of the VASC were improved by using the Fe_3O_4 NF, unlike the SASC. The thermal efficiency of the VASC using water at 0.0025 and 0.005 kg/s was 0.252 and 0.289, which was about half the thermal efficiency obtained in the SASC. In the VASC, the thermal efficiency at 0.0025 and 0.005 kg/s was increased from 0.252 to 0.405 and 0.289 to 0.5015, increasing Fe_3O_4 concentration from 0 to 0.1wt%. Also, the exergy efficiency at 0.0025 and 0.005 kg/s was increased from 0.0185 to 0.025 and 0.0183 to 0.035 when the concentration of the Fe_3O_4 was increased from 0 to 0.05wt%. And then, the exergy efficiency at 0.0025 and 0.005 kg/s was slightly decreased to 0.0244 and 0.0317, respectively.

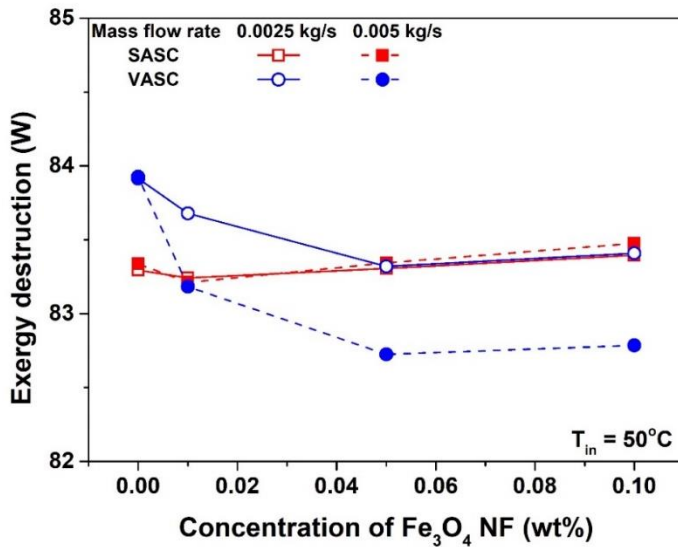
The exergy efficiency at the 0.0025 and 0.005 kg/s was increased from 0.018 to 0.249 and 0.0164 to 0.0252 when the inlet temperature was increased from 40°C to 55°C. The increase in the mass flow rate has little effect on the thermal and exergy efficiency in the SASC. The convective heat transfer is improved under a low concentration of 0.1wt%. However, it was less

sensitive to changing the mass flow rate. The thermal and exergy efficiencies of the VASC were significantly affected by the mass flow rate of the working fluid compared with that of the SASC. In the VASC, the thermal efficiency at 0.0025 and 0.005 kg/s was increased from 0.682 to 0.073 and 0.731 to 0.19. The thermal efficiency at 0.005 kg/s was higher than that at 0.0025 kg/s, and the thermal efficiency difference between 0.0025 and 0.005 kg/s was increased as increasing the inlet temperature. Also, the exergy efficiency of the VASC at 0.005 kg/s was higher than that at 0.0025 kg/s, and the exergy efficiency difference increased with the inlet temperature. When the inlet temperature was 50°C, the exergy efficiencies at 0.0025 and 0.005 kg/s were 0.0244 and 0.0313, respectively. When the inlet temperature of the working fluid was below 50°C, the exergy destruction due to the temperature difference between the inlet and outlet of the solar collector accounted for the largest proportion of the total exergy destruction.

In contrast, the exergy destruction caused by heat lost to the surroundings was relatively small. However, as the inlet temperature of the working fluid was increased, the temperature difference between the inlet and outlet was reduced, and the portion of exergy destruction caused by the temperature difference of the solar collector decreased; in contrast, the exergy destruction by the heat loss increased. The heat loss of the VASC was smaller than that of the SASC. Thus, it was confirmed that the exergy efficiency of the VASC was higher than that of the SASC.

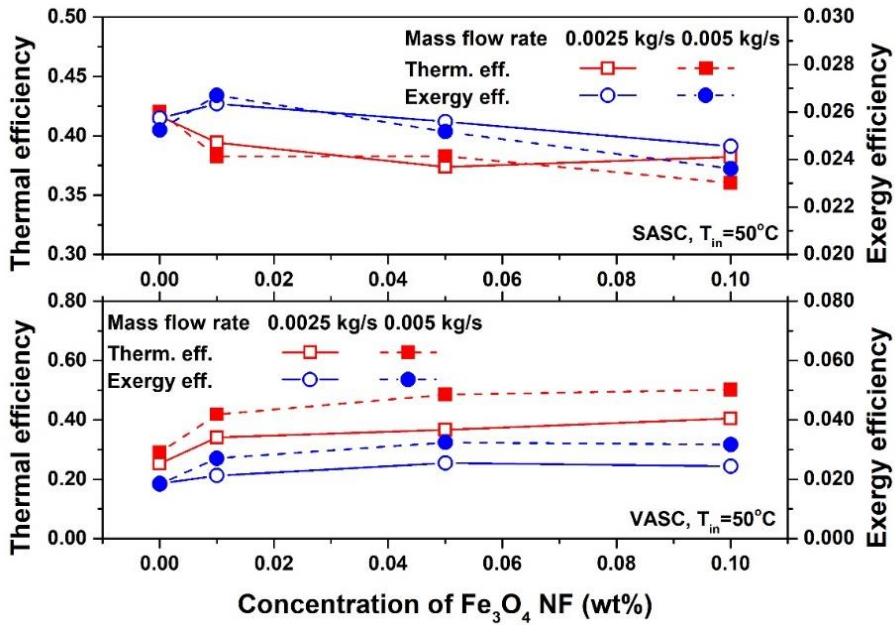


(a)

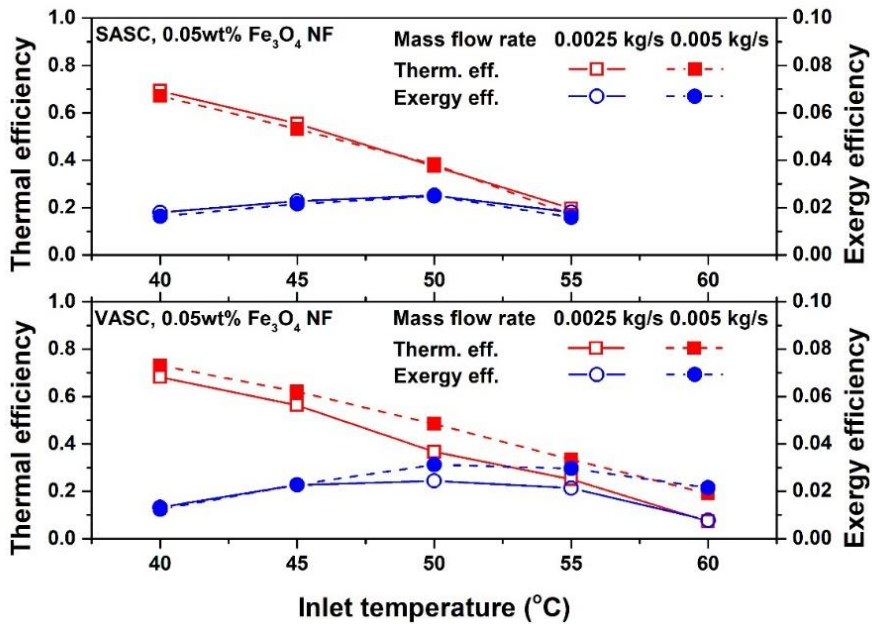


(b)

Fig. 5.9 Exergy destruction of the SASC and VASC; (a) Effect of inlet temperature, (b) Effect of Fe₃O₄ NF concentration



(a)



(b)

Fig. 5.10 Thermal and exergy efficiencies of the SASC and VASC; (a) Effect of inlet temperature, (b) Effect of Fe_3O_4 NF concentration

5.4.2. VASTC with using Fe₃O₄, ATO, and Fe₃O₄/ATO hybrid NF

5.4.2.1. Thermal performance of VASTC using Fe₃O₄, ATO, and Fe₃O₄/ATO hybrid NF

The temperature difference between the inlet and outlet of the VASTC, $\tau\alpha$, F_R , U_L , and LNTD is the main parameters to evaluate the operating performance of the solar collector. Fig. 5.11 shows the temperature difference between the inlet and outlet of the VASTC when using ATO NF. when the volumetric flow rate of water was 0.4, 0.6, and 0.8 lpm, the temperature difference between the inlet and outlet was decreased from 3.6°C to 1.77°C, 2.5°C to 1.3°C and 1.98°C to 1.05°C, respectively, according to the increase of inlet temperature from 40°C to 60°C. As the inlet temperature increased, the temperature difference between the inlet and outlet was high. The improvement of the temperature difference between the inlet and outlet was the best in the concentration of 0.25wt% when using ATO NF. When the volumetric flow rate of 0.25wt% ATO NF was 0.4, 0.6, and 0.8 lpm, the temperature difference between the inlet and outlet was decreased from 4.11°C to 2.41°C, 3.03°C to 1.58°C and 2.17°C to 1.46°C, respectively, according to the increase of inlet temperature from 40°C to 60°C.

Fig. 5.12 shows the temperature difference between the inlet and outlet of the VASTC when using Fe₃O₄ NF. Compared to ATO NF, the temperature difference between the inlet and outlet when using Fe₃O₄ NF in VASTC was smaller, but the improvement effect of the temperature difference between the inlet and outlet was more significant. The temperature difference between the inlet and outlet reached the maximum at 0.075wt% Fe₃O₄ NF, and then the temperature difference between the inlet and outlet of 0.1wt% Fe₃O₄ NF was lower than it of 0.075wt% Fe₃O₄ NF. When the volumetric flow rate of 0.075wt% Fe₃O₄ NF was 0.4, 0.6, and 0.8 lpm, the temperature difference between the inlet and outlet was decreased from 3.83°C to 2.14°C, 2.85°C to 1.67°C and 2.01°C to 0.98°C, respectively, according to the increase of the inlet temperature from 40°C to 60°C. The temperature difference between the inlet and outlet when using ATO NF and Fe₃O₄ NF under critical concentration was increased. However, above the critical

concentration of ATO and Fe₃O₄ NF, the temperature difference between the inlet and outlet was reduced. It was because the optical absorption was improved according to the concentration of the NF, while the optical absorption over critical concentration was decreased due to the reflection. The optical absorption can be improved through mixing because the ATO and Fe₃O₄ NF had excellent optical absorption in different wavelengths, and the temperature difference between the inlet and the outlet when using Fe₃O₄/ATO hybrid NF can be increased.

Fig. 5.13 shows the temperature difference between the inlet and the outlet when using Fe₃O₄/0.1wt% ATO NF%. When the 0.1wt% Fe₃O₄/ATO hybrid NF flowed through the VASCT at 0.4 lpm, the temperature difference between the inlet and the outlet at $m_{\text{Fe}_3\text{O}_4}/m_{\text{Total,NP}} = 0.25$ was higher than others. As the inlet temperature increased from 40 °C to 60 °C, the temperature difference between the inlet and outlet decreased. However, it of $m_{\text{Fe}_3\text{O}_4}/m_{\text{Total,NP}} = 0.25$ was higher than others. When $m_{\text{Fe}_3\text{O}_4}/m_{\text{Total,NP}}$ was 0.25, and the temperature difference between the inlet and outlet was 3.86°C to 2.4°C. It was high compared to 0.1wt% ATO NF and 0.1wt% Fe₃O₄ NF. The improvement of the temperature difference between the inlet and outlet by change of $m_{\text{Fe}_3\text{O}_4}/m_{\text{Total,NP}}$ was similar. When 0.1wt% Fe₃O₄/ATO hybrid NF flowed through the VASTC at 0.4, 0.6, and 0.8 lpm at the inlet temperature of 40°C, the temperature difference between the inlet and outlet was highest at $m_{\text{Fe}_3\text{O}_4}/m_{\text{Total,NP}} = 0.25$. it was increased as $m_{\text{Fe}_3\text{O}_4}/m_{\text{Total,NP}}$ was increased from 0.25 to 1. This means that the thermal performance of the VASTC depends on the optical absorption performance of the NF rather than the volumetric flow rate, and the performance of VASTC can be improved by mixing nanofluids with different optical absorption characteristics for each wavelength.

Fig. 5.14 shows the $\tau\alpha$ of VASTC and the solar weight absorption coefficient according to the concentration of ATO NF, Fe₃O₄ NF and Fe₃O₄/ATO hybrid NF. The optical absorption performance was increased according to the concentration of the NF. However, as explained in Chapter 3, the spectral absorption was different according to the type of NFs. Also, the reflection was increased according to the concentration of the NF. The increase in the concentration of the NF was not always directly related to the improvement of the useful heat. As shown in Fig. 5.14

(a), the $\tau\alpha$ of ATO NF was increased from 0.307 to 0.728 as the concentration of the ATO NF was increased from 0wt% to 0.25wt%. Also, the solar weight absorption coefficient was increased from 0.524 to 0.604 as the concentration of the ATO NF was increased from 0wt% to 0.25wt%. Otherwise, as shown in Fig. 5.14 (b), increasing the concentration of the Fe_3O_4 NF was not directly related to the $\tau\alpha$ of the VASTC and the solar weight absorption coefficient. The $\tau\alpha$ was increased from 0.524 to 0.578 as the concentration of Fe_3O_4 NF increased from 0wt% to 0.075wt%. However, the $\tau\alpha$ was 0.536 at 0.1wt% Fe_3O_4 NF. It was similar to the $\tau\alpha$ of 0.1wt% Fe_3O_4 NF. The solar weight absorption coefficient of the Fe_3O_4 NF was increased from 0.31 to 0.83 as the concentration of the Fe_3O_4 NF increased from 0wt% to 0.05wt%, while it decreased from 0.83 to 0.75 as increasing the concentration of the Fe_3O_4 NF from 0.05wt% to 0.1wt%. When comparing the solar weight absorption coefficient of the ATO NF and the Fe_3O_4 NF, the solar weight absorption coefficient of the Fe_3O_4 NF was higher than the ATO NF. However, in this study, the improvement effect of the $\tau\alpha$ in the Fe_3O_4 NF was lower than in the ATO NF. Maybe, it is due to the halogen lamp used in this experiment. The color temperature of the halogen lamp was 4200 K to make the characteristics of the artificial light source as similar as possible to natural light. Nevertheless, halogen lamps have high energy in the infrared band. Both the ATO NF and the Fe_3O_4 NF have good optical absorption in the infrared band, but as the concentration increases, the amount of energy absorbed by the Fe_3O_4 NF decreases above the critical concentration due to light reflection. Therefore, when the Fe_3O_4 NF was used in the VASTC, the critical concentration of the solar weight absorption coefficient and the $\tau\alpha$ was different. Nevertheless, as shown in Fig. 5.14 (c), it was confirmed that the $\tau\alpha$ of the VASTC was improved by mixing the ATO NF and Fe_3O_4 NF. When $m_{\text{Fe}_3\text{O}_4}/m_{\text{Total,NP}}$ was 0.25 in 0.1wt% $\text{Fe}_3\text{O}_4/\text{ATO}$ hybrid, the $\tau\alpha$ was 0.574, it was higher than other 0.1wt% $\text{Fe}_3\text{O}_4/\text{ATO}$ hybrid NFs. It was confirmed that the $\tau\alpha$ at $m_{\text{Fe}_3\text{O}_4}/m_{\text{Total,NP}} = 0.25$ in 0.1wt% $\text{Fe}_3\text{O}_4/\text{ATO}$ hybrid NFs was 0.01 and 0.04 higher than the 0.1wt% Fe_3O_4 NF and the 0.1wt% ATO NF%. The ATO NF and Fe_3O_4 NF are good in optical absorption in infrared and visible light bands, respectively, and insufficient optical absorption by wavelength can be improved through an appropriate mixing

ratio. The heat transfer and the heat loss in the VASTC were affected because the improvement of optical absorption changed the thermal environment of the VASTC by increasing the concentration of NF.

Fig. 5.15 shows the F_R and the U_L of ATO NF, Fe_3O_4 NF and Fe_3O_4 /ATO hybrid NF according to the concentration of NF. Fig. 5.15 (a) shows the F_R and U_L parameters when using ATO NF. When the volumetric flow rate was 0.4 lpm, the F_R was decreased according to the increase of the ATO NF. However, when the volumetric flow rate was 0.6 and 0.8 lpm, the F_R increased as the concentration of ATO NF increased from 0wt% to 0.1wt%. Whereas the F_R was decreased as the concentration of ATO NF was increased from 0.1wt% to 0.25wt%. When 0.1wt% ATO NF flowed at 0.4, 0.6, and 0.8 lpm, the F_R was 0.709, 0.805, and 0.985, respectively. The U_L was the minimum at the concentration of 0.1wt% ATO NF, and the U_L was decreased according to the concentration of the ATO NF from 0.1wt% to 0.25wt%. When the concentration of the 0.1wt% ATO NF, the U_L at 0.4, 0.6, and 0.8 lpm was 9.38, 8.5, and 8.97 $W/m^2 \cdot ^\circ C$, respectively. When the Fe_3O_4 NF was used in VASTC, it was also confirmed that the F_R was increased, while U_L was decreased. The effect of the concentration of Fe_3O_4 NF was also different. Fig. 5.15 (b) shows the F_R and U_L using the Fe_3O_4 NF. The U_L reached a minimum at the concentration of 0.025wt%, and then it was increased. Whereas the concentration of the F_R reaching the maximum value was different in the Fe_3O_4 NF. When the Fe_3O_4 NF flowed through the VASTC at 0.4 lpm, the F_R decreased from 0.74 to 0.712 according to the concentration increase from 0wt% to 0.05wt%, while it was increased from 0.712 to 0.737 when the concentration increased from 0.05wt% to 0.1wt%. Whereas, when the volumetric flow rate was 0.6 lpm, the F_R increased from 0.785 to 0.801 with the concentration increase from 0wt% to 0.05wt%, and then it decreased above the concentration of 0.05wt%. When the volumetric flow rate was 0.8 lpm, the F_R increased from 0.809 to 0.851 according to the increase of the Fe_3O_4 NF from 0wt% to 0.075% and then decreased above the concentration of 0.075wt%. Unlike the F_R , the U_L was the minimum at the concentration of 0.025wt% Fe_3O_4 NF, and then it was increased above the concentration of the 0.025wt% Fe_3O_4 NF. When the concentration of the Fe_3O_4 NF was 0.025wt%, the U_L of the volumetric flow rate with 0.4, 0.6, and 0.8 lpm was 9.13 $W/m^2 \cdot ^\circ C$,

8.98 W/m²·°C, and 8.83 W/m²·°C respectively. The F_R and U_L were related to the internal heat transfer and the heat loss in the VASTC. The temperature distribution and the convective heat transfer in the receiver, and the optical absorption were affected by the concentration and the volumetric flow rate of the NF. The F_R and the U_L were also affected by them. The increase of the NF increased the optical absorption performance. Because the optical absorption characteristics of the ATO NF and the Fe₃O₄ NF were different, the improvement influent on the F_R and U_L was also different. As the concentration of the NF was increased, the optical absorption near the surface of the receiver was intensively performed, and the U_L was increased due to local heating near the surface of the receiver. Otherwise, the U_L was decreased by the increase of the volumetric flow rate due to increased thermal capacity. The F_R is a parameter that converts the solar energy absorbed by the STC into thermal energy, and it is affected by the heat loss and optical absorption characteristics. In the case of the ATO NF, the $\tau\alpha$ was continually increased with the increase of concentration from 0wt% to 0.25wt%. The U_L decreased by increasing the concentration from 0wt% to 0.1wt%, while it increased above the concentration of 0.1wt%. Therefore, the F_R was increased by the increase of concentration. However, at the volumetric flow rate of 0.4 lpm, the F_R was decreased because the reduction of U_L was insufficient, although the $\tau\alpha$ was increased. Therefore, the F_R was increased by increasing the concentration of the ATO NF. In the case of Fe₃O₄ NF, as shown in Fig. 3.9, the optical absorption performance is better than that of ATO nanofluid, while the optical depth is short. The effect on the reduction of the U_L is noticeable at low concentrations compared to ATO nanofluid, but The F_R was decreased by increased heat loss due to the increased optical absorption performance by increasing the concentration of Fe₃O₄ and increased reflection.

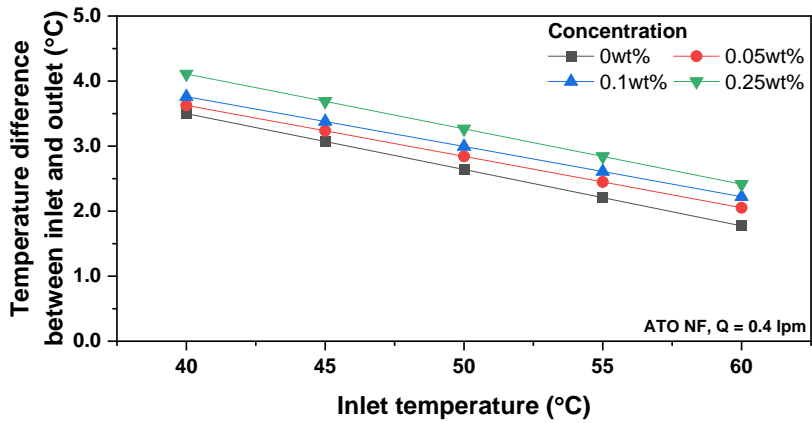
In the 0.1wt% Fe₃O₄/ATO hybrid NF, the F_R at $m_{Fe_3O_4}/m_{Total,NP} = 0.25$ was higher than others and it was decreased as the $m_{Fe_3O_4}/m_{Total,NP}$ was increased from 0.25 to 1. When the $m_{Fe_3O_4}/m_{Total,NP}$ was 0.25, the F_R at the volumetric flow rate was 0.4, 0.6 and 0.8 lpm was 0.75, 0.858 and 0.898, respectively. When the $m_{Fe_3O_4}/m_{Total,NP}=0.25$ in the Fe₃O₄/ATO hybrid NF, the F_R at the volumetric flow rate of 0.4 lpm and 0.6 lpm was increased by 6% and 7%. But the

F_R was decreased by 8.8% at the volumetric flow rate of 0.8 lpm. In 0.1wt% Fe_3O_4 /ATO hybrid NF, the U_L was minimum at $m_{Fe_3O_4}/m_{Total,NP}=0.25$. When the $m_{Fe_3O_4}/m_{Total,NP}$ was 0.25 in 0.1wt% Fe_3O_4 /ATO hybrid NF, the U_L at the volumetric flow rate of 0.4, 0.6, and 0.8 lpm was $0.42 \text{ W/m}^2 \cdot ^\circ\text{C}$, $8.06 \text{ W/m}^2 \cdot ^\circ\text{C}$, $8.01 \text{ W/m}^2 \cdot ^\circ\text{C}$, respectively, and these values were lower by 10.1%, 5.1%, and 10.7%, respectively compared to that of 0.1wt% ATO NF%. However, the U_L was increased at the $m_{Fe_3O_4}/m_{Total,NP}$ was increased from 0.25 to 1. It is because the thermal environment of the receiver was affected by the variation of the $m_{Fe_3O_4}/m_{Total,NP}$. In the case of ATO NF, the optical absorption performance in the near-infrared band is excellent, but the optical absorption in the visible light band is not good. On the other hand, Fe_3O_4 NF has excellent optical absorption performance in the visible light band compared to ATO nanofluid, but their optical absorption performance in the near-infrared band is not good. Moreover, as the concentration of Fe_3O_4 NF increases, the optical reflection increases rapidly in the visible band with ultraviolet rays and short wavelengths. Therefore, the optical absorption of the Fe_3O_4 /ATO hybrid NF can be improved by adding a small amount of Fe_3O_4 NF to the ATO NF. When the portion of the ATO NF was higher than the Fe_3O_4 NF in the Fe_3O_4 /ATO hybrid NF as shown in Fig. 5.14, the optical absorption was improved. Also, because of the uniform temperature distribution at the receiver, the F_R was increased while the U_L was decreased by the increase of the $m_{Fe_3O_4}/m_{Total,NP}$ of the Fe_3O_4 /ATO hybrid NF. However, the improvement of F_R and U_L of the Fe_3O_4 /ATO hybrid NF was insignificant when the $m_{Fe_3O_4}/m_{Total,NP}$ was from 0.25 to 1 because the presence of small amount of Fe_3O_4 NPs compensated for the insufficient optical performance of ATO NF in the visible band.

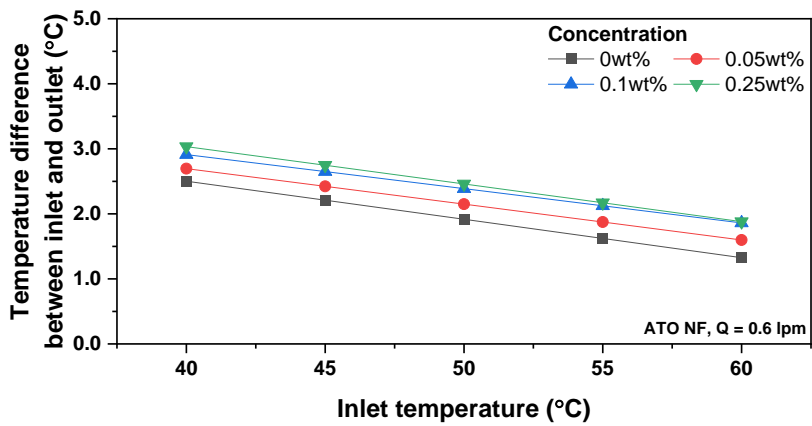
In the VASTC, the $\tau\alpha$ and the U_L is an important parameter to decide the thermal efficiency and the operating temperature range. Fig. 5.16 shows the $\left(\frac{(\tau\alpha)_{nf}}{(\tau\alpha)_w}\right)/\left(\frac{(U_L)_{nf}}{(U_L)_w}\right)$ and LNTD according to the concentration of the ATO NF, Fe_3O_4 NF, and Fe_3O_4 /ATO hybrid NF. As shown in Fig. 5.16 (a), the $\left(\frac{(\tau\alpha)_{nf}}{(\tau\alpha)_w}\right)/\left(\frac{(U_L)_{nf}}{(U_L)_w}\right)$ and LNTD was increased with an increasing of the concentration of the ATO NF from 0wt% to 0.1wt%, while those were decreased above 0.1wt%. At ATO NF

concentration of 0.1wt%, the $\left(\frac{\tau\alpha_{nf}}{\tau\alpha_w}\right)/\left(\frac{(U_L)_{nf}}{(U_L)_w}\right)$ and the LNTD was higher than others. When 0.1wt% ATO NF was used in the VASTC at 0.4, 0.6, and 0.8 lpm, the $\left(\frac{\tau\alpha_{nf}}{\tau\alpha_w}\right)/\left(\frac{(U_L)_{nf}}{(U_L)_w}\right)$ was 1.16, 1.23 and 1.16 and the LNTD was 0.06, 0.066 and 0.068, respectively. The LNTD of 0.1wt% ATO at 0.4, 0.6, and 0.8 lpm was 1.15, 1.23, and 1.24 times higher than that of water. The $\left(\frac{\tau\alpha_{nf}}{\tau\alpha_w}\right)/\left(\frac{(U_L)_{nf}}{(U_L)_w}\right)$ and the LNTD were also improved when the Fe₃O₄ NF was used in VASTC. However, the improvement effect on the $\left(\frac{\tau\alpha_{nf}}{\tau\alpha_w}\right)/\left(\frac{(U_L)_{nf}}{(U_L)_w}\right)$ and the LNTD by using the Fe₃O₄ NF was lower than those using ATO NF. When the concentration of the Fe₃O₄ NF was 0.05wt%, the maximum $\left(\frac{\tau\alpha_{nf}}{\tau\alpha_w}\right)/\left(\frac{(U_L)_{nf}}{(U_L)_w}\right)$ at the volumetric flow rate with 0.4 and 0.6 lpm was 1.14 and 1.15, respectively. Whereas, the maximum $\left(\frac{\tau\alpha_{nf}}{\tau\alpha_w}\right)/\left(\frac{(U_L)_{nf}}{(U_L)_w}\right)$ at the volumetric flow rate with 0.8 lpm was 1.12 when the concentration of the Fe₃O₄ NF was 0.025wt%. when the using Fe₃O₄ NF, the LNTD was also reaching the maximum value at the critical concentration, and then it was decreased as the variation of $\left(\frac{\tau\alpha_{nf}}{\tau\alpha_w}\right)/\left(\frac{(U_L)_{nf}}{(U_L)_w}\right)$. When the concentration of the Fe₃O₄ NF was 0.05wt%, the maximum LNTD at the volumetric flow rate of 0.4 lpm and the 0.6 lpm was 0.059 and 0.062. The maximum LNTD at the volumetric flow rate of 0.8 lpm was 0.061 when the concentration of the Fe₃O₄ NF was 0.1wt%. Fig. 5.16 (c) shows $\left(\frac{\tau\alpha_{nf}}{\tau\alpha_w}\right)/\left(\frac{(U_L)_{nf}}{(U_L)_w}\right)$ and the LNTD according to the $m_{Fe_3O_4}/m_{Total,NP}$ of the 0.1wt% Fe₃O₄/ATO hybrid NF. When the $m_{Fe_3O_4}/m_{Total,NP}$ was 0.25 in the 0.1 wt% Fe₃O₄/ATO hybrid NF, the $\left(\frac{\tau\alpha_{nf}}{\tau\alpha_w}\right)/\left(\frac{(U_L)_{nf}}{(U_L)_w}\right)$ and the LNTD was higher than other $m_{Fe_3O_4}/m_{Total,NP}$ conditions. The $\left(\frac{\tau\alpha_{nf}}{\tau\alpha_w}\right)/\left(\frac{(U_L)_{nf}}{(U_L)_w}\right)$ at the volumetric flow rate at 0.4, 0.6 and 0.8 lpm was 1.31, 1.32 and 1.32, respectively, when the $m_{Fe_3O_4}/m_{Total,NP}$ was 0.25. Among them, $\left(\frac{\tau\alpha_{nf}}{\tau\alpha_w}\right)/\left(\frac{(U_L)_{nf}}{(U_L)_w}\right)$ at the volumetric flow rate at 0.4 and 0.6 lpm in the 0.1wt% Fe₃O₄/ATO hybrid was higher than 0.1wt% ATO NF and the 0.1wt% Fe₃O₄ NF. The LNTD at the volumetric flow rate at 0.4, 0.6, and 0.8 lpm was 0.064, 0.067, and 0.0674 when the 0.1wt% Fe₃O₄/ATO hybrid NF with $m_{Fe_3O_4}/m_{Total,NP}$ of 0.25 flowed through

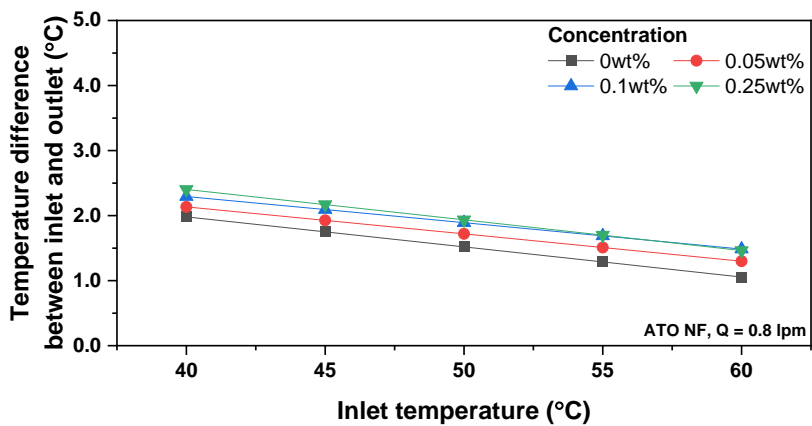
the VASTC. When the volumetric flow rate was 0.4 lpm and 0.6 lpm among LNTDs of the 0.1wt% Fe₃O₄/ATO hybrid NF with $m_{\text{Fe}_3\text{O}_4}/m_{\text{Total,NP}}$, LNTDs was higher than that of 0.1wt% ATO NF and the 0.1wt% Fe₃O₄ NF. As mentioned above, the thermal performance of the VASTC can be increased by improving the optical absorption performance due to the enhanced thermal environment in the VASTC, and it can be more improved by mixing the NFs.



(a)



(b)



(c)

Fig. 5.11 Temperature difference of ATO NF between inlet and outlet; (a) Q = 0.4 lpm, (b) Q = 0.6 lpm, (c) Q = 0.8 lpm

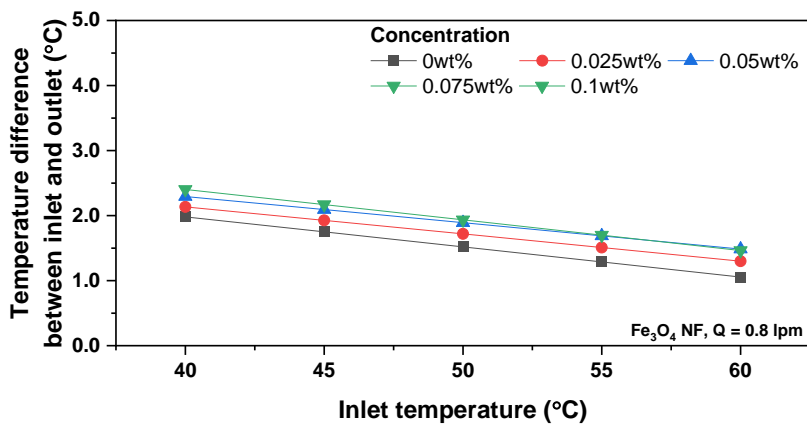
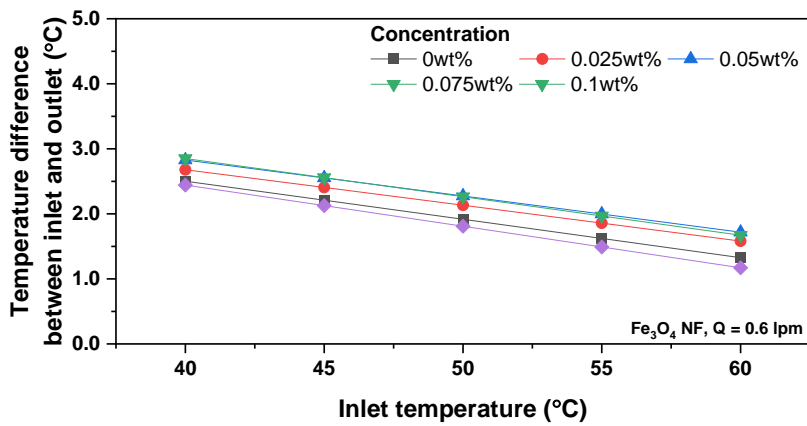
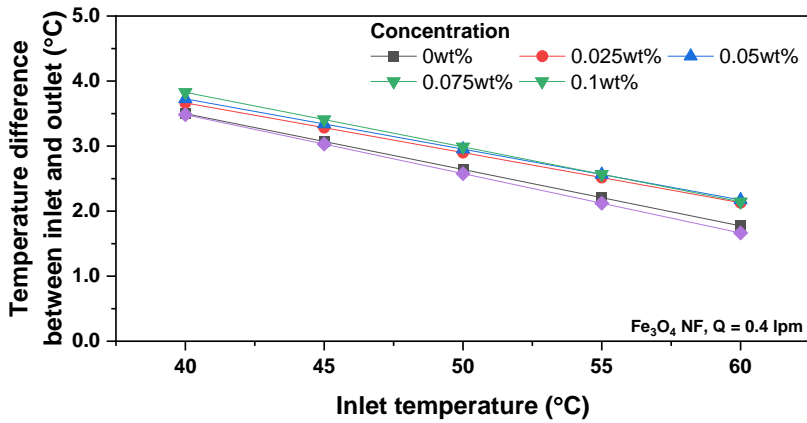
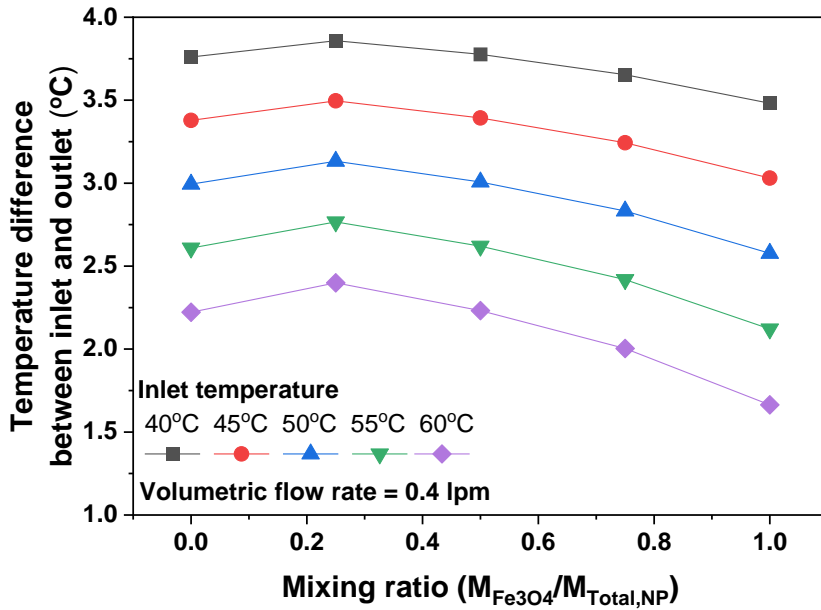
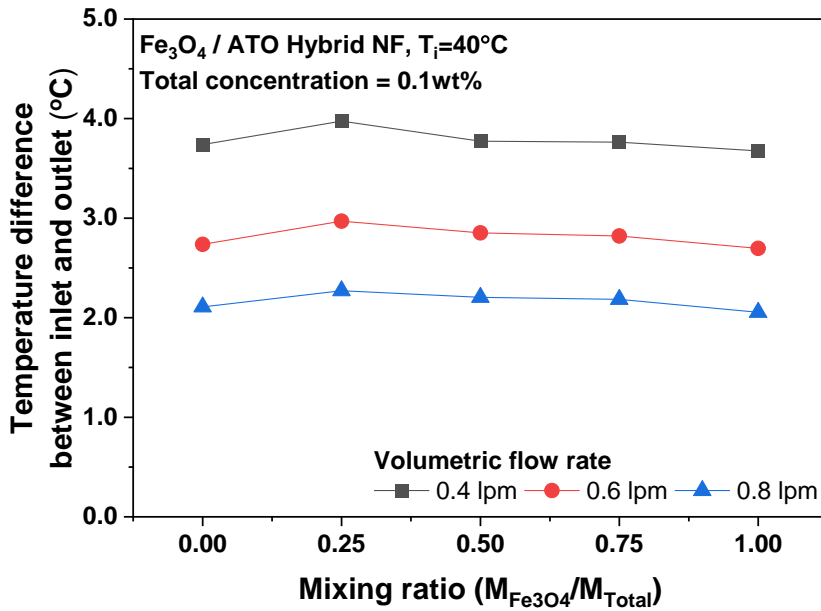


Fig. 5.12 Temperature difference of Fe_3O_4 NF between inlet and outlet; (a) $Q = 0.4$ lpm, (b) $Q = 0.6$ lpm, (c) $Q = 0.8$ lpm

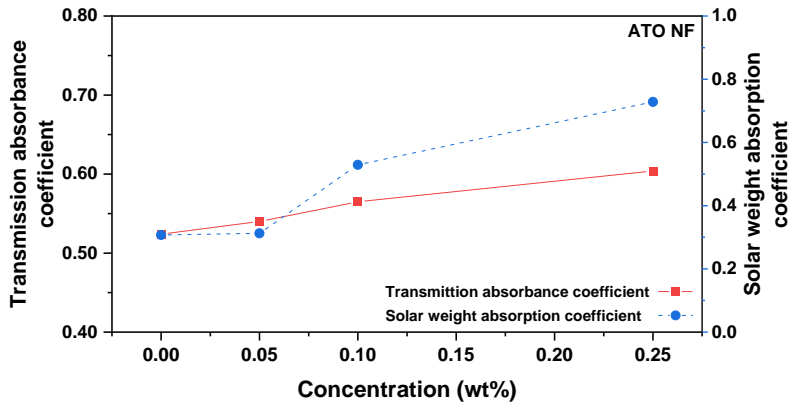


(a)

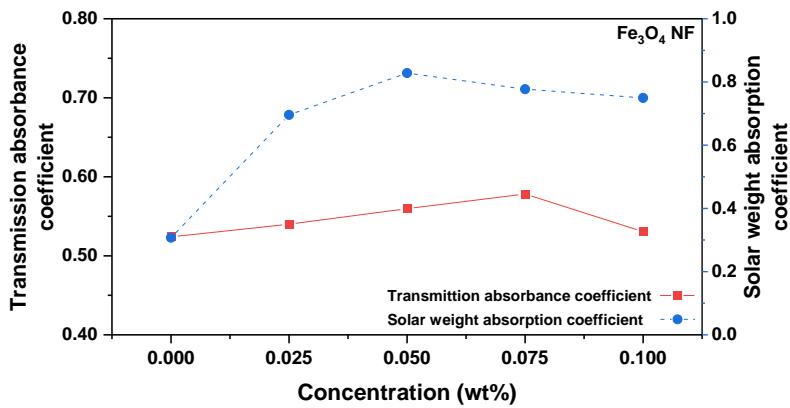


(b)

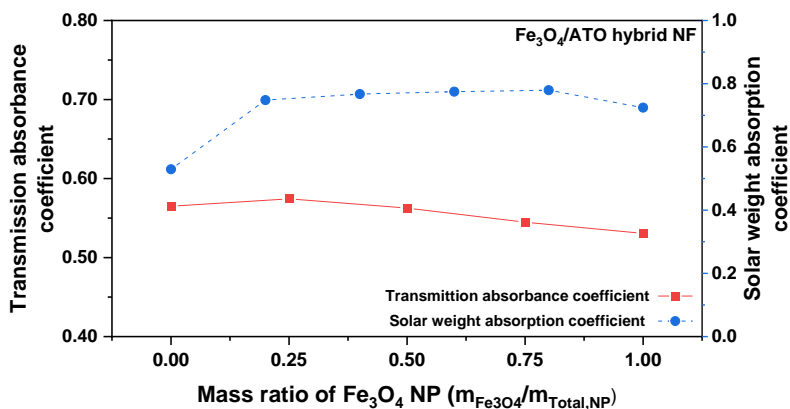
Fig. 5.13 Temperature difference of Fe_3O_4 /ATO hybrid NF between inlet and outlet; (a) $Q = 0.4$ lpm, (b) $Q = 0.6$ lpm, (c) $Q = 0.8$ lpm



(a) ATO NF

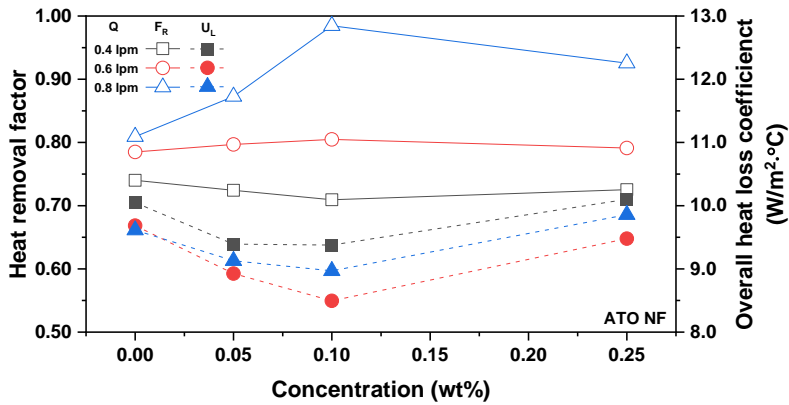


(b) Fe₃O₄ NF

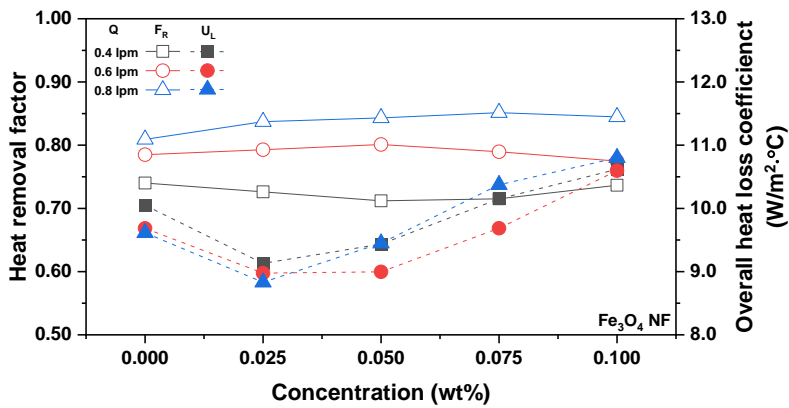


(c) Fe₃O₄/ATO hybrid NF

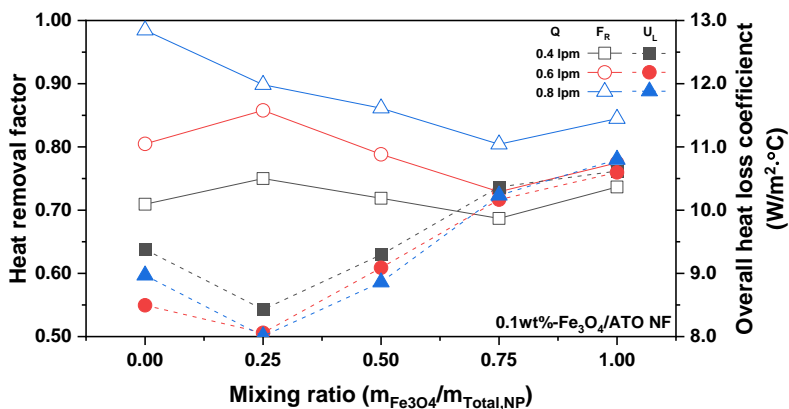
Fig. 5.14 Comparison with transmission absorbance coefficient and solar weight absorption coefficient according to the concentration of NF



(a) ATO NF

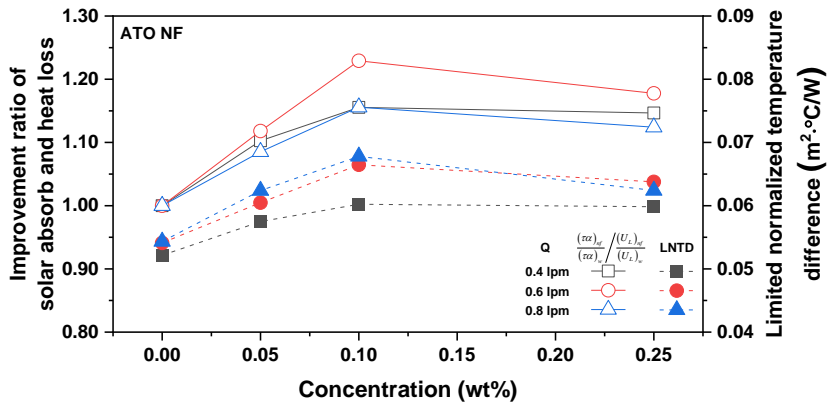


(b) Fe₃O₄ NF

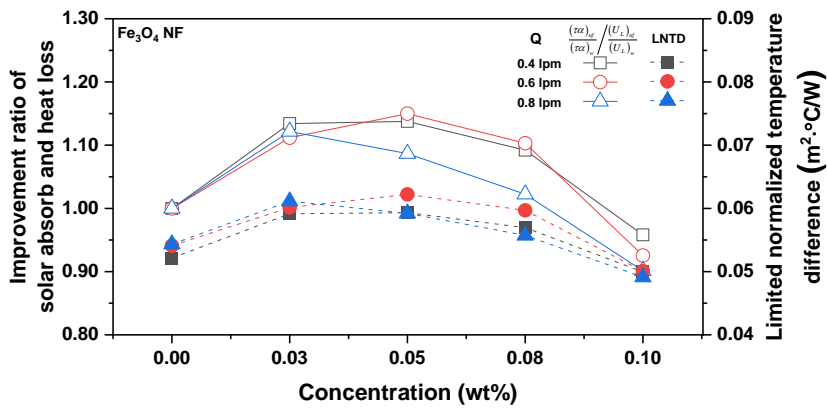


(c) Fe₃O₄/ATO hybrid NF

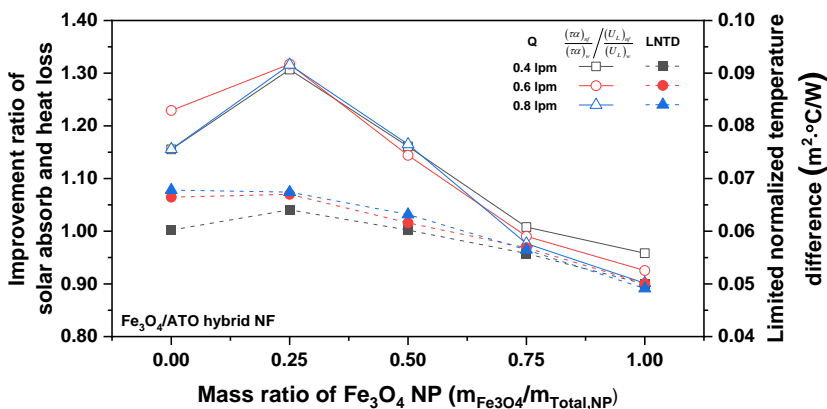
Fig. 5.15 Comparison with heat removal factor and overall loss coefficient according to the concentration of NF



(a) ATO NF



(b) Fe₃O₄ NF



(c) Fe₃O₄/ATO hybrid NF

Fig. 5.16 Comparison with improvement ratio of solar absorb and heat loss and LNTD according to concentration of NF

5.4.2.2. Thermal and exergy efficiency of VASC using Fe₃O₄, ATO, and Fe₃O₄/ATO hybrid NF

The efficiency of the solar collector decreased as the inlet temperature increased due to heat loss from the temperature difference between the solar collector and its surroundings. However, it is necessary to consider both the thermal and exergy efficiency of VASTC using ATO, Fe₃O₄, and Fe₃O₄/ATO hybrid NF because the irreversibility during the optical absorption process was different to the operating condition. Fig. 5.17 shows the thermal and exergy efficiency of ATO NF. The thermal efficiency of VASC using ATO NF decreased as the inlet temperature increased. When the volumetric flow rate was 0.6 lpm, the thermal efficiency of VASC was best when the ATO NF concentration was 0.25wt%. As the inlet temperature increased from 40°C to 60°C, the thermal efficiency of VASC using 0.25wt% ATO NF decreased from 0.388 to 0.238.

The efficiency was about 1.21–1.42 times higher than that of water. The exergy efficiency of VASC using ATO NF increased from 40°C to 55°C inlet temperatures but decreased when the inlet temperature was higher than 55°C. The exergy efficiency was highest at 0.25wt%, and the maximum exergy efficiency was 0.093, which was 1.07 times higher than that of water. The increase in volumetric flow rate also affected the thermal and exergy efficiencies of VASC. The thermal and exergy efficiencies of the ATO NF were improved by increasing the concentration of the NF and increasing the volumetric flow rate. When the inlet temperature was 55°C, the ATO NF had the best thermal and energy efficiencies at the NF concentration of 0.25wt%. As the volumetric flow rate of 0.25wt% ATO NF increased from 0.4 lpm to 0.8 lpm, the thermal efficiency increased from 0.241 to 0.287, showing an improvement of 1.29–1.32 times compared to water. The exergy efficiency of 0.25wt% ATO NF was increased to 0.091–0.094 as the volumetric flow rate increased from 0.4 lpm to 0.8 lpm, showing about a 1.06–1.07 improvement.

As the concentration of the NF was increased below the critical concentration, the $\tau\alpha$ of the VASTC can be increased, and the U_L can be decreased. The exergy efficiency can be improved due to the reduced irreversibility by improving the optical absorption and the decrease of the heat loss. Fig. 5.18 shows the thermal and exergy efficiency of Fe₃O₄ NFs. When the volumetric flow

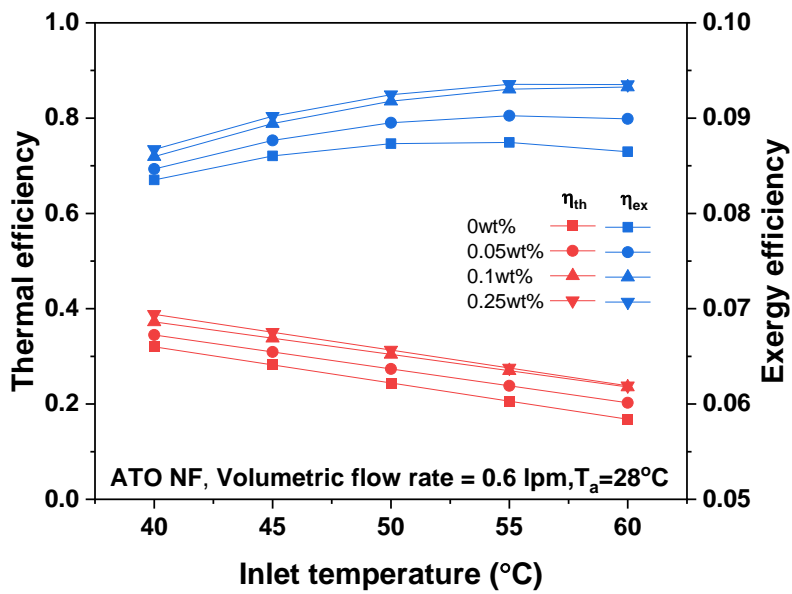
rate was 0.6 lpm, the 0.075wt% Fe_3O_4 NF had higher thermal efficiency than that of the 0.05wt% Fe_3O_4 NF at the inlet temperature of 40°C-45°C. At the inlet temperature of 40°C, thermal efficiencies of 0.05wt% Fe_3O_4 and 0.075wt% Fe_3O_4 NFs were 0.362 and 0.365, respectively. However, as the inlet temperature continued to increase, the thermal efficiency of the 0.05wt% Fe_3O_4 NF was higher than that of the 0.075wt% Fe_3O_4 NF. When the inlet temperature was 55°C, the thermal efficiency of 0.05wt% Fe_3O_4 NF was 0.253. However, 0.1wt% Fe_3O_4 NF showed lower thermal efficiency than water at the inlet temperature from 40 to 60°C. This meant that the increase in the concentration of Fe_3O_4 NF was not directly related to the improvement in the thermal and exergy efficiencies of VASC. As shown in Fig. 3.8, when the Fe_3O_4 NF concentration exceeded 0.05wt%, light reflection occurred from the ultraviolet band, and the wavelength band of light reflection increased as the concentration increased. Accordingly, an excessive concentration of the Fe_3O_4 NF may adversely affect the improvement in the thermal and exergy efficiencies. When Fe_3O_4 NF flew into VASC at 55°C, the thermal and exergy efficiencies were the highest when the concentration of Fe_3O_4 NF was 0.05wt%. When the volumetric flow rates were 0.4, 0.6, and 0.8 lpm, the thermal efficiencies were 0.217, 0.254, and 0.257, showing an improvement of 1.16, 1.23, and 1.18 times, respectively, compared to water. The exergy efficiency of 0.05wt% Fe_3O_4 NF was 0.089-0.091, which was improved by 1.05-1.07 times compared to water. As the working fluid for VASC, Fe_3O_4 NF had lower thermal and exergy efficiencies than ATO NF. In the improvement in the optical absorption according to the concentration increase, Fe_3O_4 NF was superior to ATO NF. However, the reflectance of Fe_3O_4 NF was increased, unlike ATO NF. Accordingly, when the Fe_3O_4 NF was used, the thermal and exergy efficiency of the VASTC may be improved at a low concentration, but when the ATO NF was used, the thermal and exergy efficiency of the VASTC was higher at a critical concentration.

The optical absorption performance can be improved by mixing Fe_3O_4 and the ATO NF because Fe_3O_4 and the ATO NF have different optical absorption bands. The improvement can be confirmed by analyzing the thermal and exergy efficiency of the VASTC using Fe_3O_4 /ATO hybrid NF. Fig. 5.19 shows the thermal and exergy efficiency of the VASTC using 0.1wt%

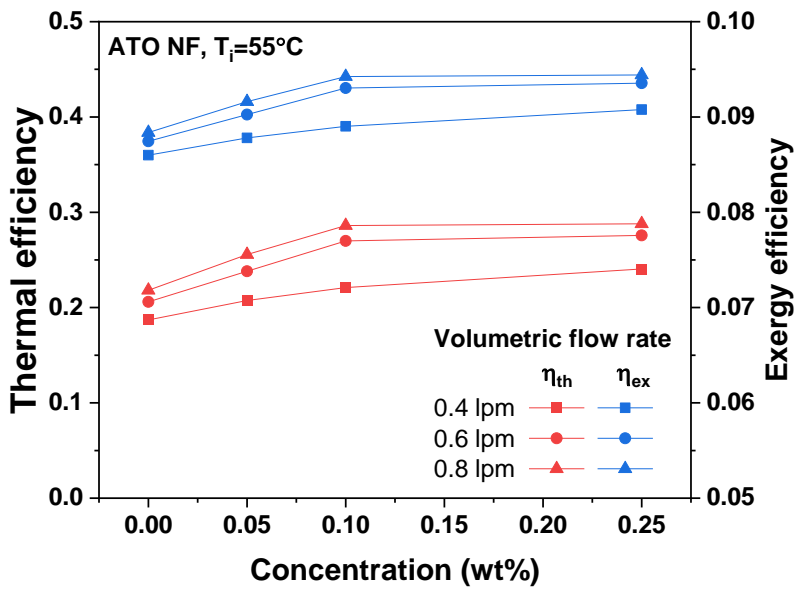
Fe₃O₄/ATO hybrid NF. The exergy efficiency for different inlet temperatures in the VASTC is depicted in Fig. 5.19 (a). The exergy efficiency was the maximum at an inlet temperature of 55°C. In the inlet temperature of 55°C, at the exergy efficiency of $m_{\text{Fe}_3\text{O}_4}/m_{\text{Total,NP}} = 0.25, 0.5$ and 0.75 in Fe₃O₄/ATO hybrid NF of total concentration with 0.1wt%, the thermal efficiency was 0.277, 0.248 and 0.221 and the exergy efficiency was 0.0936, 0.0911 and 0.0888, respectively. The thermal and exergy efficiency of 0.1wt% ATO NF was 0.27 and 0.093. When $m_{\text{Fe}_3\text{O}_4}/m_{\text{Total,NP}}$ The Fe₃O₄/ATO hybrid NF at $m_{\text{Fe}_3\text{O}_4}/m_{\text{Total,NP}} = 0.25$ confirmed that the thermal and exergy efficiency was improved more than that of 1wt% ATO NF and Fe₃O₄ NF. However, when $m_{\text{Fe}_3\text{O}_4}/m_{\text{Total,NP}}$ was 0.5 and 0.75 in Fe₃O₄/ATO hybrid NF of total concentration with 0.1wt%, the thermal and exergy efficiency of Fe₃O₄/ATO hybrid NFs was improved more than that of 0.1wt% Fe₃O₄ NF, while it was lower than that of ATO NF. It was because the optical absorption performance of the ATO and Fe₃O₄ NF is different according to the wavelength and concentration. The ATO NF has a low optical absorption improvement according to the concentration compared to the Fe₃O₄ NF. If the mixing ratio of Fe₃O₄ NF in the Fe₃O₄/ATO hybrid NF was high, the optical absorption improvement was insignificant. Therefore, the ratio of ATO NF should be high in the Fe₃O₄/ATO hybrid NF to improve the performance of VASTC.

An increased volumetric flow rate increases the thermal and exergy efficiency. The thermal and exergy efficiency of 0.1wt% Fe₃O₄/ATO hybrid NF was increased as the volumetric flow rate was increased from 0.4 to 0.8 lpm. As shown in Fig. 5.19 (b), the thermal and exergy efficiency was higher at $m_{\text{Fe}_3\text{O}_4}/m_{\text{Total,NP}} = 0.25$ than other $m_{\text{Fe}_3\text{O}_4}/m_{\text{Total,NP}}$ conditions when the volumetric flow rate of 0.1wt% Fe₃O₄/ATO hybrid NF was 0.4 and 0.6 lpm. When the volumetric flow rate of the 0.1wt% Fe₃O₄/ATO hybrid NF was 0.8 lpm, the thermal and exergy efficiency was higher at $m_{\text{Fe}_3\text{O}_4}/m_{\text{Total,NP}} = 0.5$, but the thermal and exergy efficiency of $m_{\text{Fe}_3\text{O}_4}/m_{\text{Total,NP}} = 0.25$ was similar to $m_{\text{Fe}_3\text{O}_4}/m_{\text{Total,NP}} = 0.5$. At the inlet temperature of 55, when the volumetric flow rate was 0.4, 0.6, and 0.8 lpm, the thermal efficiency of $m_{\text{Fe}_3\text{O}_4}/m_{\text{Total,NP}} = 0.25, 0.5$ and 0.75 in 0.1wt% Fe₃O₄/ATO hybrid NF was 0.234, 0.277 and

0.284, respectively. In same condition, the exergy efficiency of $m_{\text{Fe}_3\text{O}_4}/m_{\text{Total,NP}} = 0.25, 0.5$ and 0.75 in $0.1\text{wt}\%$ $\text{Fe}_3\text{O}_4/\text{ATO}$ hybrid NF was 0.0902, 0.0936 and 0.094, respectively. The thermal and exergy efficiency can be improved by increasing the volumetric flow rate owing to reduced heat loss and enhanced convective heat transfer in the receiver. In the $\text{Fe}_3\text{O}_4/\text{ATO}$ hybrid NF, the thermal and exergy efficiency can be increased by improved optical absorption performance and decreased heat loss by increased volumetric flow rate. From this, it is determined that the thermal and exergy efficiency of VASTC can be improved when $\text{Fe}_3\text{O}_4/\text{ATO}$ hybrid NF is manufactured with an appropriate mixing ratio.

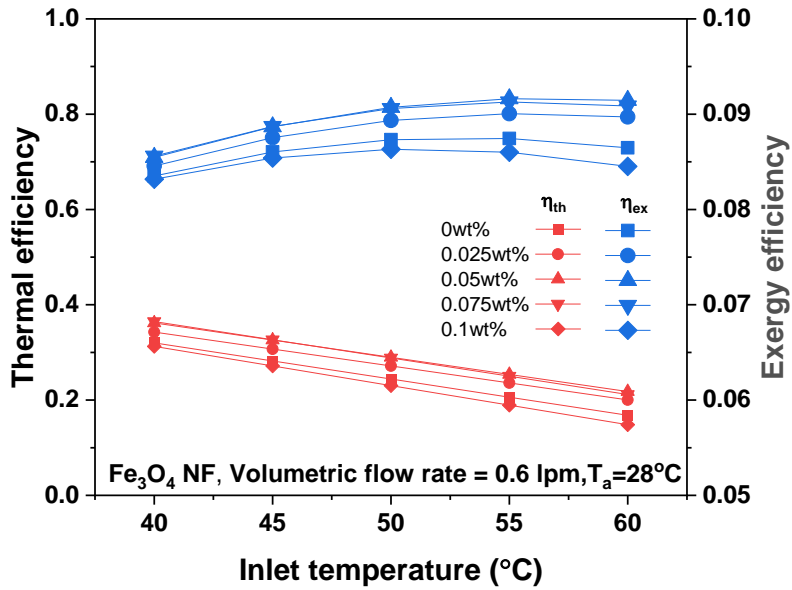


(a)

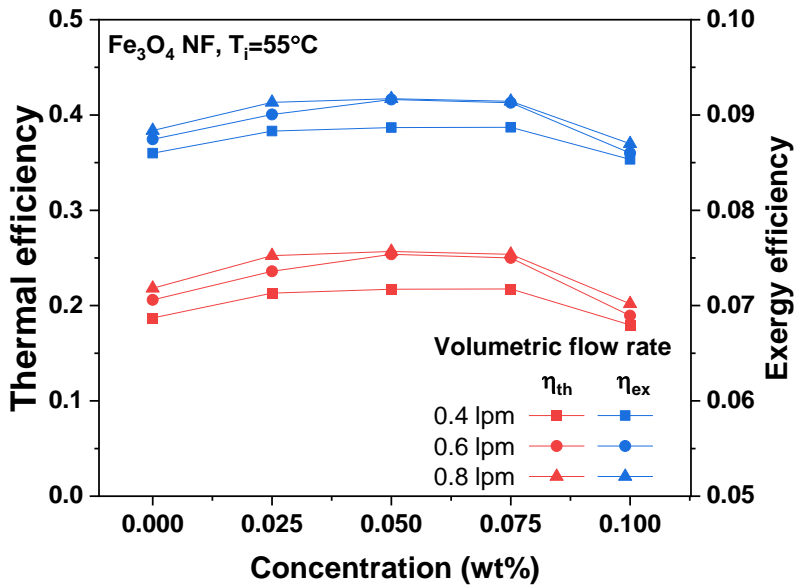


(b)

Fig. 5.17 Exergy efficiency of VASC using ATO NF; (a) Concentration effect, (b) Volumetric flow rate effect

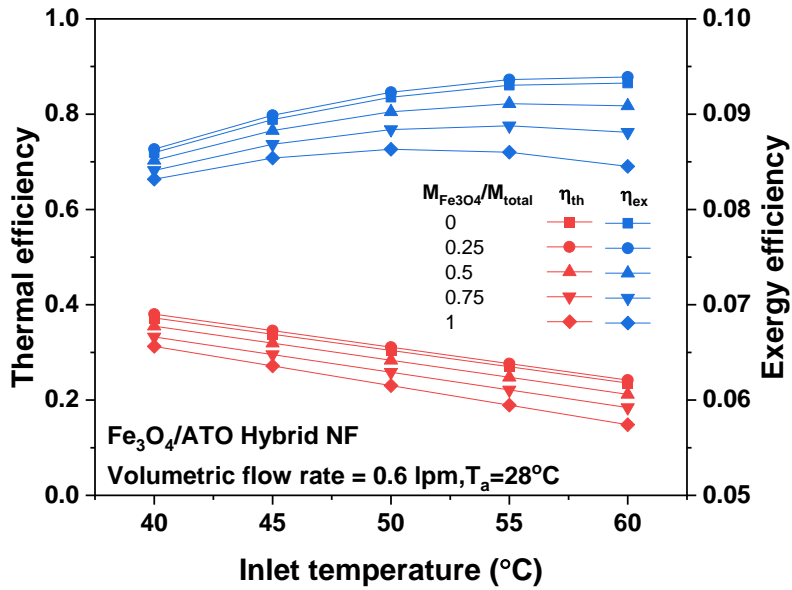


(a)

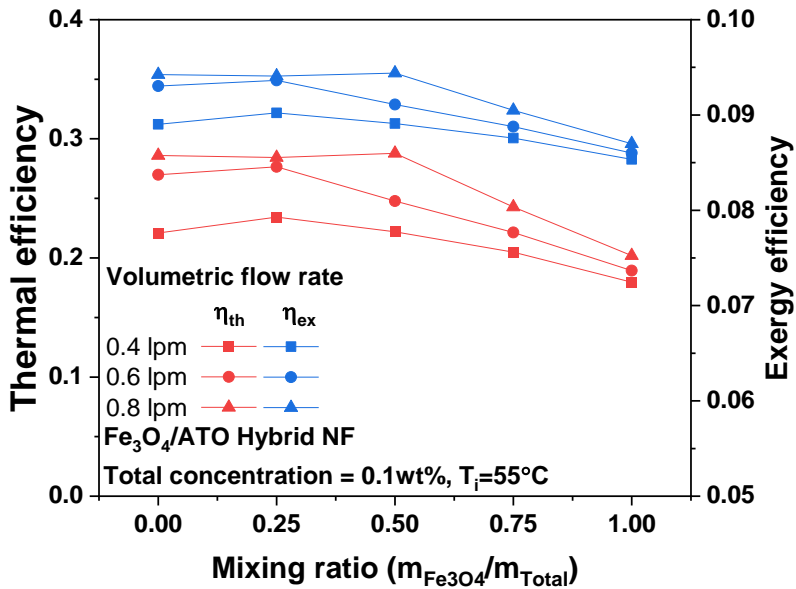


(b)

Fig. 5.18 Exergy efficiency of VASC using Fe₃O₄ NF; (a) Concentration effect, (b) Volumetric flow rate effect



(a)



(b)

Fig. 5.19 Exergy efficiency of VASC using Fe₃O₄/ATO Hybrid NF; (a) Concentration effect, (b) Volumetric flow rate effect

5.4.2.3. Performance comparison of general solar collector and VASC type solar collector

Table 5.5 compares the performance parameters of the VASTC used in this study and the performance parameters of solar collectors presented in the literature. Because the performance test conditions and the geometry of the solar collector were different, the performance parameters like $F_R(\tau\alpha)$ and F_{RU_L} were different. According to the study by Tong et al. [99], the $F_R(\tau\alpha)$ using the water in the flat plate solar collector, was 0.6362. They confirmed that The $F_R(\tau\alpha)$ of 1vol% Al_2O_3 NF and 0.5vol% CuO NF were 0.7749 and 0.7392. Besides, in the study of Choudhary et al. [98], the $F_R(\tau\alpha)$ was 0.5925 when using an ethylene glycol aqueous solution (EG: W=5:5) in a flat plate solar collector. The $F_R(\tau\alpha)$ was increased by using the NF. As the concentration of the Fe_3O_4 NF was increased to 1vol%, the $F_R(\tau\alpha)$ was increased to 0.6717.

The $F_R(\tau\alpha)$ was increased using the NF in the evacuated tube solar collector. According to the study by Sharafeldin and Grof [66], the $F_R(\tau\alpha)$ was 0.5521 when the working fluid in the evacuated tube solar collector was water. However, it was increased by using the CeO_2 NF. As the concentration of CeO_2 NF was increased to 0.035%, the $F_R(\tau\alpha)$ was increased to 0.7433. In the study of Hosseini and Dehaj [100], it was also confirmed that $F_R(\tau\alpha)$ was increased by using the TiO_2 NF. In the flat plate solar collector and the evacuated tube solar collector, the $F_R(\tau\alpha)$ can be increased by using the NF. Improved $F_R(\tau\alpha)$ in the flat plate solar collector and the evacuated tube solar collector was higher than the $F_R(\tau\alpha)$ in this study. However, according to the study of Delfani et al. [89], when using 100 ppm Al_2O_3 NF in the flat plate direct absorption solar collector, the $F_R(\tau\alpha)$ was 0.766, and it was higher than the $F_R(\tau\alpha)$ of the flat plate solar collector and the evacuated tube solar collector. It is judged that the $F_R(\tau\alpha)$ of the flat plate direct absorption solar collector was higher than the $F_R(\tau\alpha)$ of our VASTC because it has no optical loss on the reflector, and the solar energy can be absorbed by its receiver plate. Therefore, it is judged that the $F_R(\tau\alpha)$ of the VASTC can be similar to or higher than the flat plate solar collector

and the evacuated tube solar collector by optimizing the structure and improving the optical absorption.

Whereas the trend of the F_{RU_L} was different at the same type of solar collector. Studies by Tong et al. [97] and Choudhary et al. [98] about the flat plate solar collector using the NF showed the same trend in the improvement of the $F_R(\tau\alpha)$ by using the NF, while results of the F_{RU_L} by using the NF were different. Tong et al. [99] said that the F_{RU_L} of the 1vol% Al_2O_3 NF and the 0.5wt% CuO NF was 17.54 and 22.84, and they were higher than the F_{RU_L} of the water (17.24). However, Choudhary et al. [101] said that the F_{RU_L} of Fe_3O_4 NF was decreased from 7.499 to 3.694 as the concentration of the Fe_3O_4 NF was increased from 0 vol% to 1.0 vol%. In studies on the evacuated solar collector, the F_{RU_L} is increased by increasing the concentration of the NF. The F_{RU_L} of the evacuated solar collector was increased from 8.669 to 20.885 as the concentration of the CeO_2 was increased from 0% to 0.035% in the results of Sharafeldin and Grof [66]. Besides, in the study of Hosseini and Dehaj [100], when using the NFs with TiO_2 nanowires and TiO_2 NPs, the F_{RU_L} was 11.1 and 9.32. These values were higher than the F_{RU_L} using the water. The difference in the trend of F_{RU_L} was the same in previous studies on the VASC method. The trend on the F_{RU_L} of Delfani et al. [89] and this study was also different. The F_{RU_L} was increased to 24.05 as the concentration of Al_2O_3 NF was increased to 100 ppm in the study of Delfani et al. [89]. The F_{RU_L} when using the NF was higher than the F_{RU_L} with 18.59 and 20.18 using a receiver plate with black and reflective material. However, in this study, the F_{RU_L} with 7.194 of 0.1wt% Fe_3O_4/ATO NF was lower than the F_{RU_L} with 7.977 of the water, although the F_{RU_L} with 8.831 and 8.133 when using 0.075wt% Fe_3O_4 NF and 0.25wt% ATO NF was higher than the F_{RU_L} of the water. The insulation performance of the VASC in this study was reasonable compared to the direct absorption solar collector in Delfani et al. [89] due to using the vacuum tube. Therefore, it means that the F_{RU_L} of the VASTC can be decreased due to low heat loss of the convection and radiation compared to previous studies of Sharafeldin and Grof [66] and Hosseini and Dehaj [100] on the performance of the evacuated solar collector using the NF. However, it is judged that the F_{RU_L} when using the NF can be increased or decreased by thermal environment condition surrounding the solar collector and the performance of the

insulation because it was reported that the F_{RU_L} could be decreased by using the NF in case that insulation performance of the solar collector as the study of Choudhary et al. [101] was good. If the F_{RU_L} is decreased, the operating limit of the solar collector can be increased. Therefore, higher heat can be produced. The flat plate solar collector used in the study of Choudhary et al. [101] has higher LNTD of 0.182 and it was higher than the LNTD in some previous studies [99] and this study. However, the LNTD of the VASTC used in the study was 0.067. It was similar or higher than other except for the study of Choudhary et al. [101].

Combining the results of this study and the previous research, it was judged that the VASTC can have equal or higher thermal performance compared to general solar collectors for low temperatures such as a flat plate solar collector and the evacuated solar collector. However, there are many problems in the application of the VASTC. Although the VASTC has the advantage of reducing the heat loss because the NF uniformly absorbed the solar energy, the long-term dispersion stability of the NF is essential because the thermal performance is significant dependent on optical absorption performance by the NF. In this study, the MWCNT NF has superior optical absorption to others, and its stability was also higher than others before the performance test of the solar collector. However, when using the MWCNT NF in solar collectors, thermal performance could not be maintained due to the precipitation of MWCNT NF, and performance test was impossible. However, no precipitation occurred in the Fe_3O_4 NF, ATO NF, and Fe_3O_4 /ATO NF. In addition, although sedimentation occurs in the NF, thermal energy should be continuously produced by the solar collector. Hot temperature can be produced using a general solar collector using the SASC method when using the water as the working fluid. However, if the dispersion problem of the NF occurred, the thermal performance was rapidly reduced because the thermal performance of the VASTC is dependent on the optical absorbance of the NF. Finally, the manufacturing cost of the NF for improving the thermal performance of solar collectors is high. As shown in Fig. 3.24, high costs are still required to manufacture working fluids to high producing thermal energy, although the concentration of using NF to improve optical absorption is lower than that of improving thermal properties. Therefore, the VASC method used for low-temperature production is inappropriate because high costs are required in the VASC method

using the NF than in the SASC method. However, in the case of the solar collector with a high concentration ratio, it has problems such as deterioration of the absorber and high heat loss. Therefore, it is judged that a solar collector with a high concentration can be used when long-term dispersion stability is secured.

Table 5.5 Performance parameter comparison with existing study

Flat plate solar collector (Mass flow rate = 0.047 kg/s), Tong et al.[99]				Flat plate solar collector (Volumetric flow rate = 60 L/h), Choudhary et al.[101]			
NF	$F_R(\tau\alpha)$	F_{RU_L}	LNTD	NF	$F_R(\tau\alpha)$	F_{RU_L}	LNTD
Water	0.6362	17.24	0.037	EG:W=5:5	0.5925	7.499	0.079
1vol% Al ₂ O ₃ NF	0.7749	17.54	0.044	0.2vol% Fe ₃ O ₄ NF	0.642	5.931	0.108
0.5vol% CuO NF	0.7392	22.84	0.032	0.6vol% Fe ₃ O ₄ NF	0.6524	4.257	0.153
				1.0vol% Fe ₃ O ₄ NF	0.6717	3.694	0.182
Evacuated tube solar collector (Mass flux = 0.017 kg/s·m ²), Sharafeldin and Grof [66]				Evacuated tube solar collector (Volumetric flow rate = 0.5 lpm), Hosseini and Dehaj [100]			
NF	$F_R(\tau\alpha)$	F_{RU_L}	LNTD	NF	$F_R(\tau\alpha)$	F_{RU_L}	LNTD
Water	0.5521	8.669	0.064	Water	0.55	8.45	0.065
0.015% CeO ₂ NF	0.6595	16.227	0.041	TiO ₂ NP NF	0.62	9.32	0.067
0.025% CeO ₂ NF	0.7123	17.785	0.04	TiO ₂ Nanowire NF	0.68	11.1	0.061
0.035% CeO ₂ NF	0.7433	20.855	0.036				
Flat plat direct absorption solar collector (Mass flow rate = 0.015 kg/s) Delfani et al. [89]				This study (Volumetric flow rate = 0.8 lpm)			
NF	$F_R(\tau\alpha)$	F_{RU_L}	LNTD	NF	$F_R(\tau\alpha)$	F_{RU_L}	LNTD
Reflective internal	0.502	20.18	0.025	Water	0.434	7.977	0.054
Black internal	0.58	18.59	0.031	0.075wt% Fe ₃ O ₄ NF	0.492	8.831	0.056
10 ppm Al ₂ O ₃ NF	0.603	20.64	0.029	0.25wt% ATO NF	0.508	8.133	0.062
50 ppm Al ₂ O ₃ NF	0.691	21.19	0.033	0.1wt% Fe ₃ O ₄ /ATO hybrid NF	0.485	7.194	0.067
100 ppm Al ₂ O ₃ NF	0.766	24.05	0.032				

6. Conclusion

This study aimed to examine the applicability of NF VASC by investigating the optical and heat transfer properties and mechanisms for the correlation between optical absorption properties and photothermal conversion coefficients of NFs such as MWCNT, Fe₃O₄, ATO NFs, and Fe₃O₄/ATO hybrid NFs. Also, based on Fe₃O₄ NF, the effect of the optical absorption characteristics on the performance of the volume absorption solar collector was investigated through analytical and experimental methods, and the approaches to the application of NFs in the VASC and SASC methods were discussed. As a result, the following conclusions were drawn regarding the optical properties of MWCNT, Fe₃O₄, ATO NFs, and Fe₃O₄/ATO hybrid NFs; heat transfer properties of SASC; and thermodynamic properties and applications of VASC.

- (1) For the optical absorption characteristics of NFs, MWCNT NF demonstrated superior optical absorption compared to Fe₃O₄ and ATO NFs. The improvement of the light transmittance according to the concentration change was the most prominent with MWCNT NF, followed by ATO NFs, and the photo thermal conversion efficiency of 0.002wt% MWCNT NF was 0.933, which was the highest among non-hybrid NFs.
- (2) Fe₃O₄ NF was excellent for improving the optical absorption in the visible ray band, and ATO NF was excellent for improving the optical absorption in the near-infrared ray band. It was possible to compensate for insufficient optical absorption by wavelength by mixing Fe₃O₄ NF and ATO NF. As for 0.1wt% Fe₃O₄ NF with $m_{\text{Fe}_3\text{O}_4}/m_{\text{Total,NP}} = 0.2$, the photo thermal conversion efficiency is 0.932, which could improve optical absorption compared to 0.002wt% MWCNT NF.
- (3) 0.002wt% MWCNT NF is a reasonable choice when considering optical absorption performance and manufacturing cost in solar energy collection. The cost of the NF for thermal energy production was high, and it was in the order of 0.0075wt% Fe₃O₄ NF > 0.1wt% Fe₃O₄ /ATO NF ($m_{\text{Fe}_3\text{O}_4}/m_{\text{Total,NP}} = 0.2$) > 0.1wt% ATO NF > 0.002wt%

MWCNT NF. Although $\text{Fe}_3\text{O}_4/\text{ATO}$ hybrid NF was expensive for thermal energy production compared to MWCNT NF, it is possibly considered an alternative to MWCNT NF due to improved optical absorption performance and reduced cost for heat production compared to Fe_3O_4 NF.

- (4) A numerical analysis based on Fe_3O_4 NF revealed that the increase in the concentration of NFs was confirmed to have been directly affected by the improvement of thermal and exergy efficiencies of FPVASC. As the concentration of Fe_3O_4 NF increased to 0.1 wt%, the optical efficiency of FPVASC was improved up to 43.5%. The improvement in optical absorption by increasing the Fe_3O_4 NF concentration reduced the irreversibility caused by the increased heat gain of FPVASC. As the Fe_3O_4 NF concentration increased from 0 wt% to 0.1 wt%, the maximum exergy efficiency increased from 0.0686 to 0.0844.
- (5) In the SASC and VASC methods, the effect of the concentration change of NF was experimentally investigated using Fe_3O_4 NF. In the SASC method, as the concentration of Fe_3O_4 NF increased, both F_R and U_L increased. Compared to the increase in F_R , the increase in U_L was more prominent, reducing thermal and exergy efficiencies. On the other hand, in the VASC method, F_R continued to increase as the concentration of Fe_3O_4 NF increased, but U_L increased after decreasing till the concentration of Fe_3O_4 NF to 0.05 wt%. It is related to the thermal environment in the receiver due to the improvement of absorbance by increasing the concentration of Fe_3O_4 NF. Fe_3O_4 NF of 0.05 wt% or less reduced heat loss by uniform temperature distribution in the receiver tube, while Fe_3O_4 NF of 0.05 wt% or more absorbed light near the receiver tube due to excessively increased optical absorption, creating a thermal environment similar to SVAC with increased U_L . As a result, the VASC heat collection method's thermal and exergy efficiency using 0.05 wt% Fe_3O_4 NF were higher than the SASC method and other Fe_3O_4 NFs. When the inlet temperature was 50°C, and the mass flow rate was 0.025 kg/s, the thermal and exergy efficiencies of 0.05 wt% Fe_3O_4 NF were 0.487 and 0.0313, respectively.
- (6) The effects of Fe_3O_4 , ATO, and $\text{Fe}_3\text{O}_4/\text{ATO}$ hybrid NFs on VASC utilization were experimentally investigated. ATO NF had higher thermal and exergy efficiencies than Fe_3O_4

NF. The 0.1wt% Fe₃O₄/ATO hybrid NF with $m_{\text{Fe}_3\text{O}_4}/m_{\text{Total,NP}} = 0.25$ exhibited improved thermal and exergy efficiencies compared to Fe₃O₄ and ATO NFs at the same concentration. An increase in the proportion of Fe₃O₄ in the 0.1wt% Fe₃O₄/ATO hybrid NF led to an insufficient effect of the mixed ATO NF with an increase in the reflectance of ultraviolet and visible light at high concentrations. However, when the proportion of the ATO NF was high, the thermal and exergy efficiencies were improved by supplementing the disadvantages of the Fe₃O₄ NF and improving the optical absorption in the visible light band of the ATO NF. As for the 0.1wt% Fe₃O₄/ATO hybrid NF at a volumetric flow rate of 0.6 lpm, the thermal efficiency was 0.277, and the maximum exergy efficiency was 0.094 at an inlet temperature of 55 °C, showing an improvement from the thermal efficiency and the maximum exergy efficiency of 0.1wt% Fe₃O₄ NF at 0.189 and 0.086, as well as those of 0.1wt% ATO NF at 0.27 and 0.093, under the same conditions. It had a maximum exergy efficiency, where the exergy efficiency was 0.094.

- (7) Compared with the existing flat plate solar collector and evacuated tube solar collector, the VASTC using the NF used in this study is judged to have equivalent solar energy absorption and low heat loss. However, unlike SASC-based solar collectors, VASTC depends on the optical absorption performance of the NF, and therefore it is necessary to secure the long-term dispersion stability of the NF. In addition, the concentration of the NF with high optical absorption is low compared to the improvement of thermal properties, but the manufacturing cost is still high. The VASC, as the solar thermal collection method, has lower heat loss than the SASC method. Therefore, it is judged that the application of the VAST method can be considered in solar collectors with high concentration ratio that have problems with the absorber damage and deterioration

7. Future work

In this study, the applicability of the VASC method using the NF to improve the performance of solar collectors was investigated. It was confirmed that the VASC method has less heat loss than the existing SASC method and can have higher thermal efficiency than the SASC method. Also, it was confirmed that the optical absorption and the performance of the VASTC could be improved by mixing NFs with different optical absorption characteristics.

The VASC method using nanofluids is attractive in terms of improving thermal efficiency. However, considering the NF manufacturing cost and dispersion stability, the VASC method using NFs has various problems. Therefore, it is judged that using NFs for the solar collector with a high concentration ratio is appropriate to using the VASC method. The solar collector with a high concentration ratio can produce high-temperature heat in a high insolation area, but it has low efficiency due to high heat loss in the collector. In addition, there is a problem in that the absorber is deteriorated or damaged because the absorber of the collector is exposed to high-intensity solar energy for a long time.

Therefore, in improving the performance of solar collector with a high concentration ratio, the volume absorption method is more valuable than low-temperature solar collector. Despite the continuous development of NF manufacturing technology, the problem on sedimentation of NFs is continuously presented. In this study, through the use of NFs, it was possible to lower the heat loss of the solar collector and improve the thermal efficiency when the absorption of solar energy was performed three-dimensionally. The VASC method is suitable for solar collectors with a high concentration ratio and loss due to local heating. In the solar collector with a high concentration ratio, local heat loss is high because a high heat flux occurs at the point entering the solar energy. In addition, because the temperature difference between the inlet and the outlet is significant, some problems such as stratification occur. Solving these problems makes it possible to improve the performance of the solar collector with a high concentration ratio. It is judged that efforts should be made to improve the performance of the solar collector with a high concentration ratio

through the use of porous materials and the introduction of structural improvement of absorbers to three-dimensionally absorb light in the collector of high-intensity solar thermal collectors.

However, because the introduction of a porous material as an absorber increases the flow storage of the absorber and causes an increase in pump power consumption and operating cost. Therefore, various experiments and analysis studies are needed to evaluate the thermal performance index and economic feasibility to evaluate its applicability. In addition, it is necessary to investigate the effect of improving the performance of the solar collector with a high concentration ratio by changing the material of the absorber and optimizing the structure. Due to the recent war between Russia and Ukraine and the strengthening of greenhouse gas regulations, the use of new and renewable energy and waste heat is becoming more critical. Solar energy is an energy source that can be easily seen in the vicinity, but its utility is low due to low energy density and convenience of energy use. However, this study is expected to contribute to the utilization and dissemination of solar energy.

Reference

- [1] Al-Ghussain L. Global warming: review on driving forces and mitigation. *Environ Prog Sustain Energy* 2019;38:13–21.
- [2] Olabi AG, Abdelkareem MA. Renewable energy and climate change. *Renew Sustain Energy Rev* 2022;158:112111. <https://doi.org/10.1016/J.RSER.2022.112111>.
- [3] Lenferna GA. Can we equitably manage the end of the fossil fuel era? *Energy Res Soc Sci* 2018;35:217–23. <https://doi.org/10.1016/J.ERSS.2017.11.007>.
- [4] Elavarasan RM, Shafiullah GM, Padmanaban S, Kumar NM, Annam A, Vetrichelvan AM, et al. A comprehensive review on renewable energy development, challenges, and policies of leading Indian states with an international perspective. *IEEE Access* 2020;8:74432–57.
- [5] Rahman A, Farrok O, Haque MM. Environmental impact of renewable energy source based electrical power plants: Solar, wind, hydroelectric, biomass, geothermal, tidal, ocean, and osmotic. *Renew Sustain Energy Rev* 2022;161:112279. <https://doi.org/10.1016/J.RSER.2022.112279>.
- [6] Zahedi AR, Labbafi S, Ghaffarinezhad A, Habibi K. Design, construction and performance of a quintuple renewable hybrid system of wind/geothermal/biomass/solar/hydro plus fuel cell. *Int J Hydrogen Energy* 2021;46:6206–24. <https://doi.org/10.1016/J.IJHYDENE.2020.11.188>.
- [7] Markvart T. *Solar Electricity*, Wiley, New York. NY, USA 2000.
- [8] Nasa. Earth's Energy Budget. Natl Aeronaut Sp Adm n.d. https://web.archive.org/web/20140421050855/http://science-edu.larc.nasa.gov/energy_budget/.
- [9] Saadatmand M, Gharehpetian GB, Moghassemi A, Guerrero JM, Siano P, Alhelou HH. Damping of low-frequency oscillations in power systems by large-scale PV farms: A comprehensive review of control methods. *IEEE Access* 2021.
- [10] Li X, Gui D, Zhao Z, Li X, Wu X, Hua Y, et al. Operation optimization of electrical-heating integrated energy system based on concentrating solar power plant hybridized with combined heat and power plant. *J Clean Prod* 2021;289:125712. <https://doi.org/10.1016/J.JCLEPRO.2020.125712>.
- [11] Al-Maliki WAK, Mahmoud NS, Al-Khafaji HMH, Alobaid F, Epple B. Design and Implementation of the Solar Field and Thermal Storage System Controllers for a Parabolic Trough Solar Power Plant. *Appl Sci* 2021;11:6155.
- [12] Yang J, Yang Z, Duan Y. Novel design optimization of concentrated solar power plant with S-CO₂ Brayton cycle based on annual off-design performance. *Appl Therm Eng* 2021;192:116924.
- [13] Sandá A, Moya SL, Valenzuela L. Modelling and simulation tools for direct steam generation in parabolic-trough solar collectors: A review. *Renew Sustain Energy Rev* 2019;113:109226. <https://doi.org/10.1016/J.RSER.2019.06.033>.
- [14] Lin M, Reinhold J, Monnerie N, Haussener S. Modeling and design guidelines for direct

- steam generation solar receivers. *Appl Energy* 2018;216:761–76.
<https://doi.org/10.1016/J.APENERGY.2018.02.044>.
- [15] Hongbing C, Yutong G, Haoyu N, Xiaoli Y, Xilin C. Optimization and Performance Study of Residential Centralized Solar Domestic Hot Water System. *Energy Procedia* 2019;158:6431–7. <https://doi.org/10.1016/J.EGYPRO.2019.01.176>.
- [16] Kim T, Choi B Il, Han YS, Do KH. A comparative investigation of solar-assisted heat pumps with solar thermal collectors for a hot water supply system. *Energy Convers Manag* 2018;172:472–84. <https://doi.org/10.1016/J.ENCONMAN.2018.07.035>.
- [17] Asadi J, Amani P, Amani M, Kasaeian A, Bahiraei M. Thermo-economic analysis and multi-objective optimization of absorption cooling system driven by various solar collectors. *Energy Convers Manag* 2018;173:715–27.
<https://doi.org/10.1016/J.ENCONMAN.2018.08.013>.
- [18] Chen Y, Xu J, Zhao D, Wang J, Lund PD. Exergo-economic assessment and sensitivity analysis of a solar-driven combined cooling, heating and power system with organic Rankine cycle and absorption heat pump. *Energy* 2021;230:120717.
<https://doi.org/10.1016/J.ENERGY.2021.120717>.
- [19] Fan Y, Zhao X, Han Z, Li J, Badieli A, Akhlaghi YG, et al. Scientific and technological progress and future perspectives of the solar assisted heat pump (SAHP) system. *Energy* 2021;229:120719. <https://doi.org/10.1016/J.ENERGY.2021.120719>.
- [20] Punniakodi BMS, Senthil R. A review on container geometry and orientations of phase change materials for solar thermal systems. *J Energy Storage* 2021;36:102452.
<https://doi.org/10.1016/J.EST.2021.102452>.
- [21] Afshan ME, Selvakumar AS, Velraj R, Rajaraman R. Effect of aspect ratio and dispersed PCM balls on the charging performance of a latent heat thermal storage unit for solar thermal applications. *Renew Energy* 2020;148:876–88.
<https://doi.org/10.1016/J.RENENE.2019.10.172>.
- [22] Huang H, Xiao Y, Lin J, Zhou T, Liu Y, Zhao Q. Improvement of the efficiency of solar thermal energy storage systems by cascading a PCM unit with a water tank. *J Clean Prod* 2020;245:118864. <https://doi.org/10.1016/J.JCLEPRO.2019.118864>.
- [23] Ray AK, Rakshit D, Ravikumar K. High-temperature latent thermal storage system for solar power: Materials, concepts, and challenges. *Clean Eng Technol* 2021;4:100155.
<https://doi.org/10.1016/J.CLET.2021.100155>.
- [24] Rohde D, Andresen T, Nord N. Analysis of an integrated heating and cooling system for a building complex with focus on long-term thermal storage. *Appl Therm Eng* 2018;145:791–803. <https://doi.org/10.1016/J.APPLTHERMALENG.2018.09.044>.
- [25] Fumey B, Weber R, Baldini L. Sorption based long-term thermal energy storage – Process classification and analysis of performance limitations: A review. *Renew Sustain Energy Rev* 2019;111:57–74. <https://doi.org/10.1016/J.RSER.2019.05.006>.
- [26] Yang T, Liu W, Kramer GJ, Sun Q. Seasonal thermal energy storage: A techno-economic literature review. *Renew Sustain Energy Rev* 2021;139:110732.
<https://doi.org/10.1016/J.RSER.2021.110732>.
- [27] Choi SUS, Eastman JA. Enhancing thermal conductivity of fluids with nanoparticles. Argonne National Lab.(ANL), Argonne, IL (United States); 1995.

- [28] Yu W, Choi SUS. The Role of Interfacial Layers in the Enhanced Thermal Conductivity of Nanofluids: A Renovated Maxwell Model. *J Nanoparticle Res* 2003;5:167–71. <https://doi.org/10.1023/A:1024438603801>.
- [29] Tawfik MM. Experimental studies of nanofluid thermal conductivity enhancement and applications: A review. *Renew Sustain Energy Rev* 2017;75:1239–53.
- [30] Glory J, Bonetti M, Helezen M, Mayne-L’Hermite M, Reynaud C. Thermal and electrical conductivities of water-based nanofluids prepared with long multiwalled carbon nanotubes. *J Appl Phys* 2008;103:94309. <https://doi.org/10.1063/1.2908229>.
- [31] Gao Y, Wang H, Sasmito AP, Mujumdar AS. Measurement and modeling of thermal conductivity of graphene nanoplatelet water and ethylene glycol base nanofluids. *Int J Heat Mass Transf* 2018;123:97–109. <https://doi.org/10.1016/J.IJHEATMASSTRANSFER.2018.02.089>.
- [32] Huminic G, Huminic A, Fleaca C, Dumitrache F, Morjan I. Thermo-physical properties of water based SiC nanofluids for heat transfer applications. *Int Commun Heat Mass Transf* 2017;84:94–101. <https://doi.org/10.1016/J.ICHEATMASSTRANSFER.2017.04.006>.
- [33] Abdolbaqi MK, Azmi WH, Mamat R, Sharma K V., Najafi G. Experimental investigation of thermal conductivity and electrical conductivity of BioGlycol–water mixture based Al_2O_3 nanofluid. *Appl Therm Eng* 2016;102:932–41. <https://doi.org/10.1016/J.APPLTHERMALENG.2016.03.074>.
- [34] Esfe MH, Afrand M, Karimipour A, Yan W-M, Sina N. An experimental study on thermal conductivity of MgO nanoparticles suspended in a binary mixture of water and ethylene glycol. *Int Commun Heat Mass Transf* 2015;67:173–5.
- [35] Moldoveanu GM, Huminic G, Minea AA, Huminic A. Experimental study on thermal conductivity of stabilized Al_2O_3 and SiO_2 nanofluids and their hybrid. *Int J Heat Mass Transf* 2018;127:450–7. <https://doi.org/10.1016/J.IJHEATMASSTRANSFER.2018.07.024>.
- [36] Abareshi M, Goharshadi EK, Mojtaba Zebarjad S, Khandan Fadafan H, Youssefi A. Fabrication, characterization and measurement of thermal conductivity of Fe_3O_4 nanofluids. *J Magn Magn Mater* 2010;322:3895–901. <https://doi.org/10.1016/J.JMMM.2010.08.016>.
- [37] Agarwal R, Verma K, Agrawal NK, Duchaniya RK, Singh R. Synthesis, characterization, thermal conductivity and sensitivity of CuO nanofluids. *Appl Therm Eng* 2016;102:1024–36. <https://doi.org/10.1016/J.APPLTHERMALENG.2016.04.051>.
- [38] Shahsavari A, Saghafian M, Salimpour MR, Shafii MB. Effect of temperature and concentration on thermal conductivity and viscosity of ferrofluid loaded with carbon nanotubes. *Heat Mass Transf* 2016;52:2293–301.
- [39] Suresh S, Venkataraj KP, Selvakumar P, Chandrasekar M. Synthesis of Al_2O_3 –Cu/water hybrid nanofluids using two step method and its thermo physical properties. *Colloids Surfaces A Physicochem Eng Asp* 2011;388:41–8.
- [40] Ali HM. In tube convection heat transfer enhancement: SiO_2 aqua based nanofluids. *J Mol Liq* 2020;308:113031. <https://doi.org/10.1016/J.MOLLIQ.2020.113031>.
- [41] Hazbehian M, Mohammadiun M, Maddah H, Alizadeh M. Analyses of exergy efficiency for forced convection heat transfer in a tube with CNT nanofluid under laminar flow conditions. *Heat Mass Transf* 2017;53:1503–16.

- [42] Choi TJ, Park MS, Kim SH, Jang SP. Experimental study on the effect of nanoparticle migration on the convective heat transfer coefficient of EG/water-based Al₂O₃ nanofluids. *Int J Heat Mass Transf* 2021;169:120903.
- [43] Sharifpur M, Solomon AB, Ottermann TL, Meyer JP. Optimum concentration of nanofluids for heat transfer enhancement under cavity flow natural convection with TiO₂ – Water. *Int Commun Heat Mass Transf* 2018;98:297–303. <https://doi.org/10.1016/J.ICHEATMASSTRANSFER.2018.09.010>.
- [44] Sharifi S, Aligoodarz MR, Rahbari A. Thermohydraulic performance of Al₂O₃-water nanofluid during single-phase flow and two-phase subcooled flow boiling. *Int J Therm Sci* 2022;179:107605. <https://doi.org/10.1016/J.IJTHEMALSCI.2022.107605>.
- [45] Kamel MS, Lezsovits F. Enhancement of pool boiling heat transfer performance using dilute cerium oxide/water nanofluid: An experimental investigation. *Int Commun Heat Mass Transf* 2020;114:104587. <https://doi.org/10.1016/J.ICHEATMASSTRANSFER.2020.104587>.
- [46] Wu S, Zhu D, Zhang X, Huang J. Preparation and melting/freezing characteristics of Cu/paraffin nanofluid as phase-change material (PCM). *Energy & Fuels* 2010;24:1894–8.
- [47] Dayou S, Ting TW, Vigolo B. Comparison of heat transfer performance of water-based graphene nanoplatelet- and multi-walled carbon nanotube-nanofluids in a concentric tube heat exchanger. *Diam Relat Mater* 2022;125:108976. <https://doi.org/10.1016/J.DIAMOND.2022.108976>.
- [48] Zheng D, Wang J, Chen Z, Baleta J, Sundén B. Performance analysis of a plate heat exchanger using various nanofluids. *Int J Heat Mass Transf* 2020;158:119993. <https://doi.org/10.1016/J.IJHEATMASSTRANSFER.2020.119993>.
- [49] Kumar A, Subudhi S. Experimental investigation on the thermophysical properties of low concentration magnetic colloidal suspensions (nanofluids) with the variations in temperature & magnetic field. *J Magn Magn Mater* 2021;526:167723. <https://doi.org/10.1016/J.JMMM.2020.167723>.
- [50] Rajnak M, Timko M, Kurimsky J, Dolnik B, Cimbala R, Tobias T, et al. Electrical conduction in a transformer oil-based magnetic nanofluid under a DC electric field. *J Magn Magn Mater* 2018;459:191–6. <https://doi.org/10.1016/J.JMMM.2017.11.023>.
- [51] Ali K, Faridi AA, Ahmad S, Jamshed W, Khan N, Alam MM. Quasi-linearization analysis for heat and mass transfer of magnetically driven 3rd-grade (Cu-TiO₂/engine oil) nanofluid via a convectively heated surface. *Int Commun Heat Mass Transf* 2022;135:106060. <https://doi.org/10.1016/J.ICHEATMASSTRANSFER.2022.106060>.
- [52] Milanese M, Colangelo G, Creti A, Lomascolo M, Iacobazzi F, De Risi A. Optical absorption measurements of oxide nanoparticles for application as nanofluid in direct absorption solar power systems - Part I: Water-based nanofluids behavior. *Sol Energy Mater Sol Cells* 2016;147:315–20. <https://doi.org/10.1016/j.solmat.2015.12.027>.
- [53] Said Z, Saidur R, Rahim NA. Optical properties of metal oxides based nanofluids. *Int Commun Heat Mass Transf* 2014;59:46–54. <https://doi.org/10.1016/J.ICHEATMASSTRANSFER.2014.10.010>.
- [54] Said Z. Thermophysical and optical properties of SWCNTs nanofluids. *Int Commun Heat Mass Transf* 2016;78:207–13.

- <https://doi.org/10.1016/J.ICHEATMASSTRANSFER.2016.09.017>.
- [55] Sonnenenergie DG für. Planning and Installing Solar Thermal Systems: A Guide for Installers, Architects and Engineers. Earthscan; 2010.
- [56] Bellas D V., Lidorikis E. Design of high-temperature solar-selective coatings for application in solar collectors. *Sol Energy Mater Sol Cells* 2017;170:102–13. <https://doi.org/10.1016/J.SOLMAT.2017.05.056>.
- [57] McDonald GE. Spectral reflectance properties of black chrome for use as a solar selective coating. *Sol Energy* 1975;17:119–22. [https://doi.org/10.1016/0038-092X\(75\)90067-5](https://doi.org/10.1016/0038-092X(75)90067-5).
- [58] Zhang QC. Recent progress in high-temperature solar selective coatings. *Sol Energy Mater Sol Cells* 2000;62:63–74. [https://doi.org/10.1016/S0927-0248\(99\)00136-1](https://doi.org/10.1016/S0927-0248(99)00136-1).
- [59] Lee K-D. Deposition of Solar Selective Coatings for High Temperature Applications. *J Korean Sol Energy Soc* 2008;28:33–42.
- [60] Kansara R, Pathak M, Patel VK. Performance assessment of flat-plate solar collector with internal fins and porous media through an integrated approach of CFD and experimentation. *Int J Therm Sci* 2021;165:106932. <https://doi.org/10.1016/J.IJTHERMALSCI.2021.106932>.
- [61] Veera Kumar A, Arjunan T V., Seenivasan D, Venkatramanan R, Vijayan S. Thermal performance of an evacuated tube solar collector with inserted baffles for air heating applications. *Sol Energy* 2021;215:131–43. <https://doi.org/10.1016/J.SOLENER.2020.12.037>.
- [62] Saravanan A, Jaisankar S. Heat transfer augmentation techniques in forced flow V-trough solar collector equipped with V-cut and square cut twisted tape. *Int J Therm Sci* 2019;140:59–70. <https://doi.org/10.1016/j.ijthermalsci.2019.02.030>.
- [63] Choudhary S, Sachdeva A, Kumar P. Investigation of the stability of MgO nanofluid and its effect on the thermal performance of flat plate solar collector. *Renew Energy* 2020;147:1801–14. <https://doi.org/10.1016/J.RENENE.2019.09.126>.
- [64] Sharafeldin MA, Gróf G. Evacuated tube solar collector performance using CeO₂/water nanofluid. *J Clean Prod* 2018;185:347–56. <https://doi.org/10.1016/j.jclepro.2018.03.054>.
- [65] Eidan AA, AlSahlani A, Ahmed AQ, Al-fahham M, Jalil JM. Improving the performance of heat pipe-evacuated tube solar collector experimentally by using Al₂O₃ and CuO/acetone nanofluids. *Sol Energy* 2018;173:780–8. <https://doi.org/10.1016/J.SOLENER.2018.08.013>.
- [66] Sharafeldin MA, Gróf G, Abu-Nada E, Mahian O. Evacuated tube solar collector performance using copper nanofluid: Energy and environmental analysis. *Appl Therm Eng* 2019;162:114205. <https://doi.org/10.1016/J.APPLTHERMALENG.2019.114205>.
- [67] Otanicar TP, Phelan PE, Golden JS. Optical properties of liquids for direct absorption solar thermal energy systems. *Sol Energy* 2009;83:969–77. <https://doi.org/10.1016/j.solener.2008.12.009>.
- [68] Minardi JE, Chuang HN. Performance of a “black” liquid flat-plate solar collector. *Sol Energy* 1975;17:179–83. [https://doi.org/10.1016/0038-092X\(75\)90057-2](https://doi.org/10.1016/0038-092X(75)90057-2).
- [69] Abdelrahman M, Fumeaux P, Suter P. Study of solid-gas-suspensions used for direct absorption of concentrated solar radiation. *Sol Energy* 1979;22:45–8. [https://doi.org/10.1016/0038-092X\(79\)90058-6](https://doi.org/10.1016/0038-092X(79)90058-6).

- [70] Burke AR, Etter DE, Hudgens CR, Wiedenheft CJ, Wittenberg LJ. Thermal and photochemical studies of solar energy absorbers dissolved in heat transfer fluids. *Sol Energy Mater* 1982;6:481–90. [https://doi.org/10.1016/0165-1633\(82\)90033-8](https://doi.org/10.1016/0165-1633(82)90033-8).
- [71] Amjad M, Jin H, Du X, Wen D. Experimental photothermal performance of nanofluids under concentrated solar flux. *Sol Energy Mater Sol Cells* 2018;182:255–62. <https://doi.org/10.1016/j.solmat.2018.03.044>.
- [72] Jin X, Lin G, Zeiny A, Jin H, Bai L, Wen D. Solar photothermal conversion characteristics of hybrid nanofluids: An experimental and numerical study. *Renew Energy* 2019;141:937–49. <https://doi.org/10.1016/j.renene.2019.04.016>.
- [73] Guo C, Liu C, Jiao S, Wang R, Rao Z. Introducing optical fiber as internal light source into direct absorption solar collector for enhancing photo-thermal conversion performance of MWCNT-H₂O nanofluids. *Appl Therm Eng* 2020;173:115207. <https://doi.org/10.1016/j.applthermaleng.2020.115207>.
- [74] Hazra SK, Ghosh S, Nandi TK. Photo-thermal conversion characteristics of carbon black-ethylene glycol nanofluids for applications in direct absorption solar collectors. *Appl Therm Eng* 2019;163:114402. <https://doi.org/10.1016/J.APPLTHERMALENG.2019.114402>.
- [75] Gorji TB, Ranjbar AA. A numerical and experimental investigation on the performance of a low-flux direct absorption solar collector (DASC) using graphite, magnetite and silver nanofluids. *Sol Energy* 2016;135:493–505. <https://doi.org/10.1016/j.solener.2016.06.023>.
- [76] Gupta HK, Agrawal G Das, Mathur J. Investigations for effect of Al₂O₃-H₂O nanofluid flow rate on the efficiency of direct absorption solar collector. *Case Stud Therm Eng* 2015;5:70–8. <https://doi.org/10.1016/J.CSITE.2015.01.002>.
- [77] Menbari A, Alemrajabi AA, Rezaei A. Heat transfer analysis and the effect of CuO/Water nanofluid on direct absorption concentrating solar collector. *Appl Therm Eng* 2016;104:176–83. <https://doi.org/10.1016/J.APPLTHERMALENG.2016.05.064>.
- [78] Delfani S, Karami M, Akhavan-Behabadi MA. Performance characteristics of a residential-type direct absorption solar collector using MWCNT nanofluid. *Renew Energy* 2016;87:754–64. <https://doi.org/10.1016/J.RENENE.2015.11.004>.
- [79] Kumar A, Dixit CK. Methods for characterization of nanoparticles. *Adv. nanomedicine Deliv. Ther. nucleic acids*, Elsevier; 2017, p. 43–58.
- [80] Ebrahimi R, de Faoite D, Finn DP, Stanton KT. Accurate measurement of nanofluid thermal conductivity by use of a polysaccharide stabilising agent. *Int J Heat Mass Transf* 2019;136:486–500. <https://doi.org/10.1016/J.IJHEATMASSTRANSFER.2019.03.030>.
- [81] Cobos DR. Using the KD2 Pro to measure thermal properties of fluids. *Appl Note*, Decagon Devices 2010.
- [82] Li D, Zheng Y, Li Z, Qi H. Optical properties of a liquid paraffin-filled double glazing unit. *Energy Build* 2015;108:381–6. <https://doi.org/10.1016/J.ENBUILD.2015.09.039>.
- [83] Wang Q, Wei W, Li D, Qi H, Wang F, Arıcı M. Experimental investigation of thermal radiative properties of Al₂O₃-paraffin nanofluid. *Sol Energy* 2019;177:420–6. <https://doi.org/10.1016/J.SOLENER.2018.11.034>.
- [84] ASTM G. 173-03. Standard tables for reference solar spectral irradiances: direct normal and hemispherical on 37° tilted surface. American Society for Testing and Materials; 2012.

- [85] Chen N, Ma H, Li Y, Cheng J, Zhang C, Wu D, et al. Complementary optical absorption and enhanced solar thermal conversion of CuO-ATO nanofluids. *Sol Energy Mater Sol Cells* 2017;162:83–92.
- [86] <https://koreanano.co.kr/main/main.html>.
- [87] <http://knpnano.com/main.asp>.
- [88] Mao Y, Yang M, Wang T, Wu F, Qian B. Influence of vacuum level on heat transfer characteristics of maglev levitation electromagnet module. *Appl Sci* 2020;10:1106.
- [89] Delfani S, Karami M, Akhavan-Behabadi MA. Performance characteristics of a residential-type direct absorption solar collector using MWCNT nanofluid. *Renew Energy* 2016;87:754–64. <https://doi.org/10.1016/j.renene.2015.11.004>.
- [90] Garg HP, Shukla AR, Madhuri I, Agnihotri RC, Chakraverty S. Development of a simple low-cost solar simulator for indoor collector testing. *Appl Energy* 1985;21:43–54. [https://doi.org/10.1016/0306-2619\(85\)90073-X](https://doi.org/10.1016/0306-2619(85)90073-X).
- [91] Riffat S, Mayere A. Performance evaluation of v-trough solar concentrator for water desalination applications. *Appl Therm Eng* 2013;50:234–44. <https://doi.org/10.1016/J.APPLTHERMALENG.2012.05.028>.
- [92] Ozsoy A, Corumlu V. Thermal performance of a thermosyphon heat pipe evacuated tube solar collector using silver-water nanofluid for commercial applications. *Renew Energy* 2018;122:26–34. <https://doi.org/10.1016/j.renene.2018.01.031>.
- [93] ISO - ISO 9806-1:1994 - Test methods for solar collectors — Part 1: Thermal performance of glazed liquid heating collectors including pressure drop n.d. <https://www.iso.org/standard/17678.html> (accessed April 22, 2021).
- [94] Sharafeldin MA, Gróf G. Evacuated tube solar collector performance using CeO₂/water nanofluid. *J Clean Prod* 2018;185:347–56. <https://doi.org/10.1016/J.JCLEPRO.2018.03.054>.
- [95] Sharafeldin MA, Gróf G. Efficiency of evacuated tube solar collector using WO₃/Water nanofluid. *Renew Energy* 2019;134:453–60. <https://doi.org/10.1016/j.renene.2018.11.010>.
- [96] Kaya H, Arslan K, Eltugral N. Experimental investigation of thermal performance of an evacuated U-Tube solar collector with ZnO/Ethylene glycol-pure water nanofluids. *Renew Energy* 2018;122:329–38. <https://doi.org/10.1016/j.renene.2018.01.115>.
- [97] Sint NKC, Choudhury IA, Masjuki HH, Aoyama H. Theoretical analysis to determine the efficiency of a CuO-water nanofluid based-flat plate solar collector for domestic solar water heating system in Myanmar. *Sol Energy* 2017;155:608–19. <https://doi.org/10.1016/j.solener.2017.06.055>.
- [98] Gupta HK, Agrawal G Das, Mathur J. An experimental investigation of a low temperature Al₂O₃-H₂O nanofluid based direct absorption solar collector. *Sol Energy* 2015;118:390–6. <https://doi.org/10.1016/j.solener.2015.04.041>.
- [99] Tong Y, Lee H, Kang W, Cho H. Energy and exergy comparison of a flat-plate solar collector using water, Al₂O₃ nanofluid, and CuO nanofluid. *Appl Therm Eng* 2019;159:113959. <https://doi.org/10.1016/J.APPLTHERMALENG.2019.113959>.
- [100] Hosseini SMS, Shafiey Dehaj M. Assessment of TiO₂ water-based nanofluids with two

- distinct morphologies in a U type evacuated tube solar collector. *Appl Therm Eng* 2021;182:116086. <https://doi.org/10.1016/J.APPLTHERMALENG.2020.116086>.
- [101] Choudhary S, Sachdeva A, Kumar P. Time-based analysis of stability and thermal efficiency of flat plate solar collector using iron oxide nanofluid. *Appl Therm Eng* 2021;183:115931. <https://doi.org/10.1016/J.APPLTHERMALENG.2020.115931>.

한 글 요약

나노유체의 광열변환특성 기반 체적흡수 집열기의 성능 연구

이 름 함 정 균

지도교수 조 홍 현

학 과 조선대학교 일반대학원

기계공학과

본 연구에서는 태양열 집열기의 성능 개선을 위해 나노유체를 활용한 체적흡수 태양열 집열기의 특성에 대해 조사를 수행하였다. 나노유체를 활용한 체적흡수 태양열 집열기의 특성을 파악하기 위해 MWCNT, Fe₃O₄, ATO 나노유체의 광열변환 과정의 메커니즘에 대해 조사를 수행하였다. 전산유체해석을 통해 Fe₃O₄ 나노유체를 이용한 평판형 체적흡수 태양열 집열기의 열적 특성에 대해 조사를 수행하였다. 또한, 실험적으로 나노유체가 태양열 집열방법에 미치는 영향성의 평가와 광흡수 특성이 상이한 Fe₃O₄, ATO 나노유체와 Fe₃O₄/ATO 하이브리드 나노유체를 이용해 광흡수 특성이 태양열 집열기의 열적 특성에 미치는 영향성을 조사하였다.

나노유체의 광흡수도 개선은 MWCNT > Fe₃O₄ > ATO 순으로 나타났으며, 0.002wt% MWCNT 나노유체의 광열변환계수는 0.933 으로 단일 나노유체를 가장 우수하였다. 하지만 상이한 파장별 광흡수 특성을 갖는 Fe₃O₄와 ATO 나노유체 혼합을 통해 광흡수도 개선이 가능하며, 0.1wt% Fe₃O₄/ATO 하이브리드 나노유체에서 $m_{Fe_3O_4}/m_{Total} = 0.2$ 인

경우 광열변환효율은 0.932 로 MWCNT 나노유체와 동등한 광흡수도를 확보할 수 있음이 확인되었다. 광흡수 성능을 고려한 제조원가 측면에서 0.002wt% MWCNT 나노유체는 다른 나노유체에 비해 높은 광흡수 성능을 가지며, 저렴하기 때문에 체적흡수식 집열방법을 활용한 태양열 집열기의 작동유체로 적합하다. 광흡수 성능을 고려한 나노유체의 제조원가는 0.075wt% Fe₃O₄ NF > 0.1wt% Fe₃O₄ /ATO NF ($m_{Fe3O4}/m_{Total,NP} = 0.2$) > 0.1% ATO NF > 0.002wt% MWCNT NF 순으로 높다. 0.1 wt% Fe₃O₄ /ATO NF ($m_{Fe3O4}/m_{Total,NP} = 0.2$)는 0.002wt% MWCNT 나노유체와 동등한 성능을 갖고, 0.075wt% Fe₃O₄ NF 보다 광흡수 성능을 고려한 제조원가가 저렴하기 때문에 체적흡수식 태양열 집열기의 작동유체의 대안으로 고려할수 있다.

전산유체해석을 통해 Fe₃O₄ 나노유체를 이용한 평판형 체적흡수 태양열 집열기의 열적 특성을 조사한 결과, 나노유체의 농도변화에 의한 광흡수도 개선이 체적흡수 태양열 집열기의 성능을 결정하는 주요변수임이 확인되었다. Fe₃O₄ 나노유체의 농도가 0 에서 0.1wt%까지 증가함에 따라 평판형 체적흡수 태양열집열기의 광학효율은 최대 43.5%, 최대 액서지 효율은 0.0844 까지 개선되었다.

태양열 집열기의 집열방법에 따라 나노유체의 영향성이 다르며, 집열방법에 따라 태양열 집열기의 성능 개선을 위해 나노유체의 물성 개선에 대한 접근법도 다름이 Fe₃O₄ 나노유체의 활용을 통해 확인되었다. 표면흡수 집열방법의 경우, Fe₃O₄ 나노유체 농도가 0.1wt%까지 증가함에 따라 태양열 집열기 내 열전달 성능지표인 F_R 과 태양열 집열기의 열손실지표인 U_L은 물을 사용할 때 보다 각각 최대 4.27% 와 5.19% 증가되었다. 반면 체적흡수 집열방법의 경우, F_R은 Fe₃O₄ 나노유체 농도가 0.1wt%까지 증가함에 따라 지속적으로 증가하여 최대 11.75% 증가한 반면 U_L은 Fe₃O₄ 나노유체 농도가 0.05wt%까지 증가 시 물 대비 최대 6.37% 감소 후, 증가하였다. 이는 최적흡수 태양열 집열기에 사용된 나노유체의 광흡수도에 의해 결정되며, 과도하게 증가된 광흡수도는 수집기

표면인근에서 광흡수가 이루어져 오히려 체적흡수 집열기의 열효율이 감소됨이 있음이 확인되었다.

나노유체의 광흡수 특성은 체적흡수 태양열 집열기의 성능을 결정하는 주요변수로, 파장대별 상이한 광흡수도를 갖는 나노유체의 혼합을 통해 체적흡수 태양열 집열기의 성능 개선이 가능함이 확인되었다. 0.1wt% $\text{Fe}_3\text{O}_4/\text{ATO}$ 하이브리드 나노유체에서 $m_{\text{Fe}_3\text{O}_4}/m_{\text{Total}} = 0.25$ 인 경우, 0.1wt% Fe_3O_4 나노유체와 0.1wt% ATO 나노유체에 비해 열효율과 엑서지 효율이 개선되었다. 0.1wt% $\text{Fe}_3\text{O}_4/\text{ATO}$ 하이브리드 나노유체는 체적유량이 0.6 lpm 일 때, 엑서지 효율은 입구온도가 55°C 에서 열효율과 최대 엑서지 효율은 0.277 과 0.094 으로, 동일조건에서 0.1wt% Fe_3O_4 와 0.1wt%의 엑서지 효율인 0.189, 0.086 과 0.1wt% ATO 나노유체의 열효율과 엑서지효율인 0.27 과 0.93 에 비해 개선됨이 확인되었다. 이는 ATO 나노유체의 미흡한 가시광선 대역의 광흡수도를 Fe_3O_4 나노유체의 혼합을 통해 광흡수도가 개선된 영향으로 판단된다. 이를 종합하여 판단시, 나노유체를 활용한 체적흡수 태양열 집열방법은 나노유체의 광흡수 성능 개선을 통해 태양열 집열기의 성능 개선 이 가능하며, 표면흡수 집열방법을 대체할 수 있는 방법이라 판단된다.

본 연구에 사용된 나노유체를 이용한 체적흡수식 태양열 집열기는 기존 평판형 태양열 집열기와 진공관형 집열기와 비교 시 동등한 태양에너지 흡수와 낮은 열손실을 가지는 것으로 판단된다. 그러나 체적흡수식 태양열 집열기는 표면흡수식 태양열 집열기와 달리 나노유체의 광흡수 성능에 의존하므로 나노유체의 장기적 분산 안정성 확보가 필요하다. 또한, 열적 특성의 향상에 비해 광흡수율 개선에 필요한 농도는 낮으나 여전히 제조원가가 높다. 하지만 체적흡수식 집열방법은 표면흡수식 집열방법보다 열손실이 낮기 때문에 흡수체의 손상, 열화, 열손실 문제가 있는 고집광 태양열 집열기에 체적흡수식 집열방법의 도입은 고려할 수 있다고 판단된다.

감사의 글

(Acknowledgement)

시간이란 것은 참으로 빨리 지나가는 것 같습니다. 학부연구원생으로 실험실 문을 두드린 지가 엇그저께 같은데, 벌써 박사학위를 마무리 짓는 날이 다가오고 있네요. 그때, 그 시절부터 지금까지 참으로 많은 일이 있었습니다. 힘든 날도 많이 있었지만 그보다 즐거운 날이 많아, 지금까지의 삶에 있어 정말로 많은 의미를 부여하는 것 같습니다. 학위는 개인이 받는 것이지만, 지금의 제가 있기까지 주변의 많은 분들이 도움을 주셔서, 적절한 감사의 표현이 떠오르지 않네요.

박사과정을 시작할 때 어떻게 보면 남들과 다른 길을 선택해서 불안하셨을 텐데 묵묵히 지지해주신 아버지, 어머니, 미화, 대균이, 매제, 고모 정말로 고맙습니다. 그리고, 지금의 자리에 오기까지 많은 인생에 대한 조언과 학문에 대한 가르침을 주신 지도교수님인 조홍현 교수님 감사합니다. 아직도 부족하지만 교수님의 지도편찬에 부끄럽지 않도록 앞으로도 노력하도록 하겠습니다. 그리고, 바쁘신 와중에서도 논문지도를 해주신 오동욱 교수님, 박정수 교수님, 이호성 교수님, 박차식 교수님 감사합니다. 연구자의 자세와 태도, 논문 작성의 방법론 등 많은 것을 배웠습니다.

그리고 학부연구원때부터 지금까지 힘들 때마다 이런저런 하수연들 들어주고 뒤에서 지지해준 윤찬아 고맙다. 쓴 말, 좋은 말 해준 말들이 포기하지 않고 지금까지 학위과정을 할 수 있는 원동력을 줬어. 너가 앞에서 당겨주고 뒤에서 밀어줘서 지금의 자리에 도착하라 수 있었어. 형민, 광현, 우빈아. 먼저 사회에 나가 이런 저런 조언을 해주기도 하고, 힘들 때 같이 놀아주기도 하고, 그런 것이 쉼터가 되줘서 힘을 낼 수 있었다.

선배로서 잔소리도 많이 했지만 든든히 뒤를 받쳐준 실험실 현 일동인 민정이, 민준이, 의, 헤민이, Tsogtbilegt, hamza, 나영이, 명재야. 너희가 도와줘서 무사히 학위논문을 마무리할 수 있었다. 힘든 내색을 하지 않아서, 항상 미안하고 고맙다. 너희들

하고 동고동락하면서 즐긴 실험실 시간이 너무 빨리 지나가는 게 정말 아쉽고, 자랑스러운 시간이라고 생각해. 그리고 Veerakumar, 학위논문 작성할 때, 멘탈 흔들릴 때마다 조언해줘서 고마워.

그리고 짬 시간 마다 서로 이것저것 수다를 떨기도 하고, 하소연을 하기도 하고, 자랑하기도 하고, 열유체 파트 분위기를 좋게 만드는데 공헌을 한 지능형열시스템 실험실, 차세대에너지동력시스템 실험실, 열전달 실험실, 유동가시화 실험실의 원로 장들인 터기, 원준, 대현, 호성, 성근아. 너희 덕에 이것 저것 새로운 것도 많이 듣고, 생각도 해본 것 같다.

각각 감사를 표하기에는 너무 많은 사람들에게 도움을 받은 것 같습니다. 학위과정은 이제 끝났지만, 저의 인생은 이제 시작한 것 같습니다. 지금까지 받은 도움을 베풀려면 앞으로 더욱 정신하겠습니다.

도움을 주신 모든 분들께 감사드립니다.

함정균 올림